ADVANCEMENTS IN MEASURING AND MODELING THE MECHANICAL AND HYDROLOGICAL PROPERTIES OF SNOW AND FIRN: MULTI-SENSOR ANALYSIS, INTEGRATION, AND ALGORITHM DEVELOPMENT

by

Tate G. Meehan

A dissertation

submitted in partial fulfillment

of the requirements for the degree of

Doctor of Philosophy in Geophysics

Boise State University

August 2022

BOISE STATE UNIVERSITY GRADUATE COLLEGE

DEFENSE COMMITTEE AND FINAL READING APPROVALS

of the dissertation submitted by

Tate G. Meehan

Dissertation Title: Advancements in Measuring and Modeling the Mechanical and Hydrological Properties of Snow and Firn: Multi-sensor Analysis, Integration, and Algorithm Development

Date of Final Oral Examination: 02 May 2022

The following individuals read and discussed the dissertation submitted by student Tate G. Meehan, and they evaluated the student's presentation and response to questions during the final oral examination. They found that the student passed the final oral examination.

H.P. Marshall, Ph.D.	Chair, Supervisory Committee
Ellyn Enderlin, Ph.D.	Member, Supervisory Committee
Grady Wright, Ph.D.	Member, Supervisory Committee
Elias Deeb, Ph.D.	Member, Supervisory Committee

The final reading approval of the dissertation was granted by H.P. Marshall Ph.D., Chair of the Supervisory Committee. The dissertation was approved by the Graduate College.

DEDICATION

Is not something bestowed, it is maintained. In publication, the dedication of these efforts are inked, but the feelings of dedicated work and integrity shouldn't be forgotten, nor remembered, but unwavering. To complete this dissertation, alongside my colleagues, I dedicated myself to completing geophysical surveys in cold and harsh environments, and to the accuracy and testament of scientific and mathematical analysis, to arrive at the best estimates presented within. This work is the culmination of far too many people to fully acknowledge. To those whom helped and supported this work, you are remembered. And to any readers, I appreciate your dedication which led you to engage in this dissertation.

ACKNOWLEDGMENTS

The *SnowMicroPenetrometer Applications for Winter Vehicle Mobility* study was conducted for the Assistant Secretary of the Army for Acquisition, Logistics, and Technology under project number 465395, "Boreal Aspects of Ensured Maneuver (BAEM)," which is part of the U.S. Army Engineer Research and Development Center (ERDC) 6.2 Remote Assessment of Infrastructure for Ensured Maneuver (RAFTER) Program managed by Ms. Danielle Whitlow ERDC Geotechnical and Structures Laboratory (GSL). This work is continuing under project number 471941, "Remote Assessment of Snow Mechanical Properties" and "Mobility in Peat and Northern Soils," under the Entry and Sustainment in Complex Contested Environments Program managed by Dr. John Rushing, GSL.

The work was performed by the LiDAR and Wetlands Group and the Terrain and Ice Engineering Group of the Remote Sensing / Geographic Information System Center of Expertise (CEERD-RS) and the Force Projection and Sustainment Branch (CEERD-RRH) of the Research and Engineering Division (CEERD-RR), U.S. Army Engineer Research and Development Center, Cold Regions Research and Engineering Laboratory (ERDC-CRREL). At the time of publication, Dr. Elias Deeb was lead for the LiAR and Wetlands Group; Mr. Stephen Newman was lead for the Terrain and Ice Engineering Group; Mr. David Finnegan was Chief, CEERD-RS; Mr. Justin Putnam was Acting Chief, CEERD-RRH; and Mr. Jared Oren was Acting Chief, CEERD-

RR. The Deputy Director of ERDC-CRREL was Mr. David B. Ringelberg, and the Director was Dr. Joseph L. Corriveau. COL Ivan P. Beckman was Commander of ERDC, and Dr. David W. Pittman was the Director.

Greenland Traverse for Accumulation and Climate Studies was funded by the National Science Foundation Office of Polar Programs: Awards 1417921 and 1417678. Additional support of the works *Reconstruction of historical surface mass balance* $1984 - 2017$ *from GreenTrACS multi-offset ground-penetrating radar*, *Firn and Radiostratigraphy Modeling using the 1D Kinematic Wave Equation*, and *Ice Sheet Surface Property Retrieval and Automatic Firn Layer Tracing from Airborne Radar* was awarded through the NASA Idaho Space Grant Consortium Graduate Fellowship and the STEM Student Employment Program through the U.S. Army Engineer Research and Development Center, Cold Regions Research and Engineering Laboratory.

Spatially Distributed Snow Water Equivalent from Ground-based and Airborne Sensor Integration at Grand Mesa, Colorado, USA and *Over-snow Vehicle Mobility Index Assessment and Prediction* research was funded under the U.S. Army Engineer Research and Development Center (ERDC) Basic Research Program through Program Element 601102/Project AB2/Task 1. Funding was also provided by the NASA Terrestrial Hydrology Program (THP) in coordination with the SnowEx program awards NNX17AL61G and 80NSSC18K0877. We wish to thank all of the scientific participants and logistical support staff of the SnowEx 2020 campaign, who helped make this research possible.

The *Ground-penetrating Radar Experiments at Camp Arenales, Chile* effort was sponsored by the Assistant Secretary of the Army for Defense, Export and Cooperation under the U.S. – Chile Extreme Environments Project, Program Element 622144,

Project BL7, Task 01.

Quantifying Firn Depth and Density in the Percolation Zone of Wolverine Glacier, Alaska, was supported by the U.S. Geological Survey, Climate Research and Development Program, Benchmark Glacier Project.

The findings of this document are not to be construed as an official Department of the Army position unless so designated by other authorized documents. Permission was granted by the Director, Cold Regions Research and Engineering Laboratory, to publish this information. The use of trade, product, or firm names in this document is for descriptive purposes only and does not imply endorsement by the U.S. Government.

ABSTRACT

Estimating snow mechanical properties – such as elastic modulus, stiffness, and strength – is important for understanding how effectively a vehicle can travel over snow-covered terrain. Vehicle instrumentation data and observations of the snowpack are valuable for improving the estimates of winter vehicle performance. Combining in-situ and remotely-sensed snow observations, driver input, and vehicle performance sensors requires several techniques of data integration. I explored correlations between measurements spanning from millimeter to meter scales, beginning with the SnowMicroPenetrometer (SMP) and instruments applied to snow that were designed for measuring the load bearing capacity and the compressive and shear strengths of roads and soils. The spatial distribution of snow's mechanical properties is still largely unknown. From this initial work, I determined that snow density remains a useful proxy for snowpack strength. To measure snow density, I applied multi-sensor electromagnetic methods. Using spatially distributed snowpack, terrain, and vegetation information developed in the subsequent chapters, I developed an over-snow vehicle performance model. To measure the vehicle performance, I joined driver and vehicle data in the coined Normalized Difference Mobility Index (NDMI). Then, I applied regression methods to distribute NDMI from spatial snow, terrain, and vegetation properties. Mobility prediction is useful for the strategic advancement of warfighting in cold regions.

The security of water resources is climatologically inequitable and water stress causes international conflict. Water resources derived from snow are essential for modern societies in climates where snow is the predominant source of precipitation, such as the western United States. Snow water equivalent (SWE) is a critical parameter for yearly water supply forecasting and can be calculated by multiplying the snow depth by the snow density. In this work, I combined high-spatial resolution light detection and ranging (LiDAR) measured snow depths with ground-penetrating radar (GPR) measurements of two-way travel-time (TWT) to solve for snow density. Then using LiDAR derived terrain and vegetation features as predictors in a multiple linear regression, the density observations are distributed across the SnowEx 2020 study area at Grand Mesa, Colorado. The modeled density resolved detailed patterns that agree with the known interactions of snow with wind, terrain, and vegetation. The integration of radar and LiDAR sensors shows promise as a technique for estimating SWE across entire river basins and evaluating observational- or physics-based snow-density models. Accurate estimation of SWE is a means of water security.

In our changing climate, snow and ice mass are being permanently lost from the cryosphere. Mass balance is an indicator of the (in)stability of glaciers and ice sheets. Surface mass balance (SMB) may be estimated by multiplying the thickness of any annual snowpack layer by its density. Though, unlike applications in seasonal snowpack, the ages of annual firn layers are unknown. To estimate SMB, I modeled the firn depth, density, and age using empirical and numerical approaches. The annual SMB history shows cyclical patterns representing the combination of atmospheric, oceanic, and anthropogenic climate forcing, which may serve as evaluation or assimilation data in climate model retrievals of SMB.

The advancements made using the SMP, multi-channel GPR arrays, and airborne LiDAR and radar within this dissertation have made it possible to spatially estimate the snow depth, density, and water equivalent in seasonal snow, glaciers, and ice sheets. Open access, process automation, repeatability, and accuracy were key design parameters of the analyses and algorithms developed within this work. The many different campaigns, objectives, and outcomes composing this research documented the successes and limitations of multi-sensor estimation techniques for a broad range of cryosphere applications.

TABLE OF CONTENTS

LIST OF TABLES

LIST OF FIGURES

LIST OF ABBREVIATIONS

H_s Snow depth

H_{veg} Vegetation height

S_{veg} Proximity to vegitation

Z_g Bare earth elevation

Z_s Snow-covered earth elevation

∂xH_s east component of snow depth gradient

∂xZ_g east component of bare earth elevation gradient

∂xZ_s east component of snow surface elevation gradient

∂yH_s north component of snow depth gradient

∂yZ_g north component of bare earth elevation gradient

∂yZ_s north component of snow surface elevation gradient

$aspectH_s$ aspect of snow depth

$aspectZ_g$ aspect of bare earth elevation

$aspectZ_s$ aspect of snow surface elevation

sxH_s slope of snow depth

sxZ_g slope of bare earth elevation

sxZ_s slope of snow surface elevation

1D One-dimensional

2D Two-dimensional

AAV Assault Amphibious Vehicle

APC Armored Personnel Carrier

ASO Airborne Snow Observatory

BAEM Boreal Aspects of Ensured Maneuver

C Center

CD Coast Down

CMP Common Midpoint Gather

CO Common Offset Gather

CRIM Complex Refractive Index Method

CRREL Cold Regions Research and En-

gineering Laboratory

DGPS Differential Global Positioning System

EM Electromagnetic

ERDC Engineer Research and Development Center

F-K Frequency-Wavenumber

GEN3ENS Ensemble of the Third Generation Reanalysis Models

GIS Geogrphic Information System

GMSP Grand Mesa Skyway Study Plot

GPR Ground-Penetrating Radar

GPS Global Positioning System

GreenTrACS Greenland Traverse for Accumulation and Climate Studies

GrIS Greenland Ice Sheet

GTC15 GreenTrACS Core 15

H Horizontal Polarization

HH Horizontal-Horizontal Polarization

HiCARS High Capability Airborne Radar Sounder

HK Homodyned-K type distribution

HL Herron and Langway Model

HMMWV High Mobility Multipurpose Wheeled Vehicle

HV Horizontal-Vertical Polarization

IMU Interitial Measurement Unit

IOP Intensive Observation Period

IQR Interquartile Range

IRH Isochonous Refleciton Horizon

LiDAR Light Detection and Ranging

LMO Linear Moveout

LVSR Logistics Vehicle System Replacement

LWC Liquid Water Content

LWD Lightweight Deflectometer

M3C2 Multiscale Model to Model Cloud Compare

MAE Mean Absolute Error

ME Mean Error

MERRA Modern-Era Retrospective analysis for Research and Applications

MLR Multiple Linear Regression

MOBLP Mobility Loop

MTVR Medium Tactical Vehicle Replacement

MxHL MxRadar - Herron and Langway Model

MxRadar Multi-channel, Multi-offset, Radar

N North

NATC Nevada Automotive Test Center

NDMI Normalized Difference Mobility Index

NIR Near-Infrared

NMO Normal Moveout

OIB Operation IceBridge

PCA Principle Component Analysis

QC Quality Control

RAFTER Remote Assessment of Infrastructure for Ensured Maneuver

RMSD root-mean-square difference

RMSE root-mean-square error

RWY Runway

S South

SLF Operation IceBridge

SMB Surface Mass Balance

SMP SnowMicroPenetrometer

SUSV Small Unit Support Vehicle

SWE Snow Water Equivalent

TWT Two-Way Travel-time

TXY Taxiway

V Vertical Polarization

INTRODUCTION

Snow exists very close to the temperature at which it melts or sublimates, and because of this, snow undergoes rapid and complex metamorphism. Snow accumulated, metamorphosed, and ablated under various meteorological forcings affect its persistence and nature on the ground. Snow metamorphism may construct or destruct bonds between grains, and these processes occur differently in wet and dry snow. Dry snow metamorphism is driven by temperature gradients. When the gradient is large enough ($> 0.1°C/cm$) vapor migrates along the gradient moving mass from one grain to the next forming weak and transient bonds. When the temperature gradient is small, snow forms into rounded and well bonded grains. Depending on the liquid water volume in the snow pack, wet snow metamorphism may form cohesive or cohesionless bonds. In environments where snowpacks do not completely ablate, multiple years of accumulated snow compacts due to overburden pressure and forms the sintered bonds of firn. When the pore space of firn becomes impermeable, glacial ice is formed.

The strength of bonds on the microscale gives rise to the cohesive properties of snow at the macroscale. Snow macro-mechanical properties – such as elastic modulus, stiffness, and strength – in effect, govern vehicle performance by supporting compressive and shear forces. Vehicle instrumentation data and mechanical observations of the snowpack can thereby improve the estimates of winter vehicle performance in

a modeled framework. Combining in-situ and remotely-sensed snow observations, driver input, and vehicle performance sensors requires several techniques of data integration, which I explored later in this dissertation. In-situ measurements of snow mechanics are difficult to make, and are often inferred from geophysical data inversion.

The SnowMicroPenetrometer (SMP) measures the force required to penetrate the snow with very high depth resolution. The SMP is driven through the snow at a constant rate causing linear elastic strain, and is capable of measuring the individual rupture forces of snow gain bonds and micro-mechanical properties via data inversion. I found correlations between the SMP measurements and instruments applied to snow that were designed for measuring the load bearing capacity and the compressive and shear strengths of roads and soils. In place of direct observations of snowpack mechanics, I determined that snow density remains a useful surrogate for snowpack strength. Using spatially distributed snowpack, terrain, and vegetation information developed in the subsequent chapters, as an extension of this work, I developed an over-snow vehicle performance model. The Normalized Difference Mobility Index (NDMI) joins driver and vehicle data to characterize over-snow vehicle performance. Using the spatial snow, terrain, and vegetation properties as predictor varibles, NDMI was distributed throughout the area of interest. The strategic advancement of warfighting in cold regions relies on the accurate foresight of mobility logistics. The application of mobility prediction directly supports military campaigns.

The security of water resources is climatologically inequitable, and the future of water security is at risk. Changes to the supply and demand of water requires storage and distribution strategies that better meet the legal, economic, political, cultural, and social needs of water users. Rivers and basins form international boundaries and

require the cooperation of various nation's stakeholders for fair resource distribution. Stresses to water supply are hence a cause of international conflict, and conversely, water surpluses can be exchanged as peace.

Water resources derived from snow are essential for modern societies in climates where snow is the predominant source of precipitation, such as the western United States. Snow water equivalent (SWE) is a critical parameter for yearly water supply forecasting and can be calculated by multiplying the snow depth by the snow density. Depth and density are highly valued hydrological properties of snow, as the estimation of depth and density are then a means to water security. Remote sensing advancements made it possible to measure snow depth at basin-wide scales, but snow density has remained challenging to measure over large spatial extents.

Radar techniques are the most prevalent for remotely sensing snow density because of the relationships existing between dielectric permittivity (a main constituent of electromagnetic wave propagation) and snow density. In media with low conductivity, such as snow, electromagnetic (EM) wave propagation speed is controlled by the dielectric permittivity. At ground-penetrating radar frequencies, snowpacks may be simplified as layered homogeneous porous solids with an ice matrix and pore space containing a mixture of air and water. Applying this snowpack concept, the measurement of the EM wave speed yields the dielectric permittivity; and thereby depth, density, and SWE. With information about the propagation velocity of the snow, such as density measured in a snow pit, GPR two-way travel-time (TWT) can directly estimate the snow depth. Conversely if snow depth is known, TWT can directly solve for snow density. Or, by applying a ray-path function of TWT versus antenna separation (offset), the velocity, and thereby snow depth and density,

can be estimated. I developed fundamentals and applications of GPR by deploying various multi-channel configurations and developing signal processing and data inversion algorithms to accurately measure the snow depth, density, and water equivalent in polar firn and seasonal snow cover. Wave speed estimation relies on interpreting TWT from radargrams, which is a laborious process that requires expert knowledge of radar theory and digital signal filtering. Over the course of the campaigns analyzed, thousands of kilometers of multi-channel radar data were collected. I automated the signal processing and manual picking of travel-times using scripted workflows and multi-channel coherence methods. Drawing from geostatistical analysis, I gained insights to the wind, terrain, and vegetation interactions that affect snow density and showed that TWT exhibits spatial variability similar to that of SWE.

In our changing climate, snow and ice mass are being permanently lost from the cryosphere. Mass balance is an indicator of the (in)stability of glaciers and ice sheets, measured as the sum of surface mass inputs and losses (surface mass balance) and discharged mass. Surface mass balance may be estimated by multiplying the thickness of any annual snowpack layer by its density. Though, unlike applications in seasonal snowpack, knowing which depths constitute the annual layers is non-trivial. In perennial snowpacks (firn) of glaciers, firn accumulates like sediment in ocean basins, forming depositional stratigraphic horizons in isochronous layers. Stratigraphic layering augments a tree-ring like temporal component to the firn that is embedded in the radargram. In the second chapter, I used the snow accumulation and density estimated by multi-channel GPR wave speed analysis. I modeled the firn depth, density, and age using empirical and numerical approaches. Leveraging the age-depth model, I designed a radar signal process that filters along horizons of continuous stratigraphic

age. This innovation enabled the interpretation of deeper and older layers, and estimates of multidecadal and annual surface mass balance spanning $1984-2017$, within the high elevation dry-snow accumulation zone of Greenland. The annual surface-mass balance history shows cyclical patterns representing the combination of atmospheric, oceanic, and anthropogenic climate forcing. I examined wind and terrain features thought to control spatial snow density patterns, and found greater length scales of variability in the direction of the prevailing wind than in the orthogonal direction. Quantified surface density and spatial variability of snow density is useful for initializing firn compaction models used in remote sensing and climate model retrievals of surface mass balance.

In the third chapter, I combined high-spatial resolution light detection and ranging (LiDAR) measured snow depths with ground-based radar measurements of TWT to solve for snow density. Then using LiDAR derived terrain and vegetation features as predictors in a multiple linear regression, the density observations were distributed across the SnowEx 2020 study area at Grand Mesa, Colorado. The modeled density resolved detailed patterns that agree with the known interactions of snow with wind, terrain, and vegetation. The integration of radar and LiDAR sensors shows promise as a technique for estimating SWE across entire river basins and evaluating observational- or physics-based snow-density models. Accurate estimation of water equivalent is a means of water security, and the technique of combining LiDAR and GPR information results in SWE estimates within 10 % uncertainty.

Overall, the advancements made within this dissertation increased our understanding of the spatial snow distribution and the operational utility of the SMP, multi-channel GPR, and airborne radar and LiDAR in glacial and seasonal snow environments. The measurements and modeled outcomes of snow depth and density using multi-sensor techniques feeds back directly into vehicle mobility modeling, surface mass balance, and annual SWE estimation.

CHAPTER 1:

SNOWMICROPENETROMETER APPLICATIONS FOR WINTER VEHICLE MOBILITY

Abstract

The U.S. Army Cold Regions Research and Engineering Laboratory provides technical support to military forces, one area being vehicle mobility modeling over snow. Many factors control vehicle performance, including the vehicle specifications and the land surface conditions. However, estimating snow macromechanical properties – such as elastic modulus, stiffness, and strength – is critical for understanding how effectively a vehicle will travel over snow-covered terrain. Vehicle instrumentation data and observations of the snow pack are necessary to improve the estimates of winter vehicle performance. Currently, snow depth and bulk snow density alone drive the available mobility performance index.

This research deployed a SnowMicroPenetrometer (SMP) to measure hard, vehicle-compacted snow and groomed snow roads. Microstructural and micromechanical properties derived from the SMP data analysis were correlated to the Rammsonde penetrometer hardness, an established snow instrument, and to the shear-strength test vane and Light Weight Deflectometer (LWD), which are common in soil and aggregate layer assurance methods in road construction. Correlating these tools requires a new theo-ry for inverting SMP signals for micromechanical properties that relaxes the assumption of low-density snow. Additionally, a scaling law appropri-ate to this type of hard snow is required to relate the SMP observations of the microscale and the macroscale properties.

1.1 Introduction

1.1.1 Background

The U.S. Engineer Research and Development Center (ERDC) Military Engineering Program on Remote Assessment of Infrastructure for Ensured Maneuver (RAFTER) Boreal Aspects of Ensured Maneuver (BAEM) identifies the need for modeling over-snow vehicle performance, as many factors related to vehicle setup and land surface condition contribute to vehicle efficiency. Accurately estimating snow macromechanical characteristics – such as elastic modulus, stiffness, and strength – is critical for understanding how effectively a vehicle will travel over snow-covered terrain. Vehicle instrumentation data (inertial measurement units and vehicle telemetry) and observations of the snowpack (both satellite and ground-based) are necessary to improve the modeled estimates of winter vehicle performance. Currently, performance index is driven by snow depth and bulk snow density alone.

The snow characterization research effort deployed a SnowMicroPenetrometer (SMP) that was jointly developed by the ERDC Cold Regions Research and Engineering Laboratory (CRREL) and the Swiss Federal Institute for Snow and Avalanche Research (SLF) two decades ago (Schneebeli & Johnson, 1998). Our study used a SMP with a force sensor range of $0 - 500\ N$ to measure hard, vehicle-compacted snow and processed or groomed snow roads. Median values of the high-resolution snow structural profiles from the SMP are correlated to Rammsonde, shear strength test vane, and LWD values over the depth range of each independent in-situ measurement. We understand the value of the SMP as a tool for future mobility studies in different snow types through statistically significant correlation, but also understand

a lack of correlation as deficiencies of the SMP hardware, the penetration theory used, and the micro-to-macro scaling laws.

Winter vehicle mobility studies by CRREL have evaluated vehicle setup and snow condition (Shoop *et al.*, 2014); however, the SMP has not previously been applied to a mobility study. This work is the first winter vehicle mobility study to examine the usefulness of the SMP for research on military vehicle efficiency.

1.1.2 Objectives

The overarching objective of this research is to improve vehicle mobility modeling by incorporating additional snow physics. Characterizing the snow mechanical properties and their impact on vehicle mobility is challenging and requires varied field instruments and specialists with a wide range of expertise. This chapter overviews four instruments used to characterize snow for the BAEM project – the SMP, Rammsonde (ram), shear vane, and LWD (Sections 1.2.2 – 1.2.5) – and assesses required load-cell ranges of the SMP for its application to hard, vehicle-compacted snow. Within this chapter, I correlated the microphysical parameters estimated from SMP measurements to those from a suite of instruments designed or tested to measure snow mechanical properties. The work derived from this study aims to bridge micro-to-macro snow physics with the ultimate intent to infer snow structure from satellite imagery for use as initial and boundary conditions for vehicle mobility models.

1.1.3 Approach

The field site chosen for this study was the Nevada Automotive Test Center (NATC) in West Yellowstone, Montana. NATC leases the West Yellowstone Airport property from the Montana Department of Transportation Aeronautics Division for winter testing. During the winter, the airport is closed to air traffic, with the

exception of emergency rescue helicopters. NATC maintains the site and the various test vehicles during the winter months. Our study, the NATC campaign, accomplishes the objectives through the following tasks:

- Perform vehicle tests in various snow-surface conditions at the NATC test site, West Yellowstone, Montana.
- Sample the snow within hours after vehicle tests with the suite of instruments. This includes manual measurements of snow depth, density, hardness, shear strength, deflection, dielectric permittivity, and near-infrared (NIR) photography.
- Develop automated signal processing for SMP analysis and solve for the snow microstructural properties, applying the method of Marshall & Johnson (2009).
- Apply statistical regression analysis to draw correlations between the measurements of the ram, shear vane, LWD, and the microphysical parameters derived from the SMP.

Our approach is limited by the abilities of the various instruments to measure particular snow types. The SMP exhibited difficulty penetrating groomed snow roads, the ram and shear vane exhibited difficulty measuring soft or virgin snow, and the LWD requires groomed snow.

1.2 Field Campaign and Data Acquisition

1.2.1 Study-site Background

During late January 2018, NATC operated Marine Corps vehicles in several snow conditions (processed snow road, ice lane, trafficked snow, and virgin snow) using

various performance setups (tire pressure configurations, differential configurations, towed/pulling/load carrying) to conduct mobility performance tests (traction, drag-bar, and coast down). During a coast-down test, the test vehicle is accelerated to a constant velocity on tarmac or groomed road before entering a virgin snow-pack, roughly 50 cm deep, through which the vehicle rolls to a stop. Beside coast-down tests, the other tests were simple vehicle passes through virgin or rutted snow. The CRREL and Boise State University snow characterization team measured the snowpack using a suite of instruments with the objective of recording the snow conditions before and after alteration by the military vehicles. In all test scenarios, measurements were taken in the resulting tracks and area between the tracks, where the undercarriage of the vehicle resulted in a belly drag that compacted the snow to a lesser degree.

This chapter discusses the results from data acquired using the SMP, ram, shear vane, and LWD (Sections 1.2.2 – 1.2.5). Figure 1.1 identifies the acquisition locations for each day of the NATC campaign. Throughout the data analysis, this chapter uses the following nomenclature: date (XX), cardinal location (north (N), south (S), and center (C), snow type/location (runway (RWY), taxiway (TXY), mobility loop (MOBLP), and virgin snow (VS)), and vehicle name (e.g. Medium Tactical Vehicle Replacement (MTVR) and Logistics Vehicle System Replacement (LVSR)), and test type (e.g. coast down (CD)) when applicable or unique.

Figure 1.1: Satellite imagery of the NATC facility at the West Yellowstone airport during snow-off conditions. Waypoints plotted indicate the locations studied during the field campaign.

1.2.2 SnowMicroPenetrometer

The SMP (Figure 1.2) is a mechanically driven sonde penetrometer capable of measuring the hardness of the snowpack through high-resolution sampling of penetration force (F) versus displacement (d), as the snow deforms in multiple modes (tension, compression, and shear). This instrument samples the penetration force 250 times per millimeter and drives through the snowpack at a rate of 20 mm/s. This corresponds to a strain rate above 10^{-3}, such that the snow behaves in a nearly linear elastic manner with brittle failure (Shapiro *et al.*, 1997). Thus, in theory, the SMP is capable of measuring the individual ruptures of snow-grain bonds that are in contact with the penetrometer tip. The SMP was initially designed to operate in light alpine snowpacks and to be sensitive to structural weaknesses within the snowpack, at penetrations forces of approximately 0.01 N, for understanding and assessing avalanche hazard (Schneebeli & Johnson, 1998).

The standard SMP load cell is sensitive to a range of forces between 0 and 42 N (Pielmeier, 2003). For the NATC campaign, the SMP was equipped with a higher capacity load cell that enables the SMP to measure forces up to 500 N. The hard-packed snow conditions created by and for the vehicle testing demand the increased dynamic range of the load cell, which has previously been used for hard wind-packed snow in the Arctic and Antarctic. The increased dynamic range comes at a cost in force resolution and noise floor, as the analog-to-digital converter used for both the low and high ranges is currently the same and the noise level is higher for the larger-range force sensor.

The SMP outputs a binary format data file (.pnt) that is unpacked using Python or MATLAB code. The Python code, SnowMicroPyn, was developed by SLF and is

Figure 1.2: The SMP mounted on a sled at the West Yellowstone airfield during the NATC campaign. The SMP was developed and designed by Dr. Martin Schneebeli (SLF) and Dr. Jerome Johnson (CRREL) in the mid-1990s. The pictured sled was designed and built by Dr. Matthew Sturm (CRREL).

used primarily for extracting a Global Positioning System (GPS) location from the data header file. Within this chapter I developed MATLAB scripts that automate the signal processing and apply the inversion code of Marshall & Johnson (2009) for estimation of the micromechanical and microstructural snow properties.

The SMP can acquire high-resolution force resistance profiles rapidly and with little-to-no strenuous effort in the field. The SMP was mounted in a sled with two runners and an open floor. The SMP sled was indexed with five positions separated by 20 cm to allow for five acquisitions per sled location. After the five positions were acquired, the sled was advanced. This configuration allowed for transport of the SMP across the snow without disturbing the snow beneath the penetrometer. The SMP was operated from a battery powered console with an integrated GPS and data logger. The SMP had a maximum penetration depth of 61 cm, and the operator may

optionally define the depth of penetration for the profile. When the selected depth is reached or if the SMP is unable to penetrate (hard snow or the ground), the probe is automatically reversed. SMP profiles are individually stored in binary .pnt files on a removable secure digital card.

Data was acquired in a series of transects crossing perpendicular to the vehicle tracks. The typical transect would begin in the virgin snow; advance across the tire rut, the belly drag, and the second tire rut; and conclude in the virgin snow on the opposite side of the vehicle path. This resulted in five SMP test positions, each with five SMP measurements that were 20 cm apart in each snow condition. Figure 1.3 presents the SMP penetration-force profiles after signal processing (Section 1.3). The snow surface is automatically picked within the signal processing algorithm and is identified by a red X. An air gap exists between the SMP and the snow surface. In virgin snow, this distance is approximately 10 cm. When the SMP is suspended above a tire rut, this distance is greater, as shown in Figure 1.3c. NIR photographs corroborate the stratigraphic layers seen in the SMP profile through virgin snow. However, the stratigraphy is destroyed in trafficked snow and is not clearly visible in the NIR spectrum. The SMP is capable of resolving stratigraphic layers present in trafficked snow by measuring the snow penetration force with greater vertical resolution and sensitivity.

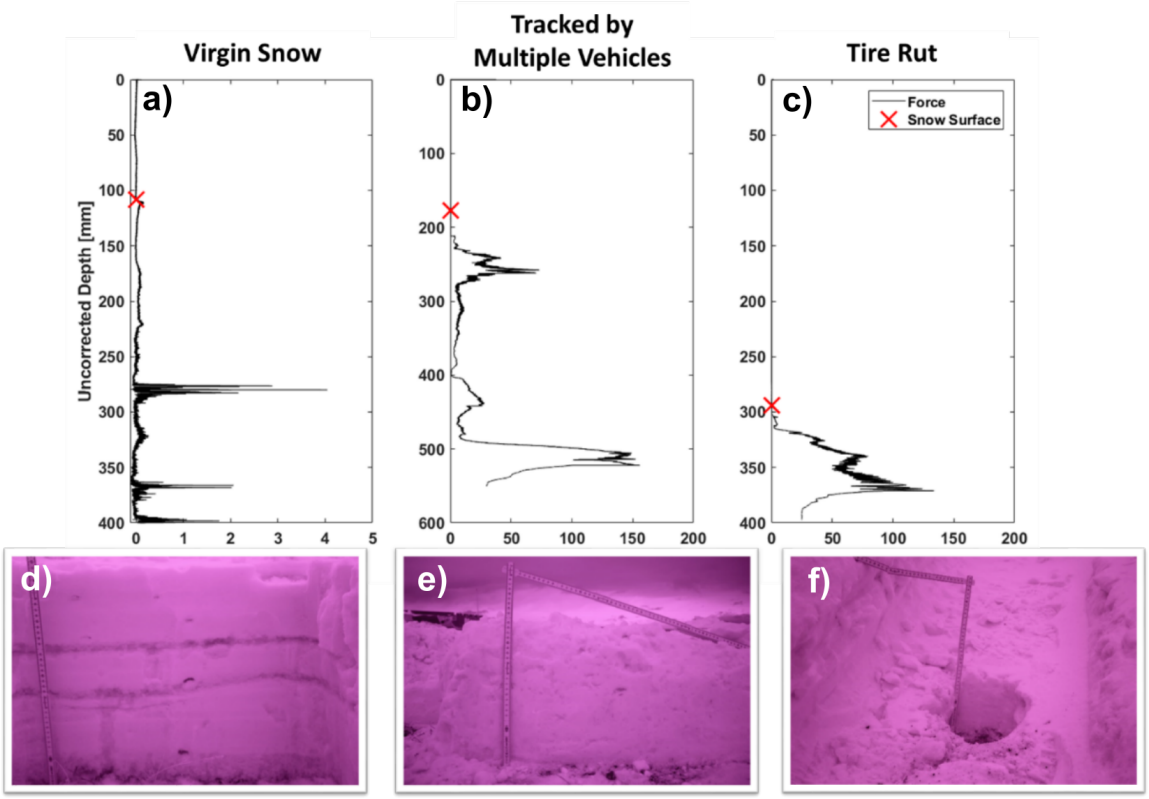

Figure 1.3: Example SMP hardness profiles acquired in the three important snow conditions: *a)* virgin snow, *b)* snow trafficked by multiple vehicles, and *c)* a tire rut. SMP force profiles are shown after signal processing. The signal processing algorithm automatically identifies the snow surface, indicated by the red X. NIR photographs *d), e),* and *f)* correspond to *a), b),* and *c),* respectively. NIR photography reveals the snow stratigraphy in the virgin snow, and lack there of in the driven snow. The SMP is capable of identifying snow layers not obvious to the eye or to manual measurements.

1.2.3 Rammsonde Penetrometer

The ram penetrometer is one of the early hardness penetrometers (Bader, 1954a) and is the standard instrument for determining snow hardness in the field. The value of ram hardness indicates the resistance of individual snow layers to vertical penetration (Abele, 1963). The ram (Figure 1.4) has the capability of retrieving a hardness measurement at the snow surface and within stratigraphic intervals of the snow, though measurements of ram hardness are typically reported as a bulk value over the measurement profile. Snow microstructural properties cannot be estimated from bulk measurements of ram hardness. Abele (1963) developed the correlation between unconfined compressive strength of processed snow and ram hardness and conveyed the underlying theory and mechanics of the tool.

The snow characterization team manually tabulated in the field the data acquired by the ram. The ram hardness index

$$R = \frac{WHn}{z_n} + W + Q \tag{1.1}$$

is formulated from the hammer weight (W), the drop height (H), the weight of the penetrometer (Q), the penetration depth per the number of hammer blows (z_n), and the number of hammer blows applied to achieve an interval of penetration (n). Abele (1963) provides an overview of the instrument design and the basis for Equation 1.1. The ram team sampled each test location carefully as to not disturb the snow for its measurement or the measurements of the other instruments in the field. Ram hardness profiles were recorded in the virgin snow, belly drags, and tire ruts for comparison with the SMP profiles.

Figure 1.4: CRREL's Dr. Sally Shoop using the ram to measure the hardness of a vehicle belly drag after a coast-down test at NATC.

1.2.4 Shear Vane

The team measured surface shear strength by using a Geonor H-60 handheld vane tester (henceforth shear vane). The shear vane has an orthogonal, cross-shaped blade. The standard vane blade and length come in three sizes, and the size is chosen based on the snow strength. Custom vane sizes are also sometimes used. The vane is inserted into the snow to a depth covering the entire vane, and then a steady rotational force is applied until the snow shears. The maximum shear force is recorded as kilopascals. The shear-strength values for each site are the average of three measurements. ASTM D2573–18 (ASTM International, 2018) details the use of the shear vane in soils.

The shear-vane measurements were recorded at the snow surface of pits together with temperature, density, and snow height. Virgin and soft belly-drag snow provided insufficient strength for measurement with this tool with the exceptions of measurements made in vehicle belly drags on 30 January at the North mobility loop entrance and 31 January at the South runway, limiting the number of observations for this study. The field scientist manually recorded the maximum shear stress applied by this instrument. Shear-vane measurements were repeated several times at each snow pit to estimate the shear-strength distribution.

1.2.5 Light Weight Deflectometer

The LWD measures the ground deflection when an impact load is applied to a plate that has a geophone at its center. The LWD is conventionally used for quality control and assurance of soil and aggregate layers in road construction. Using the LWD on snow surfaces is a new application for the device (Wieder *et al.*, 2019). As the applied load increases, the deflection will increase for a linear, elastic material. Snow in many circumstances does not behave as a linear elastic material (Shapiro *et al.*, 1997);

however, at the high strain rates used in this study, a linear elastic approximation is reasonable. On 25 January 2018, the snow characterization team deployed the LWD on groomed snow surfaces over paved asphalt at high strain rate. Under these conditions, the snow was thought to be a rigid body and to behave elastically. Various geophone configurations were tested, yet only the central geophone recorded useable waveforms for analyses (Wieder *et al.*, 2019).

SMP profiles were collected coincident with LWD tests on the processed snow road in ruts and unaltered surfaces. This shallow and hard snow proved difficult to penetrate with the SMP and damaged the instrument hardware. We examined a reduced sample of data in this study to compare the LWD and SMP and found no significant correlation between these instruments (Section 1.6).

1.3 Data Analysis

The snow characterization team acquired 383 SMP penetration-force profiles during the NATC campaign. The binary data files were read and processed repeatedly as a batch. Section 1.3.1 describes the Python and MATLAB codes that perform the signal processing. Section 1.3.2 outlines the data inversion and microphysical snow properties. Section 1.3.3 details the correlation analysis between the SMP-derived microphysical snow properties and the additional instruments.

1.3.1 SMP Automated Signal Processing

Preprocessing

Signal preprocessing begins within the Python script provided by SLF for georeferencing the SMP trace with longitude and latitude coordinates with approximately 3 m accuracy. This information is exported as a .txt file that is read into the signal

processing code. The open-source Python code is used for this task only, and the following routines take place in MATLAB. The binary .pnt file is read into memory and written to a structure that contains the metadata and the SMP signal. GPS locations are then joined to the data structure.

Prior to spinning up the signal processing routine, we reviewed each raw SMP trace for quality control. The classification strategy in Lutz *et al.* (2009) and Pielmeier & Marshall (2009) was used to identify traces that have no error (C1), exhibit a linear trend and/or an offset in the trace (C2), exibit dampened signal microvariance (segments of the trace that have lower variance than the normal air signal) (C3), and traces that exhibits errors of types C2 and C3 (C4). Trends and offsets are corrected if the C2 error is observable in the air signal (Figure 1.5). Data that experiences C3 errors are prevalent in low-strength, virgin snow because of the reduction in resolution of the 500 N load cell. Snow element ruptures cannot be detected in data segments suffering from C3 errors (Figure 1.8). The quality control classifications are supplemental metadata that enable automation for drift correction and the snow-surface identification.

Snow Surface Identification and Depth Correction

The processing routine first identifies the snow surface. A duplicate, temporary trace is smoothed with a 0.25 mm moving window average (62 samples). Smoothing aides in preventing false surface detection. The variance of the smoothed trace is then calculated within a 1 mm moving window. The program then extracts a segment of the trace while the penetrometer tip is driving through the air and calculates the mean variance of this segment. We establish a threshold variance of $49\sigma^2$ relative to the mean variance of the extracted air signal. Once this threshold is exceeded, the

program identifies the snow surface. Because the SMP trace begins recording as the penetrometer moves initially through the air gap, the depth profile is shifted by the distance to the automatically detected snow surface, such that negative depths are in the air and positive depths are distances below the snow surface.

Signal Drift Correction

After repeated use, especially in wet conditions, moisture may migrate behind the penetrometer tip and degrade the SMP signal (Lutz *et al.*, 2009); infrequently, the malfunction introduces a linear drift to the recorded SMP trace. Because the overall drift within the signal may be approximated by a linear function, a corrected force signal within the snow can be estimated by examining the signal as the tip is driven through the air. A least-squares fit is applied to the data above the snow surface to estimate the drift function. The drift function is then subtracted from the raw SMP trace, correcting the data. The raw trace shown in Figure 1.5 is type C4, as a linear trend and static offset is observable in the air signal and segments of the trace exhibit damped signal microvariance. Figure 1.5 demonstrates the result of the automated signal processing before and after snow-surface identification and drift correction.

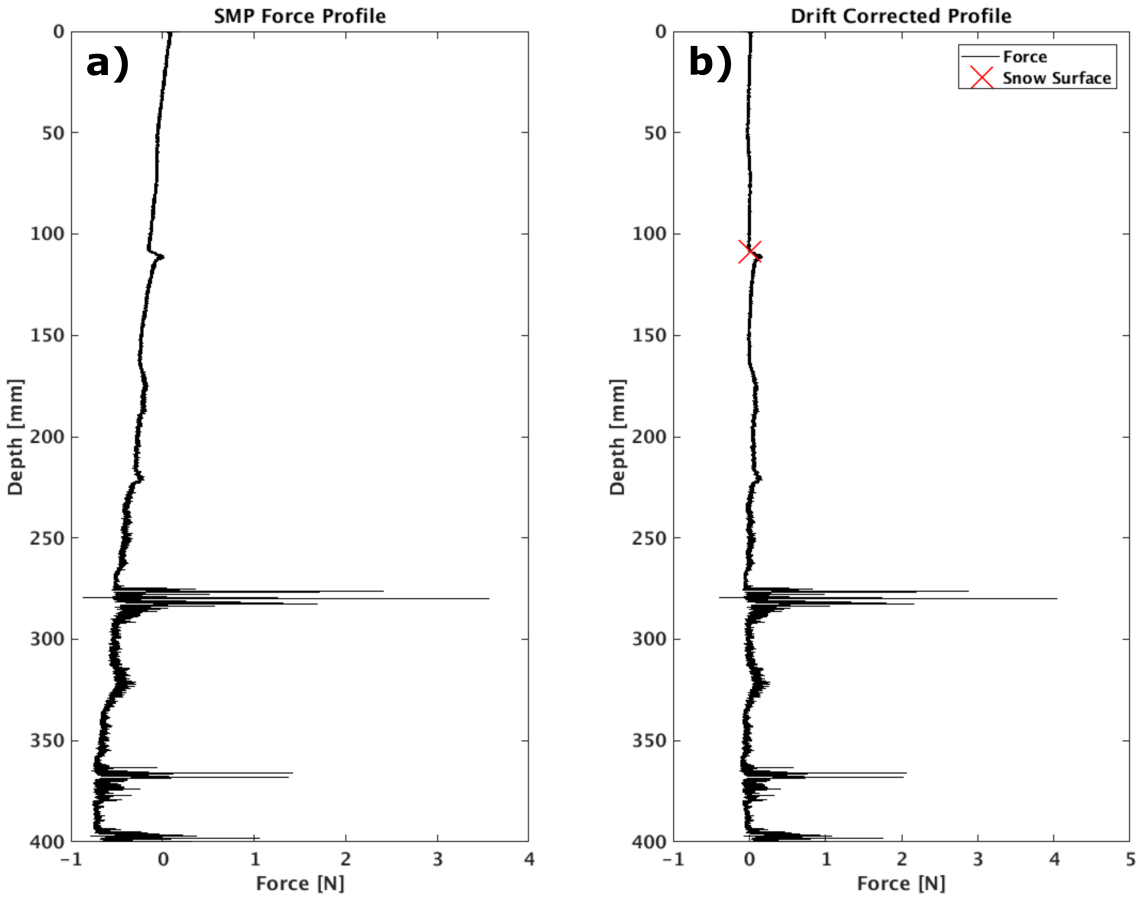

Figure 1.5: A C4-type SMP trace through virgin snow $a)$ **before and** $b)$ **after the snow-surface detection and drift correction. The depth axes of each plot is not corrected and is later reconfigured to place the snow surface at** $0\ mm$ **depth.**

1.3.2 SMP Data Inversion for Snow Microstructural and Micromechanical Properties

Underlying Theory and Assumptions

The microstructure of snow controls its compressive, tensile, and shear strength (e.g. Shapiro *et al.*, 1997; Marshall, 2005) and is thereby important for understanding the mobility of vehicles through snow-covered terrain. A physics-based theory on snow penetration through lower-density snow was first developed by (Johnson & Schneebeli, 1999). The snow penetration theory models microstructural snow elements as a cellular solid ice matrix. Each element is assumed to have a constant dimension (L) that is related to the number of measured ruptures per millimeter (Marshall & Johnson, 2009). The snow element ruptures at a rupture force (f) after some deflection length (δ) that is less than L. Snow deforming as a linear elastic material due to penetration may be defined by these basic microstructural parameters (L, f, δ) from the recorded failure of individual snow elements (Johnson & Schneebeli, 1999; Marshall & Johnson, 2009). Figure 1.6 depicts the individual snow element ruptures that are modeled by elastic events and are represented by the basic micro-structural parameters L, f, and δ.

This assumption is valid in low-density snow behaving as a foam where the compaction of snow elements is understood to be negligible. In the higher density regime ($400 - 600\ kg/m^3$), snow behaves as a porous solid, and interelement compaction has an effect on the rupture of snow elements (Marshall & Johnson, 2009), which is not accounted for in this theory. A rapid transition in the mechanical properties of dry snow exists in the density range $550 - 570\ kg/m^3$ as snow reaches the limit of

densification caused by grain packing; further densification must occur by changes to the bonds interconnecting grains (Anderson & Benson, 1963). We applied the penetration theory developed for low-density snow to the NATC study, though snow densities for vehicle-driven snow and groomed snow roads are reported in the porous solid regime (Shoop *et al.*, 2016). Beyond the scope of this report, we recommend developing additional physical theory to account for intergranular effects on rupture force caused by the closeness of grain packing and the development of grain bonding in addition to accounting for compaction of grains and bonds.

The penetrometer tip is cone-shaped with a half angle of θ. Forces measured in the vertical direction (F_z) are the sum of the normal and frictional forces

$$F_z = F_n \sin\theta + F_\mu \cos\theta = F_n(1 + \mu \cot\theta)\sin\theta \quad , \tag{1.2}$$

where F_n is the force normal to the penetrometer tip, F_μ is the frictional force tangential to the penetrometer tip, and μ is the coefficient of friction. In the following analysis the vertical displacement and total force are first transformed to distances and forces that are normal to the tip. The displacement in the normal direction is

$$d = d_z \sec\theta \quad , \tag{1.3}$$

and the force normal to the penetrometer tip is found by inverting Equation 1.2

$$F_n = \frac{F_z}{(1 + \mu \cot\theta)\sin\theta} \quad . \tag{1.4}$$

Monte Carlo Data Inversion Scheme

Johnson & Schneebeli (1999) initially developed a Monte Carlo inversion strategy that synthesized SMP penetration-force profiles by the summation of randomly distributed elements with testable values for L, f, and δ. Their results agreed well with measurements made in zirconia foam and indicated that the underlying theory is correct in low-density snow. Marshall & Johnson (2009) made significant improvements to the original inversion strategy by accounting for errors in the recovery of the microstructural parameters, especially when $L < 1\ mm$. These micromechanical and microstructural parameters were shown to be predictive of snow slope stability (Pielmeier & Marshall, 2009; Lutz *et al.*, 2009).

The Marshall & Johnson (2009) data inversion was used to solve for the snow microstructural parameters. Figure 1.6 depicts the basic strategy of the Monte Carlo inversion, where individual snow elements with testable parameters L, f, and δ, are randomly distributed. The summed contribution of the individual elements reproduces the raw penetration-force profile of the SMP when the parameters are accurately chosen, provided that the linear elastic penetration theory is valid. For clarity on the implementation and improvements made to the SMP data inversion, refer to Marshall & Johnson (2009).

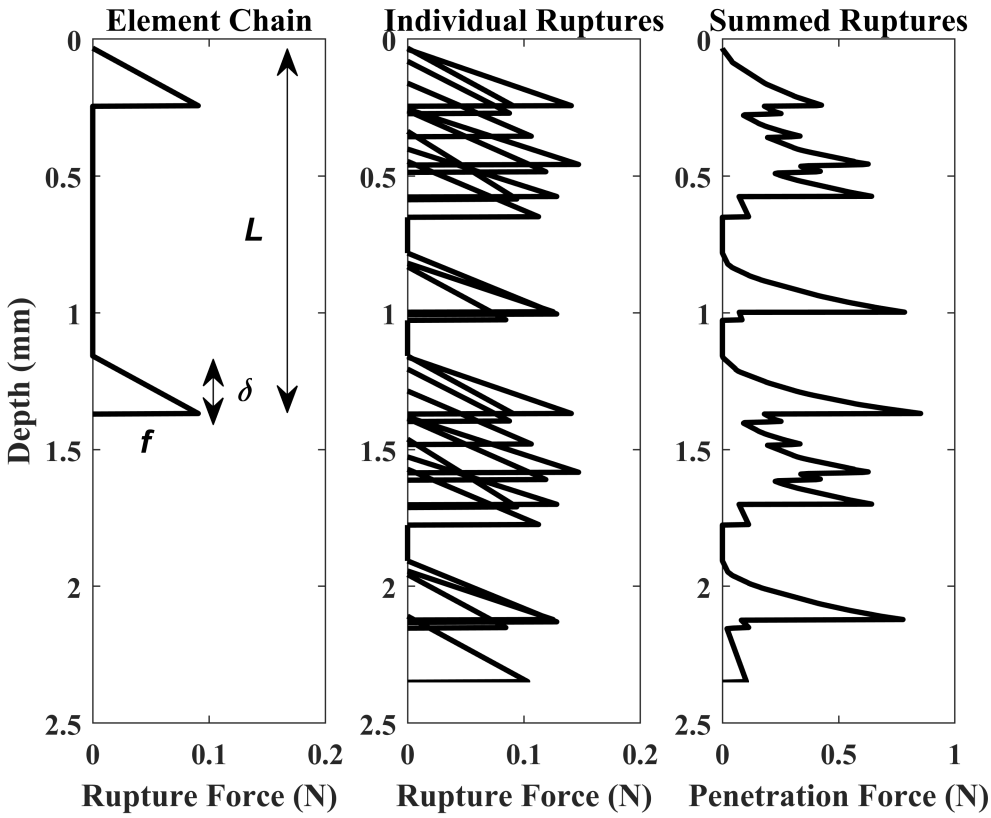

Figure 1.6: The three microstructural parameters L, f, and δ are estimated via the Monte Carlo data inversion. The objective of the data inversion is to use the summed signal (F) as measured by the SMP to invert for the basic microstructural parameters (L, f, δ).

Microstructural Parameters

Following the Monte Carlo inversion the microstructural parameters L, f, and δ, are the building blocks for additional measures of snow microstructure and micromechanics. The structural element length is estimated as

$$L = \sqrt[3]{\frac{V_T}{N}} \quad , \tag{1.5}$$

where N is the number of estimated ruptures caused by the deformation of a cylindrical volume of snow $V_T = Az$. $A = \pi r^2$ is the area of the penetrometer tip base, and z is the depth of penetration. The rupture force

$$f = \frac{\sum_{i=1}^{N} f_i}{N} \quad , \tag{1.6}$$

is the average rupture force over a distance in which N ruptures occured, and f_i is the difference in force between the N local maximum and adjacent minimum ruptures. The deflection at rupture

$$\delta = \frac{F_m z}{\sum_{i=1}^{N} f_i} \quad , \tag{1.7}$$

depends on the mean total force (Equation 1.10), the penetration distance (z), and the sum of the individual ruptures (Marshall & Johnson, 2009).

Derived Snow Microstructural Parameters

Microstructural parameters are derived from penetration force (F), the elemental microstructural parameters (L,f, and δ), the window length (calculation interval), and instrument specifications (cone length and maximum radius). Johnson & Schneebeli (1999) assumed that microstructure element locations follow a uniform random

distribution. The probability that any element is in contact with the penetrometer may then be estimated as

$$P_{c1} = \frac{\delta}{L} \quad , \tag{1.8}$$

or,

$$P_{c2} = \frac{N_e}{N_a} \quad , \tag{1.9}$$

where N_e is the number of microstructural elements engaged with the penetrometer tip, and $N_a = \frac{A_s}{L^2}$ is the number of available elements given the surface area, A_s, of the cone tip and characteristic length L.

Because the mechanical behavior of the elements is linear elastic, by the mean value theorem, the average contribution of any engaged element is $f/2$ (Marshall & Johnson, 2009). The mean penetration force normal to the tip follows from the above equations as

$$F_m = \frac{f}{2} N_e = \frac{f}{2} N_a P_c = \frac{f}{2} \left(\frac{A}{L^2} \right) \left(\frac{\delta}{L} \right) = \frac{f A \delta}{L^3} \quad , \tag{1.10}$$

while the median penetration force may be estimated from the cumulative distribution function of the penetration force

$$F_{med} = \text{median}(F) \quad . \tag{1.11}$$

Snow density is estimated from the median penetration force using an empirical relationship

$$\rho = 55.6(\ln(F_{med})) + 317.4 \quad , \tag{1.12}$$

(Pielmeier, 2003). The textural index

$$T_I = 1.45 + \frac{5.72\sigma_F}{F_m} \quad , \tag{1.13}$$

is an empirical formula related to the grain size, which depends on the mean penetration force and σ_F, the standard deviation of the penetration force (Schneebeli *et al.*, 1999).

Using Monte Carlo simulation to model the occurance of multiple simultaneous ruptures in the SMP signal, Marshall & Johnson (2009) developed a technique for estimting the true number of ruptures

$$N_T = \frac{A_s z}{L^3} \quad . \tag{1.14}$$

The true number of ruptures is substituted into Equations 1.6 and 1.7 to calculate the mean rupture force and the deflection at rupture. For a given depth window dz the mean number of measured ruptures is calculated as

$$N_m = \frac{N_t}{dz} \quad . \tag{1.15}$$

Derived Micromechanical Properties

The three fundamental microstructural parameters L, f, and δ, are difficult to interpret from an engineering perspective. These parameters are formulated to estimate the coefficient of elasticity

$$k = \frac{f}{\delta} \quad , \tag{1.16}$$

the microscale elastic modulus

$$E = \frac{k}{L} \quad , \tag{1.17}$$

and the microscale strength

$$\sigma = \frac{f}{L^2} \quad , \tag{1.18}$$

which are useful for engineering applications (Johnson & Schneebeli, 1999).

Inversion Parameters and Force Resolution

The inversion process occurs within a moving window of the SMP force trace. A 10 mm window size and 1 mm calculation interval was chosen for fast and accurate computation with adequate depth resolution. Force resolution is and the minimum force distinguishable from the signal noise floor are important for detecting and inverting for individual ruptures. A threshold for the noise floor must be established prior to data inversion. Because of the use of the higher-range SMP force sensor, the noise floor was increased and the force resolution was decreased compared to the 42 N force sensor, resulting in type C3 errors. This becomes problematic for distinguishing rupture signals in soft virgin snow and vehicle belly drags. The instrument noise floor was estimated by examining the signal above the snow surface for all SMP profiles recorded at any particular study site. The signal range was calculated within eight moving windows of increasing size (from 1 sample to 250 samples). Figure 1.7 displays the boxplots of these events as a summary.

The microphysical properties were inverted for using the median threshold value for each window size. The force sampling discretization of the SMP used in this study is 0.0065 N. This allows for a few possible threshold selections (0, 0.0065, 0.013, 0.0195, 0.026, or 0.0325 N). The coarse force discretization is problematic for

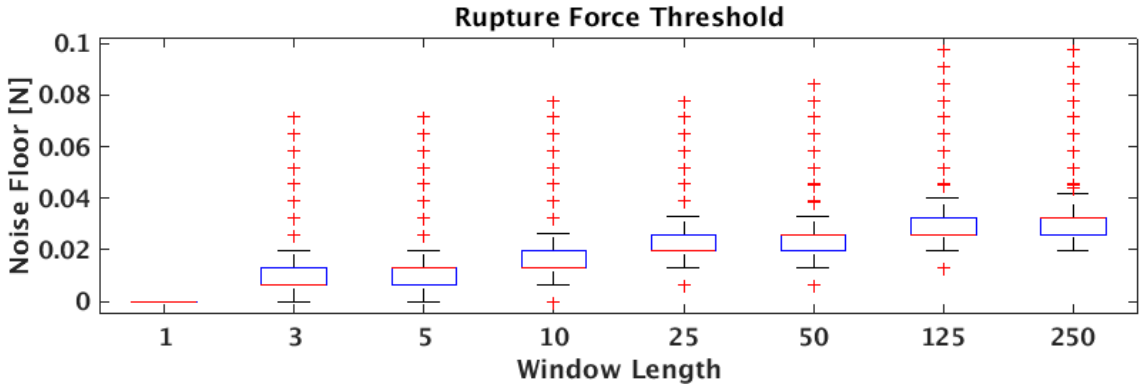

Figure 1.7: The boxplots of the SMP noise floor for increasing window lengths.

soft snow where the rupture force becomes enveloped by the noise floor, as this creates type C3 error. Figure 1.8 depicts the drift-corrected SMP trace from the virgin snow at the various force thresholds. Type C3 errors are observed in data segments shown in red.

The 0.013 N threshold is the lowest value that detected the absence of element rupture, albeit false identification within the snowpack. The 0.0195 N threshold correctly distinguishes the noise floor in the air gap and the snow signal at greater rupture forces. The greater thresholds correctly distinguish the two melt-refreeze crusts within the virgin snow. This serves as a check on the lower error bound of this method for a vehicle mobility study that has large penetration-force requirements. From the results of Figure 1.8, I selected the 0.0195 N threshold for the data inversion. The 0.0195 N threshold exceeds the previously accepted value of 0.014 N by nearly an entire force discretization. Given the current development of SMP hardware, it is challenging to resolve element ruptures within very soft snow. Future work will aim to design a high-resolution penetrometer with a larger dynamic range to allow accurate characterization of both very soft virgin snow and very hard vehicle-compacted snow or groomed snow surfaces.

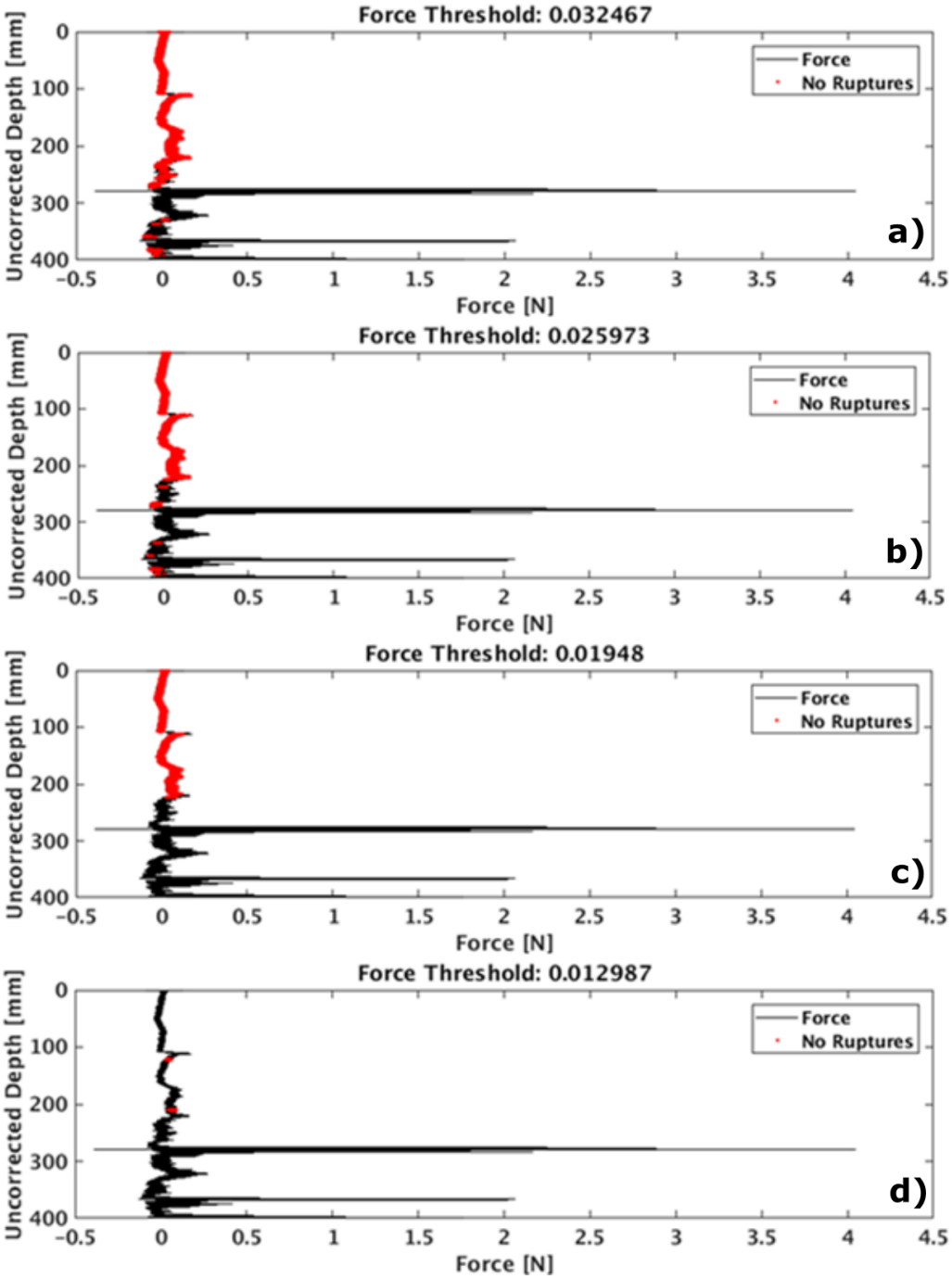

Figure 1.8: The drift-corrected SMP trace, as in Figure 1.5, tested at force thresholds that distinguished null-rupture events. Data segments that did not experience any detectable ruptures of snow elements are shown in red. I recommend the $0.0195\ N$ threshold in c) because the air signal is correctly identified and C3 error type is minimized.

1.3.3 Instrument Observation Correlation Analysis

Theory of Linear Correlation

The linear correlation coefficient was applied to the NATC data to draw meaningful relationships between the SMP microphysical parameters and the macroscale snow instruments. The linear correlation coefficient seeks to justify the existence of a physical relationship between two variables by testing whether the variations in the observed values of variable x_i are correlated with the variations in the observed values of variable x_j (Bevington & Robinson, 2003). Statistical correlation does not alone prove a physical relationship, but it is a powerful data-exploration step. Equation 1.19 calculates the linear correlation coefficient from an experimental data set

$$R_{ij} = \frac{s_{ij}^2}{s_i s_j} \quad , \tag{1.19}$$

where R_{ij} is the linear correlation coefficient between any two variables $(x_i,\ x_j)$, s_{ij}^2 is their covariance, s_i is the sample standard deviation of x_i, and s_j is the sample standard deviation of x_j.

Values of R range from 0 to ± 1 with 0 indicating no correlation and 1 indicating perfect correlation. However, the correlation coefficient does not solely indicate the goodness of correlation. Here, R is compared to the probability distribution for the parent population, which is completely uncorrelated (Bevington & Robinson, 2003). Equation 1.20 is the probability

$$P_c(R; N) = 2 \int_{|R|}^{1} p_R(R; v) dr \quad , \tag{1.20}$$

that a random sample of N data points drawn from the uncorrelated parent distribu-

tion would yield an experimental linear correlation coefficient greater than or equal to the observed magnitude of R (Bevington & Robinson, 2003). Where

$$p_R(R;v) = \frac{1}{\sqrt{\pi}} \frac{\Gamma[(v+1)/2]}{\Gamma(v/2)} \left(1 - R^2\right)^{(v-2)/2} \quad , \tag{1.21}$$

is the probability that any random sample of uncorrelated experimental data points would yield an experimental linear correlation coefficient equal to R_{ij}, and where Γ is the Gamma function and $v = N - 2$ is the number of degrees of freedom for an experimental sample on N data points.

Correlations are deemed significant if the probability value derived from Equation 1.20 is less than or equal to the desired level of statistical significance. $P_c \leq 0.05$ determined test significance for the ram hardness study; however, $P_c \leq 0.1$ determined test significance for the shear vane and LWD correlations. The larger rejection region was used for the shear vane and LWD studies because fewer sampled data are available for the analysis of these instruments.

Application of Linear Correlation

Each of the 16 microphysical parameters of the SMP data inversion and the additional raw penetration force enabled 17 independent variables to be correlated with the ram hardness measurements, shear-stress measurements from the shear vane, and elastic modulus estimates from the LWD. The data are reduced to the median for each measurement at a test location. The instruments were compared on equivalent measurement depths as follows. The ram median hardness value for the entire snow penetration was correlated with the equivalent penetration depths for median values of the SMP microphysical parameters. The shear vane was inserted 50 mm into the snowpack, and only the upper 50 mm of the SMP profile, corresponding to the same

50 mm depth interval, were considered in the correlation. The median values for the entire SMP profile through approximately 10 cm of the groomed snow-road surfaces were used for correlation with the LWD, as this was the estimated snow depth that controlled the deformation caused during the LWD test.

For this analysis, the dynamic range of the measured data is important. Sample sizes used in the correlation analysis depend on the number of test locations where the experiment was conducted and the range of snow conditions observed. The ram gives the most prevalent data set ($N = 24$) as this instrument could perform in all three snow conditions, providing one median data point for each, and was tested at eight locations. The shear vane was limited to hardened snow that could support shear load ($N = 11$). These data are composed of vehicle ruts of nine test points and vehicle belly drags from two test points. The LWD experiment is the most limited in population size ($N = 5$), as this experiment could be conducted only on processed snow roads where the SMP had difficulty penetrating. Section 1.6 provides additional information regarding snow conditions and test-point usefulness for the LWD at NATC.

1.4 Results and Discussion

1.4.1 Rammsonde

Ram and SMP profiles were gathered from the colocated test points and were classified into three snow conditions: virgin snow, vehicle belly drag, and tire ruts. Correlation analysis was conducted using the median values from each snow type at a particular location. Abele (1963) correlated ram hardness with unconfined compressive strength. Because ram hardness measured at NATC was typically too low,

this correlation does not yield physically meaningful results for this study. Of the 17 possible correlations, 4 are statistically significant: rupture force (f), mean penetration force (F_m), density (ρ), and strength (σ) ($p \leq 0.05$). Figure 1.9 summarizes the data that provide significant correlation results. Figure 1.10 provides the scatter plots resulting in significant correlations, and Figure 1.11 provides the overview of all correlations.

The NATC data express the trend that rupture force, penetration force, density, strength, and ram hardness increase when the snow was deformed by the vehicles. However, judging this trend using the notched boxplots, it is not statistically significant, as the notches overlap in many cases (Figure 1.9). This indicates that the range of parameters, rather than the median values, may be more predictive of the snow type (virgin snow, belly, or rut). The confidence interval of these relationships is quantified using correlation analysis.

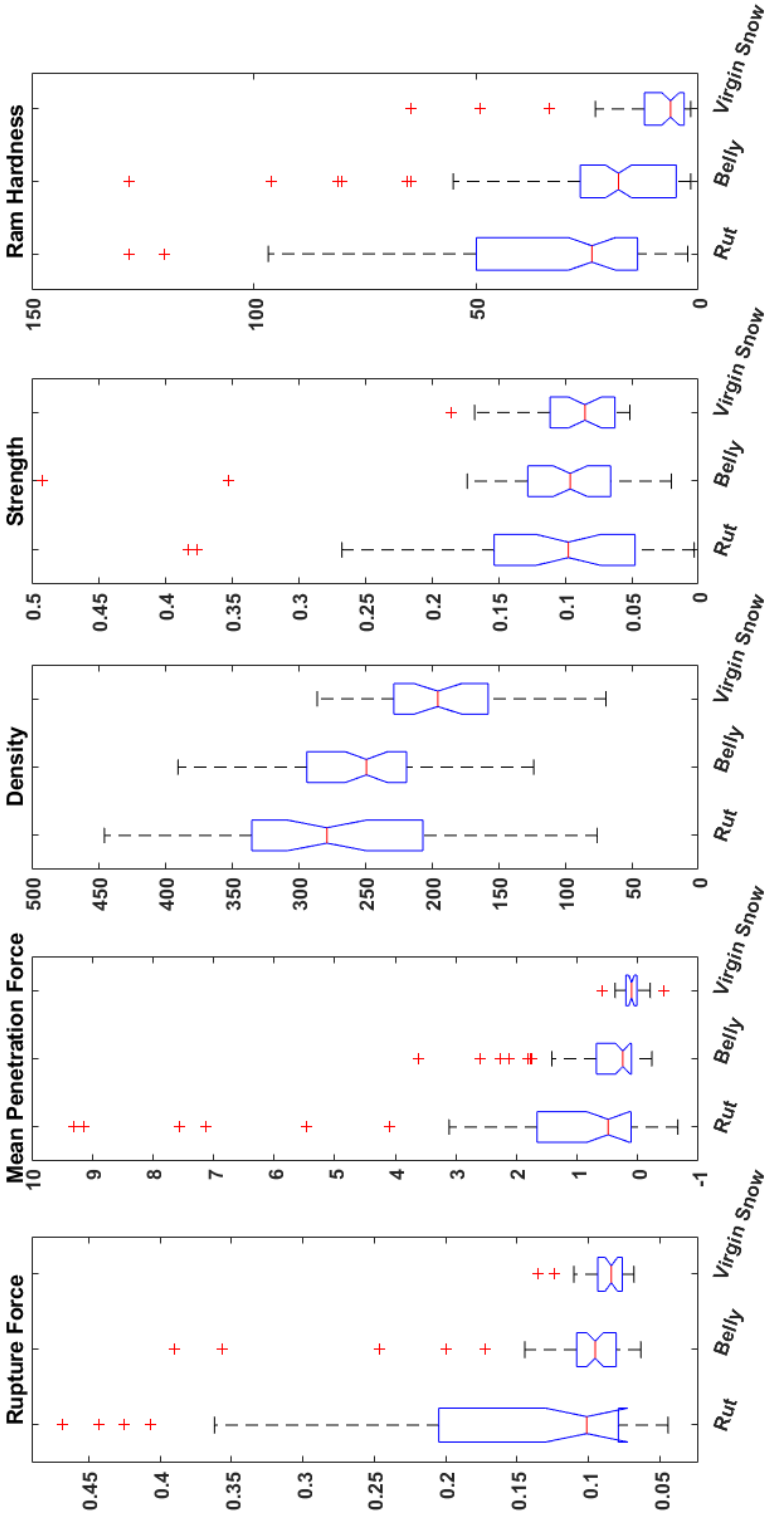

Figure 1.9: The boxplot summary of SMP and Rammsonde data that yield significant correlation ($p \leq 0.05$). The red crosses are outliers.

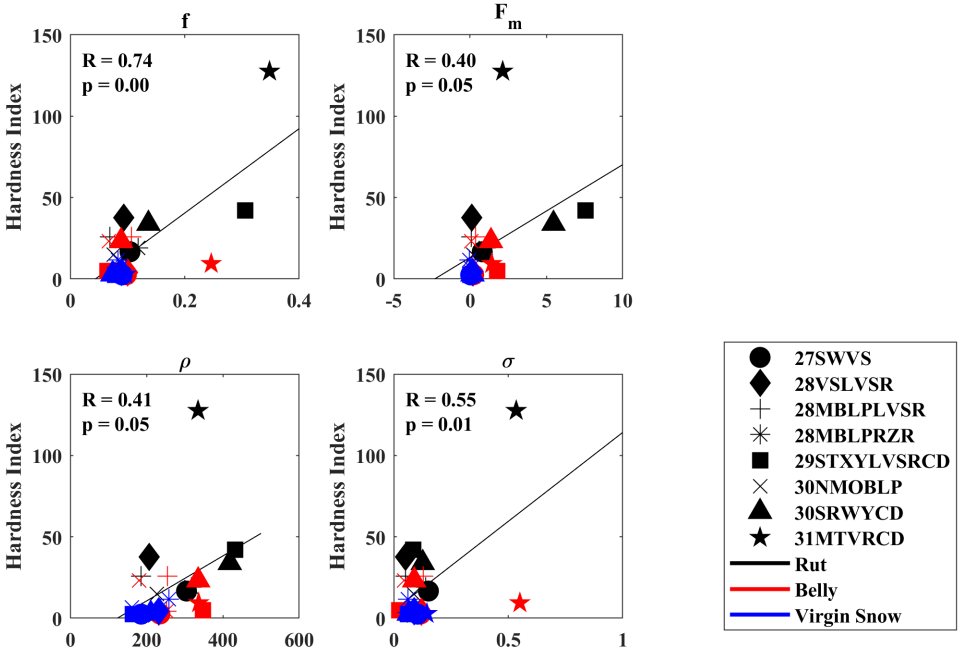

Figure 1.10: Statistically significant correlations between SMP microphysical parameters and the ram. The marker style identifies the site location, and the color represents the snow type.

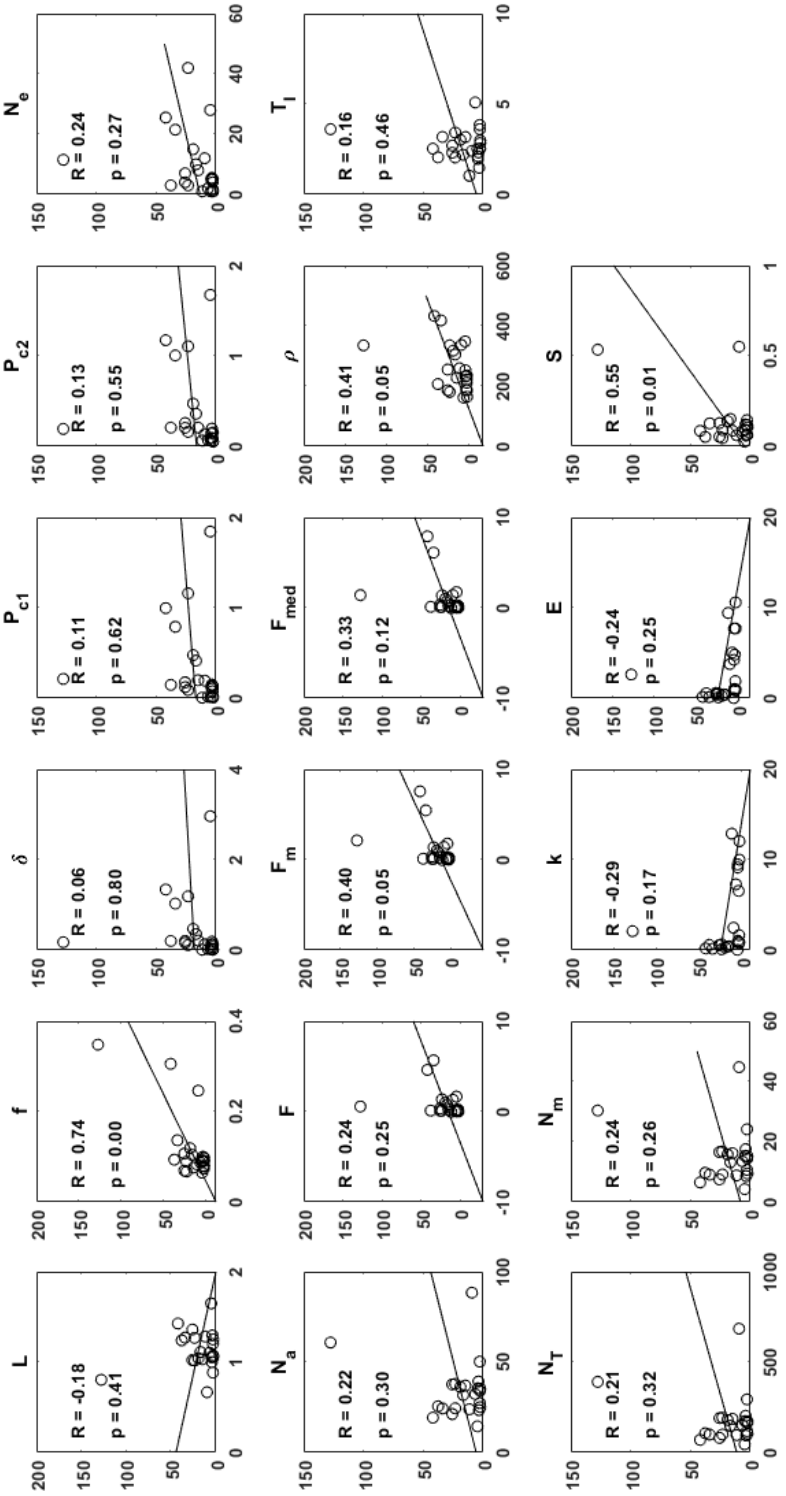

Figure 1.11: Results of the correlation between the ram hardness index and the SMP microphysical parameters.

1.5 Shear Vane

The shear-vane study was limited to only 11 sites, significantly reducing the power of the correlation analysis. Additionally, the shear-vane response is variable and spans the entire range of recordable shear strengths (from a minimum of 0 to the maximum of 130 kPa). The data summary in the boxplot of Figure 1.12 indicates that sites of similar snow condition have uncorrelated instrument response. The smaller sample population will inherently reduce the confidence value of the result, so we chose a significance level of $p \leq 0.1$ for this analysis. Of the 17 microphysical parameters, 3 had statistically significant correlations: N_T, N_a, and N_m (Figure 1.12). The inverse relationship shows that a snowpack stronger in shear will experience fewer ruptures when it fails under an applied stress. Figure 1.13 provides the overview of all tested correlations.

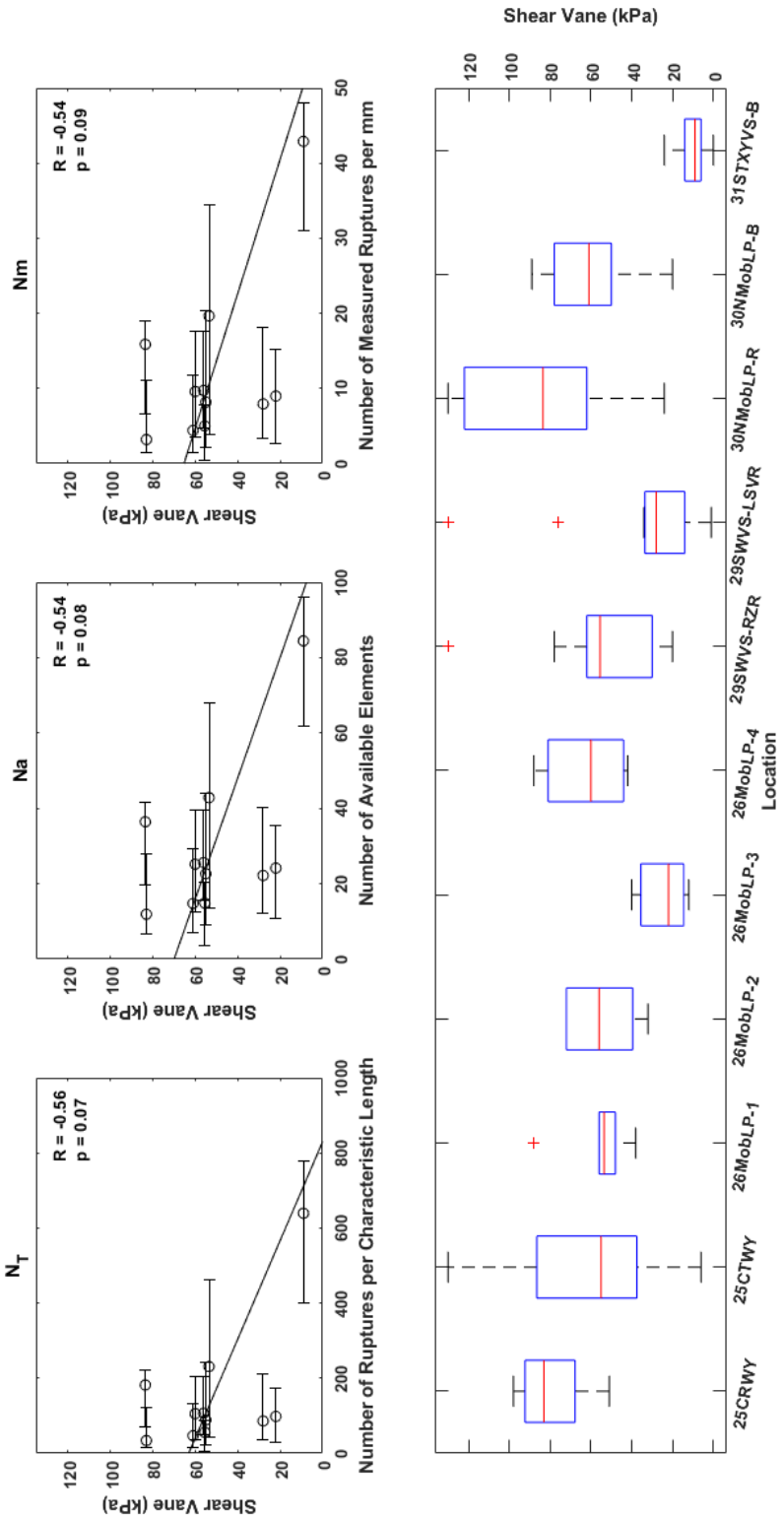

Figure 1.12: Statistically significant correlations between SMP microphysical parameters and the shear-vane measurements ($p \leq 0.1$). The boxplot summarizes the shear-vane measurements from 11 test locations.

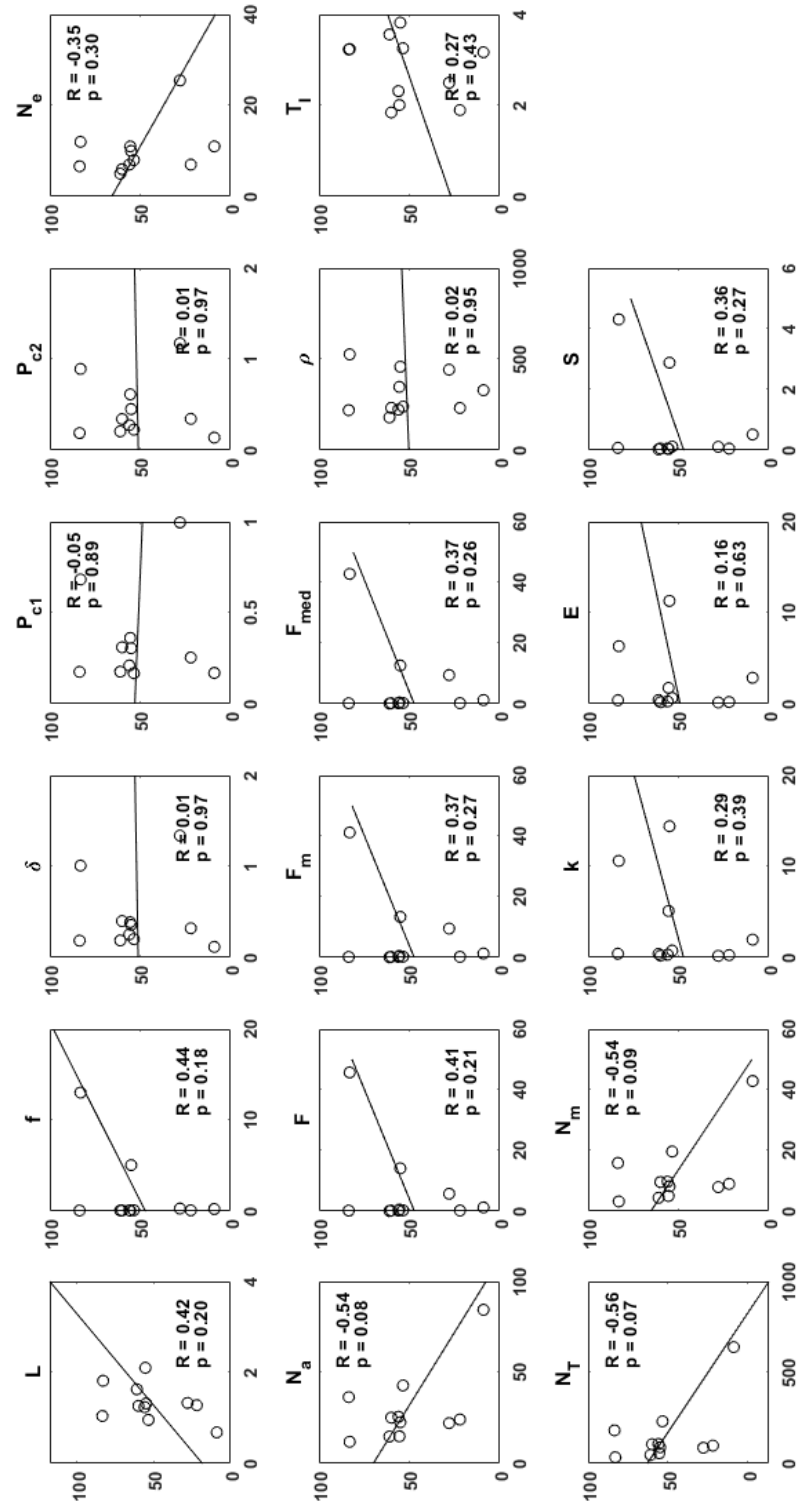

Figure 1.13: Results of the correlation between shear-vane stress and the SMP microphysical parameters.

1.6 Light Weight Deflectometer

The LWD was colocated with SMP measurements on the groomed runway and taxiway at NATC. These tests occupied 10 locations on the fresh snow road surfaces and within vehicle ruts (notated in Figures 1.14 and 1.15 by RR and LR for right rut and left rut, respectively). Correlation analysis was applied to determine if the snow at these locations behaves in a linear elastic manner. The effective elastic modulus E^* is derived from the linear slope of the deflection measured at the central geophone and the stress applied to the snow column. To create a distribution of effective elastic modulus, the bootstrapping method was applied to the least-squares regression (Efron & Tibshirani, 1986). Two samples were removed at random from the correlation analysis, and the linear slope was refit. This procedure was replicated 250 times for each site location. Figure 1.14 displays the results of the correlation analysis. The median value of the E^* distribution was chosen to represent the site condition. Locations that have a negative slope or $p \leq 0.05$ were removed from the analysis.

The correlation analysis was repeated between the LWD E^* and the SMP micro-physical parameters. No significant correlation was found between these measurements. Figure 1.15 presents the findings of the correlation analysis. This indicates that there is a scaling between the microscale mechanical properties that the SMP measures and the macroscale properties measured by the LWD, which is not well understood. A new theory for inverting SMP signals for micromechanical properties, which relaxes the assumption of low-density snow, and a scaling law appropriate to this type of hard snow are required to relate the SMP observations at the microscale and the macroscale properties measured by the LWD.

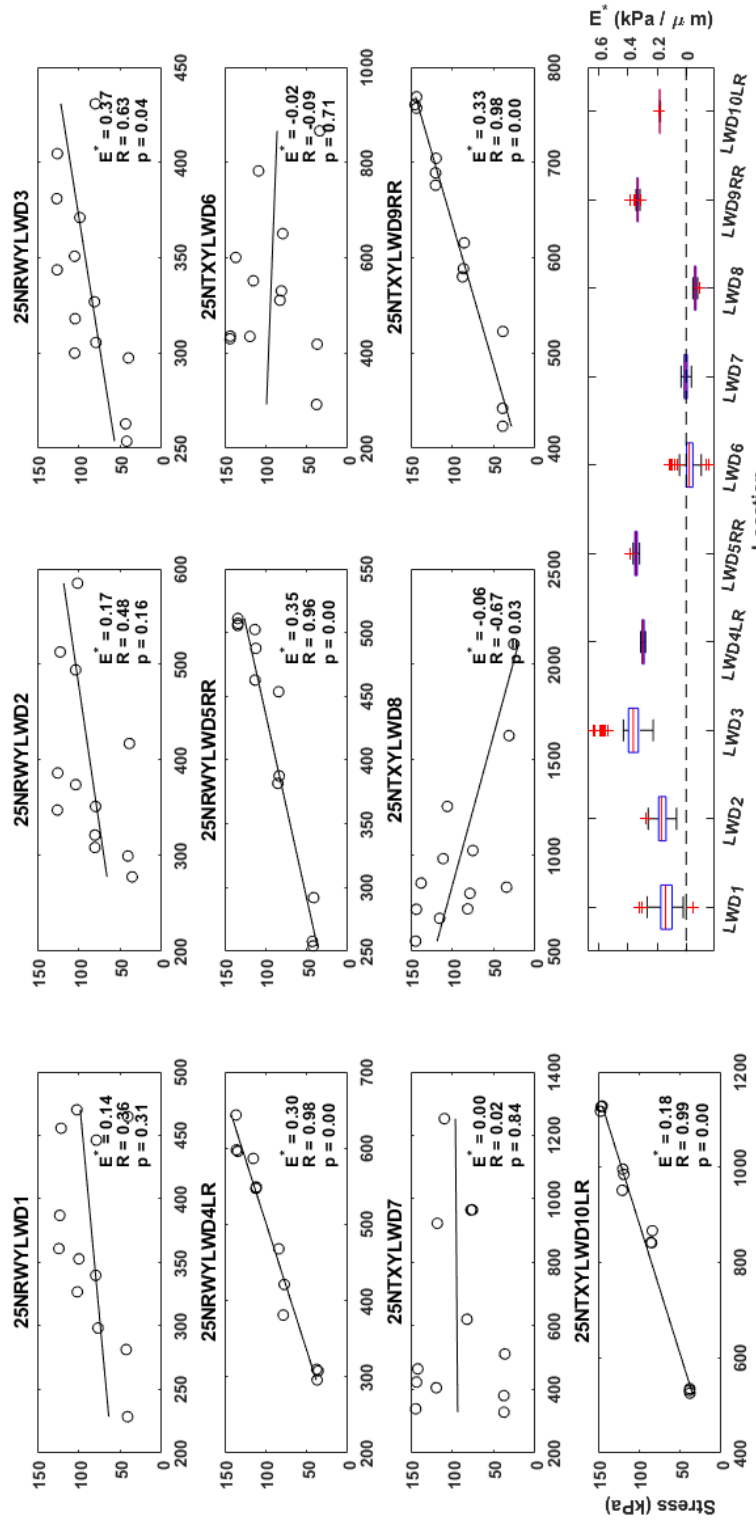

Figure 1.14: Results for the effective linear elastic property of groomed snow roads at NATC. Locations with negative slope or p-value < 0.05 were excluded from the correlation analysis.

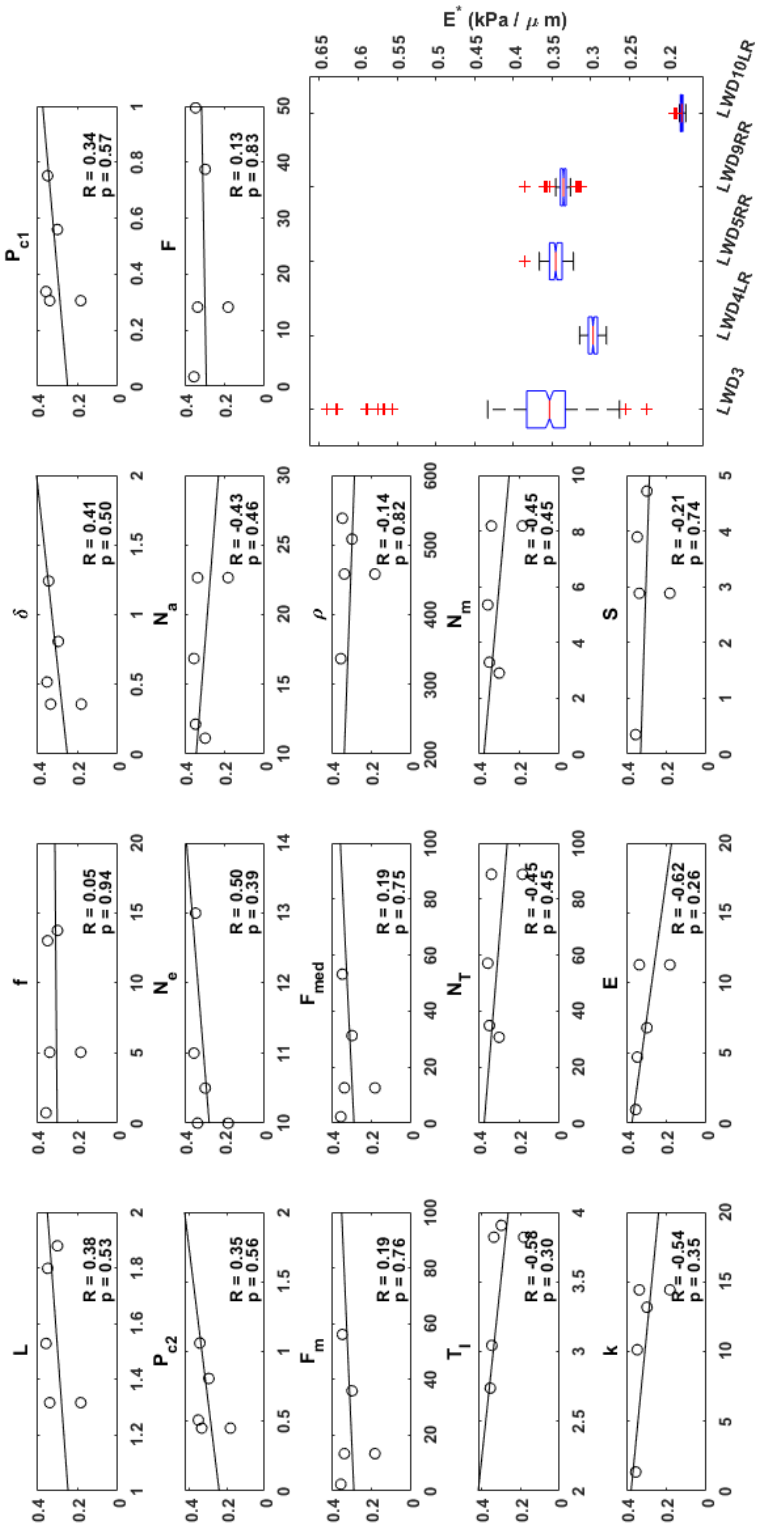

Figure 1.15: Results of the correlation analysis between E^* and the SMP microphysical parameters. No significant correlation was found.

1.7 Conclusion

The 2018 winter testing at NATC allowed evaluation of the SMP for more compacted snow and comparison of the SMP with more traditional snow characterization instruments, specifically the Rammsonde penetrometer, shear vane, and the LWD. We developed an automated signal processing routine for the SMP signal by joining the preprocessing and classification strategy of Lutz *et al.* (2009) with the inversion methods of Marshall & Johnson (2009). Measured ruptures are sensitive to the force discretization during signal analog-to-digital conversion and during the inversion process. We find it is more robust to study rupture force than penetration force because the magnitude of the rupture is not dependent on the absolute penetration force, so this parameter does not suffer from errors caused by instrument drifting. Type C3 errors cannot be remedied by signal processing and must be accepted as a limitation of the hardware; future efforts will focus on penetrometer development with a larger dynamic range and higher force resolution. Other methods of analysis were trialed, including using the maximum value and normalizing each site by the median prior to correlation analysis. However, the median value correlation provided the strongest results. The significant correlation between ram hardness and SMP strength coincides with prior findings (Abele, 1963), though the strength reported by the SMP is a multimode strength rather than unconfined compressive strength. This serves as a check on the methods being developed in a lower range of snow strengths and densities (approximately $100 - 450\ kg/m^3$).

Shear-vane measurements were restricted to locations with compacted snow, primarily vehicle ruts, with two exceptions of measurements made in vehicle belly drags on 30 January at the North mobility loop entrance and 31 January at the South run-

way. The snow was strong enough to support these measurements because the mobility loop snow was compacted by many vehicle passes – becoming strongly sintered – and a daytime warming period late in the week was met with very cold overnight temperatures, which created a melt-freeze cycle that formed strongly bonded snow. The small range of testable snow conditions for the shear vane limited the study and likely resulted in weakened correlations. Several centimeters of fresh snow fell during the study, leaving a soft surface layer atop the groomed surface. For the LWD experiment, the vehicle compaction (rutting) provided the additional stiffening to the snow road necessary for linear elastic behavior, because repeated LWD impacts in soft snow nonlinearly decrease the deflection of the central geophone. Insignificant correlation results likely arise from the small sample size ($N = 5$) and the similar snow conditions at the LWD test locations.

The SMP has not previously been applied to vehicle-driven snow. Processed snow roads and snow after deformation by vehicles exhibit high density and strengths that exceed the capability of the current SMP design. By using a $500N$ force sensor in the SMP, a larger dynamic range of snow conditions was measured at the expense of force resolution. Even with this higher range sensor, there were many snow conditions relevant to this study that were too hard for the SMP. To further improve the capability of the SMP for vehicle studies, a more powerful tool that can drive through very hard snow at a constant rate, minimizes type C2 errors, and uses a larger bit analog-to-digital converter to remediate type C3 errors should be developed to better resolve penetration forces in hard snow. Anchoring to a vehicle, similar to the LWD, is likely required. Advancements to the instrumentation should also be met with advancements to the penetration theory. Accounting for snow ruptures influ-

enced by interlocking snow elements away from the penetrometer tip can improve the application of the SMP. Accurate and large spatial scale measurement of the snow microphysics can serve as initial and boundary conditions for snow models and be a map for the analysis of remote-sensing imagery for vehicle mobility.

CHAPTER 2:

RECONSTRUCTION OF HISTORICAL SURFACE MASS BALANCE 1984 – 2017 FROM GREENTRACS MULTI-OFFSET GROUND-PENETRATING RADAR

Abstract

We present continuous estimates of snow and firn density, layer depth, and accumulation from a multi-channel, multi-offset, ground-penetrating radar traverse. Our method uses the electromagnetic velocity, estimated from waveform travel-times measured at common-midpoints between sources and receivers. Previously, common-midpoint radar experiments on ice sheets have been limited to point observations. We completed radar velocity analysis in the upper $\sim 2\ m$ to estimate the surface and average snow density of the Greenland Ice Sheet. We parameterized the Herron & Langway (1980) firn density and age model using the radar-derived snow density, radar-derived surface mass balance ($2015 - 2017$), and reanalysis-derived temperature data. We applied structure-oriented filtering to the radar image along constant age horizons and increased the depth at which horizons could be reliably interpreted. We reconstructed the historical instantaneous surface mass balance, which we averaged into annual and multidecadal products along a 78 km traverse for the period $1984 - 2017$. We found good agreement between our physically constrained parameterization and a firn core collected from the dry snow accumulation zone, and gained insights into the spatial correlation of surface snow density.

2.1 Introduction

The Greenland Ice Sheet (GrIS) expresses high variability in ice loss, and hence sea level rise, due to the regional scale variability in the processes governing mass balance (Lenaerts *et al.*, 2019). Surface mass balance (SMB) contributes just over half ($\sim 52\%$) of GrIS mass loss, but ice sheet wide SMB simulated from regional climate models maintains $\sim 25\%$ uncertainty (Shepherd *et al.*, 2020). Efforts to improve SMB

simulation (e.g. Fettweis *et al.*, 2017) are limited by the scarcity of observations, which are required to evaluate the model performance (e.g Noël *et al.*, 2016). Traditionally, SMB measurements are made at the point scale during infrequent field efforts, through the laborious process of excavating snow pits or drilling firn cores. The sparseness of snow pit observations on the GrIS limits the testable correlation lengths and tends to debilitate spatial correlation analysis. Consequentially, surface density measurements have shown no spatial correlation over length scales of tens to hundreds of kilometers (Fausto *et al.*, 2018). Due to the unknown variability of density and SMB, point measurements used to parameterize a firn model (e.g. Zwally & Li, 2002) must be extrapolated to regional scales cautiously. In space-borne altimetry retrievals of GrIS mass balance, the uncertainty in modeled corrections for snow densification required to convert a measured change in ice sheet volume to a change in mass causes $\sim 16\%$ uncertainty (Shepherd *et al.*, 2020).

Ground-penetrating radar (GPR) surveys are capable of imaging layers of accumulated snow (e.g. Vaughan *et al.*, 1999). However, conventional, single-offset GPR analysis requires an independent measurement of firn density to estimate the accumulation (Navarro & Eisen, 2009). Point SMB measurements often provide the required density information to extrapolate the density profile along the track of the radar sounding (e.g. Hawley *et al.*, 2014; Overly *et al.*, 2016). Yet, relying on sparse firn cores to extrapolate density over tens to hundreds of kilometers may bias the derived accumulation estimates. For example, ice lenses sampled in a firn core increase the average density and can be incorrectly extrapolated over tens of kilometers, as these features are uncorrelated over tens of meters (Brown *et al.*, 2011). For the period $1971 - 2016$, greater than 10% bias to the SMB is possible, when

firn cores are not available for extrapolation (Lewis *et al.*, 2019). Inaccuracies are greater in southern Greenland, which is experiencing increasing near-surface firn densification as a result of atmospheric warming (Graeter *et al.*, 2018), than in central Greenland. Parameterization of snow and firn densification continues to improve (e.g. Meyer *et al.*, 2020); yet, evolving the firn using full energy balance modeling remains operationally challenging and is limited spatially by the unknown heterogeneities of surface snow density, accumulation, and melt (Vandecrux *et al.*, 2018). Surface snow density parameterizations formulated around temperature and wind speed (e.g van Kampenhout *et al.*, 2017), are arguably less preferable than density measurements because of uncertainties in estimating wind speed and modeling the unknown length scale variability that exists in the GrIS snow (Fausto *et al.*, 2018).

Radar retrievals of snow density are an appealing alternative to *in situ* observations of snow and firn because the methods are nondestructive and rapidly acquire vast amounts of data. However, few methods for continuously mapping snow and firn density exist (e.g. Grima *et al.*, 2014b) due to the complexities of data inversion. In this work we present the analysis of multi-channel, multi-offset, radar (MxRadar) imagery along a 78 km traverse in the GrIS dry snow accumulation zone to demonstrate the capability of this method, which has the advantage of ascertaining snow and firn density, and depth, and thereby SMB, independently. Of the previous studies applying GPR velocity analysis, none have performed continuous estimates throughout tens of kilometers distance (e.g. Bradford *et al.*, 2009). We based our MxRadar workflow on the analysis of the radar surface wave, which exhibits linear moveout (LMO), and the fall 2014 isochronous reflection horizon (IRH) to estimate the surface snow density, column average density, horizon depth, and $2015-2017$ SMB. We then input

our data into the Herron & Langway (1980) firn density and age model. We use the firn model to further enhance the MxRadar imagery and extend the historical period of the SMB reconstruction to $1984 - 2017$ with instantaneous (~ 14 days) temporal intervals. We compare the resulting SMB against a firn core and quantify the length of spatial correlation that exists in surface snow density. We quantify the bias reduction in SMB derived using the measured-modeled, MxRadar–Herron & Langway (1980) method. Then we provide a discussion of the results, limitations and advantages of the method, and future directions. We developed our analysis within the interior region of Greenland where there was significant spatial variation in accumulation, but little melt, to develop confidence in this type of radar retrieval for density and SMB.

2.2 Greenland Traverse for Accumulation and Climate Studies

The Greenland Traverse for Accumulation and Climate Studies (GreenTrACS) is a multi-disciplinary study of recent SMB changes in the West Central percolation and dry snow accumulation zones of the GrIS. During the Spring of 2016 and 2017 we traveled a total of 4436 km by snowmobile from Raven/DYE-2 to Summit Station along the elevation contour straddling the percolation zone, and along West-East "spurs" perpendicular to the elevation contours. Throughout the expedition we collected 16 shallow ($22 - 32$ m) firn cores and dug 42 snow pits; 16 pits were coincident with the cores and the 26 others were dug at the ends of the spurs (Fig. 2.1 and Fig. 2.2). Our GreenTrACS field seasons occurred prior to the on-set of melt to reduce the complexity of radar data inversion. The cores and the coincident snow pits were sampled for density, isotopic chemistry, dust, and trace elements to define annual

layer depths for measuring SMB (e.g. Graeter *et al.*, 2018; Lewis *et al.*, 2019). As firn cores are strategically located point measurements, GPR imagery is often leveraged to spatially extend the record of firn stratigraphy between core sites for accumulation studies (e.g. Spikes *et al.*, 2004; Miège *et al.*, 2013). We operated a suite of radar instruments spanning the frequency range $0.4 - 18\ GHz$; the focus of this study is the MxRadar.

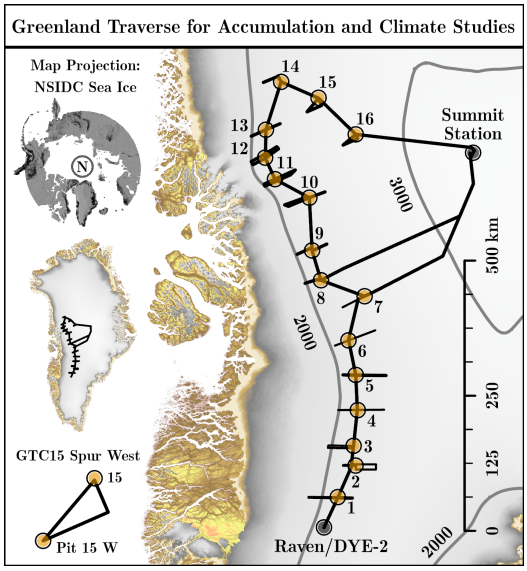

Figure 2.1: GreenTrACS firn cores (GTCs) are numbered $1 - 16$. Ground-penetrating radar surveys were conducted along spur traverses and the main route that links the GTCs. We developed our radar processing and analyses at GTC15 Spur West (lower left inset). The $2000\ m\ asl$ contour envelopes the western spurs. Surface elevation was acquired from Morlighem (2017) and Porter *et al.* (2018).

2.2.1 Study Area

GreenTrACS Core 15 (GTC15) is the second most northern core site of the GreenTrACS campaign ($47.197°W$, $73.593°N$) and is $\sim 2600\ m$ above sea level. GTC15 had an average annual temperature of $-25.7 \pm 1.0\ °C$ (*Modern-Era Retrospective analysis for Research and Applications* (MERRA), 1979-2012), and an average annual SMB of $0.306 \pm 0.021\ m\ w.e.\ a^{-1}$ (1969-2016). The site experiences little to no melt, mea-

sured as the average melt feature percentage determined by normalizing each year's ice layer water equivalent by the annual water equivalent and then averaging (0.47%, 1969-2016).

GTC15 Spur West is a triangular, clockwise circuit that departs from and returns to GTC15 (Fig. 2.1 inset). The first of three transects is 15 km in length, bearing 157°, and begins at GTC15. The second transect is 30 km in length at 246.5° which ends at Pit 15 W. The final transect is 33 km in length from Pit 15 W to GTC15 and bearing 40.5°. The GrIS surface of GTC15 Spur West was wind-affected snow with sastrugi $\lessapprox 25$ cm in height. We estimated the average meteorological wind direction of 152° using monthly 10 m zonal and meridional wind speeds from the ensemble of the third generation reanalysis models (GEN3ENS) for the period $1979 - 2012$ (Birkel, 2018). The average wind direction is approximately parallel to the first transect of GTC15 Spur West, approximately orthogonal to the second transect, and 21.5° oblique to the third transect. The cyclicity in the topographic profile (Fig. 2.2) results from our return to GTC15 along a path oblique to the path approaching Pit 15 W. The SMB changes significantly across the $\lessapprox 5$ km wide trough between distances $40 - 50$ km. But, we do not observe preferential windward and leeward affects to the accumulation pattern here, because the orientation of the transects crossing this topographic trough are approximately orthogonal to the average wind direction. We selected this particular spur to develop our processing and analyses because of the apparent interplay between the surface elevation, SMB, and heterogeneous layering observed in the radar imagery. Yet, we have foregone any topographic corrections in the radar processing.

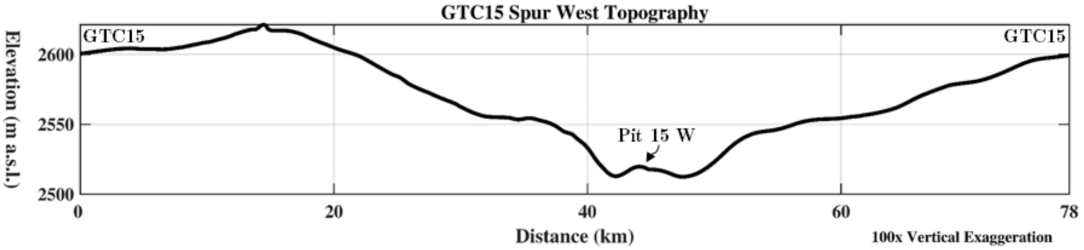

Figure 2.2: Topographic profile of GreenTrACS Core 15 Spur West. The topographic undulation near Pit 15 W is responsible for increases and decreases in accumulation. The initial $15\ km$, up to the point of maximum elevation of the profile, are directed into the predominant wind, making this a leeward slope. The predominant wind blows approximately orthogonal across the next $30\ km$ of the GTC15 Spur west traverse and is 21.5° oblique to the final $33\ km$ of GTC15 Spur West.

2.2.2 Field Methods

The MxRadar is a Sensors & Software 500 MHz GPR deployed with a multi-channel adapter in a multi-offset configuration using three transmitting and three receiving antennas (Fig. 2.3). During data acquisition, the transmitting and receiving channels were multiplexed to form nine radargrams which have independent antenna separations (offsets). The antennas were co-polarized, perpendicular to the direction of travel, and all are specified at 500 MHz with greater than two octave bandwidth. However, dependent on the antenna pairing, the actual central frequency and bandwidth varied on the order of tens of MHz. Our methods and analysis are tailored to produce meaningful data for the evaluation and improvement of snow cover and firn models and regional climate and reanalysis modeling of SMB.

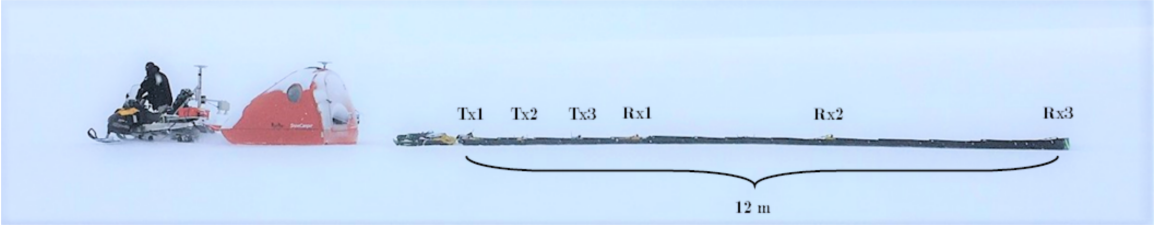

Figure 2.3: The MxRadar streamer array has three transmitting (Tx) and three receiving (Rx) antennas, which form nine independent offsets that were linearly spaced from $1.33 - 12\ m$ apart. We simultaneously acquired nine continuous radargrams (one for each constant offset) and then binned the source-receiver pairs into common-midpoint (CMP) gathers.

2.3 Analysis Methods

We review multi-offset GPR methods for SMB calculations in Section 2.3.1 to clarify the advantages of the multi-offset technique that are also important for interpreting the results. We provide much of the methodological detail in the Appendix A. Here, we touch on the methodology to simplify our strategy for reconstructing the

historical SMB for the period $1984 - 2017$ along GTC15 Spur West. We considered SMB rather than the accumulation rate because of unaccounted mass lost to sublimation and ablation. SMB is conventionally measured using GPR by interpreting a select few IRHs using a constant age interval and applying the average normalized firn density over this interval (e.g. Lewis *et al.*, 2019). Instead, we relied on the models of density and age, which were discretized in depth at a comparable resolution to the GPR data, and generated a SMB model with instantaneous ($\sim$ 14 day) temporal intervals (Appendix A.3). We averaged annual SMB from many realizations of the instantaneous SMB model in a Monte Carlo simulation to assess uncertainty (Appendix A.4). We estimated the multidecadal average SMB, invoking the central limit theorem, by repeatedly drawing from 10 of the 33 annual SMB distributions at random and averaging.

To parameterize the firn model, we first completed conventional signal processing on the nine radargrams, which consisted of a two octave bandpass filter around 500 MHz, amplitude gain corrections for wavefront spreading, coherent noise removal (background subtraction), and random noise removal (smoothing). Then we interpreted the air wave, surface wave, and a shallow reflection (Fig. 2.4) on each of the nine images using a semi-automatic picking algorithm (Appendix A.1). We inverted the travel-times of the surface wave and the shallow reflection (Section 2.3.1) to estimate the average electromagnetic (EM) propagation velocity and depth of the dry snow and firn in a least-squares approach (Appendix A.2), which used random resampling of the data to estimate uncertainties (Appendix A.4). We then applied a petrophysical model (Wharton *et al.*, 1980) which relates the EM velocity of dry snow and firn to its density (Appendix A.3).

Our measured-model approach relied on the Herron & Langway (1980) empirical firn density and age model, hereafter HL, which requires three input parameters: average snow density, average annual accumulation, and 10 m firn temperature. We parameterized the HL model with the MxRadar snow density, MxRadar SMB ($2015-2017$), and MERRA 2 m air temperature as a proxy for firn temperature (Loewe, 1970), to model the stratigraphic age and density of the firn. We assessed the firn model accuracy and sensitivity to parameterization to illustrate the accuracy of the MxRadar-HL (MxHL) firn density (Appendix A.5). We justified tuning the age model to improve our estimates of SMB in a process that jointly updated the age-depth and SMB models according to the radiostratigraphy.

The age model allowed us to convert the time domain radar image into the stratigraphic age domain, known as the Wheeler (1958) domain. In principle, the firn structure can be estimated by the age model because the statrigraphy was deposited in isochronous layers. The imaged firn structure can be flattened by converting the time domain GPR image into the Wheeler domain because the rows of the Wheeler image maintain a constant age. We ensured the relative structure of the age model by picking five horizons of the Wheeler transformed radiostragraphy with an average epoch of 5.3 ± 2.7 years (the latest being the 1991 horizon) and perturbing the age model with the interpolated residuals to re-flatten the Wheeler image. We developed a structure-oriented noise-suppression filter which operates along the radar reflection horizons in the Wheeler domain to eliminate remnant noise after conventional GPR signal processing (Appendix A.6). This innovative signal processing technique allowed SMB estimates to depths at which previously the stratigraphy was uninterpretable due to the low signal-to-noise ratio. We then converted the filtered radargram from

the Wheeler domain into the depth domain and interpreted 16 IRHs with an average epoch of 2.1 ± 1.7 years dating back to 1984. We calculated the error between the GTC15 geochemically determined age-depth scale and the 16 picked IRHs and interpolated a second grid of perturbations which we applied as a final update to the age model. We calculated the instantaneous SMB by taking a numerical derivative of the age-depth model $\left(\frac{\mathrm{d}z}{\mathrm{d}a}\right)$ and multiplying it by the MxHL density model (Eq. (A.20)).

2.3.1 Review of Multi-offset Radar

Common-midpoint (CMP) radar surveys are practiced in glaciology to estimate the EM wave speed of the ice, air, and/or water mixture (e.g. Eisen *et al.*, 2002). The wave speed is related to firn density and liquid water content using a dielectric mixture formula for a two or three phase relationship (e.g. Looyenga, 1965; Wharton *et al.*, 1980). In most studies, the CMP survey is treated as a point measurement of the firn vertical density profile, which is less laborious than extracting a core, but offers less vertical resolution and accuracy. Prior to GreenTrACS, CMP experiments on ice sheets were limited to point observations. We synthesized continuous CMP data by towing a streamer of nine antenna pairs that were linearly spaced from $1.33 - 12$ m apart (Fig. 2.3). While the antenna pairs in this deployment did not have a common midpoint, we rebinned the constant offset radargrams for each pair independently, such that the analysis was performed on offset gathers with common midpoints.

Interpreting the Near-surface Waves

Numerous geophysical methods exist for velocity analyses of CMP data gathers. Analyses of reflection data can be divided into two fundamental categories by the question, "Does the analysis assume normal moveout?" Normal moveout (NMO) is the reflection travel-time dependence on offset that arises from a homogeneously-

layered and planar subsurface structure (within the distance of the maximum antenna offset) that exhibits small vertical velocity heterogeneity (Al-Chalabi, 1974). Previous studies avoided classical NMO analysis, instead using less automated, more computationally expensive methods that favored accuracy (Bradford *et al.*, 2009; Brown *et al.*, 2012, 2017). Many caveats of NMO velocity analysis and sources of error in the radar common-midpoint analysis are discussed in Barrett *et al.* (2007). We demonstrate that NMO analysis of the snow and shallow firn yields a satisfactory result for data with low noise (see Appendix A.5), as ice sheet stratigraphy in the high elevation accumulation zone is close to homogeneous and planar at the length scale of the radar streamer array.

Linear moveout (LMO) is the one-way travel-time dependence on offset of radar waves traveling directly from the transmitter through the air over the ice sheet and through the snow under the ice sheet surface to the receiver antenna. We assumed that the air wave expresses the linear moveout velocity $c \approx 0.2998\ m/ns$ to calibrate the timing of the multi-channel system (Appendix A.2). To analyze the surface wave, we assumed that the shallow, surficial snow is also planar and homogeneous at the scale of the maximum offset. We identified the air wave, surface wave, and a near surface reflection and their respective moveout behavior in Fig. 2.4. The travel-times of these waves were interpreted using a horizon tracking algorithm (see Appendix A.1). The linear methods for LMO and NMO velocity analysis are described in Appendix A.2 and the methods for estimating the surficial and average snow density and depth of the fall 2014 IRH are discussed in Appendix A.3. We quantified the uncertainty of the density, depth, age, and SMB used to parameterize the HL model in Appendix A.4.

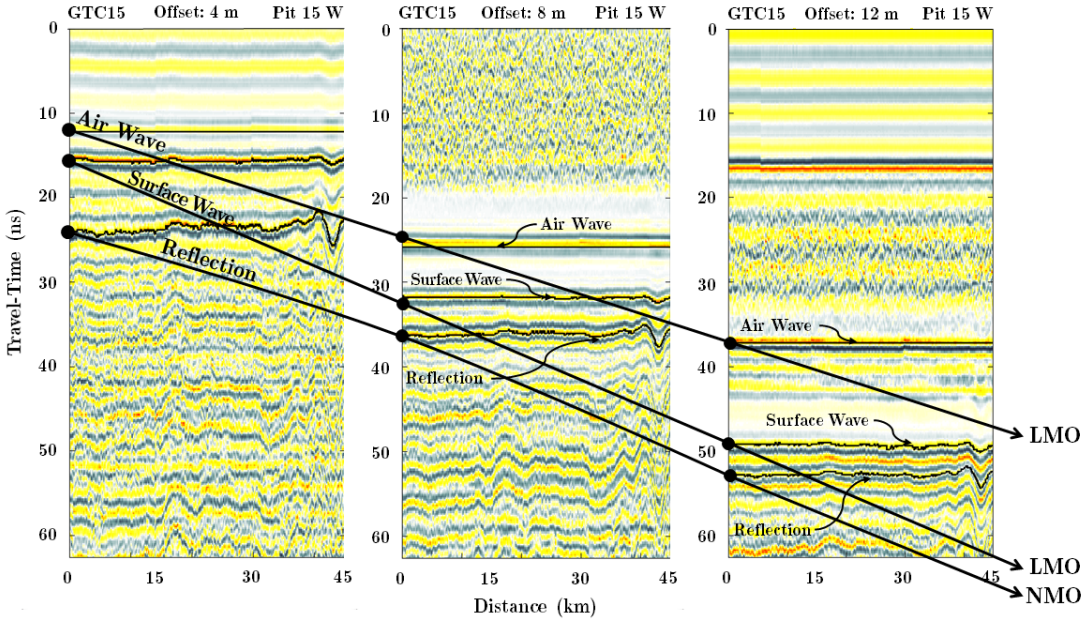

Figure 2.4: This offset gather is represented by radargrams recorded at offsets 4, 8, and 12 m along the initial 45 km of GTC15 Spur West, and is annotated to convey the waveforms used in our analysis and the concepts of normal moveout (NMO) and linear moveout (LMO). Consider the traces at zero distance for each offset as a CMP gather. The air wave and surface wave arrivals are modeled by a linear expression of travel-time as a function of offset (Eq. (A.1)). The air wave is the first to arrive and expresses a more shallow slope (faster velocity) than the surface wave which is impeded while traveling through the snow. The annotated reflection expresses nonlinear moveout which is approximated by NMO (Eq. (A.2)). The surface-wave (LMO) and reflection (NMO) annotated in this diagram are used to estimate the surface snow density, average snow density, and depth of the fall 2014 isochronous reflection horizon (IRH). The age of the horizon was determined at GTC15 and allowed us to estimate the $2015 - 2017$ SMB (see Appendix A.3), and in turn, is used to parameterize the HL model (see Appendix A.5).

Critically Refracted Waves

Lateral energy travels on direct raypaths from transmitter to receiver, but also on raypaths that are critically refracted at the free-surface. An upgoing reflected wave can become critically refracted along the air/snow interface upon exiting the snow surface. These refracted waves appear in Fig. 2.4 as multiple air wave arrivals succeeding the initial air wave. In Appendix A.2.1 we provide a discussion of the critically refracted wave phenomena with an accompanying snowpack model and exercise to support and demonstrate the critically refracted raypath.

2.3.2 Spatial Correlation of Surface Snow Density

The LMO and NMO estimated snow densities are independent measurements of the snow density above the interpreted radar horizon. The GPR surface wave maintains a fairly consistent depth level ($\sim 0.5\ m$, Eq. (A.17)), but the NMO reflection horizon does not. To mitigate the effects of depth on the correlation we extracted the rows of the MxHL density model corresponding to the average depth of the LMO ($0.5\ m$) and NMO ($1.92\ m$) horizons interpreted for velocity analysis (Fig. 2.4). We used Pearson (1907) correlation to determine the relationship between the density at $0.5\ m$ depth and the density at $1.92\ m$ depth. Additionally, we conducted variogram analysis (Matheron, 1963) on the LMO estimated snow density for each of the three transects of GTC15 Spur West. We determined the length scale over which there is consistent spatial correlation of the surface snow density across all three transects as the distance where the three experimental variograms diverge. We understand this divergence point as the experimental range of the variogram with the shortest length scale of correlation. We determined the experimental range of the remaining two variograms at a the second divergence point and as a significant slope break or

change in concavity/convexity.

2.4 Results

The multi-offset radar travel-time inversion determined the GrIS surface snow density and average snow density without manual observations (Fig. 2.5). We estimated the $2015-2017$ SMB from the MxRadar-derived snow depth and density using the GTC15 age of the near-surface IRH (Fig. 2.5). The LMO and NMO densities were independently estimated and strongly correlate ($R^2 = 0.67$, $p = 0$). Spatial patterns in the LMO derived snow density are consistent for three azimuths up to 2 km lag distance (Fig. 2.6). The multidecadal average 10 m wind direction from GEN3ENS ($1979-2012$) along GTC15 Spur West is approximately 152°. With information on the predominant wind direction, a closer look at Fig. 2.6 reveals directionality in the spatial pattern of surface snow density. The range of the variogram for the 157° transect (in the direction of the predominant wind) is $\gtrapprox 6$ km, the range of the 246.5° transect (orthogonal to the predominant wind) is ~ 2 km, and the range of the 40.5° transect (oblique to the predominant wind) is ~ 3 km.

By combining the radar-derived density and SMB with MERRA 2 m temperature we accurately parameterized the HL firn density and age model. For depths up to ~ 22.5 m the mean absolute error between GTC15 densities and MxHL densities is 9.6 kg/m^3, with a bias of $\lessapprox 1$ kg/m^3, and rms error of 12.2 kg/m^3. We find that extrapolating the GTC15 densities along GTC15 Spur West introduces an insignificant (on the order of 1%) bias to the SMB of -0.004 m $w.e.$ a^{-1} and rms error of 0.005 m $w.e.$ a^{-1}. The MxHL firn model permitted radar imaging in the depth and stratigraphic age domains. In Fig. 2.7 and Fig. 2.8, we illustrate our structure-oriented filter along GTC15 Spur West between $35-55$ km distance, where the largest

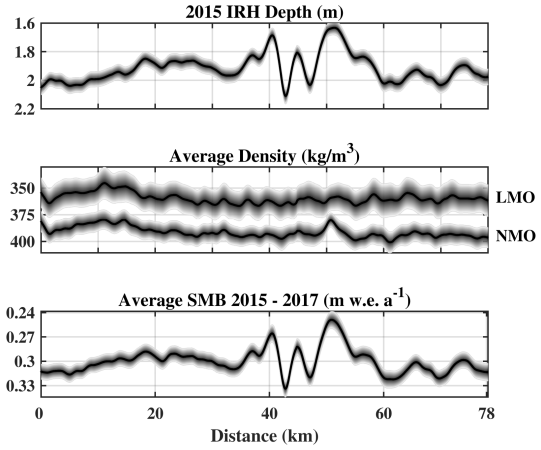

Figure 2.5: The MxRadar inversion parameter distributions along GTC15 Spur West. The LMO and NMO densities were independently estimated and strongly correlate ($R^2 = 0.67$, $p = 0$). The MxHL model is parameterized by the average of the LMO and NMO densities, the $2015 - 2017$ average SMB, and MERRA ($1979 - 2012$) average $2\ m$ temperature.

heterogeneity in firn stratigraphy occurs. After applying structure-oriented filtering, we were able to interpret significantly more IRHs and refine the age-depth model to an accuracy of ±31 days (see Appendix A.4).

We reconstructed the temporal SMB history from Jan. 1984 to Jan. 2017 and compare our result to the GTC15 firn core derived SMB in Fig. 2.9. The MxHL SMB history has a mean absolute error of 0.038 $m\ w.e.\ a^{-1}$, a bias of 0.004 $m\ w.e.\ a^{-1}$, and an rms error of 0.047 $m\ w.e.\ a^{-1}$. Uncertainty in the SMB measured from GTC15 was calculated following Graeter *et al.* (2018). Average uncertainty in annual SMB is 0.036 $m\ w.e.\ a^{-1}$ and 0.044 $m\ w.e.\ a^{-1}$ for MxHL and GTC15, respectively. The mean thickness of an annual layer for the period $1984 - 2017$ is 57.9 cm as measured at GTC15. The mean absolute error in the thickness of an annual layer estimated by MxHL is 7.8 cm, which contributes 0.039 $m\ w.e.\ a^{-1}$ (13%) error in the SMB reconstruction on average. Density inaccuracies in the SMB reconstruction result in

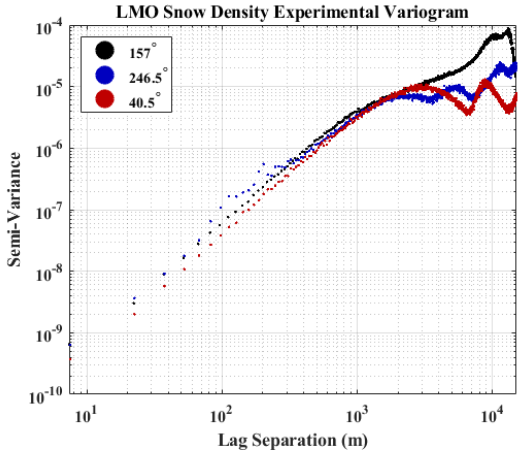

Figure 2.6: We calculated experimental variograms of the LMO estimated snow density along the three azimuths of GTC 15 Spur West using lag separations up to $15\ km$**. Plotted in log-log space, the linearity of each variogram slope indicates that spatial correlation among the three azimuths exists up to** $\sim 2\ km$ **distance. Correlation beyond this distance is difficult to assess given the limited azimuths and lag separations possible for GTC 15 Spur West. However, predominant wind direction appears to have a control on the correlation length, as evidenced by the** $\gtrapprox 6\ km$ **range of the** $157°$ **transect variogram (in the direction of the predominant wind) and shorter,** $\sim 2\ km$ **and** $\sim 3\ km$ **ranges of the** $246.5°$ **transect (orthogonal to the predominant wind) and** $40.5°$ **transect (oblique to the predominant wind), respectively.**

a $0.004\ m\ w.e.\ a^{-1}$ (1.3%) error on average. The MxHL $1984-2017$ multidecadal average SMB is $0.297 \pm 0.016\ m\ w.e.\ a^{-1}$ and is a good estimator of the GTC15 $1984-2017$ multidecadal average SMB ($0.301 \pm 0.025\ m\ w.e.\ a^{-1}$). At GTC15 the $2015-2017$ average SMB is within the uncertainty bounds of the multidecadal averages spanning $1969-2017$, the oldest period spanned by the core, and $1984-2017$ the period spanned by the MxRadar imagery.

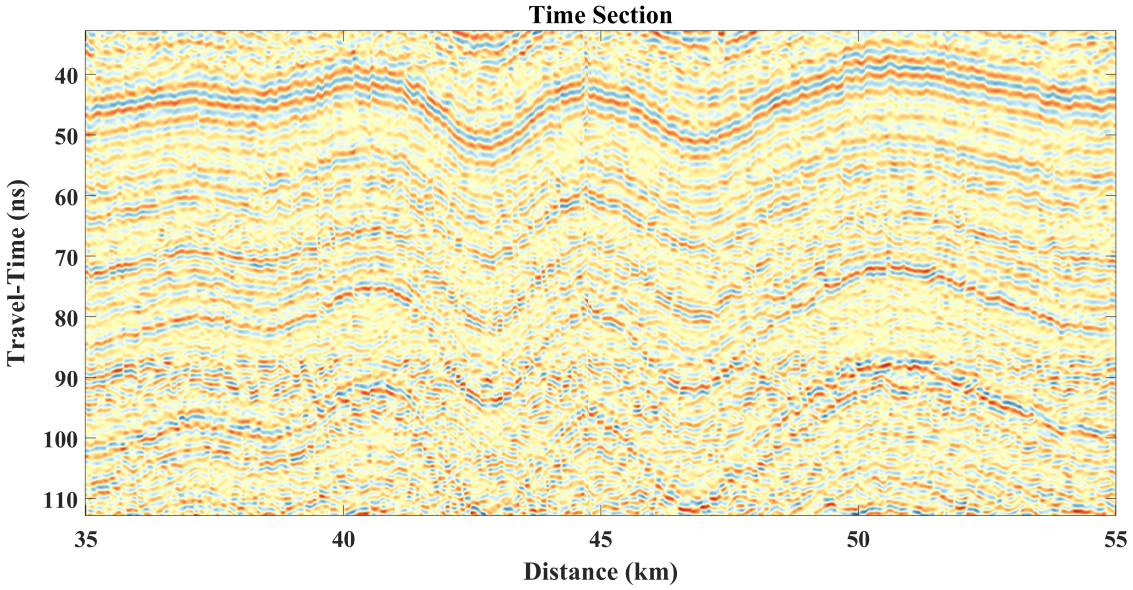

Figure 2.7: Conventional GPR processing was applied to each of the nine constant offset radargrams. We then performed NMO correction to project each constant offset image to zero offset. We stacked the NMO corrected radargrams together to synthesize one conventional GPR travel-time image. The travel-time image remains quite noisy, and it is difficult to interpret due to the discontinuities along the reflection horizons.

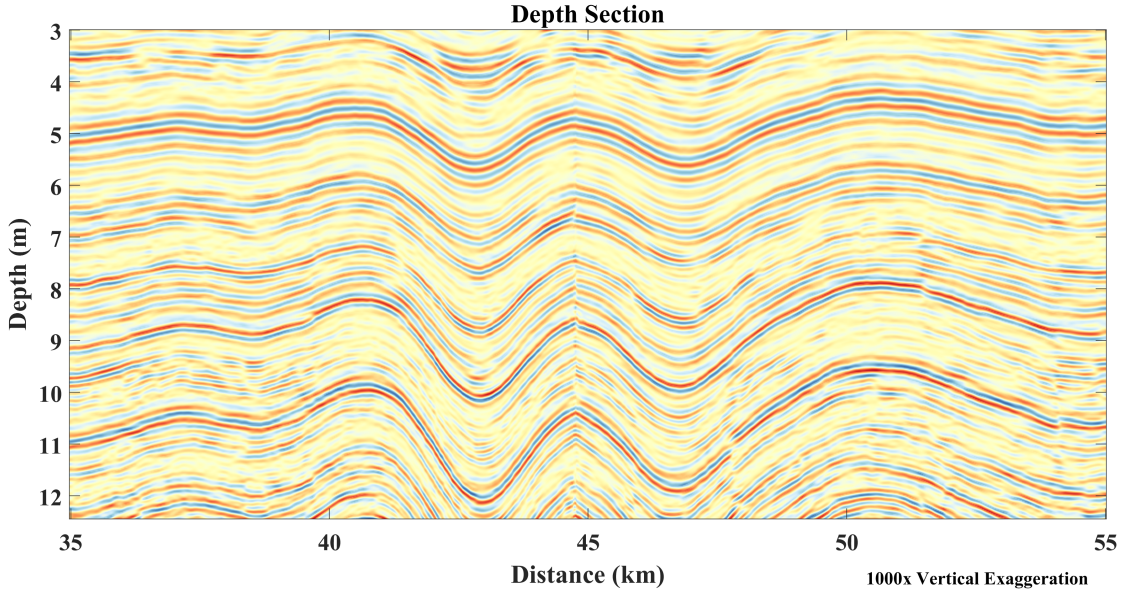

Figure 2.8: The travel-time image (Fig. 2.7) is first transformed into the stratigraphic age domain, known as the Wheeler (1958) domain. Then we applied structure-oriented filtering to the Wheeler domain image and converted into the depth domain. The depth section, taken from GTC15 Spur West, has remarkable continuity along the reflection horizons, which allows us to interpret IRHs to $\sim 22.5\ m$ depth. The undulation in the firn stratigraphy is caused by spatial variability in snow accumulation. It is necessary to interpret along steeply varying undulations like these to evaluate high resolution ($< 5\ km$) regional climate model simulations of SMB. However, without the structure-oriented filter we would be unable to track the reflection horizons along the undulations.

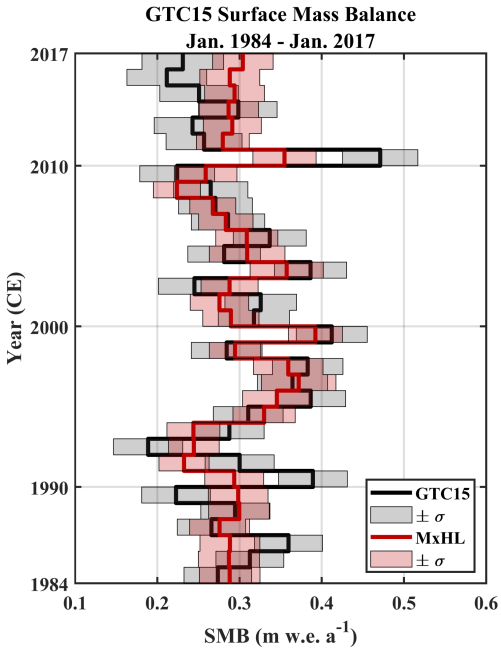

Figure 2.9: The GTC15 and MxHL historical SMB for Jan. 1984 – Jan. 2017. Uncertainty in GTC15 SMB ($\pm\sigma$) was estimated following Graeter *et al.* (2018). Uncertainties in the MxHL $1984-2017$ SMB ($\pm\sigma$) were propagated by Monte Carlo simulations of firn models generated from the parameter distributions of snow density, $2015-2017$ SMB, and MERRA temperature. We applied ± 31 days uncertainty to the measured ages of isochrones within the simulations.

2.5 Discussion

We independently assessed the four sources of uncertainty in the MxHL SMB (depth, density, temperature, and age) and then propagated these uncertainties through the MxHL model by Monte Carlo simulation to estimate the SMB mean and standard deviation for each year of $1984-2017$. On average, the difference between GTC15 and MxHL SMB is small enough to accept the MxHL measured-modeled densities in place of extrapolating the measured firn core density along GTC15 Spur West. Extrapolated densities are likely to be much less accurate farther from core sites and in the percolation zone, due to increased near-surface pore space reduction caused by melt water infiltration (Harper *et al.*, 2012). We also expect the accuracy of the

HL density model to break down at elevations within the percolation zone (Brown *et al.*, 2012). Annual fluctuations in density, and density excursions due to warming events, are not captured in the HL model. Using the MxRadar, we have the ability to measure the density profile in the percolation zone with additional layer picking for near-surface velocity analysis, but the NMO approach is sensitive only to the average density of intervals in between the layer picks (Dix, 1955) and is susceptible to errors due to subsurface velocity heterogeneities and data noise (Al-Chalabi, 1974).

In the upper $\sim 2\ m$ of the firn column we replaced modeled densities with a linear fit between the two radar measurements of snow and firn density using the surface wave and the reflection from the fall 2014 IRH. This reduced the near-surface bias present in the HL density profile and we found strong correlation between the densities of these independent radar measurements. The richness of the MxRadar data stream permits geostatistical analysis at the sub-kilometer scale. We found that local (on the order of 1 km neighborhood) processes control the GrIS dry snow density. The similarity in spatial patterns of radar estimated surface snow density, up to $\sim 2\ km$ lag distance, contrasts with the findings that no correlation exists between surface snow density, latitude, longitude, or elevation (Fausto *et al.*, 2018), which is likely due to the limited observations of snow density at the $< 1\ km$ and $< 10\ km$ scales within the *Surface Mass Balance and Snow Depth on Sea Ice Working Group* dataset (Montgomery *et al.*, 2018). Our variogram analysis was tested to 15 km lag separations along three azimuths: 157°, 246.5°, and 40.5°. In the direction of the prevailing wind, we found $\gtrapprox 6\ km$ correlation distance with diminishing correlation length for transects increasingly orthogonal to the prevailing wind. We found that the SMB decreased with increasing slope on the leeward, 157°, transect, which cor-

roborated the findings of Arcone *et al.* (2005). We did not find trends in SMB with slopes of the 246.5°, and 40.5° transects, as these transects were approximately orthogonal and 21.5° oblique to the predominant wind direction, respectively. Future application of this method to the $4000+$ km traverse will allow the exploration of surface density variations at much larger scales and at additional orientations relative to the prevailing winds.

The $2014-2017$ SMB appears to be overestimated by MxHL, though the near-surface radar velocity analysis was focused on this range. We support the radar findings here with the understanding that firn samples recovered from these depths are susceptible to *in situ* losses due to their unconsolidated nature. The radar retrieval has a sample footprint of approximately ~ 25 m (twice the length of the antenna array) and is nondestructive, while the borehole diameter is $\sim 8cm$ and samples only one point in space. It is also likely that the age model is less accurate nearest the ice sheet surface due to core sample loss; however, we sacrifice greater accuracy in the radar domain because of the limitations in our ability to interpret depth image. The fall 2014 horizon was the latest IRH measured in our analysis. Picking annual reflection horizons later than 2014, near the model boundary, created steep gradients in the numerical derivative required to estimate the SMB which yielded erroneous values.

We see evidence of the 2012 melt event (Nghiem *et al.*, 2012) in the filtered depth image (Fig. 2.8). At three meters depth, the top of the reflection sequence represents January 2013, and at four meters depth, the bottom of the sequence is January 2011. This IRH sequence expresses fading and discontinuity that, we hypothesize, is the result of 2012 melt water infiltration. Measured at GTC15, the 2011 annual layer has

a melt feature percentage of 7.9%. However, melt water induced firn densification does not explain the inaccuracy in 2010 MxHL SMB, as 2010 recorded 0% melt feature percentage at GTC15. The MxHL density model is accurate within the 2010 annual layer, rather our estimate of the 2010 annual layer thickness is 22 *cm* thinner than measured at GTC15. This is the second largest error in annual layer thickness, only behind the 2015 layer which was estimated to be 24 *cm* thicker than measured at GTC15 because of the aforementioned issues in estimating SMB near the model boundary. The degraded image quality of the $2011 - 2013$ IRH sequence inhibited our ability to interpret the age sequence accurately enough to define the annual layer thicknesses for 2011 and 2012. Instead, we relied on interpolation to approximate the thickness of these horizons. The leading source of error in the historical SMB reconstruction are inaccuracies in the age model that result from limitations in our ability to interpret the radar image, even after applying the structure-oriented filter.

The multidecadal average SMB for the period $1984-2017$ at GTC15 has remained nearly constant. Yet, sinusoidal variability in SMB on the decadal time scale is apparent in the MxHL historical SMB reconstruction and is confirmed by GTC15 SMB. Decadal variability in the MxHL reconstruction would not be observable without the application of structure-oriented filtering and interpretation that permitted an accurate instantaneous SMB model. For GPR imagery expressing small or gradual SMB variability it may be sufficient to apply the structure-oriented filter in the Wheeler domain without the steps of interpretation, age model corrections, and image re-flattening (Appendix A.6). The snow density estimation component is unique to the multi-offset radar and integral in our ability to parameterize the HL model. However, the structure-oriented filtering can be applied to any GPR imagery of isochronous

firn, provided a stratigraphic age model in the radar travel-time domain is used as a proxy for the firn structure.

Along GTC15 Spur West, we expect the largest errors due to firn advection to occur across the studied undulations (Fig. 2.7 and Fig. 2.8), where the SMB gradient is largest and oscillating. The two undulations here represent the same feature observed on outbound and inbound traverses, and serve as a demonstration of the repeatability of the methods. In regions where the spatial gradient in SMB is dynamic or ice sheet surface velocities are large, the advection of firn mass decreases the accuracy of radar estimated SMB. On Pine Island Glacier, with ice surface velocities on the order of $10 - 10^3\ m\ a^{-1}$, strain corrections applied to the accumulation model amounted to a 1% correction to the $1986 - 2014$ average SMB (Konrad *et al.*, 2019). Ice surface velocities along GTC15 Spur West are on the order of $10\ m\ a^{-1}$ (Joughin *et al.*, 2018), and therefore we accept a contribution of error that is an order of magnitude less than the uncertainty, by not applying corrections for the SMB due to advection.

2.6 Conclusions

GreenTrACS conducted the first multi-offset GPR traverse on the Greenland Ice Sheet, covering a total distance of 4436 km. We examined a 78 km section of the GreenTrACS 2017 traverse (GTC15 Spur West) to develop the methodology for multi-offset GPR wave velocity, imaging, and uncertainty analyses to accurately quantify the surface snow density, average snow density, firn density, instantaneous SMB, annual SMB, and multidecadal average SMB for the period $1984 - 2017$. Using travel-time inversion of the radar waveforms, we continuously mapped Greenland snow density without manual observations of the snow. We found consistent spatial correlation of near-surface density for separations up to 2 km distance and evidence to

support the prevailing wind direction as a source of correlation up to 6 km distance. We found significant correlation ($R^2 = 0.67$, $p = 0$) between near-surface snow density and average snow density of the upper 2 m. We demonstrated the use of the Herron & Langway (1980) model that was parameterized by the radar-derived snow density, radar-derived SMB ($2015 - 2017$), and MERRA 2 m air temperature, to estimate firn density and age. Our measured-modeled firn density in the dry snow accumulation zone accurately represents the firn core but can be performed continuously along a traverse in the field without destructive measurements.

GreenTrACS Core 15 Spur West presented an interesting challenge because of spatial SMB variability that is enhanced by the surface topography. In the dry snow zone, the topographic effect induces undulations in the firn stratigraphy which steepen with depth, due to the persistence of increased accumulation. Folds in the firn stratigraphy are difficult to image clearly with conventional GPR processing methods. Using seismic interpretation methods, we facilitated structure-oriented filtering by utilizing the firn age model to determine the firn structure. In doing so, we furthered the application of the IRH theory, which is integral in SMB analyses conducted with radar imagery. This innovation enabled our interpretation of deeper (from 16.60 ± 0.04 m to 20.15 ± 0.04 m at GTC15) and older (from 1991 ± 31 days to 1984 ± 31 days) layers and permitted tuning the age model to a degree of accuracy which allowed us to derive instantaneous estimates of SMB which we averaged annually and multidecadally. Future work will include application of this methodology to the entire $4000+$ km GreenTrACS traverse, with independent evaluation at the 16 core sites.

To reduce the labor in interpreting the radar imagery of future work, it would be advantageous to model the firn age-structure using the kinematic wave equation (Ng

& King, 2011) to capture the advection process imprinted on the radiostratigraphy without having to interpret the Wheeler domain radargram. We picked horizons in the Wheeler domain as a necessary step in applying the structure-oriented filter to the GTC15 Spur West radargram. This interpretive process could be avoided by generating the relative age using the kinematic wave equation. Yet, this model requires an independent estimate of firn density and accumulation to satify the initial and boundary conditions. Deep learning techniques have been recently applied to seismic imaging that automate structure-oriented filtering and horizon interpretation problems. By generating synthetic seismograms from numerical structural models as training data (Wu *et al.*, 2020), relative stratigraphic age models have been recovered from real seismic data and used for automated isochrone horizon interpretation (Geng *et al.*, 2020). The kinematic wave firn model could serve as a basis for generating synthetic radargrams to be used in a deep learning application for historical SMB reconstruction.

CHAPTER 3:

SPATIALLY DISTRIBUTED SNOW WATER EQUIVALENT FROM GROUND-BASED AND AIRBORNE SENSOR INTEGRATION AT GRAND MESA, COLORADO, USA

Abstract

During the Intensive Observation Period of the NASA SnowEx 2020 campaign at Grand Mesa, Colorado, snow pit, depth probe, ground-based radar, and airborne light detection and ranging (LiDAR) observations of the snowpack were acquired. We developed a method for automatically determining two-way travel-time (TWT) of the 1 GHz ground-penetrating radar (GPR) reflection off the ground surface beneath the snow cover by maximizing the coherence between co- and cross-polarized GPR channels. We validated the accuracy of the travel-time picks at radar transect cross-over locations (N = 870, R = 0.78, RMSE = 0.9 ns). Combining radar travel-times with LiDAR derived snow depths yielded snow density and correlation length scale estimates along the GPR tracks. To extend this result, we developed a Multiple Linear Regression model that, once trained using LiDAR–GPR derived snow density, predicted the column average snow density within the LiDAR domain without dependence on GPR travel-times. LiDAR-based snow depths agree with those estimated from GPR TWTs using the modeled density (R = 0.74, RMSE = 11 cm). The modeled density shows spatial variability related to the interactions of wind, terrain, and vegetation. Densities in wind affected areas are greater than downwind areas that are protected by forest stands. Using the modeled densities and the LiDAR measured snow depths, we distributed the snow water equivalent (SWE) across the entire domain, and found good agreement with the pit measured SWE (N = 96, R = 0.78, RMSE = 41 mm).

3.1 Introduction

Snowpacks act as a natural reservoir of water vital to modern societies where supply is primarily derived from seasonal snow. In the western United States, over 50 % of the total runoff originates as snowmelt (Li *et al.*, 2017). The total availability and timing of snowmelt is critical to the performance of water management systems and the security of water resources, as existing reservoirs were designed based on historical levels of snowpack storage (Barnett *et al.*, 2005). Anthropogenic climate change has contributed to the declining western U.S. snowpack over the past 50+ years (Pierce *et al.*, 2008, e.g), and by the end of the 21st century, snow water equivalent (SWE) in the western U.S. is projected to decline by $\sim 50 \pm 10$ % (Siirila-Woodburn *et al.*, 2021). As global temperatures rise, the western U.S. is expected to become increasingly warmer and drier with greater interannual variability in precipitation (Masson-Delmotte *et al.*, 2021). The observed change in climate is causing an earlier onset of spring snowmelt with earlier peak flows and diminished summertime flows (Masson-Delmotte *et al.*, 2021). Unprecedented storm events, such as atmospheric rivers (Zhu & Newell, 1994), and rain-on-snow events (McCabe *et al.*, 2007) increase the stress on water management systems. Additional, unanticipated inflow from midwinter storm run-off can cause the failure of reservoir systems, as was the case with the 2017 Oroville Dam spillway failure (Koskinas *et al.*, 2019), and inflict casualty and hardship to communities downstream. Changes to the supply and demand of snow derived water will require storage and distribution strategies that better meet the legal, economic, political, cultural, and social needs of water users (Huss *et al.*, 2017).

In response to declining snowpacks (Mote *et al.*, 2018) and the increased demand

on water resources (e.g. Achhami *et al.*, 2018) in the western U.S., attention has been given to measuring, modeling, and developing new techniques for SWE estimates (e.g. Lettenmaier *et al.*, 2015). The objective of NASA's snow experiment (SnowEx) campaign is to test a suite of remote sensing instruments, which measure SWE, and can be deployed on a satellite platform for global monitoring (Marshall *et al.*, 2019). Accurate space-borne snow depth estimates have been achieved from passive microwave sensors (Tedesco *et al.*, 2010), Sentinel-1 radar returns (Lievens *et al.*, 2019, 2022), WorldView stereo digital surface models (McGrath *et al.*, 2019), and light detection and ranging (Hu *et al.*, 2021, LiDAR;) aboard ICESat-2 (Abdalati *et al.*, 2010). Optical techniques have the ability to measure snow depth directly, by differencing repeated acquisitions during periods with and without snow cover (e.g. Deems *et al.*, 2013), whereas microwave techniques raise questions about signal penetration, depolarization, and backscattering. Because of the advantages of greater spatial resolution and flexible scheduling to target acquisitions during periods of interest, airborne LiDAR has become a prime candidate for estimating snow depth and is being flown operationally for integration with hydrologic modeling at the catchment scale (Hedrick *et al.*, 2018). Regardless of choice in snow depth retrieval, an estimate of snow density is required to convert snow depths to SWE, and bulk density often provides the greatest source of uncertainty in SWE estimates, especially in deeper snow (Raleigh & Small, 2017).

Snow density is typically measured in a time consuming and spatially limited manner by excavating and weighing snow samples of a known volume from a snow pit or snow core. Because snow depth varies in space more significantly than density (e.g. Elder *et al.*, 1991; Sturm *et al.*, 2010) and depth measurements may be collected

more rapidly, throughout a campaign, density is observed far less frequently (e.g. Elder *et al.*, 1998; Rovansek *et al.*, 1993). As a result, snow sampling strategies tend to be too coarse to examine the 100 – 101 m scale spatial variability of snow density (e.g. Fassnacht *et al.*, 2010). A recent campaign in Arizona collected nearly 1000 density measurements at 10 – 20 m intervals to capture the range of processes (i.e. elevation, slope, aspect, and forest attributes) that influence snow densification, and from these observations bulk snow density was distributed using artificial neural networks (Broxton *et al.*, 2019).

Often, empirical models provide the means to spatially distribute density in SWE estimates. Linear regression models developed using snow depth alone are often unsuccessful because the snow load only has a linear effect on bulk density, while grain-bond characteristics can have an exponential effect (Sturm & Holmgren, 1998). The accuracy varies among linear snow density models that are parameterized by features such as net radiation, elevation, slope, curvature, and snow depth, as the success of such approaches is dependent on the time of year and snow climate (e.g. Elder *et al.*, 1998; López-Moreno *et al.*, 2013). Successful regression models parameterized by snow depth have been split up into elevation and month of year classes (Jonas *et al.*, 2009) or day of year and snow cover classification (Sturm *et al.*, 2010) to account for the effects snow depth and snow aging have on density. Over the timescale of days to weeks, densification processes of freshly accumulated snow result in negative correlation between snow depth and density, while over the timescale of months or longer, depth and density tend to be positively correlated (McCreight & Small, 2014). By differentiating between the short and long timescales of densification, McCreight & Small (2014) developed a linear density model capable of accurate daily density

estimates for converting depth to SWE at distributed measurement stations. Sets of linear models based on snow depth and climate predictors using snow telemetry data from the western U.S., Canada, and Alaska showed improvements in accuracy when compared to previous models (Hill *et al.*, 2019).

Snow density can also be estimated with process-based snow models, which may account for changes in bulk snow density due to new snowfall, metamorphism, and compaction. The representations of snow densification ranges in complexity, with some models utilizing more simple time-dependent compaction curves and other models representing snow compaction dynamically as a function of snow viscosity and overburden pressure. Essery *et al.* (2013) found that the dynamic models offer more consistent and accurate characterization of snowpack. However, there has been a range of performance in snow density simulation, even for a single physics-based model. For example, Snobal (Marks *et al.*, 1992) yielded low errors (mean absolute difference of 24 kg/m^3) in a study of the California Sierra Nevada (Painter *et al.*, 2016) but higher errors (root-mean-square error up to 142 kg/m3) in a study of the Canadian Rockies (Lv & Pomeroy, 2020). Egli *et al.* (2009) found similar capabilities in estimating snow density with physics-based models and empirical models at a point location in Switzerland. In contrast, Raleigh & Small (2017) found that the choice of snow density model (empirical or physical) produced differences in spatial distributions and basin mean estimates of snow density in California.

Despite numerous techniques for modeling snow density, there are a limited number of studies on how models characterize spatial variations in snow density and the underlying processes related to density variations; because few techniques exist for continuous spatial measurement of snow density to validate modeled estimates. Radar

techniques are the most prevalent for remotely sensing snow density, because of the relationships existing between dielectric permittivity (a main constituent of electromagnetic wave propagation) and snow density (e.g. Matzler, 1996). Passive microwave emission measurements combined with radiative transfer modeling is an established theoretical basis for retrieving snow density and ground permittivity (Schwank *et al.*, 2015). Though this technique has been proven experimentally at the plot scale (Lemmetyinen *et al.*, 2016), initializing the ground temperature and roughness remains challenging for satellite application. Ground-penetrating radar (GPR) is typically a ground-based method that records the amplitude and travel-time of a series of echoes from short-pulse electromagnetic waves as an image in range-time and position coordinates. With information about the propagation velocity of the snow, GPR can estimate the snow depth, or by exploiting a ray path function of travel-time versus antenna separation (offset) the velocity can be estimated, and thereby the snow depth and density. Interpreting GPR transect imagery is a laborious process that requires expert knowledge of digital signal filtering and manual picking of travel-times. Though complex, multi-offset GPR has continuously measured snow depth and density along transects of hundreds of meters in alpine mountains (Griessinger *et al.*, 2018) to tens of kilometers in Greenland (Meehan *et al.*, 2021). Drone-based aerial photogrammetry combined with GPR measurements has measured snow density along transects, which were interpolated across the study-plot scale (Yildiz *et al.*, 2021). Airborne radar surface echo analysis has measured snow and firn density at the regional scale in Antarctica (Grima *et al.*, 2014c). Indeed, radar derived snow observations require calibration and validation, which vexingly, remains limited due to the challenges of in-situ observation.

Our work addresses the need for high accuracy, distributed density measurements to improve parameterizations of snow densification processes and reduce model uncertainty. To do this, we inferred hundreds of thousands of measurements of the electromagnetic propagation velocity in snow by combining LiDAR measured snow depth and GPR measured two-way travel-times (TWT). Then via a two-phase dielectric mixture model, we converted velocity to dry-snow density (Section 2.4.3). Using variogram analysis, we determined the spatial correlation length of LiDAR snow depth, GPR TWT, the resulting bulk density, and SWE at Grand Mesa (Section 2.5). We then used the density inferred along the GPR transects to train a Multiple Linear Regression (MLR) model that distributed density within a 4.5 by 3.5 km domain using terrain and vegetation predictors derived solely from the LiDAR data (Section 2.6). These data and the rich validation data acquired during the NASA SnowEx 2020 Intensive Observation Period (IOP) at Grand Mesa, Colorado, provide the means to assess the accuracy of the LiDAR snow depths, the LiDAR–GPR measured snow density, the distributed density, and the SWE we derived therefrom (Section 3). In addition, we present a novel method to automate the post-processing and TWT interpretation (layer picking) through accurate and objective ground reflection detection (Sections 3.2.2 and 3.2.3). This advance opens the possibility for the operational use of GPR, by eliminating the time-consuming steps of data post-processing and manual interpretation of radar images.

3.2 Methods

3.2.1 Study Area

Grand Mesa, Colorado, is a high-elevation subalpine plateau with an average elevation of $\sim$ $3,200$ m and an area of $\sim 1,300$ km^2. Grand Mesa has a cold and dry continental snow climate, low relief, and varying vegetation cover from shrub steppe and subalpine meadow to dense conifer forest. These factors, along with the close proximity to a major airport make Grand Mesa an ideal study area for evaluating airborne snow remote-sensing techniques.

The Grand Mesa IOP spanned 27 January – 12 February, 2020. During that time, 154 snow pits were excavated and nearly 38,000 in-situ snow depth measurements were collected. The snow pits were distributed in forested and unforested areas along the swaths of the three airborne remote-sensing campaign flight lines (Figure 3.1). A conventional L-band GPR was pulled by ski in forested areas of central Grand Mesa and into unforested areas on the forest perimeters during 30 January – 1 February and 5 February. A multi-polarization L-band GPR was pulled by snowmobile in the unforested areas of the central and south regions of western Grand Mesa on 28 and 29 January, and 4 February, 2020. The snowmobile was driven along the edges of the many forested stands in the survey domain, but did not travel through densely treed areas. Throughout this week, we acquired 144 km of quasi-gridded snowmobile-driven radar transects, and 16 km of skied spiral transects in the forest that were occupied by coincident depth measurements. We used a 4.5 km by 3.5 km portion of the LiDAR acquisition to bound the GPR transects (Figure 3.1). The GPR transects acquired beyond the LiDAR boundary were omitted from our analysis. The different

GPR systems and data acquisition strategies are recounted in Section 3.2.2 and the data processing and TWT interpretation methods are detailed in Section 3.2.3.

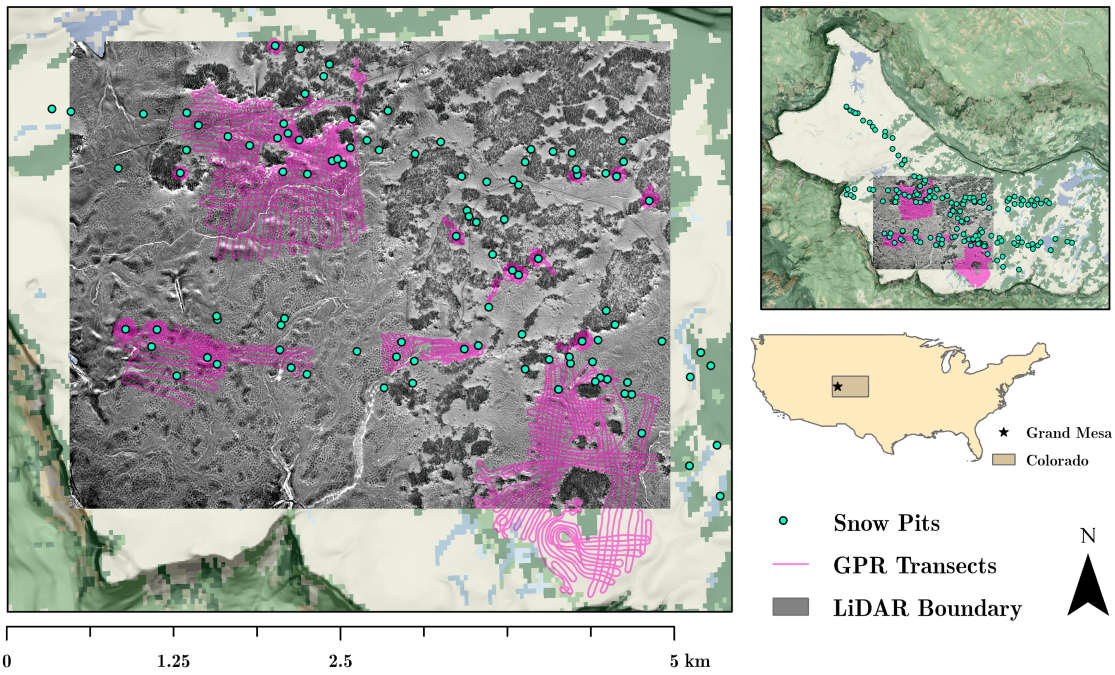

Figure 3.1: Study area map of the snow pit locations, GPR transects, and LiDAR boundary. These data were acquired during the NASA SnowEx 2020 Intensive Observation Period at Grand Mesa, Colorado (Hiemstra *et al.*, 2021) Land cover classification data were accessed from the 2016 National Land Cover Database (Homer *et al.*, 2020). Slope hillshade data were accessed from the USGS 3D Elevation Program (Lukas & Baez, 2021). Cartographic boundary files were accessed from the Census Bureau's MAF/TIGER geographic database (Bureau, 2020). The geographic coordinate projection of these maps is UTM Zone 12 N; EPSG code 32612.

3.2.2 GPR Data Acquisition

Two GPR instruments were operated during the first week of the Grand Mesa IOP. In the forested areas, by ski we pulled a conventional L-band GPR within a sled that was equipped with a Differential Global Positioning System (DGPS) receiver. Whereas, in unforested areas, we deployed a multichannel L-band (1 GHz) GPR configured with one transmitting antenna and two receiving antennas that were

oriented parallel (H) and orthogonal (V) to the transmitter (H). The transmit and receive antennas were separated by 25 cm. Using this GPR configuration we simultaneously acquired the radar imagery in co- and cross-polarizations (HH & HV). The multi-polarization GPR array was fastened within a sled and towed behind a snowmobile at approximately 3 m/s. The DGPS receiver was located on the snowmobile 5 m away from the GPR array, so we applied a geometric correction to relocate the coordinate positions to the antenna midpoint of each channel.

The GPR systems were operated continuously, collecting approximately 30 traces per second, given the duration of the time window (30 ns), the sample interval (0.1 ns), and the number of stacks acquired (2). Due to differences in the traversed speed, the spatial interval of the GPR traces collected via snowmobile is approximately 10 ± 1 cm, while the interval for traces collected by ski is 5 ± 1 cm. We used piecewise cubic Hermite interpolating polynomials (Kahaner *et al.*, 1989) to fix a geolocation to every acquired trace, as the GPS acquisition rate was 1 Hz. We estimated the accuracy of the georeferencing at 70 cm, which is on the order of the GPR footprint. This estimate follows from adding the horizontal dilution of precision (50 cm) and uncertainty in the sled location (50 cm) in quadrature.

3.2.3 GPR Data Processing

We expected the rough ground surface to depolarize the L-Band radar signal and proposed the coherence between the co- and cross-polarized channels as a filter that illuminates the ground reflections and removes the planar reflections of the snow stratigraphy. We paired the co- and cross-polarization radargrams into shot gathers, which are the bins of traces that share the same transmitter location. The automatic travel-time pick is determined by maximizing the coherence between the co- and

cross-polarization shot gathers. We applied the unnormalized cross-correlation sum as our measure of coherence,

$$C(t) = \frac{1}{2} \sum_{j=1}^{N} \left\{ \left[\sum_{i=1}^{M} S_{i,t} \right]^2 - \sum_{i=1}^{M} S_{i,t}^2 \right\} \quad , \tag{3.1}$$

which is half of the summed difference between the energy of the stacked traces and the energy of the input traces (Neidell & Taner, 1971). The calculation in Equation 3.1 is performed in a sliding window (length $N = 11$) that is evaluated at every sample (t) of the GPR signal ($S_{i,t}$) for channels i ($M = 2$). The HH-HV coherence (C_{HH-HV}) at each shot location is then normalized between zero and one by dividing by the maximum coherence of the trace

$$C_{HH-HV} = \frac{C}{\max(C)} \quad . \tag{3.2}$$

Because the GPR channels have an offset of 25 cm (one wavelength), the incident waves are approximately normal to the reflection horizon and the two channels sum coherently.

We determined the TWT from the ground surface beneath the snow cover, by selecting the travel-time with the maximum coherence of each trace. Because the maximum coherence occurs at the center of the two nanosecond wavelet (Booth *et al.*, 2010), we subtracted one nanosecond from the automatic pick to estimate the first break of the reflection. We then applied a median filter to remove outliers and reviewed the automatic picks for any systematic errors. Manual inspection revealed that less than 1 % of the automatic picks required correction. To illustrate this, automated picks are overlaid on the radargrams from a 900 m long transect in Figure

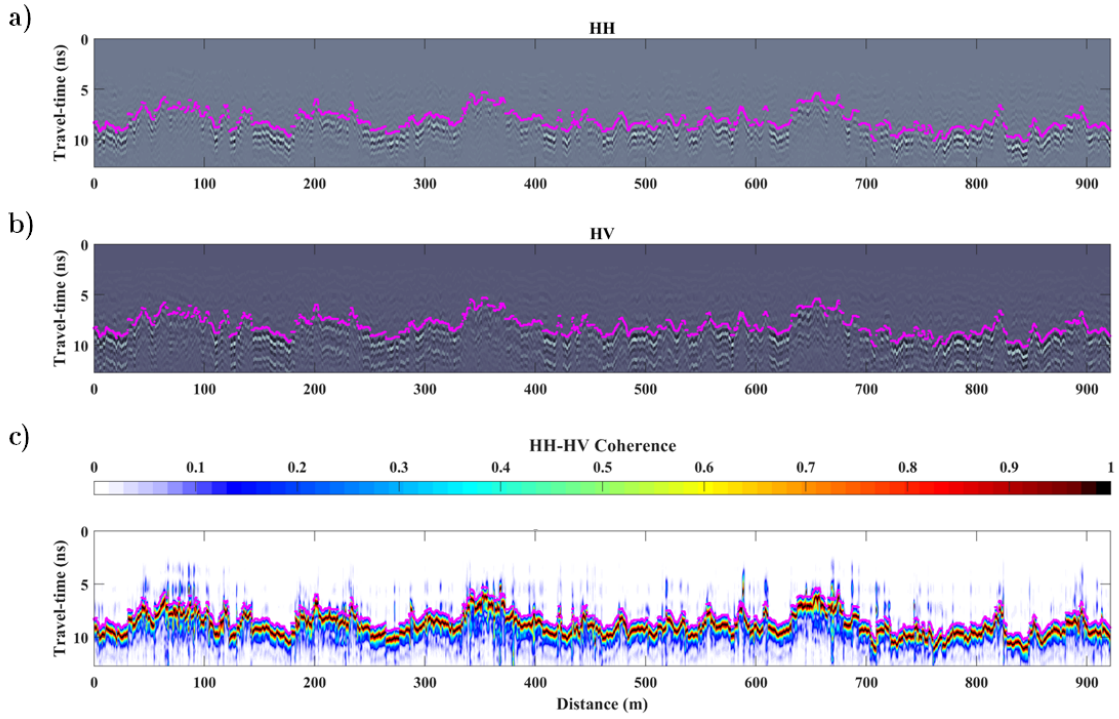

Figure 3.2: A 900 m **transect presenting the** a) **HH and** b) **HV GPR profiles and** c) **the coherence of these radargrams calculated using Equations 3.1 and 3.2. The automatically determined TWTs are illustrated in magenta.**

3.2. The resulting TWT data produced from this method and used in this study are available through the National Snow and Ice Data Center (Meehan, 2021b).

3.2.4 Snow Observations

In-Situ Measurements

Snow pits were measured in great detail for the snow depth, density, water equivalent, temperature, wetness, liquid water content, grain size, and stratigraphy (Vuyovich *et al.*, 2021). Snow density was measured in the snow pits every 10 cm from the snow surface to the ground using a 1000 cm^3 wedge sampler, resulting in a continuous density profile. Per protocol, each density measurement was sampled once more in an adjacent column and if the difference between these samples exceeded 10 %, a third

time. The bulk density at each of the snow pits was then calculated by averaging all measurements for each snow pit. The average density sampled from each of the columns shows high repeatability with a mean absolute difference of 2.5 %. Using the same sampling strategy, the dielectric permittivity was measured using resonant frequency capacitor. Liquid water content was estimated by combining the density and dielectric permittivity in an empirical formula, and showed that the snowpack remained dry throughout the IOP (Webb *et al.*, 2021). Snow depth measurements were collected using geolocated probes along spiral transects which were centered around pits (Hiemstra *et al.*, 2020).

LiDAR Snow Depth

Snow depth was estimated from repeated airborne LiDAR point cloud surface elevations of snow-free and snow-covered terrain using the Multiscale Model to Model Cloud Compare (M3C2) method (Lague *et al.*, 2013). The M3C2 method operates directly on point cloud data, computes the local distance between two point clouds at a scale that is appropriate for the surface roughness, and estimates a confidence interval for each distance measurement. The Airborne Snow Observatory (ASO) performed the snow-free acquisition on September 26, 2016 (Painter *et al.*, 2016; Painter & Bormann, 2020), and Quantum Spatial, Inc. acquired a time-series of snow-covered surface elevations during the IOP. We selected the February 1, 2020, flight to minimize temporal collection differences with the GPR and resulting errors due to snow redistribution and compaction. We removed vegetation following methods in (Štroner *et al.*, 2021) and transformed the 2016 snow-free vertical datum into NAVD88/Geoid 12B (the same as 2020 snow-on) using NOAA VDatum 4.3 software (NOAA, 2021). Then, we applied the M3C2 method as computed in (Hojatimalekshah *et al.*, 2021)

to estimate snow depth. The relative accuracy of the snow depth measurement was estimated at 7 cm, based on the maximum standard deviation of the M3C2 method. After computing the snow depth, the 3 m ASO bare-earth and vegetation data products were resampled to the 1 m resolution of the snow-covered SnowEx 2020 LiDAR acquisitions and the coordinate system was transformed from UTM zone 13 N to UTM zone 12 N.

LiDAR-GPR Inferred Density

We combined the LiDAR snow depths with the GPR TWTs to measure the average snow density at the co-located points. To co-register the LiDAR coordinates within a 1 m radius of the GPR TWTs we applied a k-d tree searcher (Bentley, 1975). We then used the median values of the TWTs within a 1 m radius of these coordinates to interpolate to the LiDAR grid. The average electromagnetic wave speed of the snowpack was estimated using

$$\mathrm{v_s} = 2\frac{\mathrm{z_s}}{\mathrm{TWT}} \quad , \tag{3.3}$$

for each of the coincident LiDAR snow depths (z_s) and GPR two-way travel-times (TWT). We then related the electromagnetic wave speed to the dry snow density using the Complex Refractive Index Method (Wharton *et al.*, 1980, CRIM;)

$$\rho_s = \rho_i \left(1 - \frac{v_a\left(v_i - v_s\right)}{v_s\left(v_i - v_a\right)}\right) \quad . \tag{3.4}$$

The CRIM equation relies on the known wave speeds of the pore-space ($v_a = 0.3\ m/s$) and ice matrix ($v_i = 0.169\ m/ns$), the measured bulk wave speed of the snowpack (v_a; Equation 3.3), and the density of ice ($\rho_i = 917\ kg/m3$) to determine the dry

snow density (ρ_s ; Equation 3.4).

3.2.5 Spatial Correlation of Snow Depth, Travel-time, and Bulk Density

We examined the differences in snow properties between forested and unforested areas using generalized relative semi-variograms (Isaaks & Srivastava, 1989). The generalized relative semi-variogram describes the percentage of variability relative to the mean as a function of separation distance between observations. To estimate the spatial variability of the snow depth, TWT, density, and the resulting SWE of the 1 m gridded data along the radar transects, the experimental variograms were first calculated in 1 m bins up to a 250 m lag, and then fit using exponential models to estimate the range, sill, and nugget parameters (e.g. Cressie, 1985). From the exponential model we multiplied the estimated range parameter by three to estimate the correlation length, the distance where the variogram reaches 95 % of the sill. We created 250 realizations of the experimental variogram calculation and model fit for each variable using 10 % random subsampling to assess the mean and standard deviation of the variogram parameters (Efron & Tibshirani, 1986).

3.2.6 Modeling Spatial Density

To distribute the spatial observations of average snow density to areas without GPR observations, we applied MLR (Andrews, 1974, Supporting Information 1.3). We examined the 4.5 $km \times 3.5$ km area of the LiDAR domain, which closely bounded the extent of the GPR survey. A set of normalized predictor variables were developed using the elevations of four LiDAR rasters: bare earth elevation (Z_g), snow-covered elevation (Z_s), snow depth (H_s), and vegetation height (H_{veg}); the aspect, slope, x and y derivatives of the elevation rasters (excluding H_{veg}); and the distance to the nearest

vegetation $\geq 0.5\ m$ (S_{veg}). For denoising, the elevation, vegetation height, and snow depth rasters were median filtered in a $5\ m \times 5\ m$ window, and the derivatives of these rasters (slope, aspect, ∂x, and ∂y) were median filtered within a $25\ m \times 25\ m$ window. The MLR coefficients are applied to the predictor variables of the LiDAR rasters to estimate the LiDAR–GPR measured average snow density (the response variable). Once the coefficients are trained, the model distributes the average snow density throughout the LiDAR domain. For greater detail on the parameter estimation and predictor importance see Appendix B.3 and B.4. We also trained a set of MLR coefficients using the snow density observations of 96 snow pits located within the LiDAR study area, as the response variable, and the LiDAR predictors to distribute density (Appendix B.3.2).

3.2.7 GPR Snow Depth

The process of measuring snow depth using GPR travel-times requires an estimate of the wave speed, which we developed from the dry-snow density (Section 3.2.4). It would be circular to measure the snow depth with the GPR using the estimated the wave speed directly from the LiDAR snow depths and GPR TWTs, as in Equation 3.3. Instead, we rely on the modeled spatial snow density for wave speed conversion to alleviate this circularity. The GPR traces were converted to depth using the modeled wave speed by applying a 1D interpolation (Margrave & Lamoureux, 2019). We also converted the automatic TWT picks to depth using the modeled wave speed by rearranging Equation 3.3 and solving for z_s.

3.3 Results

3.3.1 LiDAR and GPR Snow Depth

The LiDAR snow depths show a trend increasing from west to east with deeper snow around the perimeter of treed areas and shallow snow on the ground beneath tree canopies (Figure 3.3). This pattern is consistent with previous snow depth distribution studies of Grand Mesa (e.g. McGrath *et al.*, 2019). The mean snow depth for the entire domain is 92.4 cm with a standard deviation of 18.4 cm. In unforested areas ($H_{veg} < 0.5\ m$), the mean snow depth is $96.4 \pm 14.8\ cm$, while in the forest ($H_{veg} \geq 0.5\ m$), the mean snow depth is $79.4 \pm 22.5\ cm$. The in-situ snow depth observations compare well with the LiDAR snow depths ($R = 0.78$, $RMSE = 11\ cm$, $ME = 0\ cm$).

We found good agreement among the LiDAR snow depth measurements and the snow depths estimated from the GPR TWTs and the MLR snow density used for wave speed and depth conversion. Over the GPR transects, the correlation between the LiDAR measured snow depths and the GPR estimated snow depths is R = 0.74 with a RMSE of 11 cm and a bias of 0 cm. If we used the densities directly estimated from the LiDAR snow depth and GPR TWT, we found a similar result ($R = 0.75$, $RMSE = 10\ cm$). For comparison, if the mean density of all snow pits measured during the Grand Mesa IOP (277 kg/m^3) were used for the wave speed conversion the correlation between the measured and the estimated snow depths slightly decreases to $R = 0.72$ and the RMSE is unchanged (11 cm). We also trained the MLR using the average density measured in the snow pits within the LiDAR domain to distribute the density. Using the densities modeled from the snow pit data and repeating this

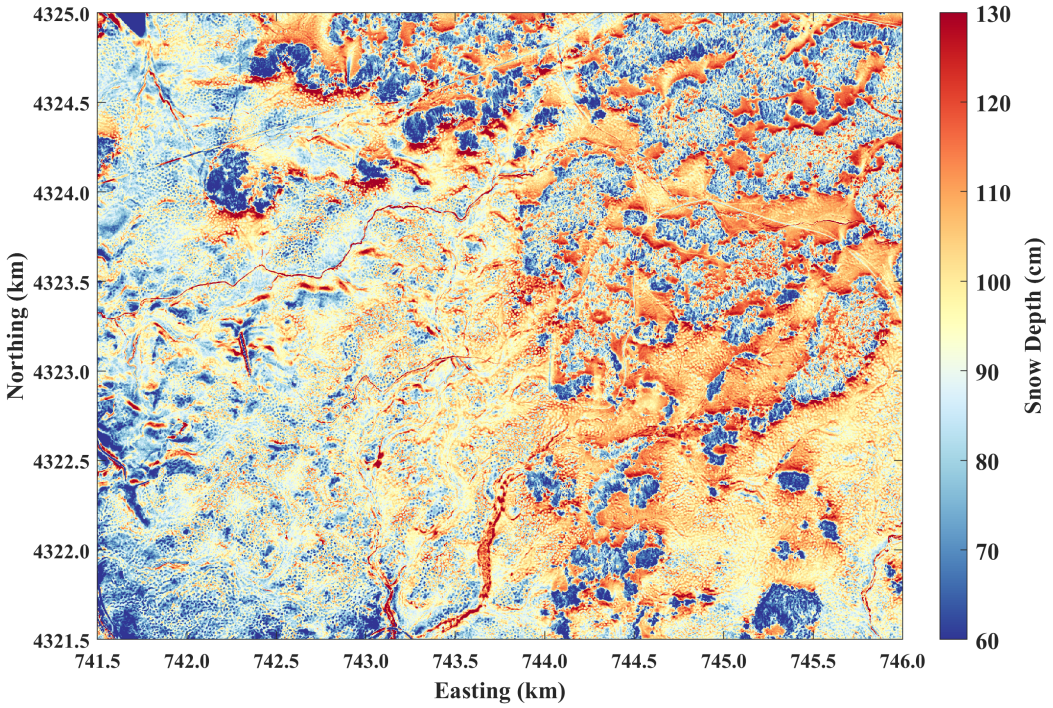

Figure 3.3: One meter resolution snow depths from the February 1, 2020 flight. The mean snow depth of this domain is 92.4 cm with a standard deviation of 18.4 cm. The western half of the domain is relatively unforested area, while the eastern half of the domain is characterized by stands of dense forest (see Figure 3.1).

exercise, we observed similar accuracy ($R = 0.74$, $RMSE = 11\ cm$, $ME = 0\ cm$). The comparison between the LiDAR and GPR estimated snow depths in Figure 3.4 shows exceptionally strong correlation ($R = 0.91$, $RMSE = 5\ cm$). However, the overall accuracy of the spatial registration between the LiDAR and GPR varies on the order of a few meters. We found that errors in the registration of these data are the leading source of error in the densities measured therefrom. Our process of removing outlier density measurements (Appendix B.2.1) alleviates errors caused by spatial misalignments.

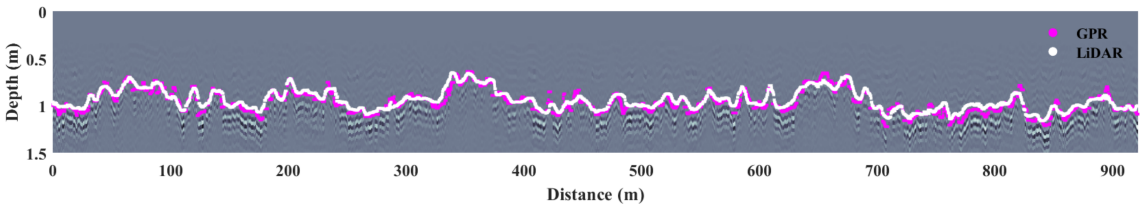

Figure 3.4: The example GPR image and automatic travel-time picks (magenta) in Figure 3.2 have been converted to depth using the MLR modeled densities for wave speed conversion. The LiDAR snow depths are overlaid in white. In this example the correlation between LiDAR measurements and GPR snow depth estimates is $R = 0.91$ and the RMSE is $5\ cm$.

3.3.2 LiDAR-GPR Measured Density

The increase in correlation between LiDAR and GPR snow depths, albeit slight, when using the measured spatial density, rather than the snow pit mean, indicates that the GPR transects observed real spatial variability in average snow density. The mean bulk density measured along the GPR transects is $271 \pm 36\ kg/m^3$. The spatial patterns of the LiDAR–GPR measured average snow density appear bimodal, where the density measured in the western half of the domain is greater than the tree protected eastern half (Figure 3.5). The mean bulk density measured in snow pits within 500 m of the radar transects is $274 \pm 24\ kg/m^3$. The distributions have similar means and variance, as assessed by the Z-test score of 0.1. The median densities within 12.5 m radius of the snow pits are correlated with the snow pit densities ($N = 37$, $R = 0.44$, $RMSE = 29\ kg/m^3$).

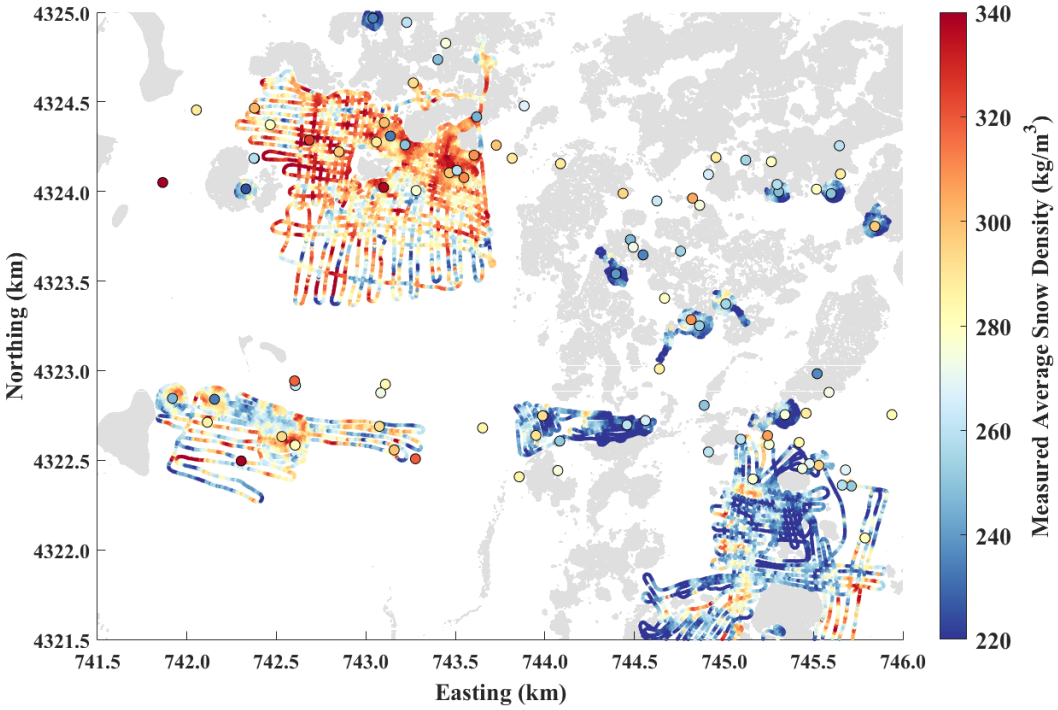

Figure 3.5: Average snow density was measured by combining LiDAR snow depths with GPR TWTs. Average density measured in the 96 snow pits within the LiDAR boundary are overlaid as larger makers. Forested areas and reservoirs are masked in grey.

3.3.3 Spatial Correlation of LiDAR Snow Depth GPR Travel-Time and Measured Density

The generalized relative semi-variogram allows us to examine the expected percentage variability between observations for a given distance separation. We observed differences in the length scales of variability among depth, density, SWE, and TWT between forested and unforested areas of Grand Mesa (Figure 3.6). In the unforested areas the correlation length of snow depth is 71 ± 2 m, density is 96 ± 1 m SWE is 102 ± 1 m, and TWT is 105 ± 2 m. Adjacent measurement variability is 9 ± 0 % of mean depth, 2 ± 0 % of mean density, 14 ± 0 % of mean SWE, and 14 ± 0 % mean TWT. Maximum variability estimated as the sill of the variogram is 26 ± 0 % of mean depth, 18 ± 0 % of mean density, 34 ± 0 % of mean SWE, and 26 ± 0 % of mean TWT. Correlation length scales in forested areas for depth (17 ± 2 m), density (75 ± 2 m), SWE (70 ± 9 m), and TWT (64 ± 6 m), are all less than observed in the unforested areas. The relative variability in depth is 10 ± 2 % for adjacent observations and 51 ± 2 % maximum variability. Variability in SWE is 32 ± 1 % between adjacent observations and 46 ± 1 % at maximum. TWT similarly has 31 ± 1 % variability among adjacent observations and 45 ± 1 % at maximum. The relative variability in density, however, is lower with adjacent measurements having 1 ± 0 % and maximum variability of 13 ± 0 % or average. This finding is consistent with density observations having approximately 2.5 % variability on average. For context, the median distance between snow pits is 146 m, which indicates that average snow pit observations are independent of each other and are unable to resolve spatial patterns.

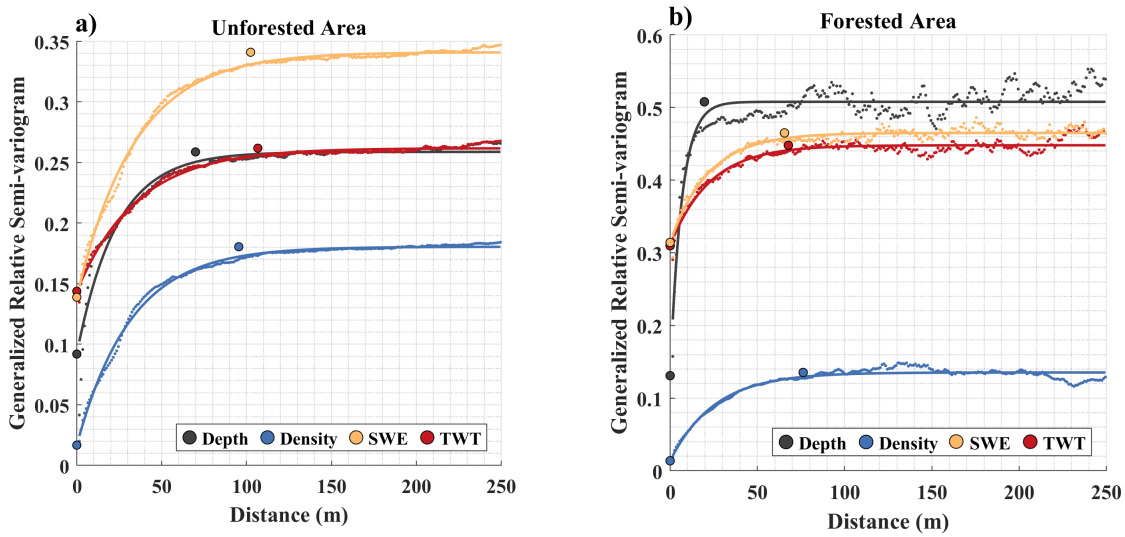

Figure 3.6: Generalized relative semi-variograms in a) unforested and b) forested areas for LiDAR snow depth, GPR TWT, and average density measured along the GPR transects. Experimental variograms were fit with an exponential model to determine the variogram parameters. The larger makers represent the nugget, sill, and correlation length estimated by Monte Carlo subsampling. Generally, variability is lower and the length scale of variability is larger in the unforested areas than in the forests.

3.3.4 Multiple Linear Regression Modeled Density

The modeled densities in Figure 3.7 display striking spatial patterns. A large-scale gradient in density, which decreases from west to east, shows higher snow density in the unforested areas than in areas that are protected from the wind by trees. A mix of wind processes are evident in bedform density anomalies such as snow waves, barchans, and dunes which show realistic heterogeneity. The distribution patterns of snow density agree with the prevailing west-southwest wind direction and vegetation (University of Utah, 2022, Appendix 3.2.6). In unforested areas, the model densities have a mean and standard deviation of $273 \pm 23\ kg/m^3$, while in the forested areas the density is lower on average at $257 \pm 22\ kg/m^3$. Compared to the densities measured along GPR transects in both the forested and unforested areas, the modeled densities have the correlation $R = 0.64$ and $RMSE = 28\ kg/m^3$.

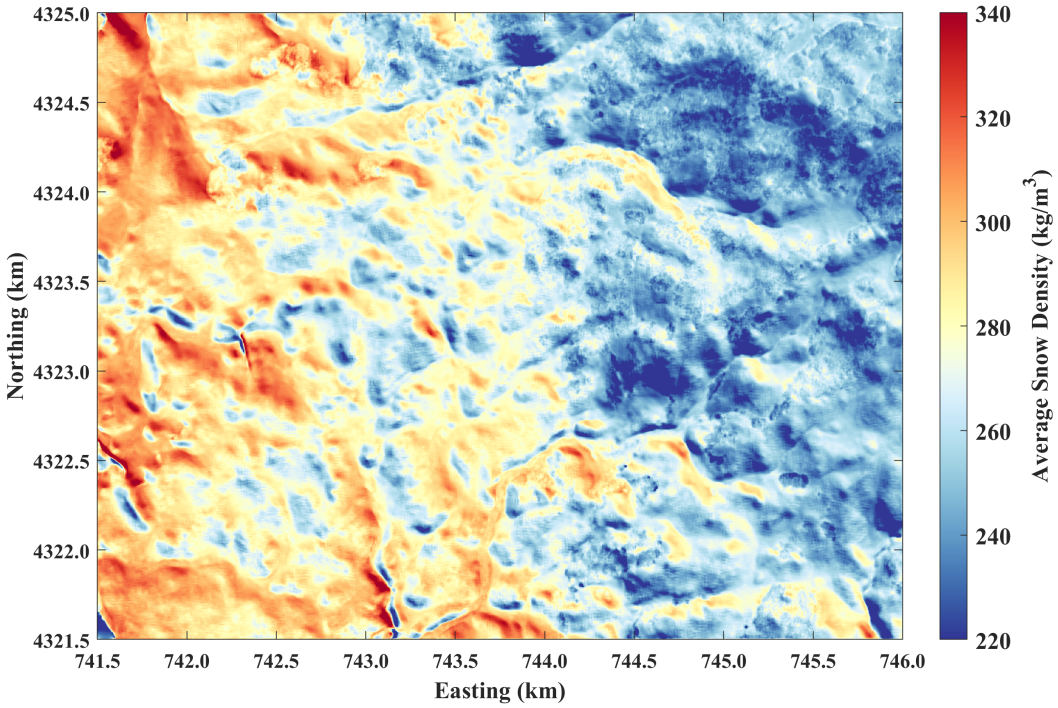

Figure 3.7: Average snow density estimated by Multiple Linear Regression. Density is higher in the wind affected, unforested terrain, and lower in tree protected areas. Snow drifting appears to cause large bedform density anomalies with the windward side of having higher density than the leeward side.

3.3.5 Spatially Distributed Snow Water Equivalent

SWE was distributed within the 4.5 $km \times 3.5$ km domain by combining the MLR estimated snow density with the LiDAR snow depths (Figure 3.8). The average and standard deviation of SWE throughout the domain is 248 ± 52 mm, where unforested areas have greater SWE (262 ± 40 mm) and forested areas have less SWE (204 ± 61 mm). Decreased SWE and increased variability within forest stands corroborates previous work on wind-terrain-vegetation characterization of Grand Mesa (Webb *et al.*, 2020). Minimum SWE was found in the southwest corner of the domain and in dense forests. SWE is greatest around the perimeter of forested areas and in the northwest quadrant. Greater snow depths and lower densities in the northeastern quadrant indicate that the prevailing wind redistributes snow to the forested areas. The effects of wind transport and densification in western half of the domain reduces the snow depth while increasing the bulk density. Wind redistribution is also evidenced by snow drifts which tend to have less SWE on the windward side and increased SWE on the leeward side. Stippling patterns are the effect of low-stature vegetation ($H_{veg} < 0.5$ m) and boulders, which tend to reduce snow depth and to a lesser degree reduce the modeled average density. The bimodal nature of the modeled snow density and greater snow depth between forested areas homogenizes the SWE distribution.

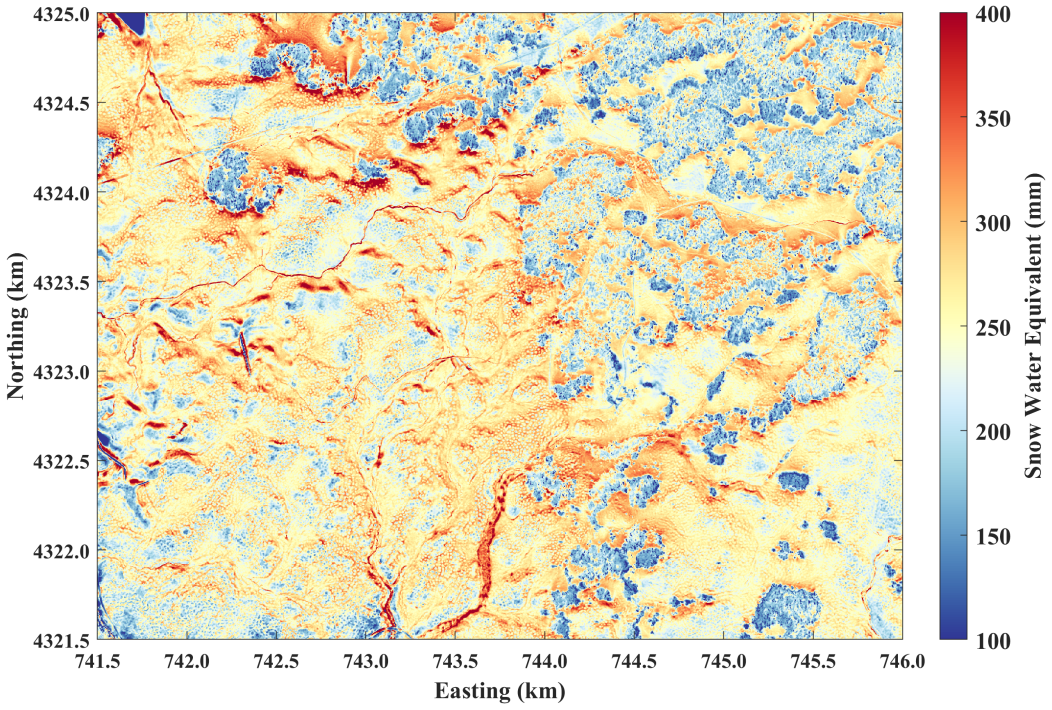

Figure 3.8: Snow water equivalent was distributed spatially by combining the MLR modeled density with the LiDAR snow depths. Forests and wind soured areas tend to have less SWE, where the perimeters of forest stands have greater SWE. The stippled texture is the result of low-stature vegetation ($H_{veg} < 0.5$) and boulders, which acts to reduce snow depth and to a lesser effect decrease the snow density.

3.3.6 Evaluation of Measured-Modeled SWE

We compared the MLR-estimated average snow density, LiDAR snow depth, and SWE to observations at all snow pits within the 4.5 $km \times 3.5$ km domain. Of these 96 snow pits, we identified 10 outliers where the absolute difference between observed and modeled density exceeds 50 kg/m^3 (twice the RMSE). We present the evaluation with and without these outlying observations for comparison (Figure 3.9). The correlation significantly improves between observed and modeled density from $R = 0.19$ ($RMSE = 25$ kg/m^3) to $R = 0.4$, though the RMSE slightly increased ($RMSE = 26$ kg/m^3). Snow depth and SWE are strongly correlated to the observations and are relatively insensitive to the removal of outlying data. SWE has a correlation of $R = 0.74$ ($RMSE = 39$ mm) that slightly improves to $R = 0.78$ ($RMSE = 41$ mm) when outlier snow pits are removed. The statistics for snow depth are also nearly unchanged by removing the observed outliers ($R = 0.77$, $RMSE = 12$ cm). Comparative plots and statistics for these snow properties explicitly in the forest and unforested areas is provided in Appendix B.5.

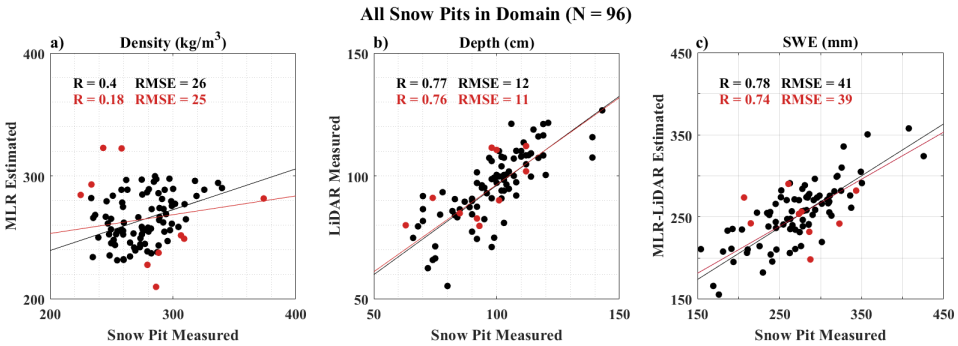

Figure 3.9: *a*) **Snow density,** *b*) **snow depth, and** *c*) **snow water equivalent are compared to the observations of the 96 snow pits that are within the** $4.5\ km \times 3.5\ km$ **domain. Red markers are outlying locations where the absolute difference between observed and modeled density exceeds** $50\ kg/m^3$ **(twice the RMSE). The red trend line and statistics use all 96 data points, while the black trend line and statistics exclude the outliers. The accuracy of the estimated SWE is primarily controlled by the LiDAR snow depths, and these snow properties are rather insensitive to locations with density outliers.**

3.3.7 Contributions to SWE Uncertainty

We found that snow depth contributes greater variability to the estimated SWE than the MLR modeled density and that the variability of snow depth increased in forests while density did not. Within the forest stands, the coefficient of variation (CV; the standard deviation divided by the mean) for snow depth is 0.28, approximately three times greater than that of the distributed density, 0.09. In the unforested areas the CV for snow depth, 0.15, is nearly twice that of the distributed density, 0.08.

The errors between LiDAR measured and evaluated snow depth are correlated with the LiDAR measured snow depth ($R = -0.39$), and the errors between MLR estimated and snow pit measured density are correlated with modeled density ($R = 0.58$), but the errors among snow depth and density are uncorrelated with negligible

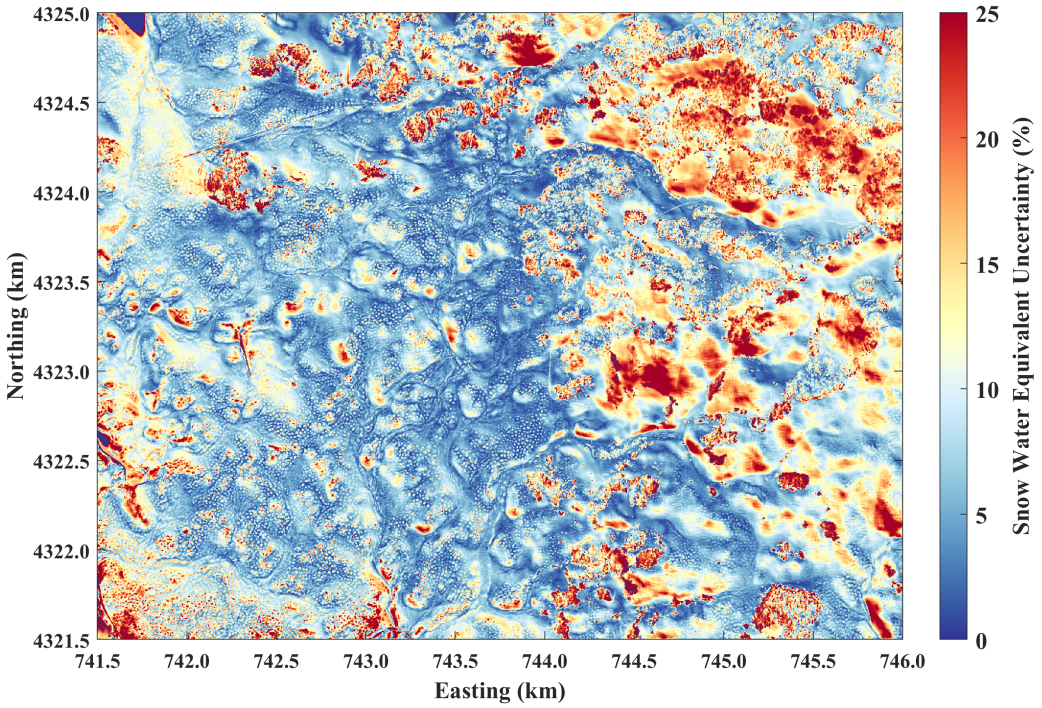

Figure 3.10: Uncertainty in snow water equivalent estimated by summing in quadrature relative uncertainty in snow depth and average snow density following Raleigh & Small (2017). The spatial distribution of uncertainty tends to be greatest in the shallower and lower density snow underneath tree canopies and least in the deepest snow caught in drifts around the perimeters of forest stands.

covariance. Using simple linear regression, we modeled the errors as a function of LiDAR measured snow depth or MLR modeled density. By summing the relative error terms in quadrature, we estimated the SWE uncertainty to first order (Raleigh & Small, 2017). The distributed relative SWE uncertainty is presented in Figure 3.10 and is uncorrelated with SWE. The median SWE uncertainty is 8 %, which breaks down to 13 % median uncertainty in the forest and 7 % median SWE uncertainty in the unforested areas. The median contribution of SWE uncertainty due to snow depth is 4 % and the median contribution due to density uncertainty is 5.5 %, showing that density is a slightly larger source of SWE uncertainty than depth.

3.4 Discussion

This work advances the utility of GPR for seasonal snow applications, by successfully estimating bulk snow density and SWE through the integration of remotely sensed LiDAR and GPR observations. Grand Mesa is a good site for testing our approach of combining LiDAR and GPR for SWE retrieval, yet presents many challenges for GPR analysis because of the abrupt discontinuities along reflection horizons due to vegetation and boulders on the ground surface. By exploring effects of depolarization on L-Band GPR signals, we developed a new, automated GPR processing workflow that accurately identifies the ground surface beneath the snow-cover. This advance encourages the collection of large GPR data sets and removes the subjectivity involved in the GPR post-processing and interpretation, by alleviating the labor of manually interpreting radargrams through an objective function.

Sensitivity analysis showed how measurement errors propagate into the LiDAR–GPR measured snow density (Appendix B.2). We found that measurement errors on the order of 10 cm for LiDAR and 1 ns for GPR may translate into errors in the density measurement of 150 kg/m^3 or greater. The error in the LiDAR—GPR density measurements was reduced from approximately 150 kg/m^3 to 30 kg/m^3 by median filtering and interpolating through outliers (Appendix B.2.1). In some locations the registration may be nearly exact between the two instruments, and the resulting error will be low (e.g. Figure 3.4). We found by cross-correlating the GPR and co-located LiDAR snow depth transects, that misalignments of approximately $1 - 5$ m are possible. While the signal of each instrument is coherent, the leading source of error in our density measurement is spatial misalignments (potentially sourced from geolocation inaccuracies, point cloud to raster processing, and coordinate transformations)

that are on the scale of the 1 m resolution data products. To evaluate how spatial misalignment impacts the training data, predictor data, and the MLR model output, and to estimate the uncertainties introduced from integrating the cross-platform sensor data, we created multiple sets of training data by effectively perturbing where LiDAR—GPR transects are aligned via cross-correlation lagging, and introduced common practice mistakes in the sensor integration, such as mixing the geographic coordinate system of the data between NAD83 and WGS84. We found that perturbing the sensor integration introduces less than 1 kg/m^3 error in the modeled density on average (up to 2 % in forest stands), that outlier filtering is robust to sensor integration errors, and this error is small in effect to the overall SWE uncertainty.

An effort of our work characterized the measurement uncertainties and the resulting SWE uncertainty, in pursuit of the goal for 10 % uncertainty in global SWE estimation (National Academies of Sciences Engineering and Medicine, 2018). Based on the evaluation of the remotely sensed or modeled snow properties with in-situ measurements, we used simple linear regression to model uncertainties spanning both forested and unforested areas. The uncertainty in LiDAR snow depth varies spatially and is dependent on landscape characteristics such as slope and vegetation (Deems *et al.*, 2013). However, our evaluation of snow depth in forested and unforested areas did not suggest that LiDAR snow depth errors were greater beneath the tree canopy. The choice of uncertainties propagated through the SWE uncertainty analysis (Section 3.3.7) dictates which factor, depth or density, will have the greater contribution to the overall SWE uncertainty. For the midwinter Grand Mesa snowpack, we found that the importance of uncertainties in density and depth are site and sub-seasonally dependent. Uncertainty in midwinter SWE tends to reduce at peak SWE, where

snow depth and density are greater. Our findings are within the remarkably difficult to achieve 10 % goal, and point to the success and accuracy of the joint LiDAR—GPR methodology for SWE retrieval.

We tested the model sensitivity to training and learned how much data is required for accurate density estimation. Using approximately 3,000 TWTs (1 % of the total) from random subsets, we obtained density models that are statistically identical to those generated from the larger data set (Appendix B.3.1). Though random sampling is not a practical method for GPR data acquisition and analysis, this exercise showed that the amount of GPR information required to train the model parameters is not as important as collecting data in a variety of landscape and snow-cover characteristics. The large GPR grid in unforested areas captured the high degree of spatial heterogeneity and improved LiDAR spatial predictor importance, while GPR acquired in forests added necessary data for estimating sub-canopy snow density.

Additionally, we used the 96 snow pits within the study area as training data to distribute density (Appendix B.3.2). The distance between snow pit observations is on the order of the length scale of variability for snow density, as estimated from the variogram analysis. The model trained on sparse snow pit observations has lessened predictive capability, and is about as useful as the average density of the snow pits for estimating SWE. We found that densities estimated from GPR TWTs and LiDAR snow depths are preferred because of the spatial continuity and areal coverage. Snow pits are an invaluable source of calibration and validation observations, but are time intensive to sample on large scales. For example, a team of two can fully sample a SnowEx pit in two hours, which for the approximately 100 snow pits in the study area, amounts to $\sim$ 400 hours of labor (excluding the time to quality control (QC),

curate the snow pit logs, and travel to and from the field site). The 160 km of GPR data used in this work required approximately 20 hours to collect and an additional 20 hours to QC TWTs, which amounts to $\sim$ 40 hours, or roughly a 90 % reduction in field labor.

The density measurements inferred from GPR profiles additionally allowed us to quantify the spatial length scales of density variability, whereas the distance between snow pits makes these observations independent of each other. Using variogram analysis, we determined that measurements of density up to $\sim$ 100 m apart in unforested areas and $\sim$ 75 m apart in forests are correlated. These findings significantly differ from a previous variogram analysis that found correlation lengths for snow density of less than 10 m (Yildiz *et al.*, 2021). However, the relatively small size of the study area (200 m in largest dimension) may not support spatial analysis of snow distribution on the 10^2 m scale. And it may be, that we have identified an additional longer, lower spatial frequency scaling of snow density. Our analysis of the correlation length of LiDAR snow depths generally agrees with scale-breaks identified in previous studies within forested and unforested areas (Deems *et al.*, 2006; Marshall *et al.*, 2006; Trujillo *et al.*, 2009). Corollary to SWE, two-way travel-time in dry snow depends both on snow depth and density. We found that TWT and SWE consistently exhibited similar correlation lengths and variability of adjacent observations in the forested and unforested areas. This finding supports TWT as an informer of spatial SWE variability, however, in unforested areas SWE has greater maximum variability than TWT. Snow density exhibited greater variability and longer correlation length in the unforested areas than in the forests, which indicates that wind exposure increases the variability and conversely the close proximity to vegetation which shelters

the snow, tends to reduce spatial density variability.

The LiDAR predictors were inspired by theory of wind-terrain-vegetation interactions governing snow distribution, though to keep the model design innate to LiDAR information we did not involve wind data for predictors such as maximum upwind slope (Winstral *et al.*, 2002). Of those tested, we identified the most important LiDAR features used to distribute density by regressing all combinations of the 18 predictor variables, evaluating against testing subsets, and ranking their appearance in the top 1 % of models (Appendix B.4). The slope of bare earth elevation, the slope of the snow depth, vegetation height, and proximity to vegetation $> 0.5\ m$ are the leading predictors in both, the model trained on LiDAR—GPR density, and the model trained on snow pit observations. We used a "kitchen-sink" approach to the regression modeling presented, but found comparable accuracy in models using fewer parameters. Elder *et al.* (1998) used a simpler, three feature (net radiation, slope, and elevation, with an intercept) MLR model that was trained on density observations of five snow pits and averages of five snow core transects to predict basin-wide average density and SWE. Recently, a similar study used a snow core sampling strategy to represent unique classes of basin-wide physiography, acquiring ~ 1000 observations, and used MLR and binary-classification tree models to distribute density from elevation and incoming radiation (Wetlaufer *et al.*, 2016). The dependence of density on net solar radiation may explain the good performance of these models, whereas terrain parameters such as slope and aspect indirectly relate to radiation. The mean and narrow standard deviation of density values observed during the Grand Mesa IOP ($273 \pm 24\ kg/m^3$) explains how the MLR modeled densities showed good accuracy ($RMSE = 25\ kg/m^3$) but weak correlation with the observations.

The MLR coefficients developed from a LiDAR and GPR snapshot of Grand Mesa will likely have weak predictive capability at other field sites. It may be necessary to recalibrate the model using GPR or another instrument to measure radar travel-time such as airborne frequency modulated continuous waveform radar (e.g. Yan *et al.*, 2017). The expense of acquiring airborne remote sensing data is a crux of the technique, and it may not be feasible to fly entire catchments across the breadth of snow climates. Less expensive techniques for estimating SWE distribution, such as drone-based structure from motion combined with GPR (e.g. Yildiz *et al.*, 2021), and in-situ measurement campaigns combined with regression (e.g. Wetlaufer *et al.*, 2016) or machine learning (e.g. Broxton *et al.*, 2019) models should be utilized where appropriate. However, high resolution elevation and snow depth data significantly improves modeled spatial heterogeneity in snow density.

3.5 Conclusion

We developed an innovative approach for combining GPR travel-times and airborne LiDAR snow depths to estimate spatially distributed average snow density and SWE at one-meter resolution across a $\sim$ 16 km^2 area. Our automatic and objective technique for interpreting radargrams makes a significant contribution for GPR users and data end-users, as we have enabled a fast data product with minimal post-processing labor. The continuous density measurements inferred from combining the GPR and LiDAR data allowed us to estimate the snow density and SWE variability as a function of distance between observations . We observed shorter correlation lengths for depth, density, SWE, and TWT in forest stands than in unforested areas. Relative density variability is least among these snow properties, and conversely to depth, SWE, and TWT, density variability is slightly less in forested areas than in

unforested areas. We find that wind exposure has a control on the average density and variability, and in agreement with prior studies, found that forests tend to shelter the snow pack from wind redistribution and densification. We showed that the length scales of variability between SWE and GPR TWT are similar in both forested and unforested areas. Corollary to the basis in dry snow, that depth and density formulate TWT and SWE, the agreement in spatial variability among TWT and SWE indicates that TWT is a better informer of SWE than either depth or density independently. Distributed SWE uncertainty tends to be greatest in the shallower and lower density snow beneath tree canopies, where measured variability is also greater. Snow density remains a larger contributor to SWE uncertainty than depth, however, on average SWE uncertainty was less than 10 %. High-resolution LiDAR information combined with TWT observations to estimate and distribute density shows promise for accurately estimating catchment-wide SWE.

CHAPTER 4:

EXTENTIONS AND CASE STUDIES

4.1 Firn and Radiostratigraphy Modeling using the 1D Kinematic Wave Equation

Modeling the age-depth structure of firn is advantageous for signal processing (Appendix A.6) and necessary for the forward computation of SMB (Appendix A.3). However, numerical modeling of firn evolution is also applied in the inverse computation of SMB (e.g. Ng & King, 2011). The kinematic wave equation is time reversible, a property that is leveraged in the upwinding and downwinding scheme applied for the numerical solution (Section 4.1.3). Time reversal may also be applicable for data inversion. For example a reflection horizon interpreted in depth may be propagated back to the surface. Age models have been extracted from real seismic images using a convolution neural network that was trained on synthetic seismic images (Geng *et al.*, 2020). Horizon interpretation is then automated by extracting the isochrones of the age-depth model. I generated realistic radar images using the kinematic wave model, as the initial step in extracting age-depth information from real data (Section 4.1.4).

4.1.1 Sorge's Law

In cold, dry, continental firn, such as that of Greenland's interior, under a constant rate of snow accumulation, the density (ρ) of snow at a given depth (z) does not change with time (Bader, 1954b). Meaning, firn density is given by a function of depth

$$\rho = f(z) \quad , \tag{4.1}$$

and the load of snow above a given depth is the density integrated with respect to depth

$$\sigma(z) = \int_0^z f(z)dz \quad . \tag{4.2}$$

The snow load $\sigma(z)$ was accumulated over some time. Given the SMB, the time required for a snow parcel to submerge to any depth can be solved as

$$t(z) = \frac{\sigma(z)}{SMB} \tag{4.3}$$

The vertical submergence velocity of a parcel of snow follows from differentiating Equation 4.3 with respect to time

$$v(z) = \frac{SMB}{\rho(z)} \quad . \tag{4.4}$$

This result drives the isochronal nature of the firn stratigraphy, and explains how variability in SMB creates rising and plunging horizons in the radiostratigraphy.

In result of Sorge's Law, the spatial variability of dry-firn density occurs over scales of $10^1 - 10^2$ km (Chapter 2.4), and even the largest observed variability in annual SMB has only a slight effect on the firn density variability. For example, along GTC15 Spur West, the mean absolute deviation in SMB is $\sim$ 3 %, yet over the 22.5 m range in depth the MAD in density is just 0.6 %. The maximum SMB variability measured along GTC15 is $\sim$ 20 %; however, the variability in firn density between these locations is just $\sim$ 1 %.

"Sorge's Law is applicable whenever the annual climatic cycle in the accumulation zone does not appreciably change in the course of as many years as are under consideration. The second major premise is that snow melting be insignificant," (Bader,

1954b). At GTC15 I found the temporal mean absolute deviation in annual SMB for the period $1984 - 2017$ to be 17 %. Though this temporal variability in SMB is significant climatically, by averaging over all space and depth we found that Sorge's Law holds for our application of the 1D kinematic wave equation as a firn model.

4.1.2 1D Kinematic Wave Equation

The kinematic wave equation is an approximation of the dynamic wave equation that is developed from the unsteady continuity equation and the equation of motion (Miller, 1984). Dynamic wave models are widely used in hydrology to simulate channelized or surface water flow. A firn system conceptually works as mass flow over an unconfined surface. Namely, hydrologic input propagates a wave. Input mass is submerged vertically into the glacier and advected away towards glacier termini. For a glacier mass balance application it is practical to develop the kinematic wave equation from the perspective of mass conservation

$$\rho(x,z)\frac{\partial z}{\partial t} + \frac{\partial}{\partial x}\left(u(x)\int_0^z \rho(x,\zeta)\mathrm{d}\zeta\right) = \rho_0(x)a(x) \quad , \tag{4.5}$$

where $u(x)$ is the 1D advection velocity, ζ is an integration variable, and $\rho_0(x)$ is the surface density (Ng & King, 2011). Under the assumption of steady state SMB forcing, Sorge's law holds and the submergence velocity is applied via the density terms in Equations 4.5 and 4.9 – 4.12. Using a change of variable

$$f(x,t) = \int_0^z \frac{\rho(\zeta)}{\rho_0}\,\mathrm{d}\zeta \quad , \tag{4.6}$$

the mass-conservation equation takes the form

$$\frac{\partial f}{\partial t} + \frac{\partial (uf)}{\partial x} = a(x) \quad , \tag{4.7}$$

and yields the Saint Venant kinematic wave equation

$$\frac{\partial z}{\partial t} + u(x)\frac{\partial z}{\partial x} = a(x) \quad , \tag{4.8}$$

which expresses the firn isochrone depth z as an hyperbolic partial differential equation that is forced by the net annual SMB, $a(x)$.

4.1.3 Numerical Solution of the Kinematic Wave Equation

Upwinding schemes are suited for numerical solution of the kinematic wave equation. However, Ng & King (2011) solved Equation 4.8 analytically using the method of characteristics, which is capable of solving the system in the event of a kinematic shockwave (Miller, 1984). I have implemented a second order accurate back and forth (upwinding and downwinding) error compensation and correction scheme (Selle *et al.*, 2008). The algorithm begins with a first order accurate forward Euler step

$$z_i^{n+1} = (1 - \frac{\Delta t}{\Delta x})z_i^n + u_i \rho_i^n \rho_i^0 \frac{\Delta t}{\Delta x} z_{i-1}^n + \Delta t \frac{a_i}{\rho_i^n} \quad , \tag{4.9}$$

where the super script notation represents the time step and the subscript notation represents the spatial step. Δt the time step increment and Δx the spatial step increment were chosen such that $\Delta t < \frac{\Delta x}{\max(u(x))}$ to meet the Courant-Friedrichs-Lewy stability condition. To estimate the prediction error a backward Euler step is computed from the prediction

$$\hat{z}_i^n = (1 - \frac{\Delta t}{\Delta x})\hat{z}_i^{n+1} + u_i \rho_i^{n+1} \rho_i^0 \frac{\Delta t}{\Delta x} \hat{z}_{i+1}^{n+1} - \Delta t \frac{a_i}{\rho_i^{n+1}} \quad , \tag{4.10}$$

and the prediction error is calculated and applied to the data

$$\tilde{z}_i^n = z_i^n - (\hat{z}_i^n - z_i^n)/2 \quad . \tag{4.11}$$

By taking a forward step ahead with the error corrected data, the method achieves second order accuracy in the solution of the kinematic wave equation

$$z_i^{n+1} = (1 - \frac{\Delta t}{\Delta x})\tilde{z}_i^n + u_i \rho_i^n \rho_i^0 \frac{\Delta t}{\Delta x} \tilde{z}_{i-1}^n + \Delta t \frac{a_i}{\rho_i^n} \quad . \tag{4.12}$$

4.1.4 Application of the Kinematic Wave Firn Model to GTC15

I computed the depth of the propagating kinematic wave at 6 hour time steps for 30 years along GTC 15 Spur West. The multi-offset MxHL method for ice sheet firn characterization provided the boundary values $a(x)$ and submergence factors $\rho(x, z)$ necessary for the model. In Figure 4.1, I demonstrate these isochrones at one year intervals, having used a constant and gradual advection velocity of 5 m/yr. Ideally, remotely sensed, surface velocity data can prescribe $u(x)$ in a 1D model. U and V velocity components can project the resultant velocity vector along a radar transect. In reality, the demonstrated cross section from $35 - 55$ km along GTC15 Spur W is comprised of one transect that is with the flow on heading 246.5° from 15 km to 45 km, where it begins the next transect on heading 40.5° against the flow from 45 km to 78 km. It becomes no longer care free to orient the radargram downstream and run the model without spatially continuous accumulation and density. However, a dynamic

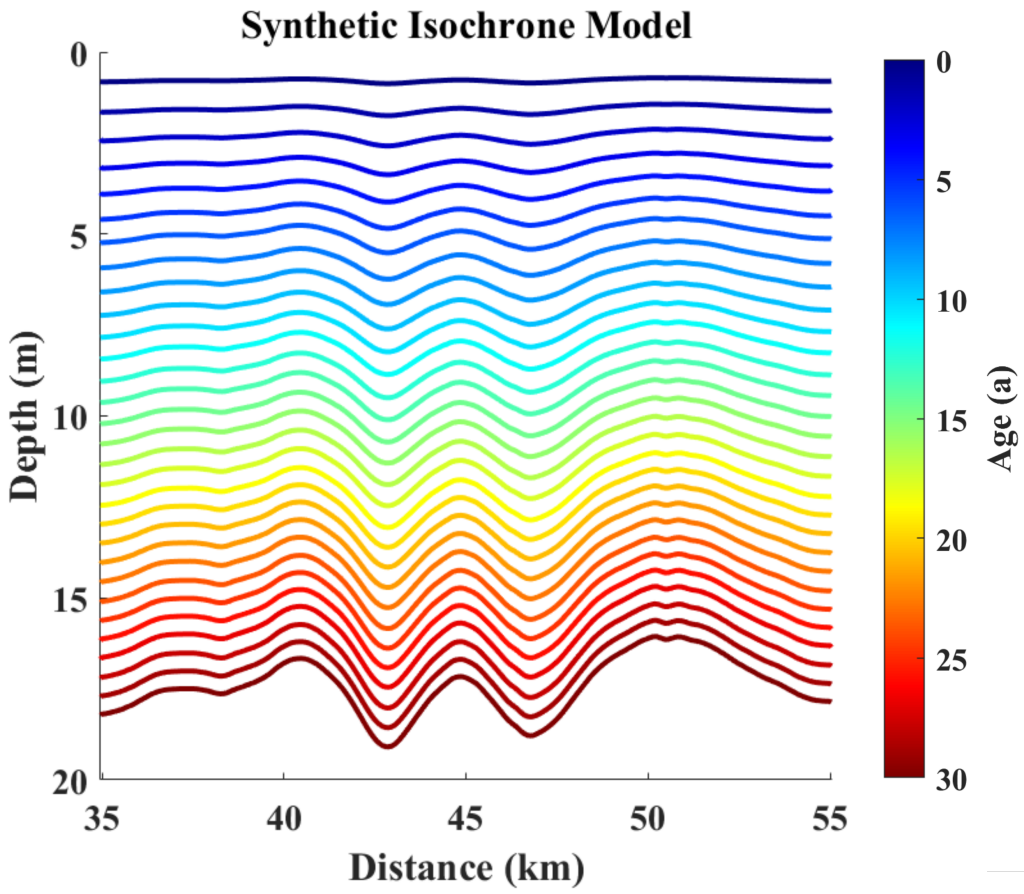

Figure 4.1: The solution of the kinematic wave equation at one year intervals for the boundary condition $a(x) = SMB_{GTC15}$ and uniform advection $u(x) = 5\ m/a$

wave model, which allows waves to propagate at two wave celerities, $c = v + \sqrt{gy}$ and $c = v - \sqrt{gy}$, would yet become unstable at this vertex due to numerical dispersion effects (Miller, 1984). An approach to spatially modeling the density information (e.g. Chapter 3) would be immediately useful in this model which relies on empirically estimated $\rho(z)$, or one that evolves the firn density numerically.

Generating Synthetic Radargrams using the Isochrone Model

I generated a synthetic GTC15 radargram from Figure 4.1. To do so, I assigned each isochrone a random reflection coefficient between -1 and 1, attenuated the reflectivity assuming spherical divergence, and convovled the spike series with a 500 MHz Ricker wavelet. To model realistic noise, the synthetic radargram was convloved with a gaussian white noise matrix and was then added the clean radargram at 50 % noise level. Compare Figure 4.2 to Figure 2.7.

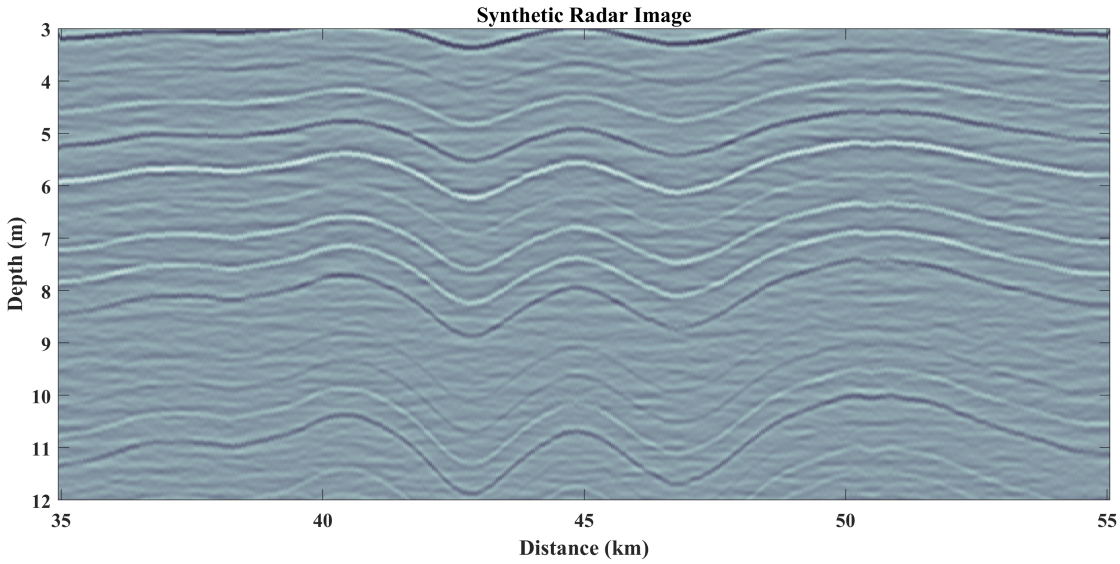

Figure 4.2: A synthetic GTC15 radargram generated from isochrones of the kinematic wave equation. Realistic noise was added to the image.

4.2 Ice Sheet Surface Property Retrieval and Automatic Firn Layer Tracing from Airborne Radar

Operation IceBridge (OIB) was a decade long NASA mission from 2009-2019 that used airborne remote-sensing instruments to observe the Antarctic and Greenlandic ice sheets, glaciers, and sea ice. With a suite of instruments (including photogrammetry, LiDAR, and Radar) OIB served as an observational bridge during the time period between the unscheduled decommissioning of the ICEsat-1 space-borne LiDAR platform and the launch of ICEsat-2. See Table 1 in Rodriguez-Morales *et al.* (2014) for a description of the suite of OIB radar instruments. The OIB ultra-wideband microwave radar developed by Panzer *et al.* (2013), known as the "Snow Radar", has the capability to resolve snow cover overlying sea ice and annual stratigraphic horizons within ice sheet firn with fine ($\sim 5\ cm$) resolution. However, interpreting, or tracing snow and firn layers, in the radargrams is a major crux of data analysis for radar derived estimates of snow accumulation. Drawing from the structure oriented filter developed in Chapter 2, I developed a surface oriented filter that improves the continuity of the radiostratigraphy. To automate the tracing of these layers, again, I applied the multi-channel coherence method developed in Chapter 3.

On the Greenland Traverse for Accumulation and Climate Studies (GreenTrACS) within the dry-snow and percolation zones of Western Greenland, we deployed a multi-channel ground-penetrating radar and developed a methodology to continuously characterize the snow and firn density and accumulation (Chapter 2). Hundreds of kilometers of the multi-channel radar traverse were colocated with OIB flights. The

the GPR derived quantification of snow and firn density and accumulation was used as evaluation for the surface density retrieval described here. The snow density, depth, and accumulation measured by the MxRadar (Figure 2.5) was colocated with an OIB flight line acqiured on April 10, 2017 (Paden *et al.*, 2014). Within this extension, I applied the small perturbation analytical backscatter model (Engman & Wang, 1987) to estimate the surface snow density from OIB Snow Radar surface reflection data. I demonstrate this backscatter inversion process, and the automatic layer tracing, along a 35 km transect that is colocated with GreenTrACS Core 15 Spur West.

4.2.1 Automatic Layer Tracing

Identifying the stratigraphic horizons within the firn is the first step towards estimating surface mass balance from radargrams. However, manual horizon interpretation is not feasible for the volume of data acquired over the decade long mission. To hurdle this crux, I developed an automated method for tracing the $\sim$ 15 most prominent reflection horizons in the shallow firn. This method draws from the the structure oriented filter and multi-channel coherence techniques described in Chapters 2 and 3 and applies binary classification to extract the continuous horizons from the radargram.

Surface Oriented Filter

Demonstrated in Appendix A.6, the stratigraphic age model was applied in a structure oriented filter which significantly improved the radar image quality. However, empirical (Appendix A.5) and numerical (Section 4.1) firn age-depth models require a posteriori knowledge of the accumulation rate and snow or firn density for initialization. Instead, the shallow $\sim$ 20 m penetration depths of the Snow Radar, make the application of a surface elevation oriented filter possible. Omitting pro-

cesses of firn advection and compaction, shallow stratigraphic undulations caused by the accumulating snow approximately follow the surface topography. Stratigraphic layers older than ~ 50 years and layering in regions of glaciers where surface velocities are large will likely not abide by this approximation and will not be resolved by this filter. The only requirement of the surface oriented filter are automatically detected surface TWT picks. The layering of the radargram is flattened to the travel-time axis by linear interpolation which applies the perturbations needed to shift each TWT to a chosen TWT datum. A smoothing kernel is then applied to the travel-time flattened image, and then the radargram is unflattened by reversing the 1D interpolation process. Figure 4.3 displays the unprocessed radargram acquired on April 10, 2017 along the $15 - 45$ km distance of GTC15 Spur West. The radargram was surface oriented, filtered, and converted to elevation assuming a constant density of 500 kg/m^3 for the firn (Figure 4.4).

Horizon Extraction from Binary Classification of Amplitude Coherence

Smooth radargrams are nice to look at, but are not too useful until the radiostratigraphy is interpreted. To automate the horizon interpretation I first applied Equation 3.1 to calculate the coherence metric among the radar traces within 25 m a radius window (Figure 4.5). Because many annual layers are present in the shallow firn, the solution to tracing of these layers is not as trivial as choosing the maximum coherence of each radar trace as demonstrated in Chapter 3. To trace many layers, the coherence image was binarized by a setting a threshold of 0.1. A low coherence threshold may be applied, because binary regions that do not continuously span the entire 5 km long data file were removed. Using this binary classification scheme the

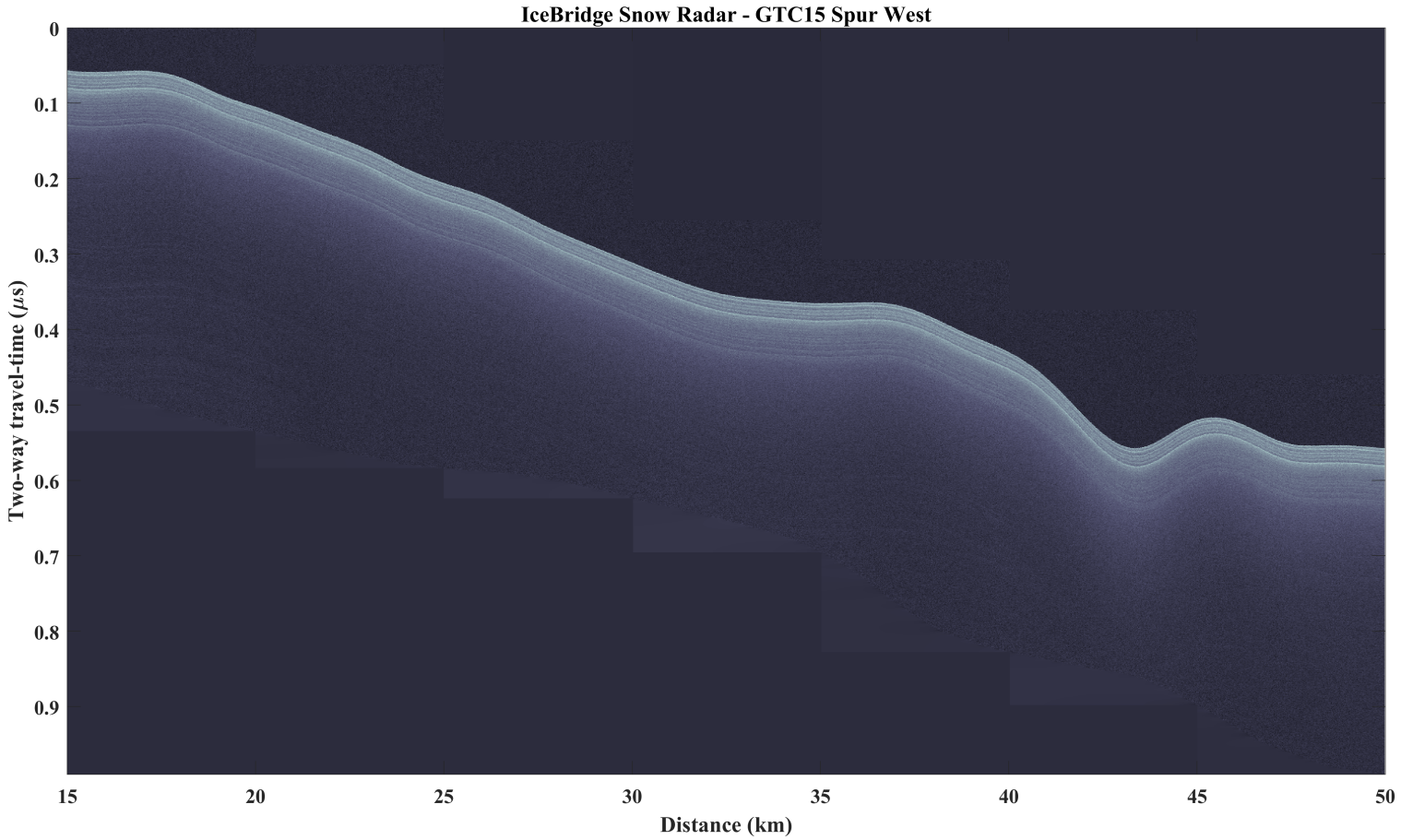

Figure 4.3: The unprocessed Snow Radar image is grainy and rather difficult to interpret.

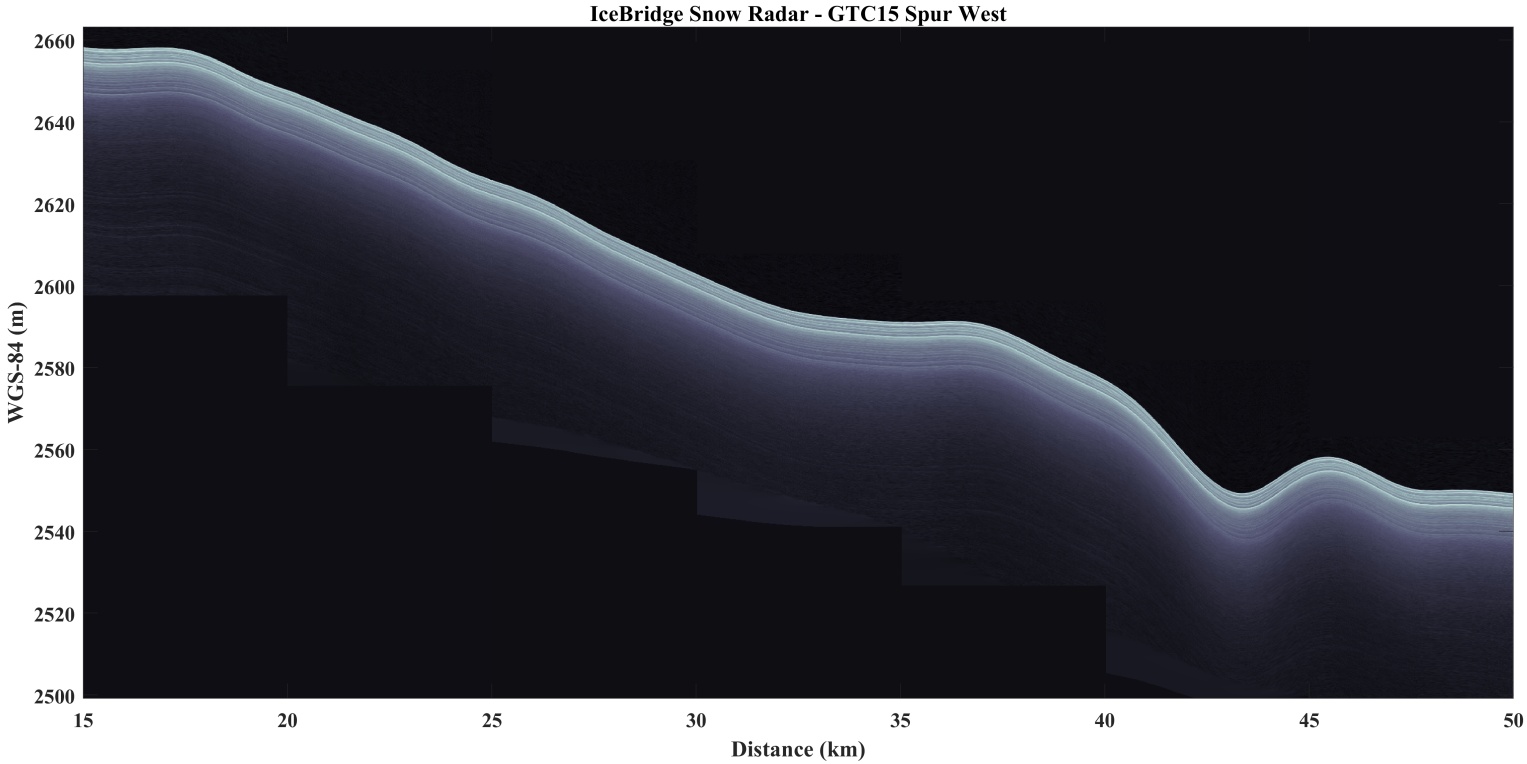

Figure 4.4: The Snow Radar image after surface oriented filtering has smooth and continuous reflection horizons and reveals layering at greater depths.

indices of the most prominent and continuous reflection horizons are extracted from the radargram. The coherence along each continuous reflection horizon is then maximized to determine the travel-time pick (see Chapter 3.2.3). The travel-time picks were converted to elevation and are displayed in Figure 4.6.

4.2.2 Radar Backscatter Inversion for Surface Properties

Radar reflections from natural surfaces may be analyzed using theoretical models of the energy scattering process, by regarding the backscattered electric field as a summation of the coherent and incoherent fields (Campbell & Shepard, 2003). A specular reflection, having all reflected fields constructing in phase, produces a coherent electric field $P_c = A_0 e^{j\varphi_0}$. Natural surfaces, such as snow, are often rough and scatter fields in random directions with an undetermined phase. Small variations in surface elevation, for example, give rise to the incoherent component $P_n = \sum_{i=1}^{N} A_i e^{j\varphi_i}$. Where A is the amplitude and φ is the phase, the coherent and incoherent fields sum

$$\mathbf{E} = A_0 e^{j\varphi_0} + \sum_{i=1}^{N} A_i e^{j\varphi_i} \quad , \tag{4.13}$$

to produce the electric field measured by a receiving antenna in the far-field. Frequency modulated continuous waveform airborne radar sounders are processed with a matched-filter to perform pulse compression (Legarsky *et al.*, 2001). Interference between the coherent and incoherent reflections cause the amplitude of the matched filter output to fluctuate. The amplitude variation from a large number of scatterers follows a homodyned-K type distribution (HK distribution) if a dominant scatterer, such as the snow surface, and random scatterers (surface roughness) are illuminated by the radar (Drumheller & Lew, 2002). The HK probability distribution

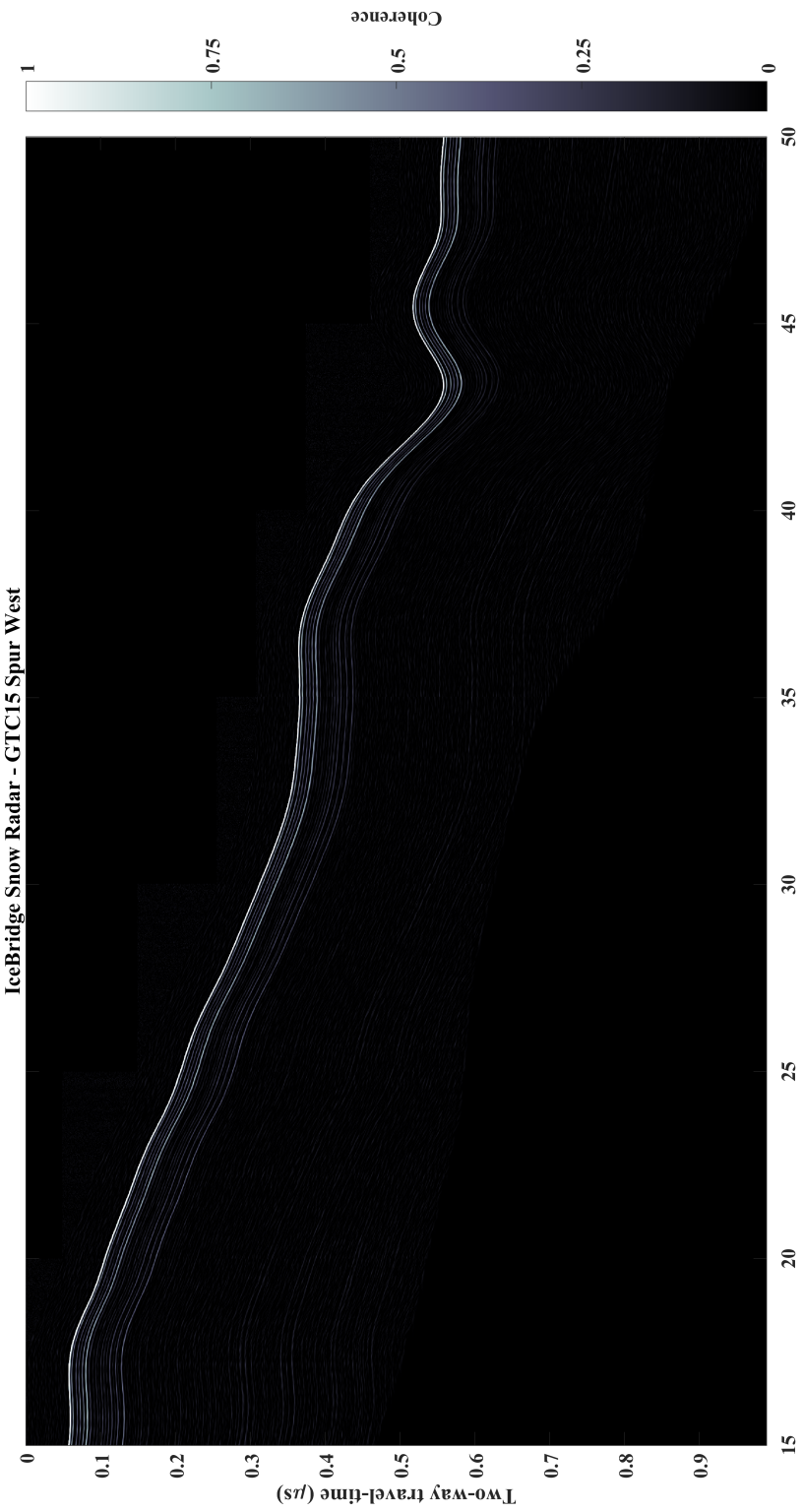

Figure 4.5: The coherence of the GTC 15 Snow Radar image obviates many prominent and continuous firn layers.

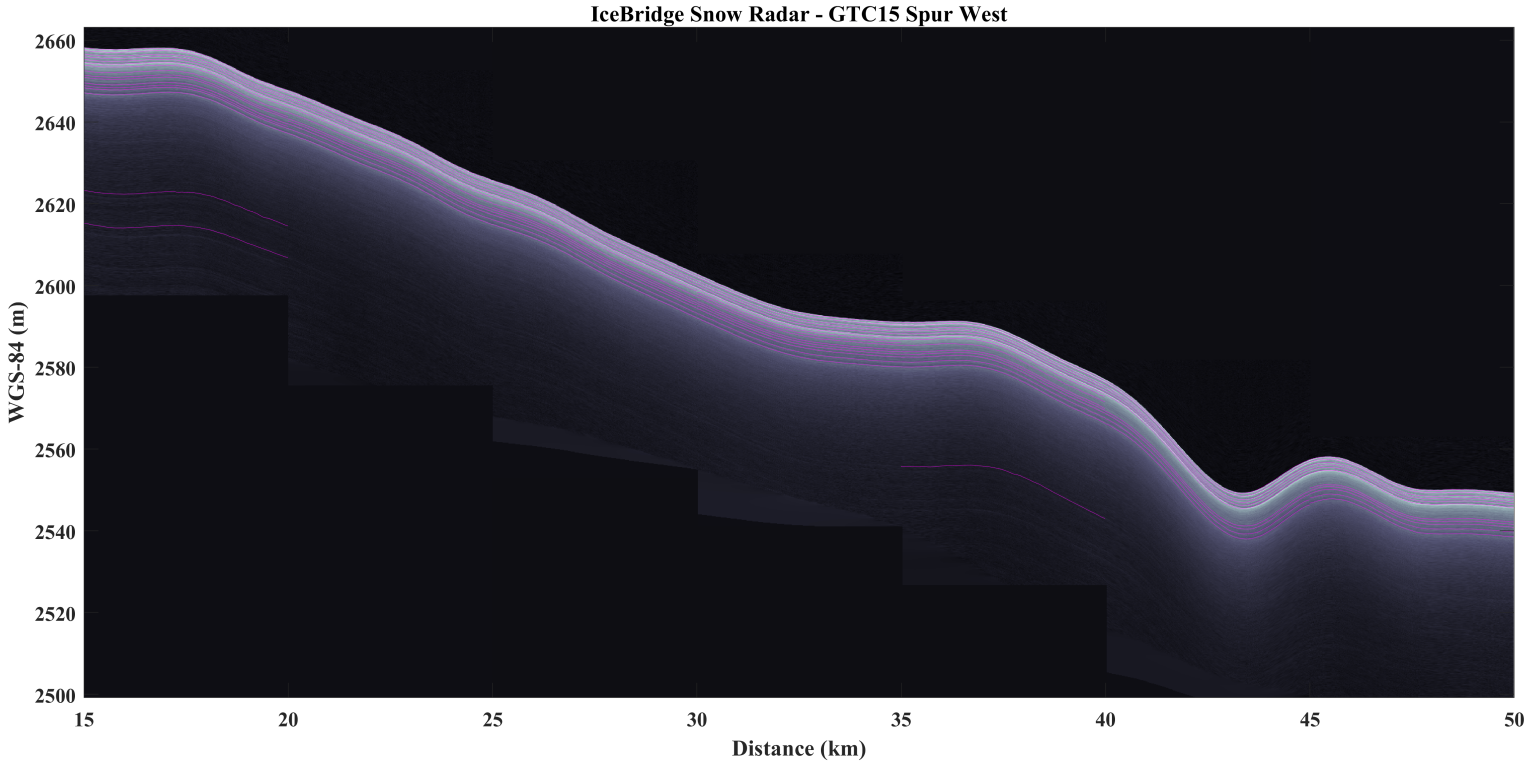

Figure 4.6: The prominent stratigraphic horizons (magenta) were automatically traces by the binarized coherence method.

$$P_{HK}(A \mid a, s, \mu) = A \int_0^{\infty} \omega \times J_0(\omega a) \times J_0(\omega A) \times \left(1 + \frac{\omega^2 s^2}{2\mu}\right)^{-\mu} d\omega \quad , \qquad (4.14)$$

where $P_{HKc} = a^2$, $P_{HKn} = 2s^2$, μ is an indicator of the scattered population, ω is an integration variable, and J_0 is the zeroth order Bessel function of the first kind, does not have a closed form and must be approximated numerically (Grima *et al.*, 2014a). To estimate the HK distribution parameters, I optimized the fit between the calibrated and normalized surface reflection amplitudes using the Nelder & Mead (1965) method from several random initializations and used the median of the parameter estimates to reduce the effect of local minima.

Radiometric Corrections

The surface amplitude data must first be corrected for variations in amplitude caused by variations in the aircraft altitude. The nominal elevation for OIB data acquisition is $h_0 = 500\ m$, where h is the aircraft range above the surface estimated from the TWT as $h = \frac{c\ TWT}{2}$. I applied a range correction of the form $G\mathbf{m} = \mathbf{d}$, where $\mathbf{d}$ is a vector of uncorrected surface reflection amplitudes and

$$G = \begin{bmatrix} 1 & (h_0 - h_1)^4 \\ \vdots & \vdots \\ 1 & (h_0 - h_m)^4 \end{bmatrix} \qquad (4.15)$$

is the design matrix containing the surface range perturbations. Where $\mathbf{m} = G^{-1}\mathbf{d}$, the radiometric correction is then applied as

$$\hat{\mathbf{d}} = \mathbf{d} - G\mathbf{m} \tag{4.16}$$

Small Perturbation Model

The power of a radar echo in a charge-free environment that is measured in the far-field can be expressed by the coherent and incoherent components as

$$P_c = r^2 e^{-(2k\sigma_h)^2} \quad , \tag{4.17}$$

and

$$P_n = \frac{1}{\pi h^2} \iint_{A_0} \sigma^0 ds \quad , \tag{4.18}$$

(Ulaby *et al.*, 1982). Where

$$r = \frac{(1-\sqrt{\varepsilon})}{(1+\sqrt{\varepsilon})} \quad , \tag{4.19}$$

is the Fresnel reflection coefficient at vertical incidence, ε is the dielectric permittivity representative of the reflecting surface to a depth of approximately one wavelength, $k = 2\pi/\lambda$ is the wavenumber, σ_h is the roughness height, A_0 is the area of the radar footprint, σ^0 is the backscattering coefficient described by the chosen model. For a natural surface with Gaussian scattering, Grima *et al.* (2012) derived the backscatter coefficient for the small perturbation model

$$\sigma^0 = 4k^4 r^2 \sigma_h^2 l^2 e^{-(kl\sin\theta)^2} \quad . \tag{4.20}$$

The small perturbation model is valid for surfaces with roughness heights and correlation lengths that are smaller than the wavelength (Engman & Wang, 1987). This theoretical basis is likely exceeded given the 5 cm wavelength of the Snow Radar and possible surface roughness heights of 25 cm or greater. Nevertheless, I found the small perturbation model capable of retrieving surface snow density using the Snow Radar. Integrating Equation 4.18 over a circular footprint gives,

$$P_n = 4k^2r^2\sigma_h^2\left(1 - e^{-\left(\frac{Dlk}{2h}\right)^2}\right) \quad , \tag{4.21}$$

where the band-limited footprint $D = 2\sqrt{hc/\Delta f}$ is bounded by the compressed-pulse width $1/\Delta f$ for the bandwidth Δf (Grima *et al.*, 2012). The power ratio of Equations 4.17 and 4.21

$$\frac{P_c}{P_n} = \frac{e^{-(2k\sigma_h)^2}}{4k^2r^2\sigma_h^2\left(1 - e^{-\left(\frac{Dlk}{2h}\right)^2}\right)} \tag{4.22}$$

is independent of the Fresnel reflection coefficient. The surface roughness height can then be estimated by solving for the root of the fixed point problem

$$\frac{P_c}{P_n} = \frac{P_{HKc}}{P_{HKn}} \tag{4.23}$$

using the analytically and empirically derived coherent and incoherent power as a function of σ_h. Along the GTC15 transect σ_h was estimated as 2.5 cm. The reflection coefficient can then be directly solved for by substituting σ_h into Equation 4.17

$$r = \sqrt{\frac{\alpha P_{HKc}}{e^{-(2k\sigma_h)^2}}} \quad . \tag{4.24}$$

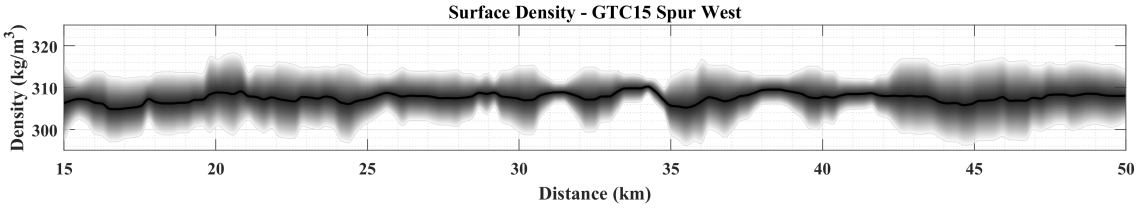

Figure 4.7: Snow surface density for the GreenTrACS Core 15 Spur West transect estimated from the surface echo of the Snow Radar.

An important calibration constant α must be included to reference the coherent power of the radar signal to a known dielectric medium. Subsequently, ε can be solved as a fixed point problem following Equation 4.19. Once the snow surface dielectric permittivity is known, a dielectric mixture model (Equation A.19) was applied to estimate the snow density of the uppermost 5 cm (Figure 4.7). This retrieval was estimated every 250 m in overlapping bins 500 m across for spatially continuous estimates.

4.2.3 Conclusions

Operation IceBridge provided a vast source of information of the cryosphere from many remote sensing platforms. Too much of this of these data are unused, in part because of the labor and subjectivity involved in data processing and analysis. Drawing from structure oriented filtering and multi-channel coherence methods, I automated the post-processing and interpretation of Snow Radar imagery from the Greenland Ice Sheet. Extending beyond problems in stratigraphic interpretation, I applied a well-known radar backscattering model to invert for the surface properties. The surface roughness was estimated at half of the 5 cm wavelength. This result supports the application of the small perturbation model for surface density retrieval from the Snow Radar. Surface density information, when used to parameterize a firn age and density model, can be joined with the automatic horizon interpretation to fully

characterize the surface mass balance.

4.3 Quantifying Firn Depth and Density in the Percolation Zone of Wolverine Glacier, Alaska

Measuring and modeling firn processes and surface mass balance on mountain glaciers is challenging because of snow process variation related to climate and orographic effects. Mountain glaciers receive large amounts snow accumulation and melt, which alters the snowpack evolution to firn. Within the percolation zone of a glacier firn experiences densification and mass losses due to surface meltwater infiltration and runoff. Meltwater infiltration forms vertical drainage features, ice lenses, and layers of ice refrozen within the firn. The wetting front may erase the isochronous stratigraphic layering and increase the densification to glacial ice through enhanced pore space reduction by grain rounding and refreezing. Simpler densification models based on Sorge's Law are not adapted to firn undergoing wet densification (Bader, 1954b). Recent generations of firn models which account for melt-driven densification and runoff (e.g. Reeh, 2008) are a large advance for mass balance modeling of percolation zones.

Multi-offset radar is capable of measuring the depth, density, wetness, and stratigraphy of firn, via velocity analyses which depend on the interpreted travel-times of reflection horizons. Radar inversion within the percolation zone is challenged by the firn structural heterogeneity and the unknown inclusion of liquid water. The workload for interpreting radargrams increases with the number of channels, and necessitates a methodology for velocity modeling minimal manual effort. From Wolverine Glacier, Alaska (Figure 4.8), I estimated firn properties along a $\sim 2\ km$ multi-offset

GPR transect moving up-glacier with the elevation gradient (Figure 4.9). Applying multi-channel coherence methods, horizon interpretation and velocity analysis were automated to estimate the firn depth and density structure.

4.3.1 Multi-offset Coherence Analysis

Normal moveout velocity analysis from multi-channel coherence was developed as a form of common midpoint (CMP) velocity analysis more than 50 years ago (Taner & Koehler, 1969). This technique first estimates $t(x)$, the travel-time measured at a receiving antenna with offset x, for zero-offset travel-time (t_0) and stacking velocity (V_{NMO}) combinations that satisfy the normal moveout equation

$$t(x) = t_0 + \sqrt{\frac{x^2}{V_{NMO}^2}} \quad . \tag{4.25}$$

The normal moveout travel-time follows along a hyperbolic trajectory. A grid search over travel-time and velocity, estimates the possible NMO travel-time hyperbolas for stacking the CMP gather. The coherence (Equation 3.1) is then computed from the amplitudes along the possible trajectories at each offset. A local maximum coherence occurs when the energy of the traces sum coherently and indicates a possible (t_0, v_{NMO}) solution. These "bull's eyes" are often manually interpreted to derive the stacking velocity function. Using nonlinear optimization, I developed an automated stacking velocity function that shows sensitivity to the heterogeneous velocity structure of the firn.

4.3.2 Firn Density Estimation

Stacking velocity analysis measures the average velocity from the surface to a given depth. Classically, I applied Dix (1955) inversion to estimate the interval ve-

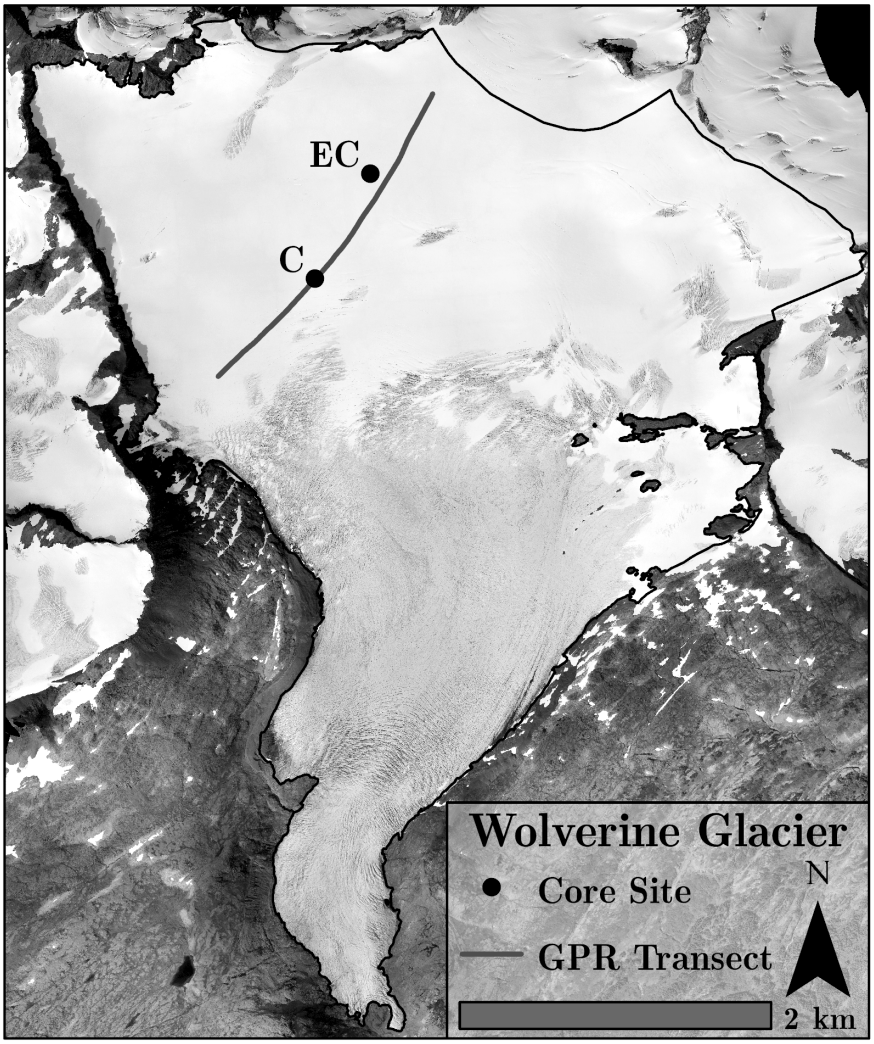

Figure 4.8: An overview map of Wolverine Glacier displaying the locations of core sites C and EC and the multi-offset GPR transect. Imagery and in-situ density data are available from the U.S. Geological Survey (McNeil *et al.*, 2019; Baker *et al.*, 2018)

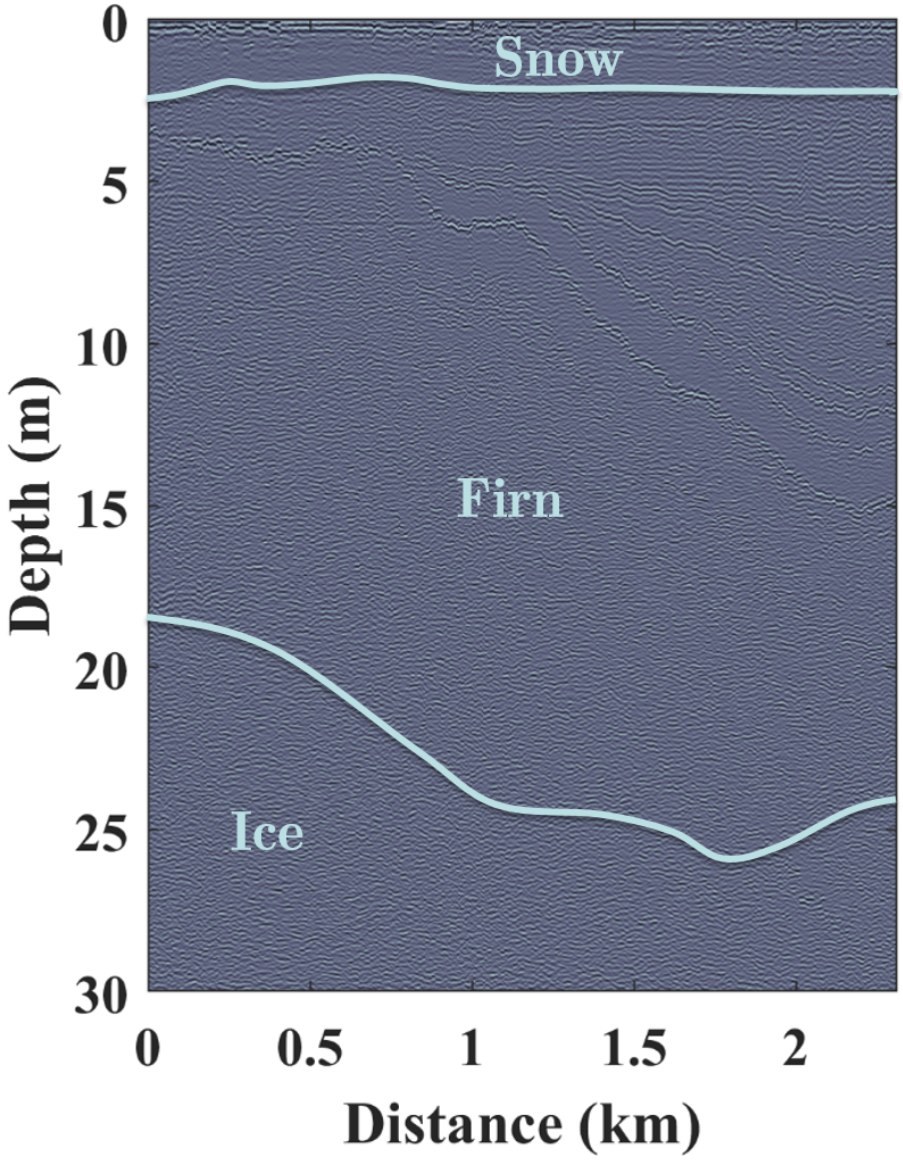

Figure 4.9: A depth interpretation of the winter snow mass and percolated firn for the transect moving up-glacier. Higher on Wolverine the the snow accumulation increases the firn depth where it develops prominent layering to $\sim$ 15 m depth. The firn appears to undergo rapid densification, and it reaches pore close off density at $\sim$ 25 m depth. The snow firn boundary was interpreted from a radar reflection horizon, while the firn to ice transition depth was determined by extracting the 830 kg/m^3 contour from the dry-firn density model.

locity model. However, stacking velocity functions that are not well approximated are susceptible to errors when converted to interval estimates. Reflection coherence analysis may contain additional apparent spectral velocity modes caused by coherent, yet out of phase energy. To derive a smooth and monotonic velocity function, the stacking velocity was modeled as an exponential function

$$v(t) = a + be^{ct} \tag{4.26}$$

that was fit using coherence-weighted nonlinear least-squares optimization (Figure 4.10). Here, the parameters $a \approx v_{ice}$ and $b \approx v_{snow}$ represent the average velocities of ice and snow. Common midpoints gathers with originally 1 m along track resolution were averaged with neighboring CMPs within a 5 m radius. The coherence was computed and fit for each stacked CMP gather along the transect to estimate the stacking velocity model (Figure 4.11). Because the instantaneous velocity is essentially the derivative of the stacking velocity model, an exponential model is good choice for a stacking velocity model, as the derivative of an exponential function is also exponential. Additionally, firn density can be modeled accurately by an exponential function (Hubbard *et al.*, 2013). Interval velocities show spatial heterogeneity that follows the stratigraphic boundaries created by snow and firn. Firn density was estimated by converting the interval velocities using the Complex Refractive Index Method (Figure 4.12). The snow in the afternoon of May 13, was moist to wet. For comparison between dry firn and partially saturated firn, a LWC of 0.5 % was applied to the density inversion.

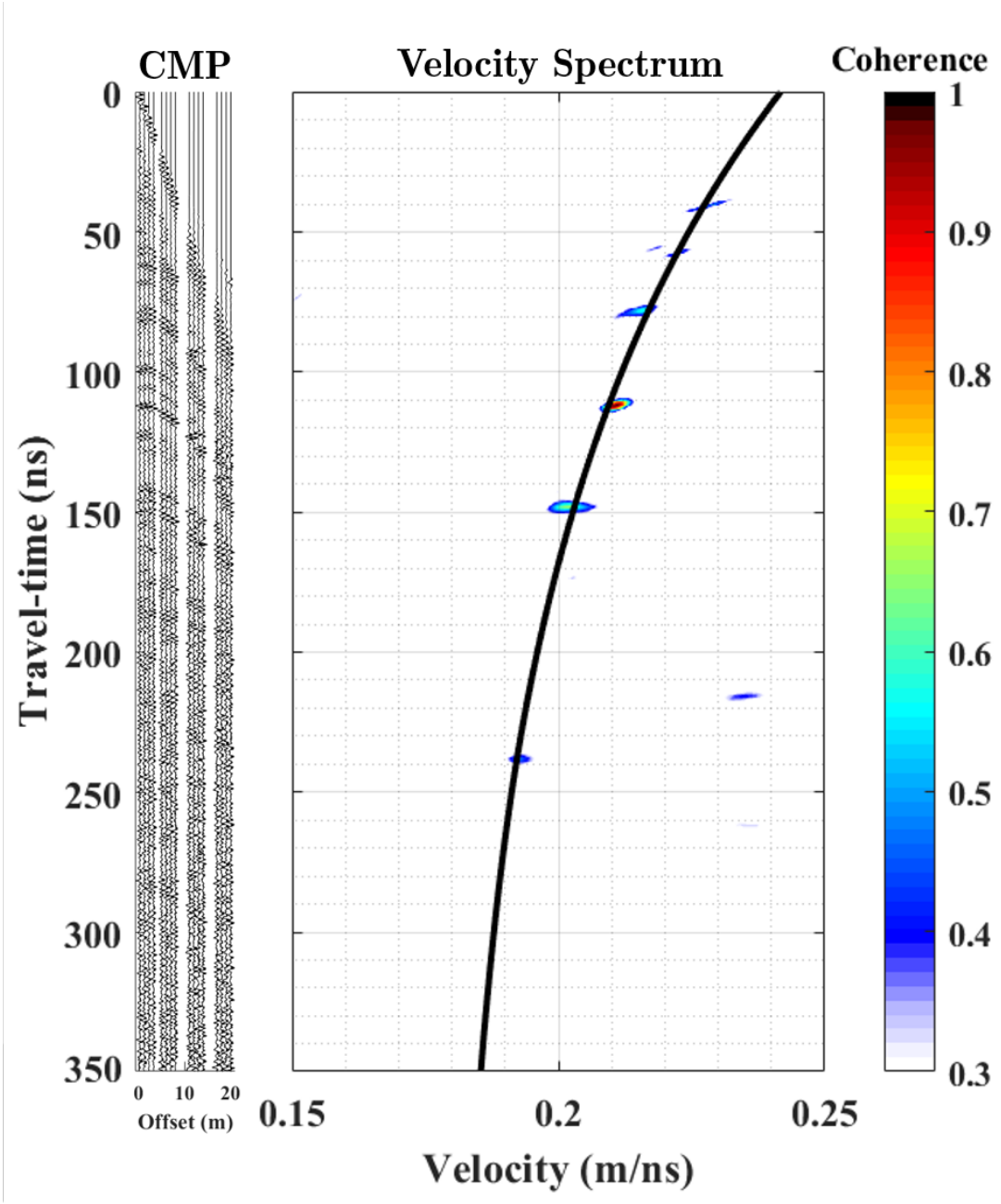

Figure 4.10: Velocity spectra were computed from the example CMP gather. The stacking velocity function was estimated by an exponential model that was fit to the velocity spectra via coherence-weighted least-squares.

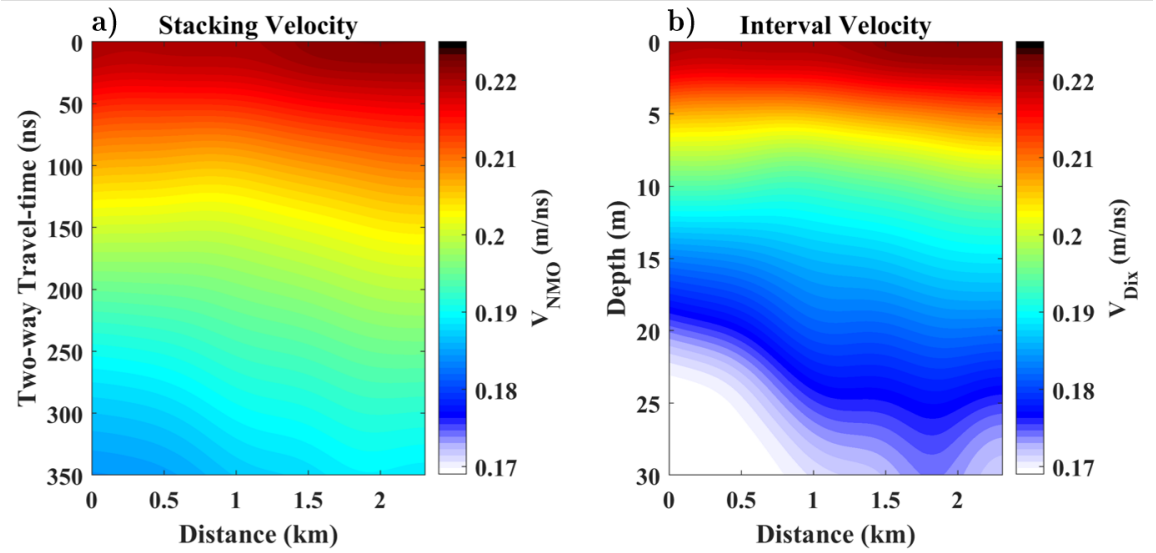

Figure 4.11: Stacking velocity was estimated by spectral velocity analysis. The interval velocities were estimated by Dix inversion. Velocity heterogeneity follows the stratigraphy development of higher elevation firn.

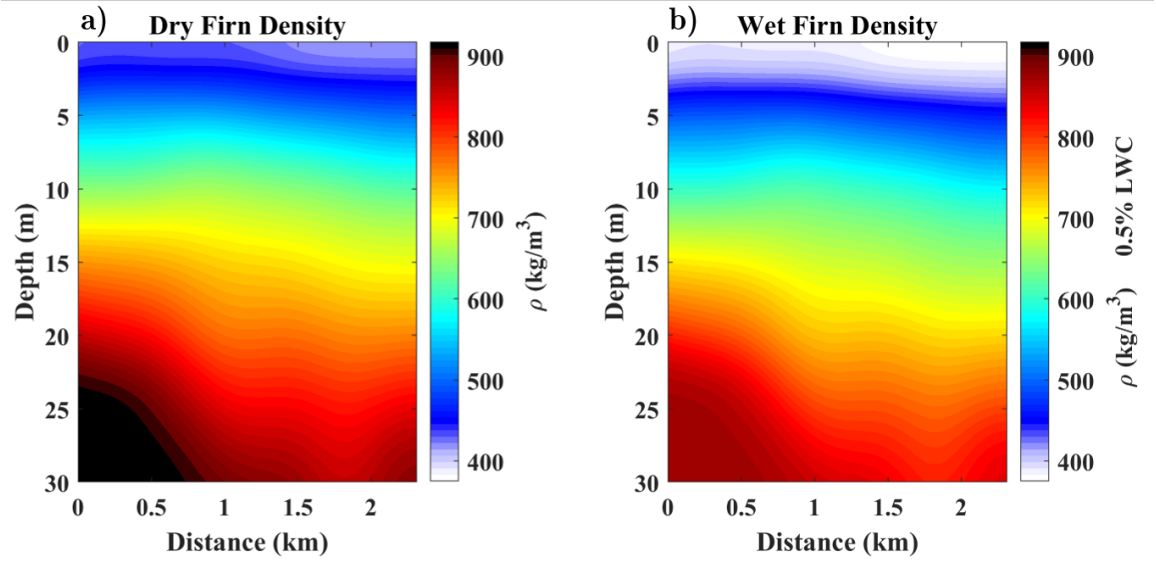

Figure 4.12: Firn density was estimated from the interval velocity model by the Complex Refractive Index Method (Equation 4.27). The density for unsaturated firn with liquid water content of 0.5 % was calculated for comparison with dry firn density. The snow surface was moist to wet during the afternoon data acquisition.

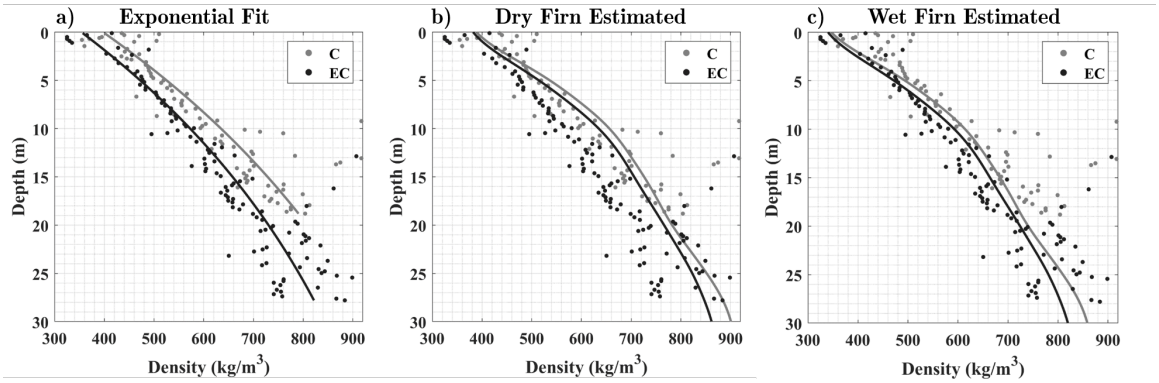

Figure 4.13: *a*) **Firn density measured at core sites C and EC was estimated with an exponential model. Measured firn density and the** *b*) **dry firn and** *c*) **wet firn density estimated by radar velocity inversion.**

4.3.3 Evaluation with Firn Cores

In-situ data was acquired at Core C during the 2021 winter mass balance campaign, however, the most recent publicly available firn core data collected at both sites is from May 2016 (Baker *et al.*, 2018). The density measured in Core C is $65 \pm 11\ kg/m^3$ greater than Core EC on average for a given depth, suggesting that compared to EC the lower elevation and SMB of Core C tends to increase the firn density. Firn density profiles from Cores C and EC are estimated by an exponential function (Figure 4.13a) and are also compared to the wave speed inversion estimated dry-firn (Figure 4.13b) and wet-firn density (Figure 4.13c).

4.3.4 Conclusion

The automated spectral velocity analysis for firn density retrieval eliminated the need for tedious and subjective travel-time picking. The density models estimated from this analysis show spatial variability that is intuitive and reveals the density transition between more shallow and deeper firn zones of Wolverine Glacier. Snow density is greater and the firn column is thinner ($\sim 20\ m$) at lower elevations. The

firn is thicker at higher elevations, where the densification rate is less, and reaches pore close off at $\sim 25\ m$. Stratigraphic layering in the percolation zone appears to be more strongly related to density than in the dry snow accumulation zone where density tends to remain independent of the stratigraphy.

4.4 Ground-penetrating Radar Experiments at Camp Arenales, Chile

Abstract

Ground-penetrating radar (GPR) was acquired during the July and August 2019 Arenales, Chile vehicle mobility campaign. Two GPR frequencies (900 and1600 MHz) were operated using three acquisition strategies: common midpoint gathers (CMP), vehicle mounted, and sled pulled. The experiments were performed in shallow ($sim10\ cm$) and deep ($\sim 150\ cm$) snow that was fully saturated with rain and meltwater. Radar velocities from CMP gathers, along with an estimate of snow density, are used to estimate the snow liquid water content. Vehicle mounted GPR recordings were analyzed for detecting changes in ground surface conditions. The sled pulled GPR acquisitions were acquired in on wet snow using both frequencies and polarizations. Interestingly, cross-polar the 1600 MHz data was able to image the ground beneath the wet snow, though the ground reflection does not appear in the co-polarized data.

4.4.1 Overview

The study site, Camp Arenales, Chile, has test locations at lower elevation, (LQ1 and LQBase) which exhibit wet, shallow, ephemeral, snow and bare soil and gravel, and at higher elevation (LQ2) which had deep saturated snow cover on top of hilly shrubland. CMP gathers were conducted at low elevation sites with thin snow cover

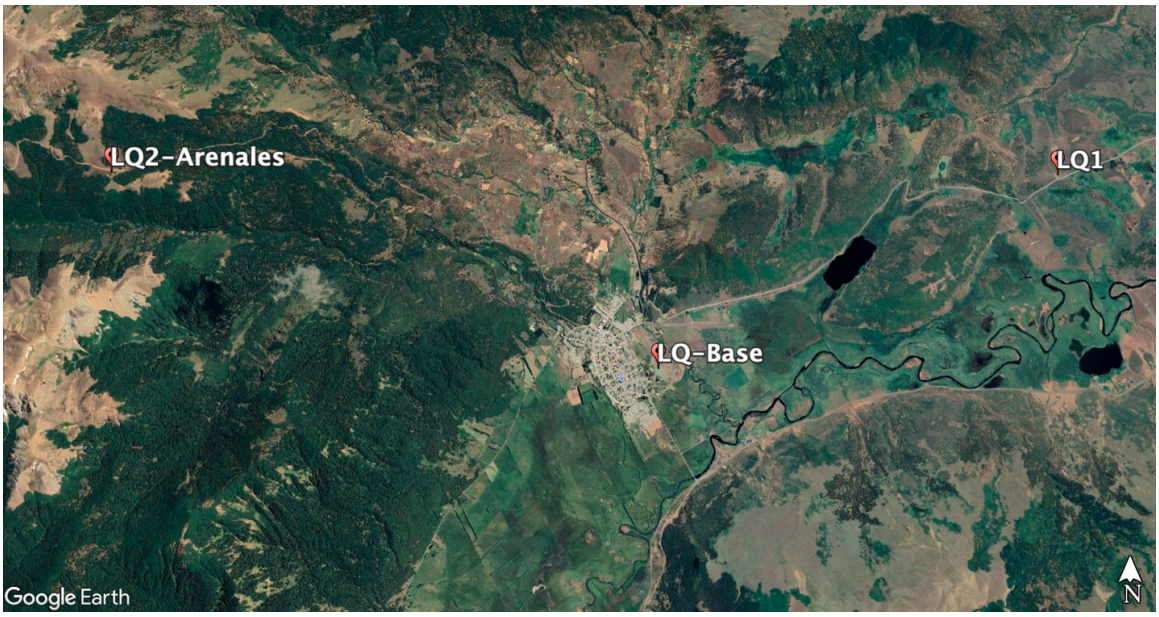

Figure 4.14: A Google Earth image showing the location of the LQ-Base, LQ1, and LQ2 sites at Arenales, Chile.

and high elevation sites with deep snow cover. Two test vehicles were used in the mobility study: The Mercedes Unimog U 4000 and the John Deere 850J Dozer. Vehicle mounted GPR experiments were conducted at the LQ1 and LQBase locations. The GPR was pulled in a sled on the snow surface at LQ2 test locations (see Figure 4.14).

4.4.2 Common Midpoint Gather Analysis

A common midpoint (CMP) gather is a measurement of the radar travel-time as a function of antenna separation, or offset. The signal processing for CMP gathers involves De-WOW filtering, bandpass filtering, and amplitude gain. A reflection measured on a multi-offset CMP gather exhibits normal moveout (NMO) in the presence of a homogenously-layered and planar subsurface structure that exhibits small vertical velocity heterogeneity (Al-Chalabi, 1974). The NMO equation approximates the non-linear travel time of reflected radar arrivals. The linearized form of NMO (Equa-

tion A.2) known as the $x^2 - t^2$ method (Green, 1938), is cast into a linear system to solve for t_0, the reflection travel-time at zero offset, and V_{NMO} the average radar velocity by method of least-squares. Snow depth is estimated from the measured velocity as in Equation A.18. The least-squares estimate of wave speed is re-solved many times using randomly sampled sub-sets of 50% of the available CMP data. This method, known as bootstrapping (Efron & Tibshirani, 1986), creates a distribution with a mean and standard deviation for each parameter (t_0, V_{NMO}, z_{NMO}, and LWC) which is used as the measure of uncertainty.

Volumetric liquid water content of the snow can be measured using the radar velocity and an estimate of the snow density. I applied a three-phase dielectric mixture model of the form

$$LWC = \frac{\sqrt{k_s} + f_i - \sqrt{k_i} f_i - 1}{\sqrt{k_w} - 1} \tag{4.27}$$

to estimate the percent liquid water content (LWC), where $k_s = \left(\frac{c}{V_{NMO}}\right)^2$ is the relative dielectric permittivity of wet snow, $f_i = \frac{\rho_s}{\rho_i}$ is the volumetric fraction of ice for snow density $\rho_s = 250\ kg/m^3$ ice density $\rho_i = 917\ kg/m^3$, $k_i = 3.15$ the relative dielectric permittivity of ice, and $k_w = 80.1$ the relative dielectric permittivity of water (Annan *et al.*, 1994).

Figure 4.15 presents the radar velocity as a function of dry snow density and LWC using the three phase complex refractive index method (CRIM). Because the relative dielectric permittivity of freshwater is approximately 25 times greater than that of ice, a small volumetric contribution of water has a large effect on the radar wave speed. In turn, it can be seen in Figure 4.15 that a significant change in density ($\pm 25\ kg/m^3$) has a less significant effect on the estimated LWC for a measured velocity.

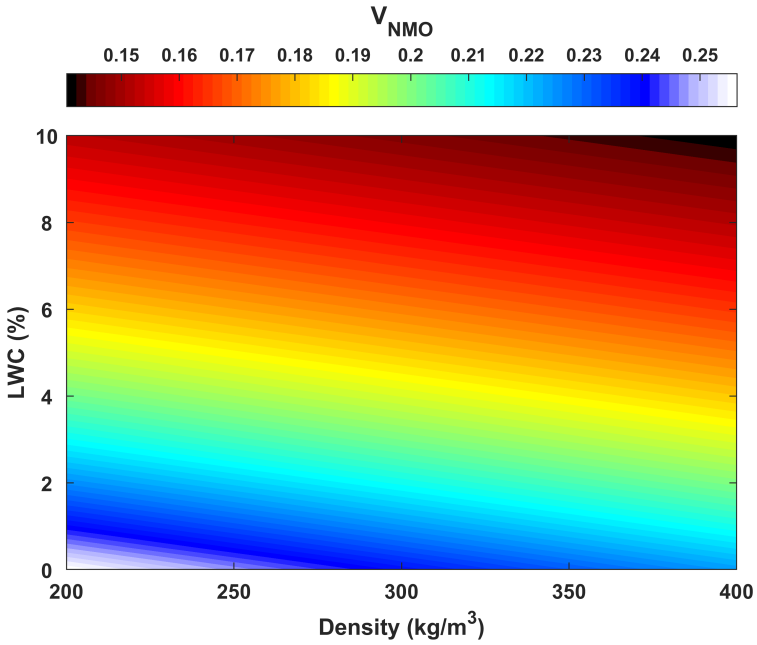

Figure 4.15: The three phase CRIM model represents the electromagnetic velocity as a function of snow density and percent LWC.

CMP Analysis of Shallow Wet Snow

The CMP gather (Figure 4.16) was picked manually using an algorithm that snaps the picks to the nearest trough of the radar wave. The initial energy of the direct airwave arrival is picked first. These picks are fit using linear regression to estimate the intercept time, or the experimental time at which the radar wave was transmitted (Appendix A.2). Time zero correction is a necessary step in NMO velocity analysis. This correction also applies backshifting, or layman's deconvolution, such that the trough, rather than the zero crossing, is set as the wavelet phase of the earliest returned energy. The thin snow cover is challenging to analyze because of interference between the direct, surface-coupled wave and the reflected wave from the snow ground interface that masks the initial reflected energy. The wavelet phase picked in the NMO velocity analysis is a later arrival with the same moveout behavior

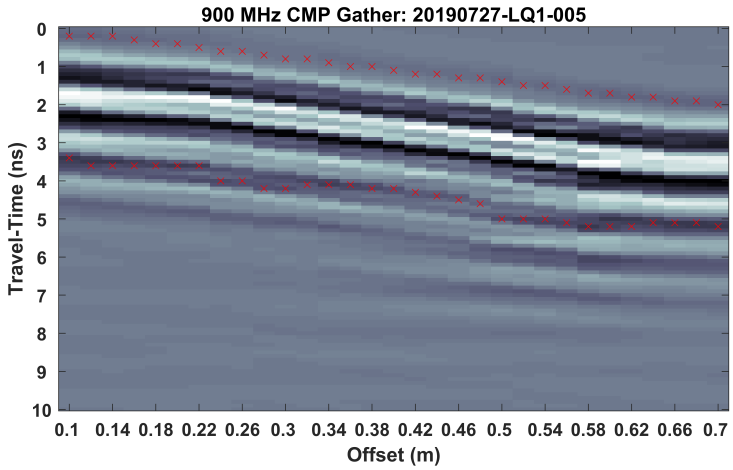

Figure 4.16: The red Xs indicate the picked radar energy. Earlier picks are the direct airwave with moveout velocity $\sim 0.3\ m/ns$, later picks are reflected energy that is far enough away from the direct energy (in time) to conduct velocity analysis. The NMO velocity of this arrival is $0.168 \pm 0.01\ m/ns$.

as the masked reflection.

The velocity estimated from the ground reflection is $0.168 \pm 0.01\ m/ns$ which yields a LWC of $7.2 \pm 1.3\%$. Velocity calculated from this arrival will be accurate, but snow depth is overestimated because t_0 was measured on the later wavelet phase; reiterating, because the initial reflected energy is contaminated by the surface wave energy due to thin snow cover that is less than the $\sim 18\ cm$ radar wavelength. The appropriate t_0 of the reflected wave is $\sim 1.5\ ns$ for a snowpack approximately 13 cm deep. The picked reflection plotted in red Xs yields a snow depth of $31.3 \pm 2.4\ cm$. To correct this depth, I subtracted one wavelength from the overestimate because the next cycle of the wavelet was used in the analysis. This yields a snow depth of $11.7 \pm 2.4\ cm$, which is consistent with measurements of snow depth at LQ1.

A second reflection is apparent in the LQ1 CMP gather (Figure 4.17). The NMO velocity measured from this reflection is $0.08 \pm 0.003\ m/ns$, which suggests that this reflection originates in the subsurface – likely from a layer in the saturated soil. The

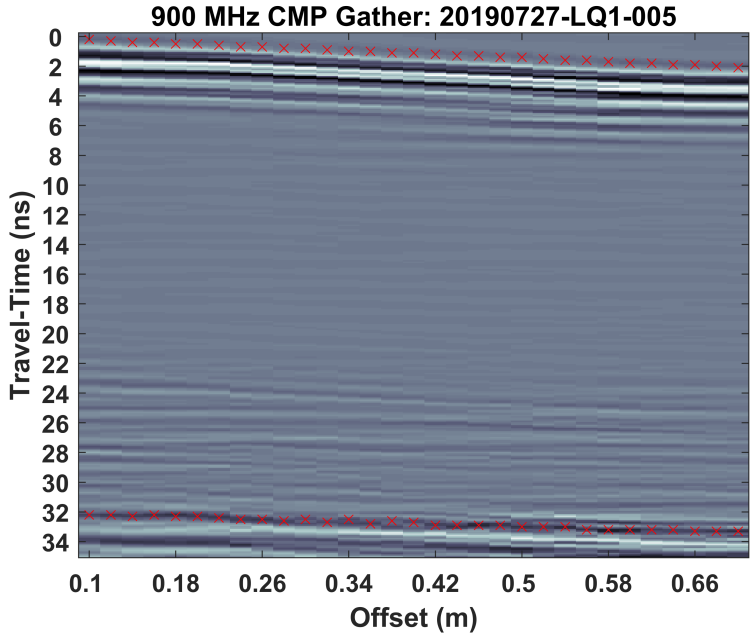

Figure 4.17: A later reflection from $t_0 \sim 32\ ns$ likely originates from a soil layer boundary as the NMO velocity measured from the red picks is $0.08 \pm 0.003\ m/ns$. The depth of this layer is $1.29 \pm 0.06\ m$ below the snow surface or $1.17 \pm 0.06\ m$ below the ground surface.

depth of this soil layer is $1.29 \pm 0.06\ m$ below the snow surface or $1.17 \pm 0.06\ m$ below the ground surface.

CMP Analysis of Deep Wet Snow

On July 30, 2019, CMP measurements were acquired using the 900 MHz and 1600 MHz systems near the LQ2 snow pit, which had an average snow density of 378 kg/m^3 and depth of 1.66 m. Because the snow was deep and very wet, the time-window of the CMP gathers was increased. This changed reduced the sample interval of the system. We estimated LWC of $3.65 \pm .35\%$ and snow depth of $1.82 \pm 0.04\ m$ from the 900 MHz CMP gather (Figure 4.18). The 1600 MHz gather was unusable largely due to frequency and offset dependent attenuation in the wet snow.

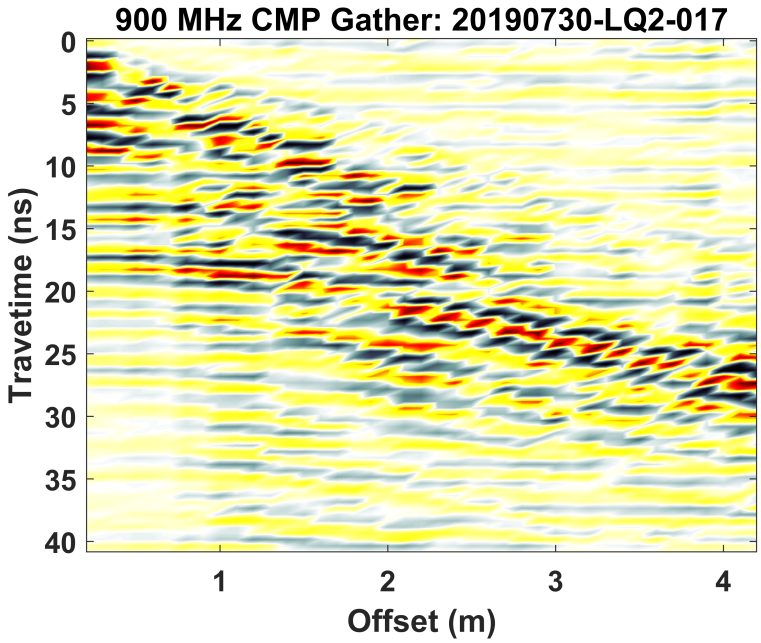

Figure 4.18: The 900 MHz CMP gather from LQ2 was acquired with a sample interval of $0.5\ ns$ which gives a nyquist frequency of 1000 MHz. The CMP gather appears rough due to trace interpolation. The data maintained enough coherency for analysis but with reduced accuracy due to discontinuity in the faint direct wave and along the reflection horizons.

4.4.3 Common Offset Gather Analysis

GPR images are typically recorded with one transmitting antenna and one receiving antenna that are separated by a fixed distance, known as a common offset (CO) gather. Opposed to a multi-offset CMP gather, which is an image of one point in space, common offset gathers are a scanning profile along some path. CO gathers were acquired by mounting the GPR to the Unimog and Deere Dozer and driving the vehicles on cross country circuits that crossed various terrain/ground surface types at LQ1. The GPR was also placed inside a sled and pulled over the deep snow at LQ2.

Vehicle Mounted GPR

The 900 MHz GPR antenna was mounted to the Unimog (Figure 4.19) and Dozer for cross country tests. The vehicles maneuvered across wet shrubland with a thin, ephemeral snow cover and gravel roads that were puddled. The GPR was operated from the cab of the Unimog by CRREL staff. For the Unimog tests, a handheld GPS was used to track the distance along the cross country circuit and a fiducial mark was recorded every 50 m by the GPR operator. The fiducial mark is necessary for estimating the positioning of the GPR traces when GPS information is not concurrently recorded with the GPR. A double mark was recorded as the radar passed over changes in surface type (e.g. snow/ no snow, shrubland/gravel, and water puddles). The GPR was not actively monitored during testing with the John Deere Dozer, because the dozer had seating for only one occupant. As a result, GPR data acquired with the dozer does not have fiducial marks and is not presented within this report, because the surface change detection methodology developed here relies on the human classification of surface change for comparison.

Figure 4.19: 900 MHz GPR antenna mounted on the Mercedes Unimog U 4000. The GPR was operated from the vehicle. Distances were marked in the GPR trace header every 50 m using a GPS odometer. Changes in the ground surface were also marked.

Terrain Change Detection

I tested the ability of GPR to detect changes in surface reflectivity associated with changes in the terrain. This analysis uses the standard GPR signal processing workflow and post-processing algorithms. The signal processing workflow is as follows: trace residual median filter, 2-octive bandpass filter, time zero correction using the Modified Energy Ratio (Wong *et al.*, 2009), principle component analysis decision based eigenimage filtering, geometric spreading correction by t^2 scaling, trace smoothing, and manual trace removal of stationary traces. The radargram was then processed for terrain characterization by taking the L_2 norm of each trace, and then calculating the variance in a moving window.

The processed radargram (Figure 4.20a) is a 200 m section of the Unimog cross country test that experienced changes in terrain. The black Xs on the axes are the 50 m fiducial marks, and the magenta Xs are double marks indicating a change in the terrain type. The type of terrain at a given position is unknown; presumably, the shubland terrain extends from 0.4 to 0.53 and 0.57 to 0.6, and the puddled gravel

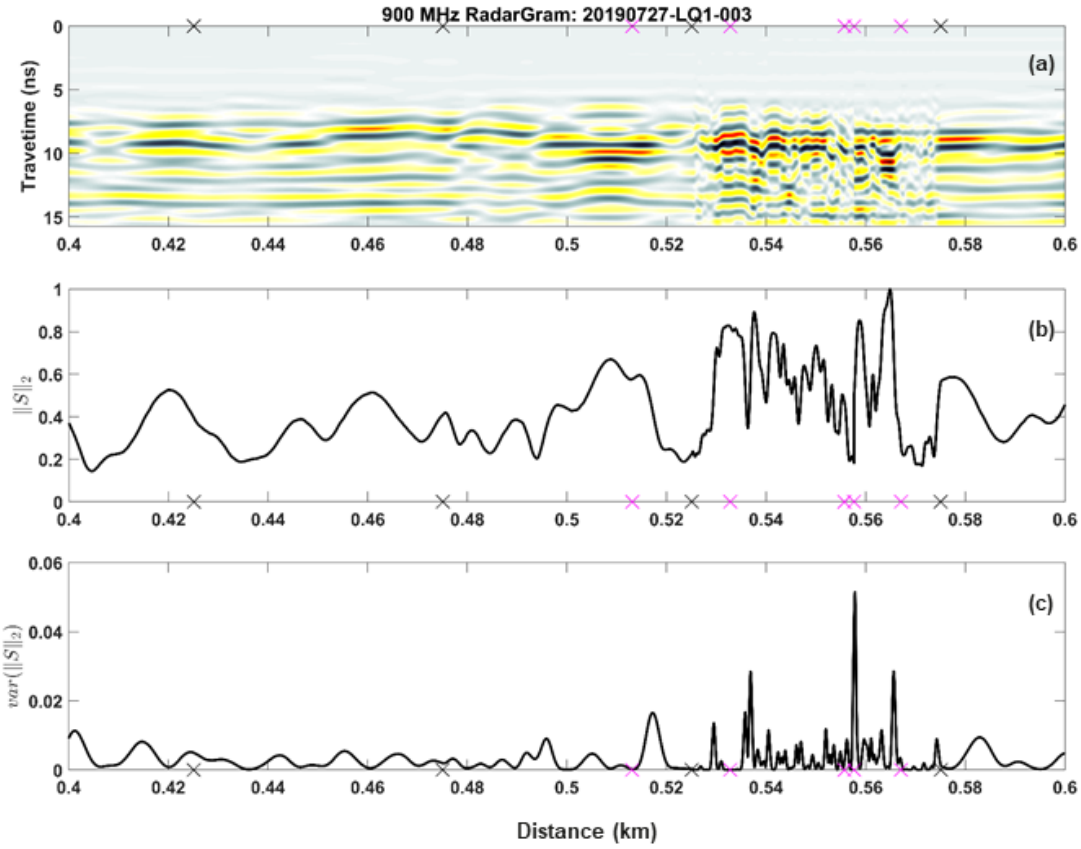

Figure 4.20: *a*) **A section of the radargram after signal processing. A faint reflection from the thin snow cover ($\sim 6\ ns$) is a precursor to the strong ground reflection ($\sim 8\ ns$).** *b*) **The maximum normalized L_2 norm of each trace has a lower frequency signal over the shrubland and higher frequency (noisy) characteristic across the (presumed) puddled gravel road.** *c*) **the variance of** *b*) **computed in a moving window of 251 traces is used as an edge detector, where the spikes indicate changes in terrain. The black Xs on the axis are the $50\ m$ fiducial marks, and the magenta Xs are double marks indicating a change in the terrain type. The spikes in** *c*) **align with the magenta marks within a small relative positioning error.**

road is the segment from 0.53 to 0.57. The L_2 norm of each trace was calculated then normalized by the maximum value (Figure 4.20b). This section contained the maximum trace norm at 565 m distance. Then the variance of normalized trace L_2 is calculated in a moving window of 251 traces (Figure 4.20c). The spikes in variance align with the magenta Xs to an acceptable positioning error on the order of meters. This fairly simple method demonstrates the usefulness of GPR for terrain change detection, that has the potential for land surface characterization in real-time applications.

Amplitude Phenomenon via Frequency and Polarization Modulation in Wet Snow

Common offset GPR experiments were conducted at LQ2 on July 29, 2019, with 900 MHz and 1600 MHz antennas. The antennas were placed in a sled and were pulled by foot on top of the snowpack. The co-polarized 900 MHz antennas were able to penetrate the deep and wet snowpack, imaging the reflection off of the ground surface (Figure 4.21). The same transect was repeated with the 1600 MHz antennas, but the co-polarized signal was unable to penetrate through the wet snow, as the image is incoherent with no obvious reflection from the snow ground interface (Figure 4.22). Experiments using cross-polarized antennas were conducted at 1600 MHz. Although the ground reflection is not as obvious as in Figure 4.21, it can be seen with cross-polarized antennas (Figure 4.23) where it is not distinguishable using co-polarized antennas (Figure 4.22). This phenomenon of L-band radar polarization can be explored for its potential in quantifying LWC, and in its potential for wet snow terrain detection and navigation.

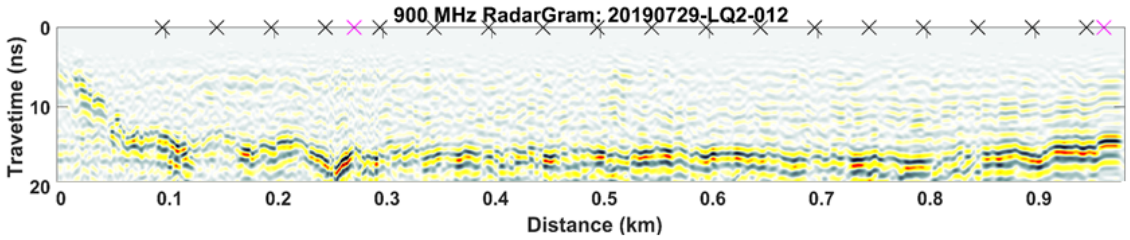

Figure 4.21: An east-west transect at LQ2 with 900 MHz antennas. The ground reflection is the brightest horizon of the image. The ground dips from ~ 5 ns to ~ 15 ns over the first 100 m of the transect then remains at ~ 15 ns.

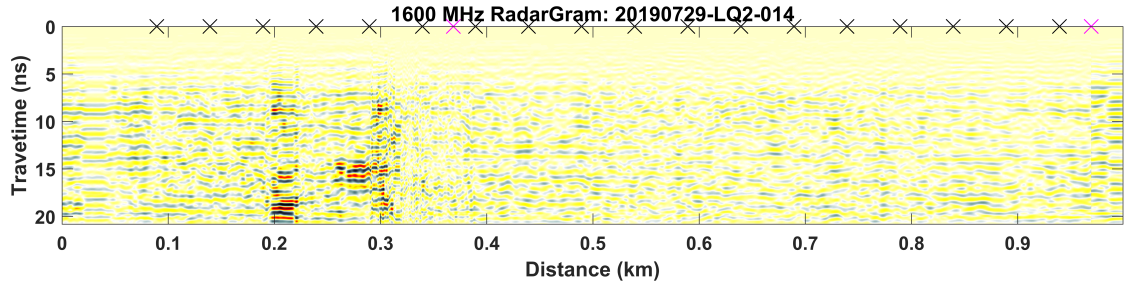

Figure 4.22: The same transect as Figure 4.21 at 1600 MHz with co-polarized antennas. The radar energy was attenuated at the higher frequency due to snow LWC. The ground reflection is not apparent in the image.

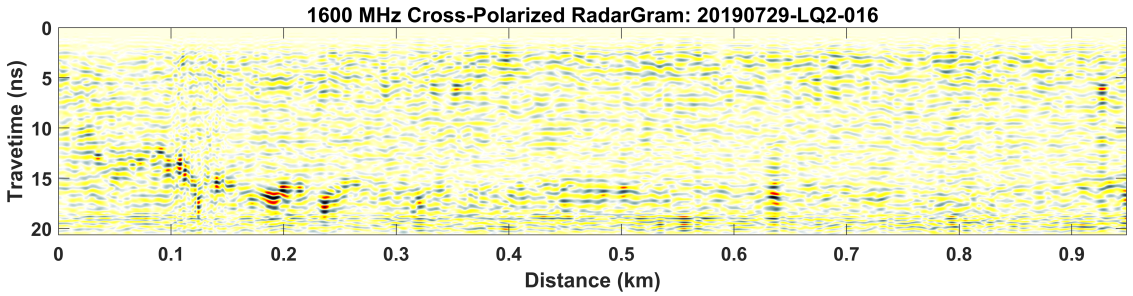

Figure 4.23: The same transect as Figure 4.22 with cross-polarized 1600 MHz antennas. The ground reflection is faint though visible (compare with Figure 4.21), where it is not visible with co-polar antennas, pretty curious.

4.4.4 Conclusion

Various ground-penetrating radar methods were tested in wet, ephemeral snow upon various terrains and in deep, wet snow, overlying hilly shrubland at Camp Arenales, Chile. Common midpoint gathers were used to determine the electromagnetic velocity of the radar signal traveling through wet snow. The velocity estimate was combined with an estimate of snow density from nearby snow pits to estimate LWC. Snow LWC was greater in the thin slushy snow ($7.17 \pm 1.33\%$) than in the deeper snow at higher elevation ($3.65 \pm 0.35\%$). Vehicle testing on cross country circuits showed that GPR can detect changes in the terrain using the magnitude and variance of the signal reflected from the ground surface in an automated way. Experiments using co- and cross-polarized 1600 MHz antennas show that in wet snow conditions where attenuation dominates, cross-polarized antennas outperform the conventional co-polarized radar acquisition.

4.5 Over-snow Vehicle Mobility Index Assessment and Prediction

During the SnowEx 2020 Grand Mesa Intensive Observation Period (IOP) a small unit support vehicle (SUSV) was performance tested. I developed a vehicle mobility performance index, coined the Normalized Difference Mobility Index (NDMI), by joining vehicle speed and driver throttle position using a difference-sum ratio. The SUSV performed best on the groomed snowmobile trails and showed reduced performance off-trail. The measured NDMI was distributed spatially by trialing both MLR and decision tree regression models that were trained on the SWE, depth, density, and LiDAR terrain and vegetation features developed in Chapter 3. I demonstrate

Figure 4.24: The BV-206 small unit support vehicle (SUSV) on Grand Mesa, Colorado.

methods for integrating vehicle and environmental data to predict SUSV mobility within a $\sim 2\ km^2$ area of the Grand Mesa study area.

4.5.1 Small Unit Support Vehicle

An over-snow vehicle has the capability to travel cross-country over snow-covered terrain, where normal wheeled (HMMWV) and tracked vehicles (AAV and APC) cannot go. The SUSV is a Swedish made, BV-206, over-snow vehicle (Figure 4.24). The SUSV has two cabins joined by an articulating drive-shaft that independently drives the four, 62 cm wide rubber tracks. The SUSV has very low ground pressure (12 kPa), and weighs 4340 kg with a carrying capacity of 2000 kg, or 17 personnel. This vehicle is amphibious and can be transported by a helicopter sling load. These advantages make the SUSV strategical for over-snow campaign advancement (Marine Corps, 1988).

Vehicle Instrumentation

The SUSV was equipped with a vehicle data acquisition system that contained a built in Inertial Measurement Unit (IMU) which measured linear accelerations in x, y

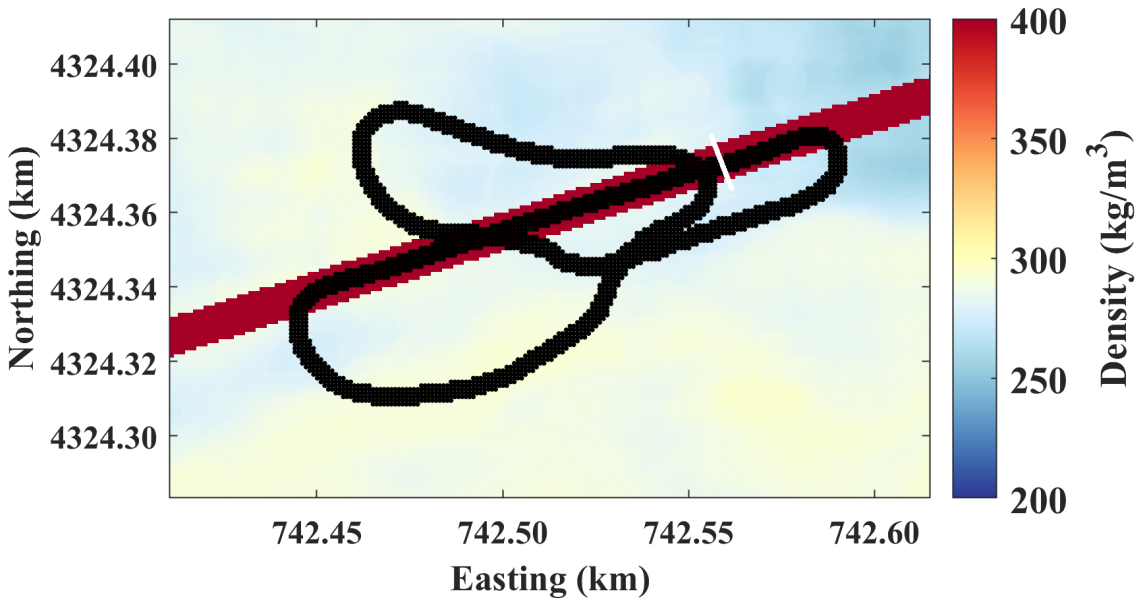

Figure 4.25: The SUSV test circuit (black) begins and ends on Land's End Loop trail (red). The stripe crossing the trail is the start/finish line (white). The circuit direction is counter-clockwise.

and z, as well as roll, pitch, and yaw. A GPS anntena attached the roof of the SUSV provided location and vehicle speed data. The vehicle data system also recorded driver inputs: steering angle, throttle position, and brake position. Wheel speed sensors equipped to the SUSV were damaged during testing and provided no usable data. Over packed snow roads, the SUSV can travel upwards of 30 *kph*. However, speeds exceeding this maximum were jarring to the instrumentation over whoops and bumps on the Land's End Loop snowmobile trail.

Vehicle Test

On January 31, 2020, the SUSV was tested on a counter-clockwise circuit beginning and ending on Land's End Loop trail (Figure 4.25). The SUSV drove along the groomed trail and cross-country in virgin snow in a quasi figure-eight. During this test the vehicle reached a top speed of 18 *kph* and maximum throttle position of 65%.

4.5.2 Normalized Difference Mobility Index

Prior to calculating NDMI, the vehicle speed

$$\widehat{V} = \frac{V}{\max V} - \frac{\min V}{\max V} \quad , \tag{4.28}$$

was normalized using 30 *kph* as the maximum speed. Throttle position (τ) is recorded as a percentage of wide open. Vehicle speed and throttle position data were then integrated using the band ratio parameter (Rouse Jr. *et al.*, 1974). The normalized difference mobility index

$$\text{NDMI} = \frac{\widehat{V} - \tau}{\widehat{V} + \tau} \tag{4.29}$$

rewards greater speed and reduced throttle. Wider throttle position penalizes the mobility index. Larger τ indicates mobility inefficiency in situations under reduced traction where throttle is applied to gain or maintain speed. At top speeds, when throttle position is reduced the NDMI approaches the maximum value near one. The NDMI for the example SUSV performance test is shown in Figure 4.26. Values $\gtrapprox 0$ indicate satisfactory vehicle mobility. This initial result is confirmation, as the NDMI distinguishes the snowmobile trail from the virgin snow. On the higher density and sintered snowmobile trail the NDMI is positive valued, while in lower density and less cohesive snow the NDMI drops below 0.

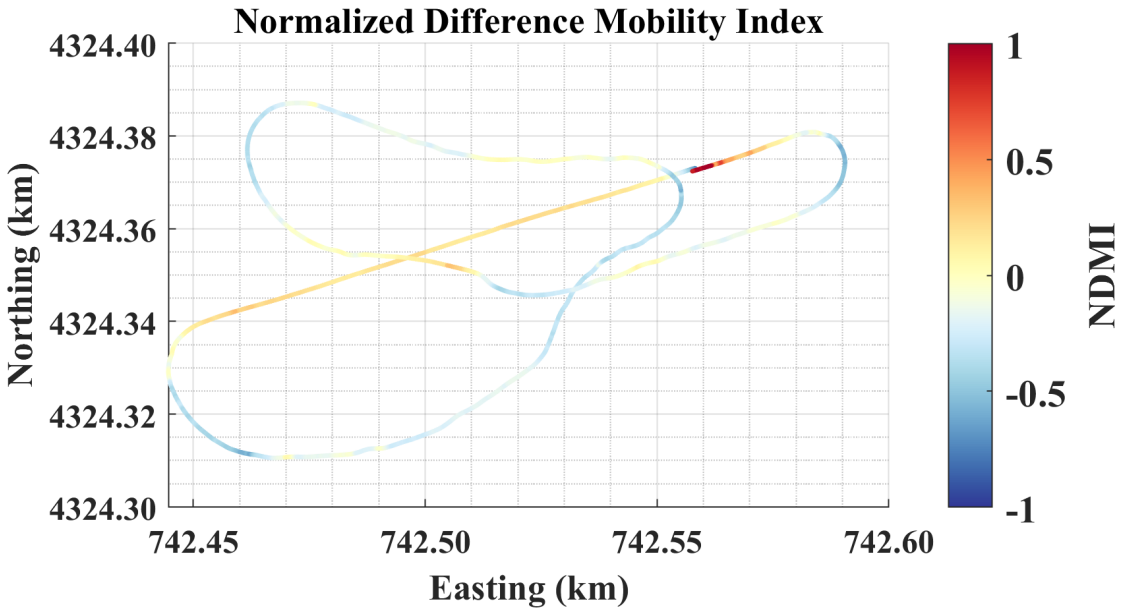

Figure 4.26: Normalized Difference Mobility Index was calculated from normalized vehicle speed and throttle position data.

4.5.3 Mobility Prediction using Snow, Terrain, and Vegetation Features

In Chapter 3 multiple linear regression of LiDAR features was applied to spatially distribute the average snow density that was measured from GPR TWT and LiDAR snow depth observations. In this extension, I applied MLR with first order interactions and bagged decision trees to spatially distribute the NDMI measured on the SUSV test course. Principal component analysis (PCA) was applied within the regression to reduce the parameter space to a set of orthogonal vectors, which together explain of 99.5 % of the data variance. Ten-fold cross-validation was applied to limit over-training.

Data Augmentation

Snow – SWE, density, and depth – terrain – elevation, slope, and aspect, of the snow surface and ground – and vegetation – height and proximity – features were established as predictors of NDMI. These predictor data were augmented or processed in the following ways prior to model training.

Snow Density The estimated spatial snow density (Figure 3.7) does not capture the unnatural density of the snowmobile trail. These data were augmented with the surface density of the snowmobile trail that was estimated from a CMP gather (Meehan, 2021a). The raster coordinates of Land's End Loop were located using a k-d tree searcher within 5 m buffer around the coordinates of the trail provided in the SnowEx 2020 GIS data (Hiemstra *et al.*, 2021). Along this path the modeled densities were replaced by random draws from the the surface density distribution (Figure 4.27b). The augmented density raster is shown in Figure 4.28

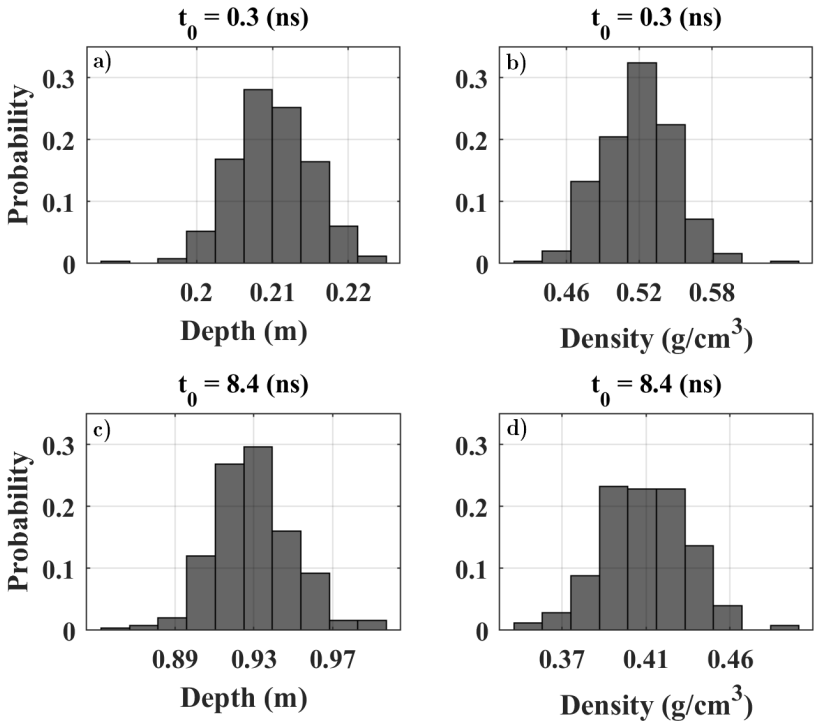

Figure 4.27: Snow surface *a)* depth and *b)* density, and *c)* total depth and *d)* bulk density were estimated from a radar CMP via linear regression with bootstrapping. The surface density distribution was randomly sampled to replace the density values along Land's End Loop (Figure 4.28)

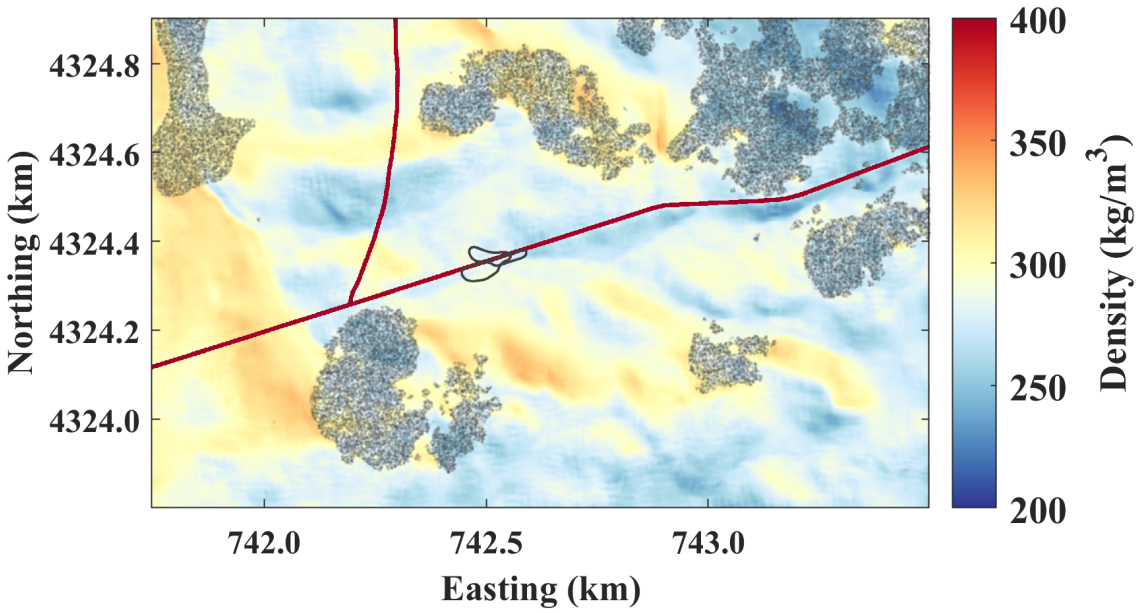

Figure 4.28: The density modeled in Chapter 3.3.4 was augmented with the surface snow density measured on the snowmobile trail. Vegetated areas are shown with stippling.

Snow Depth The LiDAR flight occurred on 1 February, 2020, the day following the SUSV testing. On average the SUSV sunk about 30 cm into the virgin snow, and thus, the SUSV left an imprint on the LiDAR estimated snow depth. As to not bias the predictor data, the LiDAR depth raster was touched up along the SUSV test trail. The pixels within a 2.5 m and a 5 m buffer of the SUSV test circuit were found using a k-d tree searcher. The surrounding pixels of the 5 m buffer that do not intersect with the 2.5 m buffer were used to estimate the local uncompacted snow depth on the SUSV cicuit. For each pixel within the 2.5 m buffer the mean snow depth from the nearest pixels of the 5 m buffer were assigned.

Sinkage The sinkage depth, represents the height which undisturbed snow must compact before a vehicle can apply tractable forces allowing for forward motion (Shapiro *et al.*, 1997). As a parameter of the predictive modeling, the expected sinkage depth (z) of the SUSV was calculated

$$z = h\left(1 - \left(\frac{\rho_o}{\rho_f}\right)\right) \quad , \tag{4.30}$$

following Shapiro *et al.* (1997), where h is the LiDAR measured snow depth, ρ_o is the initial rasterized bulk snow density, estimated from MLR (Chapter 3.2.6), and ρ_f is the final snow density, assumed to be 500 kg/m^3 after vehicle compaction. This sinkage model was developed for shallow snow, where the compacted snow makes contact with the ground. However, the estimated sinkage agreed with the sinkage of ~ 30 cm observed in the field, showing the applicability of this method in deeper snowpacks.

NDMI The k-d tree searcher was applied to grid the SUSV data to the 1 $m \times 1$ m spatial data (Chapter 3.2.4), by extracting the nearest pixels within a 1 m buffer and calculating the median. The SUSV was tested in unforested terrain, which has little information about the effect of vegetation on mobility. The assumption was made that if the distance between trees was less than 5 m the mobility would be poor. The NDMI training data were augmented with randomly sampled pixels within forests ($V_{prox} < 5\ m$). The NDMI value assigned to the vegetated pixels was drawn randomly from a normal distribution with mean of -0.9 and standard deviation of 0.1. The number of vegetated pixels approximately equalled the number of unvegetated pixels.

Northness The $0 - 360°$ aspect data ($A°$) were normalized to a northness index ($\widehat{N}$) by the transformation

$$\widehat{N} = \frac{\text{abs}(A° - 180)}{180} \tag{4.31}$$

Normalization The snow, terrain, and vegetation features (β) were centered around the median value then normalized by the interquartile range (IQR).

$$\widehat{\beta} = \frac{\beta - \text{median}\,\beta}{\text{IQR}\,\beta} \tag{4.32}$$

All predictors, excluding northness, and vegetation height, were normalized by Equation 4.32.

4.5.4 Results

Multiple Linear Regression NDMI predicted using the MLR with first order feature interactions achieved an $R^2 = 0.8$ and RMSE = 0.18. The MLR model (Figure 4.29) informs highest mobility index on the groomed trail, and good performance in average depth snow of average density. Low NDMI is predicted in deep snow drifts and heavily vegetated areas.

Bagged Decision Trees The bagged decision tree estimated NDMI (Figure 4.30) more clearly delineates Land's End Loop with the greatest performance index. Similar to the MLR results, areas with average snow depth are preferred to deep snow drifts. Heavily vegetated areas are more clearly identified by the lowest NDMI values. The bagged decision tree model has $R^2 = 0.94$ and RMSE = 0.1

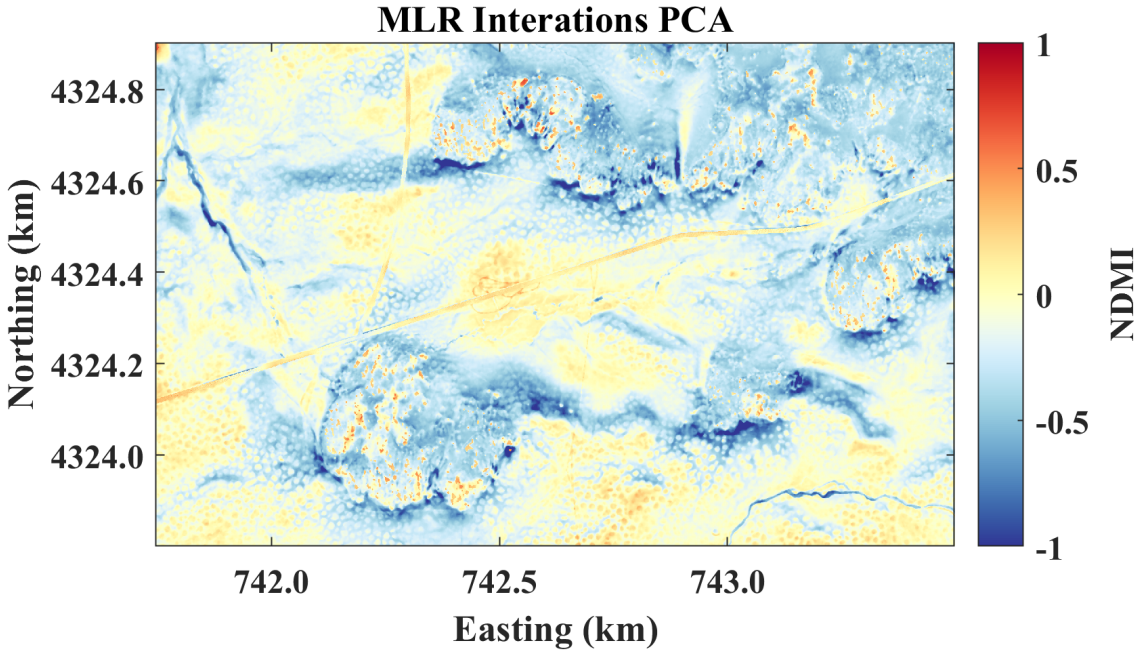

Figure 4.29: NDMI distributed using Multiple Linear Regression with first order feature interactions.

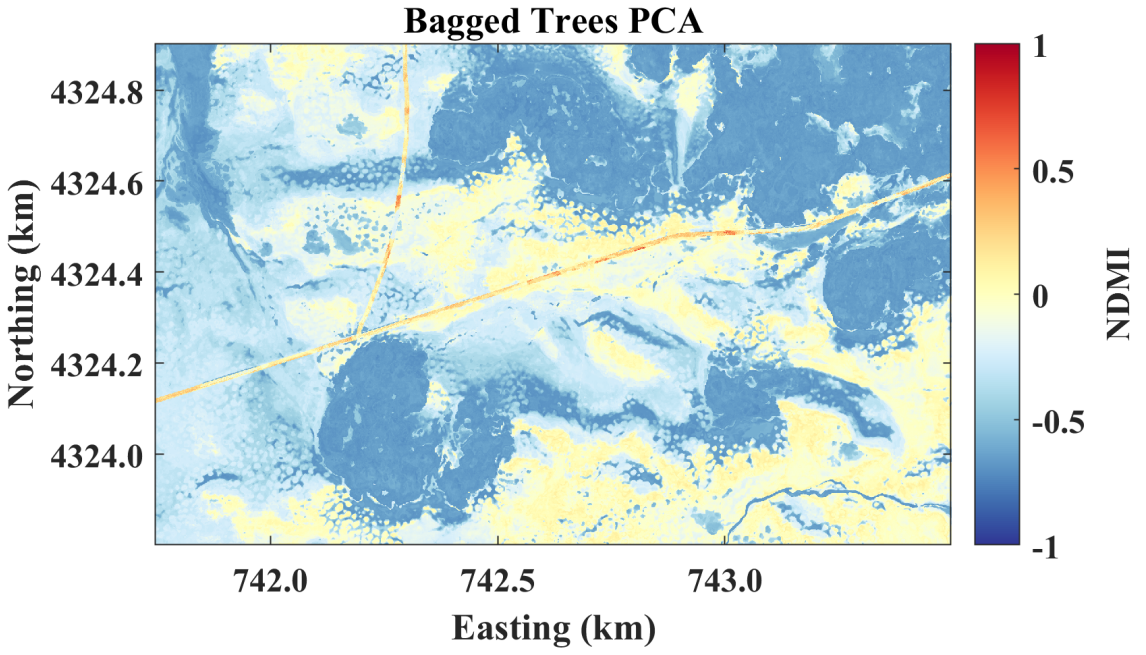

Figure 4.30: NDMI distributed using bagged decision tree regression.

4.5.5 Conclusion

Vehicle mobility maps are useful for decision making in over-snow operations. Snow, terrain, and vegetation affect vehicle performance, however, due to the spatial variability of these factors, vehicle performance is challenging to quantify and predict. To characterize vehicle performance, the Small Unit Support Vehicle was tested over virgin snow and groomed snowmobile trail on Grand Mesa, Colorado. The Normalized Difference Mobility Index was contrived as a simple indicator of SUSV performance, by joining vehicle speed and throttle position data. The NDMI was measured along a test course which traversed on- and off-trail. Snow, terrain, and vegetation information acquired via ground-based radar and LiDAR remote sensing observations were developed into a set of NDMI predictors. Using multiple linear regression and decision tree methods NDMI was predicted with a high degree of accuracy throughout a $\sim 2\ km^2$ study area. A NDMI value of 0 ± 0.1 indicates average vehicle mobility, values greater than 0.1 represent terrain where vehicle efficiency is above average, and values less than -0.1 represent terrain where vehicle efficiency is below average.

SUMMARY

Quantifying snow properties at various spatial and temporal scales requires the analysis and data integration of multiple sensors and modeled estimates. Various types of snow were assessed by comparing micromechanical property estimates with macro-scale measurements of hardness, elastic modulus, and shear strength. Spatial estimates of firn depth and density were achieved through multi-sensor radar velocity analyses. Multi-polarization radar travel-time information was integrated with airborne LiDAR seasonal snow depth information to estimate density. Regression-based prediction distributed snow properties and over-snow vehicle performance where LiDAR information was available. The algorithms developed to infer snow properties are primary to this dissertation, however these methodological advancements were used to accomplish scientific outcomes on kilometer scales – be that water equivalent estimation or vehicle mobility performance.

Snow and firn depth and density are physical properties necessary for estimating SWE and SMB. To quantify spatial variability in these properties, I applied various algorithms for multi-offset GPR inversion (horizon velocity analysis, spectral velocity analysis). Density and depth information along radar transects initialized empirical and numerical firn models for estimates at depths greater than the maximum offset of the array, due to limitations of the normal moveout approximation. Additionally, I joined remotely-sensed snow depth with ground-based TWT that was detected from

multi-polarization coherence to infer the average snow density. Using this information as the response variable in regression predicted from LiDAR features, I estimated spatially continuous snowpack density with depth invariability. Given these advances in large scale multi-offset GPR analysis, it may be possible to extrapolate density-depth information from surface elevation and accumulation inputs.

In seasonal snow, the age component of annual water equivalent estimation is trivial. For SMB quantification, the age of firn layers must be measured from chemistry and dust analysis of cores. Firn models parameterized by radar depth and density may also provide the firn age as a function of depth. I used both empirical and numerical simulations of firn age for the purposes of SMB estimation and signal processing, however the modeled ages were still calibrated to known measurements to accurately estimate annual SMB. Radar derived estimates require in-situ observations for evaluating the estimated density. As the spatial extent of radar estimated snow and firn properties increases, so does the need for in-situ observations. However, I have shown with examples from studies located in Greenland, Colorado, and Alaska, that the radar inversion processes yield meaningful results that are sensitive to the spatial variability of snow properties. Seasonal SWE, and annual SMB was estimated within 10 % uncertainty, on average. Wave-like propagation phenomena, similar to the kinematic wave propagation of firn isochrones, is apparent in the Wolverine glacier density model. In-situ observations cannot be made at the spatial resolutions required for validating the radar retrieved signal. This is a vexing problem, however, using geostatistical methods I have estimated the length scales of variability for snow density, in addition to depth and SWE. These results suggest the maximum separation distance between observations to resolve the spatial patterns. For seasonal snow on

Grand Mesa, Colorado this distance is $\lessapprox 100\ m$. While on the Greenland Ice Sheet, densification processes happen over scales $\gtrapprox 1000\ m$. These novel findings revealed the relationships between snow density and wind, terrain, and vegetation.

Coherence attributes remain a vital tool for geophysical interpretation, and are at the core of the radar process automation within this dissertation. In Chapter 2, I developed a semi-automatic horizon tracking algorithm which predicts subsequent picks by maximizing the stacked amplitude. This algorithm was applied in the horizon velocity analysis for estimating the $2015 - 2017$ SMB. Multi-offset coherence within spectral velocity analyses automated the interpretation and inversion on Wolverine Glacier. Firn layers were automatically traced from OIB Snow Radar imagery using binarized classification of the coherence among adjacent traces (Chapter 4.2.1). This technique was newly applied to calculate the multi-polarization coherence for automatic ground surface detection beneath seasonal snow cover (Chapter 3). Cross polarization was shown useful in illuminating the ground reflection in wet snow. The presence of liquid water within the pore space of snow confounds radar velocity analysis for density estimation. Currently, an estimate of dry-snow density is required for estimating LWC. The prospect for multiple polarization inversion for LWC estimation needs further exploration.

Spatial variability in the mechanical properties of snow remains largely unknown. This knowledge gap is in part due to the current capabilities of instrumentation and limitations in the theory used for data inversion. Distributing mechanical properties spatially also needs investigation. Cone penetrometers measure the combined forces normal and tangential to the cone tip. However, vertical penetration is insensitive to lateral shear forces, which are important for understanding the snow deformation

under traction loads. Several tools used for measuring roads and soil were tested for relationships with micro-mechanical properties estimated by the SMP. The Rammsonde penetrometer hardness index was found to be correlated with the rupture force, penetration force, strength, and density estimated by the SMP. Shear force measured by the shear vane at mechanical failure was found to be correlated with the number of microstructural elements engaged with the penetrometer tip. To measure snow response to shear loads, a bevameter design is possible solution under development. Without direct measurements of mechanical snow properties, inferences and spatial estimation processes remain challenging. From these experiments I decided that the path toward vehicle mobility modeling would involve snow depth and density as a surrogate for the unknown mechanical properties.

The normalized vehicle mobility index related driver and vehicle data to the terrain trafficked by the over-snow vehicle. This performance index achieved an important step in mobility data integration and was regressed against the snow, terrain, and vegetation properties developed in Chapter 3 for spatial mobility prediction. This prediction framework can be expanded to include snow mechanical properties. The NDMI value for an over-snow vehicle indicates efficiency of mobility, which is valuable information for planning logistical needs over long campaigns. SUSV tracks were identified in airborne LiDAR snow depths, which has implications for tactical reconnaissance. Over-snow vehicles are fully capable of traversing almost any snow condition, but it is clear in measurements and mobility prediction that prepared snow surfaces offer the greatest performance.

The derived snow, firn, and mobility property estimates may be assimilated into numerically modeled processes. Measurements and estimates, which capture the large scale processes and variability of snow properties at high spatial resolution, were engineered to serve as evaluation data. Importantly, estimated snow properties also rely on observations for calibration and validation. The conundrum of estimated accuracy was answered through uncertainty analyses that flow through the data process to the outcome. Process automation, repeatability, and accuracy were key design parameters for any of the algorithms developed within this work. The many different campaigns, objectives, and outcomes of this research in multi-sensor analysis documented the successes and limitations of inversion techniques for a broad range of sensors and cryosphere applications.

REFERENCES

Abdalati, Waleed, Zwally, H. Jay, Bindschadler, Robert, Csatho, Bea, Farrell, Sinead Louise, Fricker, Helen Amanda, Harding, David, Kwok, Ronald, Lefsky, Michael, Markus, Thorsten, Marshak, Alexander, Neumann, Thomas, Palm, Stephen, Schutz, Bob, Smith, Ben, Spinhirne, James, & Webb, Charles. 2010. The ICESat-2 laser altimetry mission. *Proceedings of the IEEE*, **98**(5), 735–751.

Abele, Gunars. 1963. A correlation of unconfined compressive strength and ram hardness of processed snow. *CRREL Technical Report*, 14.

Achhami, Abhusan, Kalra, Ajay, & Ahmad, Sajjad. 2018. Dynamic Simulation of Lake Mead Water Levels in Response to Climate Change and Varying Demands. *Pages 260–268 of: World Environmental and Water Resources Congress 2018*, vol. 1. Reston, VA: American Society of Civil Engineers.

Al-Chalabi, M. 1974. An Analysis of Stacking, RMS, Average, and Interval Velocities Over a Horizontally Layered Ground. *Geophys. Prospect.*, **22**(sep), 458–475.

Anderson, Don L, & Benson, Carl S. 1963. The Densification and Diagensis of Snow. *Chap. 30, pages 391–411 of:* Kingery, W.D. (ed), *Ice Snow Prop. Process. Appl.* Cambridge, MA: M.I.T. Press.

Andrews, D. F. 1974. A robust method for multiple linear regression. *Technometrics*, **16**(4), 523–531.

Annan, A P, Cosway, S W, & Sigurdsson, T. 1994. GPR for snowpack water content. *Pages 465–475 of: Fifth Int. Conf. Gr. Penetrating Radar*, vol. 2.

Arcone, Steven A., Spikes, Vandy B., Hamilton, Gordon S., & Mayewski, Paul A. 2004. Stratigraphic continuity in 400 MHz short-pulse radar profiles of firn in West Antarctica. *Ann. Glaciol.*, **39**(2002), 195–200.

Arcone, Steven A., Spikes, Vandy B., & Hamilton, Gordon S. 2005. Stratigraphic variation within polar firn caused by differential accumulation and ice flow: Interpretation of a 400 MHz short-pulse radar profile from West Antarctica. *J. Glaciol.*, **51**(174), 407–422.

Aster, Richard C, Borchers, Brian, & Thurber, Clifford H. 2019. *Parameter estimation and inverse problems*. Elsevier.

ASTM International. 2018. Standard Test Method for Field Vane Shear Test in Saturated Fine-Grained Soils.

Bader, Henri. 1954a. *Snow and its metamorphism*. Wilmette, Illinois: Snow, Ice and Permafrost Research Establishment, U.S. Army Corps of Engineers.

Bader, Henri. 1954b. Sorge's Law of Densification of Snow on High Polar Glaciers. *Journal of Glaciology*, **2**(15), 319–323.

Baker, Emily H., McNeil, Chris, Sass, Louis, & O'Neel, Shad. 2018. *Point Raw Glaciological Data: Ablation Stake, Snow Pit, and Probed Snow Depth Data on USGS Benchmark Glaciers (ver. 2.0, March 2022)*.

Barnett, T. P., Adam, J. C., & Lettenmaier, D. P. 2005. Potential impacts of a warming climate on water availability in snow-dominated regions. *Nature*, **438**(7066), 303–309.

Barrett, Brian Edward, Murray, Tavi, & Clark, Roger. 2007. Errors in Radar CMP Velocity Estimates Due to Survey Geometry, and Their Implication for Ice Water Content Estimation. *J. Environ. Eng. Geophys.*, **12**(1), 101–111.

Bentley, Jon Louis. 1975. Multidimensional Binary Search Trees Used for Associative Searching. *Communications of the ACM*, **18**(9), 509–517.

Bevington, Phillip R, & Robinson, D Keith. 2003. *Data Reduction and Error Analysis for the Physical Sciences*. 3 edn. McGraw Hill.

Birkel, Sean. 2018. *Greenland surface mass balance derived from climate reanalysis models, 1979-2017*.

Booth, Adam D., Clark, Roger, & Murray, Tavi. 2010. Semblance response to a ground-penetrating radar wavelet and resulting errors in velocity analysis. *Near Surf. Geophys.*, **8**(3), 235–246.

Bradford, John H, Nichols, Joshua, Mikesell, T. Dylan, & Harper, Joel T. 2009. Continuous profiles of electromagnetic wave velocity and water content in glaciers: an example from Bench Glacier, Alaska, USA. *Ann. Glaciol.*, **50**(51), 1–9.

Brown, Joel, Harper, Joel, Pfeffer, W. Tad, Humphrey, Neil, & Bradford, John. 2011. High-resolution study of layering within the percolation and soaked facies of the Greenland ice sheet. *Ann. Glaciol.*, **52**(59), 35–42.

Brown, Joel, Bradford, John, Harper, Joel, Pfeffer, W. Tad, Humphrey, Neil, & Mosley-Thompson, Ellen. 2012. Georadar-derived estimates of firn density in the percolation zone, western Greenland ice sheet. *J. Geophys. Res. Earth Surf.*, **117**(1), 1–15.

Brown, Joel, Harper, Joel, & Humphrey, Neil. 2017. Liquid water content in ice estimated through a full-depth ground radar profile and borehole measurements in western Greenland. *Cryosph.*, **11**(1), 669–679.

Broxton, Patrick D., Leeuwen, Willem J. D., & Biederman, Joel A. 2019. Improving Snow Water Equivalent Maps With Machine Learning of Snow Survey and Lidar Measurements. *Water Resources Research*, **55**(5), 3739–3757.

Bureau, U.S. Census. 2020. *Cartographic Boundary Files*.

Businger, Peter, & Golub, Gene H. 1965. Linear least squares solutions by householder transformations. *Numer. Math.*, **7**(3), 269–276.

Campbell, Bruce A., & Shepard, Michael K. 2003. Coherent and incoherent components in near-nadir radar scattering: Applications to radar sounding of Mars. *Journal of Geophysical Research E: Planets*, **108**(12), 1–8.

Cressie, Noel. 1985. Fitting variogram models by weighted least squares. *Journal of the International Association for Mathematical Geology*, **17**(5), 563–586.

Deems, Jeffrey S., Fassnacht, Steven R., & Elder, Kelly J. 2006. Fractal Distribution of Snow Depth from Lidar Data. *Journal of Hydrometeorology*, **7**(2), 285–297.

Deems, Jeffrey S., Painter, Thomas H., & Finnegan, David C. 2013. Lidar measurement of snow depth: A review. *Journal of Glaciology*, **59**(215), 467–479.

Dix, C. H. 1955. Seismic velocities from surface measurements. *Geophysics*, **20**(1), 68–86.

Dorn, Geoffrey A. 1998. Modern 3-D seismic interpretation. *Lead. Edge*, **17**(9), 1262–1262.

Drumheller, D.M., & Lew, Henry. 2002. Homodyned-K fluctuation model. *IEEE Transactions on Aerospace and Electronic Systems*, **38**(2), 527–542.

Efron, B., & Stein, C. 1981. The Jackknife Estimate of Variance. *Ann. Stat.*, **9**(3), 586–596.

Efron, B., & Tibshirani, R. 1986. Bootstrap Methods for Standard Errors, Confidence Intervals, and Other Measures of Statistical Accuracy. *Stat. Sci.*, **1**(1), 54–77.

Egli, L., Jonas, T., & Meister, R. 2009. Comparison of different automatic methods for estimating snow water equivalent. *Cold Regions Science and Technology*, **57**(2-3), 107–115.

Eisen, O., Nixdorf, U., Wilhelms, F., & Miller, H. 2002. Electromagnetic wave speed in polar ice: Validation of the common-midpoint technique with high-resolution dielectric-profiling and density measurements. *Ann. Glaciol.*, **34**, 150–156.

Elder, Kelly, Dozier, Jeff, & Michaelsen, Joel. 1991. Snow accumulation and distribution in an Alpine Watershed. *Water Resources Research*, **27**(7), 1541–1552.

Elder, Kelly, Rosenthal, Walter, & Davis, Robert E. 1998. Estimating the spatial distribution of snow water equivalence in a montane watershed. *Hydrological Processes*, **12**(10-11), 1793–1808.

Engman, Edwin T., & Wang, James R. 1987. Evaluating Roughness Models of Radar Backscatter. *IEEE Transactions on Geoscience and Remote Sensing*, **GE-25**(6), 709–713.

Essery, Richard, Morin, Samuel, Lejeune, Yves, & B Ménard, Cécile. 2013. A comparison of 1701 snow models using observations from an alpine site. *Advances in Water Resources*, **55**(may), 131–148.

Fassnacht, S R, Heun, C M, López-Moreno, J.I., & Latron, J. 2010. Snow Density Variability in the Rio Esera Valley , Pyrenees Mountains , 2 . Study Site. *Cuadernos de iIvestigación Geográfica*, **36**(1), 59–72.

Fausto, Robert S., Box, Jason E., Vandecrux, Baptiste, van As, Dirk, Steffen, Konrad, MacFerrin, Michael J., Machguth, Horst, Colgan, William, Koenig, Lora S., McGrath, Daniel, Charalampidis, Charalampos, & Braithwaite, Roger J. 2018. A Snow Density Dataset for Improving Surface Boundary Conditions in Greenland Ice Sheet Firn Modeling. *Front. Earth Sci.*, **6**(May), 1–10.

Fehmers, Gijs C., & Höcker, Christian F.W. 2003. Fast structural interpretation with structure-oriented filtering. *Geophysics*, **68**(4), 1286–1293.

Fettweis, Xavier, Box, Jason E., Agosta, Cécile, Amory, Charles, Kittel, Christoph, Lang, Charlotte, Van As, Dirk, Machguth, Horst, & Gallée, Hubert. 2017. Reconstructions of the 1900-2015 Greenland ice sheet surface mass balance using the regional climate MAR model. *Cryosphere*, **11**(2), 1015–1033.

Fornberg, Bengt. 1988. Generation of Finite Difference Formulas on Arbitrarily Spaced Grids. *Math. Comput.*, **51**(184), 699.

Geng, Zhicheng, Wu, Xinming, Shi, Yunzhi, & Fomel, Sergey. 2020. Deep learning for relative geologic time and seismic horizons. *Geophysics*, **85**(4), 1–47.

Graeter, K. A., Osterberg, E. C., Ferris, D. G., Hawley, R. L., Marshall, H. P., Lewis, G., Meehan, T., McCarthy, F., Overly, T., & Birkel, S. D. 2018. Ice Core Records of West Greenland Melt and Climate Forcing. *Geophys. Res. Lett.*, **45**(7), 3164–3172.

Green, C. H. 1938. Velocity Determinations by Means of Reflection Profiles. *Geophysics*, **3**(4), 295–305.

Griessinger, Nena, Mohr, Franziska, & Jonas, Tobias. 2018. Measuring snow ablation rates in alpine terrain with a mobile multioffset ground-penetrating radar system. *Hydrological Processes*, **32**(21), 3272–3282.

Grima, Cyril, Kofman, Wlodek, Herique, Alain, Orosei, Roberto, & Seu, Roberto. 2012. Quantitative analysis of Mars surface radar reflectivity at 20MHz. *Icarus*, **220**(1), 84–99.

Grima, Cyril, Schroeder, Dustin M., Blankenship, Donald D., & Young, Duncan A. 2014a. Planetary landing-zone reconnaissance using ice-penetrating radar data: Concept validation in Antarctica. *Planet. Space Sci.*, **103**, 191–204.

Grima, Cyril, Blankenship, Donald D., Young, Duncan A., & Schroeder, Dustin M. 2014b. Surface slope control on firn density at Thwaites Glacier, West Antarctica: Results from airborne radar sounding. *Geophys. Res. Lett.*, **41**(19), 6787–6794.

Grima, Cyril, Blankenship, Donald D., Young, Duncan A., & Schroeder, Dustin M. 2014c. Surface slope control on firn density at Thwaites Glacier, West Antarctica: Results from airborne radar sounding. *Geophysical Research Letters*.

Gulunay, Necati. 1986. FXDECON and complex wiener prediction filter. *Pages 279–281 of: SEG Tech. Progr. Expand. Abstr. 1986*. Society of Exploration Geophysicists.

Harper, J., Humphrey, N., Pfeffer, W. T., Brown, J., & Fettweis, X. 2012. Greenland ice-sheet contribution to sea-level rise buffered by meltwater storage in firn. *Nature*, **491**(7423), 240–243.

Hawley, Robert L., Courville, Zoe R., Kehrl, Laura M., Lutz, Eric R., Osterberg, Erich C., Overly, Thomas B., & Wong, Gifford J. 2014. Recent accumulation variability in northwest Greenland from ground-penetrating radar and shallow cores along the Greenland Inland Traverse. *J. Glaciol.*, **60**(220), 375–382.

Hedrick, Andrew R., Marks, Danny, Havens, Scott, Robertson, Mark, Johnson, Micah, Sandusky, Micah, Marshall, Hans-Peter, Kormos, Patrick R., Bormann, Kat J., & Painter, Thomas H. 2018. Direct Insertion of NASA Airborne Snow Observatory-Derived Snow Depth Time Series Into the iSnobal Energy Balance Snow Model. *Water Resources Research*, **54**(10), 8045–8063.

Herron, Michael M, & Langway, Chester C. 1980. Firn Densification: An Emperical Model. *J. Glaciol.*, **25**(93), 373–385.

Hiemstra, Christopher, Marshall, H.P., Vuyovich, Carrie, Elder, Kelly, Mason, Megan, & Durand, Michael. 2020. *SnowEx20 Community Snow Depth Probe Measurements, Version 1.*

Hiemstra, Christopher A., Vuyovich, Carrie. M., & Marshall, Hans-Peter. 2021. *SnowEx20 Grand Mesa Reference GIS Data Sets, Version 1.*

Hill, David, Burakowski, Elizabeth, Crumley, Ryan, Keon, Julia, Hu, J. Michelle, Arendt, Anthony, Wikstrom Jones, Katreen, & Wolken, Gabriel. 2019. Converting Snow Depth to Snow Water Equivalent Using Climatological Variables. *Converting Snow Depth to Snow Water Equivalent Using Climatological Variables*, 1–34.

Hojatimalekshah, Ahmad, Uhlmann, Zachary, Glenn, Nancy F., Hiemstra, Christopher A., Tennant, Christopher J., Graham, Jake D., Spaete, Lucas, Gelvin, Arthur, Marshall, Hans-Peter, McNamara, James P., & Enterkine, Josh. 2021. Tree canopy and snow depth relationships at fine scales with terrestrial laser scanning. *The Cryosphere*, **15**(5), 2187–2209.

Homer, Collin, Dewitz, Jon, Jin, Suming, Xian, George, Costello, Catherine, Danielson, Patrick, Gass, Leila, Funk, Michelle, Wickham, James, Stehman, Stephen, Auch, Roger, & Riitters, Kurt. 2020. Conterminous United States land cover change patterns 2001–2016 from the 2016 National Land Cover Database. *ISPRS Journal of Photogrammetry and Remote Sensing*, **162**(November 2019), 184–199.

Hu, Xiaojing, Hao, Xiaohua, Wang, Jian, Huang, Guanghui, Li, Hongyi, & Yang, Qian. 2021. Can the Depth of Seasonal Snow be Estimated From ICESat-2 Products: A Case Investigation in Altay, Northwest China. *IEEE Geoscience and Remote Sensing Letters*, 1–5.

Hubbard, Bryn, Tison, Jean-Louis, Philippe, Morgane, Heene, Billie, Pattyn, Frank, Malone, Terry, & Freitag, Johannes. 2013. Ice shelf density reconstructed from optical televiewer borehole logging. *Geophysical Research Letters*, **40**(22), 5882–5887.

Huss, M, Bookhagen, B, Huggel, C, Jacobsen, D, Bradley, R.S., Clague, J.J., Vuille, M, Buytaert, W., Cayan, D.R., Greenwood, G., Mark, B.G., Milner, A.M., Weingartner, R., & Winder, M. 2017. Toward mountains without permanent snow and ice. *Earth's Future*, **5**(5), 418–435.

Isaaks, Edward H., & Srivastava, R. Mohan. 1989. *Applied Geostatistics*. Oxford University Press.

Johnson, Jerome B., & Schneebeli, Martin. 1999. Characterizing the microstructural and micromechanical properties of snow. *Cold Regions Science and Technology*, **30**(1-3), 91–100.

Jonas, T., Marty, C., & Magnusson, J. 2009. Estimating the snow water equivalent from snow depth measurements in the Swiss Alps. *Journal of Hydrology*, **378**(1-2), 161–167.

Joughin, Ian, Smith, Ben E., & Howat, Ian M. 2018. A complete map of Greenland ice velocity derived from satellite data collected over 20 years. *J. Glaciol.*, **64**(243), 1–11.

Kahaner, David, Moler, Cleve, & Nash, Stephen. 1989. Numerical methods and software. *Englewood Cliffs Prentice Hall, 1989*.

Karimi, Parvaneh, & Fomel, Sergey. 2015. Stratigraphic coordinates: A coordinate system tailored to seismic interpretation. *Geophys. Prospect.*, **63**(5), 1246–1255.

Konrad, Hannes, Hogg, Anna E., Mulvaney, Robert, Arthern, Robert, Tuckwell, Rebecca J., Medley, Brooke, & Shepherd, Andrew. 2019. Observations of surface mass balance on Pine Island Glacier, West Antarctica, and the effect of strain history in fast-flowing sections. *J. Glaciol.*, jul, 1–10.

Koskinas, Aristotelis, Tegos, Aristoteles, Tsira, Penelope, Dimitriadis, Panayiotis, Iliopoulou, Theano, Papanicolaou, Panos, Koutsoyiannis, Demetris, & Williamson, Tracey. 2019. Insights into the Oroville Dam 2017 Spillway Incident. *Geosciences*, **9**(1), 37.

Lague, Dimitri, Brodu, Nicolas, & Leroux, Jérôme. 2013. Accurate 3D comparison of complex topography with terrestrial laser scanner: Application to the Rangitikei canyon (N-Z). *ISPRS Journal of Photogrammetry and Remote Sensing*, **82**(aug), 10–26.

Legarsky, J.J., Gogineni, S.P., & Akins, T.L. 2001. Focused synthetic aperture radar processing of ice-sounder data collected over the Greenland ice sheet. *IEEE Transactions on Geoscience and Remote Sensing*, **39**(10), 2109–2117.

Lemmetyinen, Juha, Schwank, Mike, Rautiainen, Kimmo, Kontu, Anna, Parkkinen, Tiina, Mätzler, Christian, Wiesmann, Andreas, Wegmüller, Urs, Derksen, Chris, Toose, Peter, Roy, Alexandre, & Pulliainen, Jouni. 2016. Snow density and ground permittivity retrieved from L-band radiometry: Application to experimental data. *Remote Sensing of Environment*, **180**(jul), 377–391.

Lenaerts, Jan T.M., Medley, Brooke, van den Broeke, Michiel R., & Wouters, Bert. 2019. Observing and Modeling Ice Sheet Surface Mass Balance. *Rev. Geophys.*

Lettenmaier, Dennis P, Alsdorf, Doug, Dozier, Jeff, Huffman, George J, Pan, Ming, & Wood, Eric F. 2015. Inroads of remote sensing into hydrologic science during the WRR era. *Water Resources Research*, **51**(9), 7309–7342.

Lewis, Gabriel, Osterberg, Erich, Hawley, Robert, Marshall, Hans Peter, Meehan, Tate, Graeter, Karina, McCarthy, Forrest, Overly, Thomas, Thundercloud, Zayta, & Ferris, David. 2019. Recent precipitation decrease across the western Greenland ice sheet percolation zone. *Cryosph.*, **13**(11), 2797–2815.

Li, Dongyue, Wrzesien, Melissa L., Durand, Michael, Adam, Jennifer, & Lettenmaier, Dennis P. 2017. How much runoff originates as snow in the western United States, and how will that change in the future? *Geophysical Research Letters*, **44**(12), 6163–6172.

Lievens, Hans, Demuzere, Matthias, Marshall, Hans-Peter, Reichle, Rolf H., Brucker, Ludovic, Brangers, Isis, de Rosnay, Patricia, Dumont, Marie, Girotto, Manuela, Immerzeel, Walter W., Jonas, Tobias, Kim, Edward J., Koch, Inka, Marty, Christoph, Saloranta, Tuomo, Schöber, Johannes, & De Lannoy, Gabrielle J. M. 2019. Snow depth variability in the Northern Hemisphere mountains observed from space. *Nature Communications*, **10**(1), 4629.

Lievens, Hans, Brangers, Isis, Marshall, Hans-Peter, Jonas, Tobias, Olefs, Marc, & De Lannoy, Gabriëlle. 2022. Sentinel-1 snow depth retrieval at sub-kilometer resolution over the European Alps. *The Cryosphere*, **16**(1), 159–177.

Loewe, F. 1970. Screen Temperatures and 10m Temperatures. *J. Glaciol.*, **9**(56), 263–268.

Looyenga, H. 1965. Dielectric constants of heterogeneous mixtures. *Physica*, **31**(3), 401–406.

López-Moreno, J. I., Fassnacht, S. R., Heath, J. T., Musselman, K. N., Revuelto, J., Latron, J., Morán-Tejeda, E., & Jonas, T. 2013. Small scale spatial variability of snow density and depth over complex alpine terrain: Implications for estimating snow water equivalent. *Advances in Water Resources*, **55**, 40–52.

Lukas, Vicki, & Baez, Vanessa. 2021. 3D Elevation Program—Federal best practices: U.S. Geological Survey Fact Sheet 2020–3062.

Lutz, Eric, Birkeland, Karl, & Marshall, Hans Peter. 2009. Quantifying changes in weak layer microstructure associated with artificial load changes. *Cold Regions Science and Technology*, **59**(2-3), 202–209.

Lv, Zhibang, & Pomeroy, John W. 2020. Assimilating snow observations to snow interception process simulations. *Hydrological Processes*, **34**(10), 2229–2246.

Margrave, Gary F., & Lamoureux, Michael P. 2019. *Numerical Methods of Exploration Seismology*. Cambridge University Press.

Marine Corps, United States. 1988. Commander's Guide to Cold Weather Operations. *Fleet Marine Force Reference Publication*, **7**(24), 252.

Marks, Danny, Dozier, Jeff, & Davis, Robert E. 1992. Climate and energy exchange at the snow surface in the Alpine Region of the Sierra Nevada: 1. Meteorological measurements and monitoring. *Water Resources Research*, **28**(11), 3029–3042.

Marshall, Hans-Peter. 2005. *Snowpack spatial variability: Towards understanding its effect on remote sensing measurements and snow slope stability.* Ph.D. thesis, University of Colorado.

Marshall, Hans-Peter, & Johnson, Jerome B. 2009. Accurate inversion of high-resolution snow penetrometer signals for microstructural and micromechanical properties. *Journal of Geophysical Research*, **114**(F4), F04016.

Marshall, Hans Peter, Koh, Gary, Sturm, Matthew, Johnson, J. B., Demuth, Mike, Landry, Chris, Deems, Jeffrey S., & Gleason, J. A. 2006. Spatial variability of the snowpack: Experiences with measurements at a wide range of length scales with several different high precision instruments. *Proceedings ISSW 2006. International Snow Science Workshop, Telluride CO, U.S.A., 1-6 October 2006*, 359–364.

Marshall, H.P., Vuyovich, Carrie, Hiemstra, Chris, Brucker, Ludo, Elder, Kelly, Deems, Jeff, Newlin, Jerry, Bales, Roger, Nolin, Anne, & Trujillo, Ernesto. 2019. NASA SnowEx 2020 Experiment Plan. 1–100.

Masson-Delmotte, Valérie, Zhai, Panmao, Anna, Pirani, Connors, Sarah, Péan, Clotilde, Berger, Sophie, Caud, Nada, Chen, Yang, Goldfarb, Leah, Gomis, Melissa Ines, Huang, Mengtian, Leitzell, Katherine, Lonnoy, Elisabeth, Matthews, Robin, Maycock, Thomas, Waterfield, Tim, Yelekçi, Ozge, Yu, Rong, & Zhou, Baiquan (eds). 2021. *IPCC, 2021: Climate Change 2021: The Physical Science Basis.*

Matheron, Georges. 1963. Principles of geostatistics. *Econ. Geol.*, **58**(8), 1246–1266.

Matzler, C. 1996. Microwave permittivity of dry snow. *IEEE Transactions on Geoscience and Remote Sensing*, **34**(2), 573–581.

McCabe, Gregory J., Clark, Martyn P., & Hay, Lauren E. 2007. Rain-on-Snow Events in the Western United States. *Bulletin of the American Meteorological Society*, **88**(3), 319–328.

McCreight, J. L., & Small, E. E. 2014. Modeling bulk density and snow water equivalent using daily snow depth observations. *Cryosphere*, **8**(2), 521–536.

McGrath, Daniel, Webb, Ryan, Shean, David, Bonnell, Randall, Marshall, Hans Peter, Painter, Thomas H., Molotch, Noah P., Elder, Kelly, Hiemstra, Christopher, & Brucker, Ludovic. 2019. Spatially Extensive Ground-Penetrating Radar Snow Depth Observations During NASA's 2017 SnowEx Campaign: Comparison With In Situ, Airborne, and Satellite Observations. *Water Resources Research*, **55**(11), 10026–10036.

McNeil, Chris, Florentine, Caitlyn, Bright, V.A.L., Fahey, M.J., McCann, E., Larsen, C.F., Thoms, E.E., Shean, D.E., McKeon, L.A., March, R.S., Keller, W., Whorton, E.N., O'Neel, Shad, Baker, Emily H., Sass, Louis, & Bollen, K.E. 2019. *Geodetic Data for USGS Benchmark Glaciers: Orthophotos, Digital Elevation Models, Glacier Boundaries and Surveyed Positions (ver 2.0, February 2022).*

Meehan, Tate G. 2021a. *SnowEx20 Grand Mesa IOP BSU 1 GHz Multi-polarization GPR CMP Snow Water Equivalent, Version 1.*

Meehan, Tate G. 2021b. *SnowEx20 Grand Mesa IOP BSU 1 GHz Multi-polarization GPR, Version 1.*

Meehan, Tate G., Marshall, H. P., Bradford, John H., Hawley, Robert L., Overly, Thomas B., Lewis, Gabriel, Graeter, Karina, Osterberg, Erich, & McCarthy, Forrest. 2021. Reconstruction of historical surface mass balance, 1984–2017 from GreenTrACS multi-offset ground-penetrating radar. *Journal of Glaciology*, **67**(262), 219–228.

Meyer, Colin R., Keegan, Kaitlin M., Baker, Ian, & Hawley, Robert L. 2020. A model for French-press experiments of dry snow compaction. *Cryosph.*, **14**(5), 1449–1458.

Miège, Clément, Forster, Richard R., Box, Jason E., Burgess, Evan W., Mcconnell, Joseph R., Pasteris, Daniel R., & Spikes, Vandy B. 2013. Southeast Greenland high accumulation rates derived from firn cores and ground-penetrating radar. *Ann. Glaciol.*, **54**(63), 322–332.

Miller, Jeffrey E. 1984. Basic Concepts of Kinematic-Wave Models. *Geological Survey Professional Paper (United States)*.

Montgomery, Lynn, Koenig, Lora, & Alexander, Patrick. 2018. The SUMup dataset: Compiled measurements of surface mass balance components over ice sheets and sea ice with analysis over Greenland. *Earth Syst. Sci. Data*, **10**(4), 1959–1985.

Morlighem, M. 2017. *IceBridge BedMachine Greenland, Version 3*.

Mote, Philip W., Li, Sihan, Lettenmaier, Dennis P., Xiao, Mu, & Engel, Ruth. 2018. Dramatic declines in snowpack in the western US. *npj Climate and Atmospheric Science*, **1**(1).

National Academies of Sciences Engineering and Medicine. 2018. *Thriving on Our Changing Planet: A Decadal Strategy for Earth Observation from Space*. Washington, D.C.: National Academies Press.

Navarro, Francisco, & Eisen, Olaf. 2009. Ground-penetrating radar in glaciological applications. *Chap. 11, pages 195–229 of:* Pellikka, Petri, & Rees, Gareth W. (eds), *Remote Sens. Glaciers*.

Neidell, N. S., & Taner, M. Turhan. 1971. Semblance and Other Coherency Measrues for Multichannel Data. *Geophysics*, **36**(3), 482–497.

Nelder, J. A., & Mead, R. 1965. A Simplex Method for Function Minimization. *The Computer Journal*, **7**(4), 308–313.

Ng, Felix, & King, Edward C. 2011. Kinematic waves in polar firn stratigraphy. *J. Glaciol.*, **57**(206), 1119–1134.

Nghiem, S. V., Hall, D. K., Mote, T. L., Tedesco, M., Albert, M. R., Keegan, K., Shuman, C. A., DiGirolamo, N. E., & Neumann, G. 2012. The extreme melt across the Greenland ice sheet in 2012. *Geophys. Res. Lett.*, **39**(20), 6–11.

NOAA. 2021. *VDatum 4.3 Vertical Datum Transformation*.

Noël, Brice, Jan Van De Berg, Willem, MacHguth, Horst, Lhermitte, Stef, Howat, Ian, Fettweis, Xavier, & Van Den Broeke, Michiel R. 2016. A daily, 1 km resolution data set of downscaled Greenland ice sheet surface mass balance (1958-2015). *Cryosphere*, **10**(5), 2361–2377.

Overly, Thomas B., Hawley, Robert L., Helm, Veit, Morris, Elizabeth M., & Chaudhary, Rohan N. 2016. Greenland annual accumulation along the EGIG line, 1959-2004, from ASIRAS airborne radar and neutron-probe density measurements. *Cryosphere*, **10**(4), 1679–1694.

Paden, John D., Li, Jilu, Leuschen, Carlton J., Rodriguez-Morales, Fernando, & Hale, Richard D. 2014. *IceBridge Snow Radar L1B Geolocated Radar Echo Strength Profiles, Version 2.*

Painter, Thomas H., & Bormann, Kathryn J. 2020. *ASO L4 Lidar Point Cloud Digital Terrain Model 3m UTM Grid, Version 1.*

Painter, Thomas H., Berisford, Daniel F., Boardman, Joseph W., Bormann, Kathryn J., Deems, Jeffrey S., Gehrke, Frank, Hedrick, Andrew, Joyce, Michael, Laidlaw, Ross, Marks, Danny, Mattmann, Chris, McGurk, Bruce, Ramirez, Paul, Richardson, Megan, Skiles, S. Mc Kenzie, Seidel, Felix C., & Winstral, Adam. 2016. The Airborne Snow Observatory: Fusion of scanning lidar, imaging spectrometer, and physically-based modeling for mapping snow water equivalent and snow albedo. *Remote Sensing of Environment*, **184**(June), 139–152.

Panzer, Ben, Gomez-Garcia, Daniel, Leuschen, Carl, Paden, John, Rodriguez-Morales, Fernando, Patel, Aqsa, Markus, Thorsten, Holt, Benjamin, & Gogineni, Prasad. 2013. An ultra-wideband, microwave radar for measuring snow thickness on sea ice and mapping near-surface internal layers in polar firn. *J. Glaciol.*, **59**(214), 244–254.

Pearson, Karl. 1907. *On further methods of determining correlation.* Vol. 16. Dulau and Company.

Pielmeier, Christine. 2003 (nov). *Textural and mechanical variability of mountain snowpacks*. Ph.D. thesis.

Pielmeier, Christine, & Marshall, Hans-Peter. 2009. Rutschblock-scale snowpack stability derived from multiple quality-controlled SnowMicroPen measurements. *Cold Regions Science and Technology*, **59**(2-3), 178–184.

Pierce, David W., Barnett, Tim P., Hidalgo, Hugo G., Das, Tapash, Bonfils, Céline, Santer, Benjamin D., Bala, Govindasamy, Dettinger, Michael D., Cayan, Daniel R., Mirin, Art, Wood, Andrew W., & Nozawa, Toru. 2008. Attribution of declining Western U.S. Snowpack to human effects. *Journal of Climate*, **21**(23), 6425–6444.

Porter, Claire, Morin, Paul, Howat, Ian, Noh, Myoung-Jon, Bates, Brian, Peterman, Kenneth, Keesey, Scott, Schlenk, Matthew, Gardiner, Judith, Tomko, Karen, Willis, Michael, Kelleher, Cole, Cloutier, Michael, Husby, Eric, Foga, Steven, Nakamura, Hitomi, Platson, Melisa, Wethington, Michael, Jr., Williamson, Cathleen, Bauer, Gregory, Enos, Jeremy, Arnold, Galen, Kramer, William, Becker, Peter, Doshi, Abhijit, D'Souza, Cristelle, Cummens, Pat, Laurier, Fabien, & Bojesen, Mikkel. 2018. *ArcticDEM*.

Raleigh, Mark S., & Small, Eric E. 2017. Snowpack density modeling is the primary source of uncertainty when mapping basin-wide SWE with lidar. *Geophysical Research Letters*, **44**(8), 3700–3709.

Reeh, Niels. 2008. A nonsteady-state firn-densification model for the percolation zone of a glacier. *J. Geophys. Res. Earth Surf.*, **113**(3), 1–13.

Rodriguez-Morales, Fernando, Gogineni, Sivaprasad, Leuschen, Carlton J., Paden, John D., Li, Jilu, Lewis, Cameron C., Panzer, Benjamin, Gomez-Garcia Alvestegui, Daniel, Patel, Aqsa, Byers, Kyle, Crowe, Reid, Player, Kevin, Hale, Richard D., Arnold, Emily J., Smith, Logan, Gifford, Christopher M., Braaten, David, & Panton, Christian. 2014. Advanced multifrequency radar instrumentation for polar Research. *IEEE Trans. Geosci. Remote Sens.*, **52**(5), 2824–2842.

Rouse Jr., John W., Hass, Robert H., Schell, John A., & Deering, Donald W. 1974. Monitoring vegetation systems in the Great Plains with ERTS. *In: Third Earth Resources Technology Satellite-1 Symposium*. NASA Goddard Space Flight Center.

Rovansek, R J, Kane, D L, & Hinzman, L D. 1993. *Improving estimates of snowpack water equivalent using double sampling.*

Rupper, Summer, Christensen, William F., Bickmore, Barry R., Burgener, Landon, Koenig, Lora S., Koutnik, Michelle R., Miège, Clément, & Forster, Richard R. 2015. The effects of dating uncertainties on net accumulation estimates from firn cores. *J. Glaciol.*, **61**(225), 163–172.

Schneebeli, Martin, & Johnson, Jerome B. 1998. A constant-speed penetrometer for high-resolution snow stratigraphy. *Annals of Glaciology*, **26**(jan), 107–111.

Schneebeli, Martin, Pielmeier, Christine, & Johnson, Jerome B. 1999. Measuring snow microstructure and hardness using a high resolution penetrometer. *Cold Regions Science and Technology*, **30**(1-3), 101–114.

Schwank, Mike, Matzler, Christian, Wiesmann, Andreas, Wegmuller, Urs, Pulliainen, Jouni, Lemmetyinen, Juha, Rautiainen, Kimmo, Derksen, Chris, Toose, Peter, & Drusch, Matthias. 2015. Snow Density and Ground Permittivity Retrieved from L-Band Radiometry: A Synthetic Analysis. *IEEE Journal of Selected Topics in Applied Earth Observations and Remote Sensing*, **8**(8), 3833–3845.

Selle, Andrew, Fedkiw, Ronald, Kim, Byungmoon, Liu, Yingjie, & Rossignac, Jarek. 2008. An unconditionally stable MacCormack method. *Journal of Scientific Computing*, **35**(2-3), 350–371.

Shapiro, Lewis H, Johnson, Jerome B, Sturm, Matthew, & Blaisdell, George L. 1997. Snow Mechanics Review of the State of Knowledge and Applications. *CRREL Technical Report*, **97**(3).

Shepherd, Andrew, Ivins, Erik, Rignot, Eric, Smith, Ben, van den Broeke, Michiel, Velicogna, Isabella, Whitehouse, Pippa, Briggs, Kate, Joughin, Ian, Krinner, Gerhard, Nowicki, Sophie, Payne, Tony, Scambos, Ted, Schlegel, Nicole, A, Geruo, Agosta, Cécile, Ahlstrøm, Andreas, Babonis, Greg, Barletta, Valentina R, Bjørk, Anders A, Blazquez, Alejandro, Bonin, Jennifer, Colgan, William, Csatho, Beata, Cullather, Richard, Engdahl, Marcus E, Felikson, Denis, Fettweis, Xavier, Forsberg, Rene, Hogg, Anna E, Gallee, Hubert, Gardner, Alex, Gilbert, Lin, Gourmelen, Noel, Groh, Andreas, Gunter, Brian, Hanna, Edward, Harig, Christopher, Helm, Veit, Horvath, Alexander, Horwath, Martin, Khan, Shfaqat, Kjeldsen, Kristian K, Konrad, Hannes, Langen, Peter L, Lecavalier, Benoit, Loomis, Bryant, Luthcke, Scott, McMillan, Malcolm, Melini, Daniele, Mernild, Sebastian, Mohajerani, Yara, Moore, Philip, Mottram, Ruth, Mouginot, Jeremie, Moyano, Gorka, Muir, Alan, Nagler, Thomas, Nield, Grace, Nilsson, Johan, Noël, Brice, Otosaka, Ines, Pattle, Mark E, Peltier, W Richard, Pie, Nadège, Rietbroek, Roelof, Rott, Helmut, Sandberg Sørensen, Louise, Sasgen, Ingo, Save, Himanshu, Scheuchl, Bernd, Schrama, Ernst, Schröder, Ludwig, Seo, Ki-Weon, Simonsen, Sebastian B, Slater, Thomas, Spada, Giorgio, Sutterley, Tyler, Talpe, Matthieu, Tarasov, Lev, van de Berg, Willem Jan, van der Wal, Wouter, van Wessem, Melchior, Vishwakarma, Bramha Dutt, Wiese, David, Wilton, David, Wagner, Thomas, Wouters, Bert, Wuite, Jan, & Team, The IMBIE. 2020. Mass balance of the Greenland Ice Sheet from 1992 to 2018. *Nature*, **579**(7798), 233–239.

Shoop, Sally A, Knuth, Margaret A, & Wieder, Wendy L. 2014. Vehicle Impact Testing of Snow Roads at McMurdo Station , Antarctica Cold Regions Research and Engineering Laboratory. *ERDC/CRREL Technical Report*, **9**(June).

Shoop, Sally A, Uberuaga, Julia, Wieder, Wendy L, & Melendy, Terry D. 2016. Snow-Road Construction and Maintenance Cold Regions Research and Engineering Laboratory. *ERDC/CRREL Technical Report*, **16**(December).

Siirila-Woodburn, Erica R., Rhoades, Alan M., Hatchett, Benjamin J., Huning, Laurie S., Szinai, Julia, Tague, Christina, Nico, Peter S., Feldman, Daniel R., Jones, Andrew D., Collins, William D., & Kaatz, Laurna. 2021. A low-to-no snow future and its impacts on water resources in the western United States. *Nature Reviews Earth and Environment*, **2**(11), 800–819.

Spikes, Vandy B., Hamilton, Gordon S., Arcone, Steven A., Kaspari, Susan, & Mayewski, Paul A. 2004. Variability in accumulation rates from GPR profiling on the West Antarctic plateau. *Ann. Glaciol.*, **39**, 238–244.

Štroner, Martin, Urban, Rudolf, Lidmila, Martin, Kolář, Vilém, & Křemen, Tomáš. 2021. Vegetation Filtering of a Steep Rugged Terrain: The Performance of Standard Algorithms and a Newly Proposed Workflow on an Example of a Railway Ledge. *Remote Sensing*, **13**(15), 3050.

Sturm, Matthew, & Holmgren, Jon. 1998. Differences in compaction behavior of three climate classes of snow. *Annals of Glaciology*, **26**(jan), 125–130.

Sturm, Matthew, Taras, Brian, Liston, Glen E., Derksen, Chris, Jonas, Tobias, & Lea, Jon. 2010. Estimating snow water equivalent using snow depth data and climate classes. *Journal of Hydrometeorology*, **11**(6), 1380–1394.

Taner, M. Turhan, & Koehler, Fulton. 1969. Velocity Sprectra-Digital Computer Derivation Applications of Velocity Functions. *Geophysics*, **34**(6), 859–881.

Tedesco, Marco, Reichle, Rolf, Low, Alexander, Markus, Thorsten, & Foster, James L. 2010. Dynamic Approaches for Snow Depth Retrieval From Spaceborne Microwave Brightness Temperature. *IEEE Transactions on Geoscience and Remote Sensing*, **48**(4), 1955–1967.

Treitel, Sven. 1974. THE COMPLEX WIENER FILTER. *GEOPHYSICS*, **39**(2), 169–173.

Trujillo, Ernesto, Ramírez, Jorge A., & Elder, Kelly J. 2009. Scaling properties and spatial organization of snow depth fields in sub-alpine forest and alpine tundra. *Hydrological Processes*, **23**(11), 1575–1590.

Ulaby, Fawwaz T, Moore, Richard K, & Fung, Adrian K. 1982. *Microwave Remote Sensing: Active and Passive, Volume II: Radar Remote Sensing and Surface Scattering and Emission Theory*. Reading, Massachusetts: Addison-Wesley.

Ulaby, Fawwaz T, Fung, Adrian K, & Moore, Richard K. 1986. *Microwave remote sensing: active and passive*. From Theory to Applications, vol. 3. Artech House.

University of Utah, National Weather Service Forecast Office in Salt Lake City. 2022. *Utah MesoWest Weather Data from the University of Utah and the National Weather Service Forecast Office in Salt Lake City*.

van Kampenhout, Leonardus, Lenaerts, Jan T. M., Lipscomb, William H., Sacks, William J., Lawrence, David M., Slater, Andrew G., & van den Broeke, Michiel R. 2017. Improving the Representation of Polar Snow and Firn in the Community Earth System Model. *J. Adv. Model. Earth Syst.*, **9**(7), 2583–2600.

Vandecrux, B., Fausto, R. S., Langen, P. L., van As, D., MacFerrin, M., Colgan, W. T., Ingeman-Nielsen, T., Steffen, K., Jensen, N. S., Møller, M. T., & Box, J. E. 2018. Drivers of Firn Density on the Greenland Ice Sheet Revealed by Weather Station Observations and Modeling. *J. Geophys. Res. Earth Surf.*, **123**(10), 2563–2576.

Vaughan, David G, Corr, Hugh F J, Doake, Christopher S M, & Waddington, Ed D. 1999. Distortion of isochronous layers in ice revealed by ground-penetrating radar. *Nature*, **398**(6725), 323–326.

Vuyovich, C. M., Marshall, H.P., Elder, K., Hiemstra, C., Brucker, L., & McCormick, M. 2021. *SnowEx20 Grand Mesa Intensive Observation Period Snow Pit Measurements, Version 1.*

Webb, R. W., Raleigh, M. S., McGrath, D., Molotch, N. P., Elder, K., Hiemstra, C., Brucker, L., & Marshall, H. P. 2020. Within-Stand Boundary Effects on Snow Water Equivalent Distribution in Forested Areas. *Water Resources Research*, **56**(10).

Webb, Ryan W., Marziliano, Adrian, McGrath, Daniel, Bonnell, Randall, Meehan, Tate G., Vuyovich, Carrie, & Marshall, Hans-Peter. 2021. In Situ Determination of Dry and Wet Snow Permittivity: Improving Equations for Low Frequency Radar Applications. *Remote Sensing*, **13**(22), 4617.

Wetlaufer, Karl, Hendrikx, Jordy, & Marshall, Lucy. 2016. Spatial heterogeneity of snow density and its influence on snow water equivalence estimates in a large mountainous basin. *Hydrology*, **3**(1).

Wharton, Russell P, Hazen, Gary A, Rau, Rama N, & Best, David L. 1980. Advancements In Electromagnetic Propagation Logging. *In: SPE Rocky Mt. Reg. Meet.*Society of Petroleum Engineers, for Society of Petroleum Engineers.

Wheeler, Harry E. 1958. Time-Stratigraphy. *Am. Assoc. Pet. Geol. Bull.*, **42**(5), 1047–1063.

Wieder, Wendy, Shoop, Sally, & Barna, Lynette. 2019 (may). *Using the light weight deflectometer to assess groomed snow and ice surfaces.* Tech. rept. Draft.

Winstral, Adam, Elder, Kelly, & Davis, Robert E. 2002. Spatial Snow Modeling of Wind-Redistributed Snow Using Terrain-Based Parameters. *Journal of Hydrometeorology*, **3**(5), 524–538.

Wong, Joe, Han, Leija, Bancroft, John C, & Stewart, Robert R. 2009. Automatic time-picking of first arrivals on noisy microseismic data. *CREWS*, 1–6.

Wu, Xinming, Geng, Zhicheng, Shi, Yunzhi, Pham, Nam, Fomel, Sergey, & Caumon, Guillaume. 2020. Building realistic structure models to train convolutional neural networks for seismic structural interpretation. *GEOPHYSICS*, **85**(4), WA27–WA39.

Yan, Jie Bang, Gomez-Garcia Alvestegui, Daniel, McDaniel, Jay W., Li, Yan, Gogineni, Sivaprasad, Rodriguez-Morales, Fernando, Brozena, John, & Leuschen, Carlton J. 2017. Ultrawideband FMCW radar for airborne measurements of snow over sea ice and land. *IEEE Transactions on Geoscience and Remote Sensing*, **55**(2), 834–843.

Yildiz, Semih, Akyurek, Zuhal, & Binley, Andrew. 2021. Quantifying snow water equivalent using terrestrial ground penetrating radar and unmanned aerial vehicle photogrammetry. *Hydrological Processes*, **35**(5), 1–15.

Yilmaz, Öz. 2001. *Seismic Data Analysis*. Society of Exploration Geophysicists.

Zhu, Yong, & Newell, Reginald E. 1994. Atmospheric rivers and bombs. *Geophysical Research Letters*, **21**(18), 1999–2002.

Zwally, H. Jay, & Li, Jun. 2002. Seasonal and interannual variations of firn densification and ice-sheet surface elevation at the Greenland summit. *J. Glaciol.*, **48**(161), 199–207.

APPENDIX A:

RECONSTRUCTION OF HISTORICAL SURFACE MASS BALANCE 1984 – 2017 FROM GREENTRACS MULTI-OFFSET GROUND-PENETRATING RADAR

We introduced the methodological concepts of our radar measured and modeled approach for reconstructing historical SMB in Section 2.3. Within Appendix A, we provide the core computations used and give more insight into the methods of velocity analysis, parameter estimation, imaging, and interpretation. The flow diagram (Fig. A.1) works through the MxHL process to show not only the radar processing steps, but also the interconnectivity between the radar measured information and the HL firn model.

We introduce our methods for interpreting the radar imagery (Appendix A.1) and conducting horizon velocity analysis (Appendix A.2). We use the radar wave velocity information for snow parameter estimation (see sections A.3 and A.4), and use these results to parameterize the MxHL model in Section A.5. We then extend the capabilities of the firn age and density models to enable our structure-oriented filter (see section A.6) and refine our estimate of SMB using relative age model updates in the stratigraphic age domain (Wheeler, 1958) and absolute age model updates in the depth domain (see section A.7).

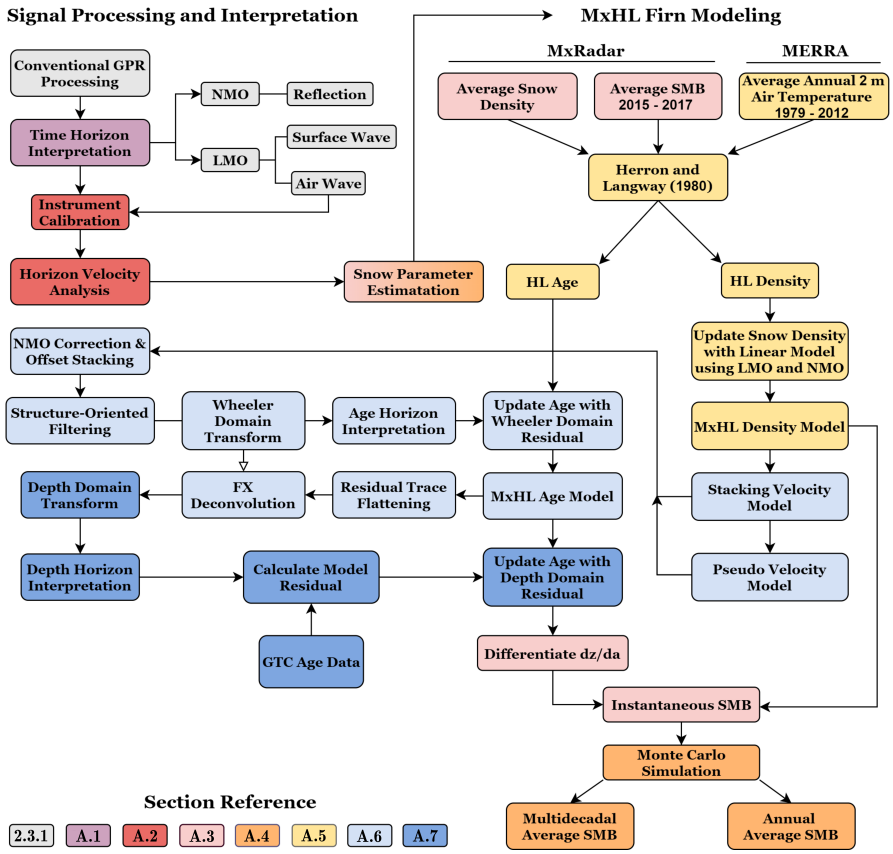

Figure A.1: The workflow for our measured-modeled historical SMB reconstruction. Colors correspond to the section reference where the concept is detailed. For example, the gradient colors of *Snow Parameter Estimation* indicate that concept spans sections A.3 and A.4.

A.1 Travel-time Horizon Interpretation

We developed a phase and amplitude tracking, semi-automatic picking algorithm to measure the travel-times of radar wavefield events. The picker is semi-automatic in that an initial pick on the horizon seeds the automatic tracking. Similar to picking algorithms described by Dorn (1998), our seeded picker transforms a window of the radargram surrounding the horizon of interest into radial distance and dip angle coordinates (r, θ) and stacks the windowed image along the θ direction. The algorithm determines the optimal direction by maximizing stacked amplitude. The subsequent

automatic pick is predicted along the linear path of maximum stack 5 traces ahead – which is the approximate length of the radar array. Then the windowed polar transformation and prediction is repeated automatically. Travel-time picks between predictions are interpolated using a distance-weighted scheme. The program has the capability to toggle manual selection or re-seed the pick if the algorithm goes awry. We picked the direct air wave, the direct surface wave, and the reflected wave from the fall 2014 layer on each of the nine radargrams for velocity analysis. These early-time events exhibit low noise with a travel-time standard deviation of 0.2 ns (1 sample). Using this layer picker, we also picked five age-horizons (see section A.6) and 16 depth-horizons (see section A.7) to update the age model for SMB calculation.

A.2 Horizon Velocity Analysis

Direct (air-coupled and surface-coupled) wave arrival times are approximated the linear travel-time equation known as linear moveout (LMO)

$$t = t_0 + \frac{x}{V_{LMO}} \quad , \tag{A.1}$$

where t is the measured one-way travel time and x is the antenna offset, with intercept time (t_0) and velocity (V_{LMO}) representing unknown parameters. Reflected radar waves exhibit non-linear travel-times as a function of offset that are approximated by NMO. The $x^2 - t^2$ method (Green, 1938) linearizes the NMO equation

$$t^2 = t_0^2 + \frac{x^2}{V_{NMO}^2} \quad . \tag{A.2}$$

where t is now the measured two-way travel time and V_{NMO} is the NMO velocity or *stacking velocity*.

Prior to velocity analysis of the surface wave and reflection, we calibrated the timing of each radar channel. Channel consistent travel-time overheads are caused within the Sensors & Software multi-channel adapter by variations in the path lengths of the circuitry and cables. During the instrument calibration process we apply corrections (on the order of nanoseconds) to the time sampling of each channel by picking the air-wave arrival times (Fig. 2.4) and solving Eq. (A.1) for the set of perturbations that let $t_0 = 0$ and $V_{LMO} = 0.2998\ m/ns$, the velocity of EM waves in free-space.

We applied linear regression for near-surface velocity analyses using the picked, one-way travel-times of direct wave arrivals traveling laterally through the shallow snow and the two-way travel-times of reflected arrivals from the fall 2014 horizon. To cast each system of equations into a matrix-vector product, the velocity parameter is linearized by its reciprocal, called slowness, as $S = \frac{1}{V}$. The linear system of equations has the form $\mathrm{G}\mathbf{m} = \mathbf{d}$ for the vector $\mathbf{d}$ containing the recorded travel-times for the respective moveout events. Equations (A.3) and (A.4) are the monomial basis functions used for linear regression of LMO and NMO events. Equations (A.5) and (A.6) are the model parameters and equations (A.7) and (A.8) are the respective data. The least squares solution for $\mathbf{m} = \mathrm{G}^{-1}\mathbf{d}$ is optionally solved in either L_2 or L_1 norm. We used the L_2 solution which was estimated by QR factorization (Businger & Golub, 1965). Advantages and convergence criteria of the L_1 solution are discussed in Aster *et al.* (2019).

$$\mathrm{G_{LMO}} = \begin{bmatrix} 1 & x_1 \\ \vdots & \vdots \\ 1 & x_m \end{bmatrix} \quad \text{(A.3)} \qquad \mathbf{m}_{\mathrm{LMO}} = \begin{bmatrix} t_0 \\ \\ S_{LMO} \end{bmatrix} \quad \text{(A.5)} \qquad \mathbf{d}_{\mathrm{LMO}} = \begin{bmatrix} t_1 \\ \vdots \\ t_m \end{bmatrix} \quad \text{(A.7)}$$

$$\mathrm{G_{NMO}} = \begin{bmatrix} 1 & x_1^2 \\ \vdots & \vdots \\ 1 & x_m^2 \end{bmatrix} \quad \text{(A.4)} \qquad \mathbf{m}_{\mathrm{NMO}} = \begin{bmatrix} t_0^2 \\ \\ S_{NMO}^2 \end{bmatrix} \quad \text{(A.6)} \qquad \mathbf{d}_{\mathrm{NMO}} = \begin{bmatrix} t_1^2 \\ \vdots \\ t_m^2 \end{bmatrix} \quad \text{(A.8)}$$

A.2.1 Critically Refracted Waves

A snowpack model with a critically refracted raypath is sketched in Fig. A.2. The following exercise calculates the travel-time of the wave following the hypothesized path.

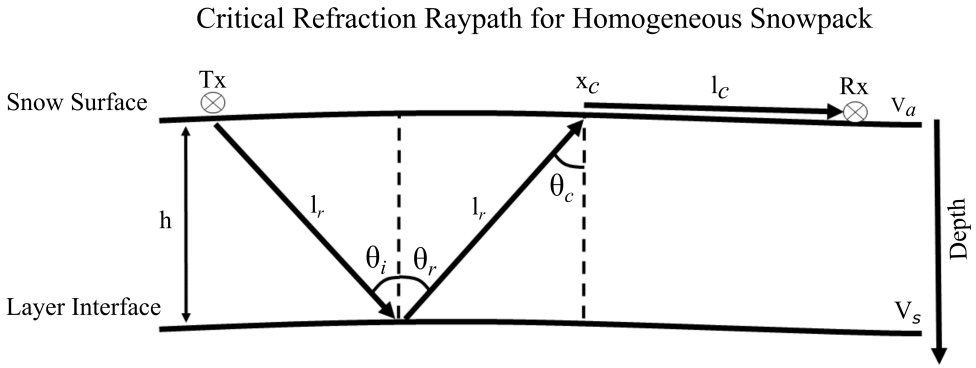

Figure A.2: The raypath of a critically refracted wave traveling through a homogeneous snowpack. The wave is reflected at a layer boundary in the firn and is refracted upon exiting the snow surface.

The snowpack is homogeneous with a thickness (h) and EM velocity (V_s). A half-space of air (V_a) is modeled above the snow surface. The transmitter and receiver antennas are on the snow surface and are separated by some offset (x). In a homogeneous medium at a reflecting interface, the reflection angle (θ_r) is equal to the

incidence angle (θ_i). Except for the case of total reflection, incoming radiation is also refracted (transmitted) at the layer interface. When a wave is traveling from a slower medium to a faster medium, according to Snell's Law

$$\frac{\sin\theta_1}{\sin\theta_2} = \frac{V_1}{V_2} \quad , \tag{A.9}$$

there is an angle of incidence that causes a critical refraction, known as the critical angle (θ_c). Critically refracted energy is refracted at 90° and travels along the interface boundary within the faster medium. By setting $\theta_2 = 90°$,

$$\frac{\sin\theta_c}{\sin 90} = \frac{V_1}{V_2} \quad , \tag{A.10}$$

$$\theta_c = \sin^{-1}\left(\frac{V_1}{V_2}\right) \quad , \tag{A.11}$$

θ_c is solved.

In Fig. A.2, $\theta_i = \theta_r = \theta_c$. A critical refraction occurs along the free-surface boundary when this equality is satisfied. The critical distance (x_c) can be solved,

$$x_c = h \cdot \tan\theta_c \quad , \tag{A.12}$$

when θ_c and h are known. The refraction path length

$$l_c = x - x_c \quad , \tag{A.13}$$

and the NMO reflection path length $2l_r$, where

$$l_r = \sqrt{\left(\frac{x_c}{2}\right)^2 + h^2} \quad , \tag{A.14}$$

are summed to calculate the refracted raypath length

$$l = 2l_r + l_c \quad . \tag{A.15}$$

The travel-time

$$t_c = \frac{2l_r}{V_s} + \frac{l_c}{V_a} \quad , \tag{A.16}$$

from Tx to Rx is calculated for any offset beyond x_c.

Travel-times calculated from this model can be used to identify the refracted waves in Fig. 2.4. Residual travel-time corrections are not applied to Fig. 2.4. Add these approximate travel-time corrections to the data gather when comparing the modeled travel-times: $(4\ m) \sim 1\ ns$, $(8\ m) \sim 1.5\ ns$, $(12\ m) \sim 3\ ns$. For reference, 0.5 wavelet cycles is ~ 0.5 ns.

A.3 Parameter Estimation: Depth, Density, and SMB

The wave propagating along the ice sheet surface is estimated to respond to snow depths no greater than the wavelength

$$z_{LMO} = \frac{V_{LMO}}{f} \quad , \tag{A.17}$$

calculated from the nominal radar frequency ($f \approx 500\ MHz$) and snow velocity (V_{LMO}). Eq. (A.17) was developed on Occam's razor. This simple approximation for

the penetration of the surface coupled wave was found to be consistent with the depth and average density measured at GTC15 and Pit 15 W. The depth of the reflection horizon for a subsurface propagating wave

$$z_{NMO} = \frac{V_{NMO} \cdot t_0}{2} \quad , \tag{A.18}$$

is estimated assuming that the NMO approximation is valid, meaning that V_{NMO} is approximately equal to the average velocity above the horizon.

The complex refractive index method (CRIM) equation relates a mixture of known dielectric properties to an estimated effective bulk property (Wharton *et al.*, 1980). We estimated the average snow density from the EM velocity by the CRIM equation

$$\rho_s = \rho_i \left(1 - \frac{V_a(V_i - V_s)}{V_s(V_i - V_a)}\right) \quad , \tag{A.19}$$

letting the snow and firn pore space be unoccupied free space with the velocity $V_a = 0.2998\ m/ns$ and the matrix to be composed of only ice with EM velocity $V_i = 0.1689\ m/ns$, and density $\rho_i = 917\ kg/m^3$ (Ulaby *et al.*, 1986). The quantities are given the subscript a for air, i for ice, or s for snow and firn. Liquid water within the firn layer was neither present within snow pits nor firn cores sampled during this field study, and is therefore not considered in Eq. (A.19).

Surface mass balance is conventionally measured using GPR by interpreting a select few IRHs using a constant age interval and applying the average normalized snow and firn density over this interval (e.g. Lewis *et al.*, 2019). Instead, we rely on the models of density and age, which are discretized in depth at a comparable resolution to the GPR data. We measured instantaneous SMB ($\dot{b}$), in meters of water

equivalent per an infinitesimal time

$$\dot{b} = \frac{\rho_s}{\rho_w} \frac{\mathrm{d}z}{\mathrm{d}a} \quad , \tag{A.20}$$

as the product of the snow and firn density, normalized by the density of water (ρ_w), and the submergence rate of stratigraphic isochrones $\left(\frac{\mathrm{d}z}{\mathrm{d}a}\right)$ in a Lagrangian reference frame. The submergence rate is the continuous equivalent of interpreting a few horizons with large age intervals. In practice, we approximated this derivative using second-order accurate finite difference weights calculated from the Fornberg (1988) algorithm, because the age-depth model is not discretized in regular intervals. The median discrete interval of the age-depth model is 14 days with a minimum interval of seven days and a maximum interval of 20 days. We found that the local truncation error of the second-order accurate derivative was 5×10^{-5} m $w.e.$ a^{-1}, which has a leading error term an order of magnitude less than what we consider to be significant.

A.4 Parameter Uncertainty: Monte Carlo Bootstrapping and Error Propagation

To ascertain the uncertainty in the radar inversion, we implemented a bootstrapping algorithm by randomly sub-sampling the CMP travel-times from the LMO and NMO horizons and re-solving the linear regression. In a roll-along fashion, travel-time observations of five neighboring CMP gathers were binned and re-sampled by removing two offsets at random and then randomly sampling one travel-time observation for each remaining offset in the bin. This algorithm creates many realizations of the intercept time and snow velocity by the jackknife technique (Efron & Stein,

1981). Realizations of depth and density were generated from the current realization of $\mathbf{m}$ following Equations (A.17) – (A.19). The bootstrapped distribution $\widehat{\mathcal{M}}$ was generated from 1000 jackknifed realizations to establish uncertainty regions (Efron & Tibshirani, 1986). A distribution was gathered for each parameter: intercept travel-time, velocity, depth, and density. The mean of $\widehat{\mathcal{M}}$ yields the expected value of the parameter ($\widehat{m}$) with a standard deviation ($\widehat{\sigma}$). We developed uncertainty regions for each bootstrapped distribution assuming the standard normal distribution

$$\widehat{m} \pm \widehat{z}\,\widehat{\sigma} \quad , \tag{A.21}$$

and assessed the z-score at $\widehat{z} = 1$, which has the central interval of $1\widehat{\sigma}$ (Efron & Tibshirani, 1986). The jackknifed estimates of variance for snow density and depth provide the means to estimate uncertainty in the $2015 - 2017$ SMB. We estimated the variance of SMB by the linear error propagation equation

$$\widehat{\sigma}_b^2 = \widehat{\sigma}_z^2\rho^2 + \widehat{\sigma}_\rho^2 z^2 + 2\widehat{\sigma}_{\rho z}\rho z \quad , \tag{A.22}$$

where the covariance $\widehat{\sigma}_{\rho z}$ was calculated from the parameter distributions. The resulting uncertainty measure is the standard interval developed from Eq. (A.21). The snow parameters and uncertainties presented in Fig. 2.5 were smoothed using a Gaussian kernal with a standard deviation of 250 m.

As we presented in Fig. 2.9, we propagated uncertainties in SMB by Monte Carlo simulation, which incorporated the uncertainty in the age of dated isochrones ($\sigma_a = \pm 31$ days) and the uncertainties in the snow parameters used to generate the firn model (Appendix A.5). We estimated the ± 31 day uncertainty by summing in

quadrature the uncertainties in the firn core age (±18 days; Rupper *et al.* (2015)) and the radar estimated depth that was mapped to the GTC15 age-depth scale (±25 days) developed by Lewis *et al.* (2019). We delimited the annual SMB calculation between January 1, 1984 and January 1, 2017, which are the complete years between the date of the earliest layer picked and the date of data acquisition. We filtered the outlying 1% of the instantaneous SMB model and interpolated between neighboring values. We quantified annual average SMB and its uncertainty using Monte Carlo simulation, by generating 1000 randomly initialized density-depth models (Appendix A.5) from the snow parameter distributions. Rather than randomly generating an age model in this process, because we updated the age-depth model by interpreting IRHs (Appendix A.6), we interpolated the age model to the depth axis that was defined by the Monte Carlo realization of the density model. We calculated the numerical derivative to estimate the instantaneous SMB (Eq. (A.20)), extracted the intervals that composed each annual layer, and averaged the samples of instantaneous SMB into one realization of annual SMB. After 1000 realizations were generated for each of 33 years in the period $1984 - 2017$, we calculated the multidecadal mean SMB and variance using Monte Carlo resampling. Repeating for 1000 simulations, we randomly sampled an annual SMB realization from 10 annual intervals and averaged. In the following section, to clarify the capabilities of the radar analysis we ignore the uncertainties in the firn core ages and demonstrate the radar inversion as the only source of uncertainty in SMB when paramertizing the MxHL model.

A.5 Parameterizing the MxRadar - Herron & Langway (1980) Model

The Herron & Langway (1980, HL) model requires three parameters: mean snow density, mean annual accumulation, and 10 m firn temperature. We use the snow properties estimated by the radar inversion (Fig. 2.5) and MERRA reanalysis temperature to parameterize the HL model in our measured-modeled, MxRadar-HL, framework. We chose the density parameter as the average of the densities estimated by the surface-wave (LMO) analysis and the reflected wave (NMO) analysis of the fall 2014 isochronous reflection horizon (IRH). We approximated the accumulation parameter using the radar estimated SMB (Eq. (A.20)) that represented the average of the previous ~ 2.5 years – as the IRH depth indicates the date November 30, 2014, established by the firn core analysis, and the date of acquisition was June 13, 2017. Mean annual 2 m air temperature was calculated from MERRA $(1979 - 2012)$ data (Birkel, 2018) and used as a proxy for 10 m firn temperature (Loewe, 1970). MERRA annual temperatures at GTC15 over the period $1979-2012$ show an increase of $0.06\pm0.01\ ^{\circ}C\ a^{-1}$ with a mean of $-25.7 \pm 1.0\ ^{\circ}C$.

We evaluated the MxHL parameterization by comparing it to the GTC15 parametization (Fig. A.3) and an optimum set of parameters that were determined by minimizing

$$\phi = \frac{\mathrm{RMS}(\tau_{HL} - \tau_{GTC15})}{\mathrm{range}(\tau_{GTC15})} + \frac{\mathrm{RMS}(\rho_{HL} - \rho_{GTC15})}{\mathrm{range}(\rho_{GTC15})} \quad , \tag{A.23}$$

using the Nelder & Mead (1965) method (NM) for nonlinear optimization. The objective function ϕ (Eq. (A.23)) measures the root-mean-squared error of the modeled

(HL) and measured (GTC15) age ($\mathcal{T}$) and density (ρ) as a percentage, normalized by the range in the data for the entire depth of GTC15 ($\sim 28.5\ m$). An objective function measured by either $\mathcal{T}$ or ρ individually does not contain a unique global solution upon minimization. We found that an appropriate fit to GTC15 $\mathcal{T}$ or GTC15 ρ could be achieved with a range of parameterizations, alluding to the non-uniqueness which we regularized by minimizing ϕ as a function of both the age and density.

Average SMB, density, and 10 m bore hole temperature measured at GTC15 provided the true parameterization for the HL model. The age-depth scale (1969-2017) was measured by analyzing seasonal oscillations of δ^{18}O, major ions, and dust observed in the firn core (Lewis *et al.*, 2019). Annual SMB was measured by combining the age-depth scale with the firn density (Lewis *et al.*, 2019). We estimated the GTC15 mean annual SMB using Monte Carlo resampling to assess uncertainties ($0.306 \pm 0.021\ m\ w.e.\ a^{-1}$). We chose the GTC15 density parameter ($359 \pm 36\ kg/m^3$), which is the "commonly reported average density over the first one or two meters of snow" (Herron & Langway, 1980, p. 7), at the interval that had the minimum residual with the optimum density. The central depth of the core interval nearest to the optimal density is $1.22 \pm 0.13\ m$. Uncertainties in the density parameter are assumed to be within 10% of the measurement. We measured firn temperatures using borehole thermistors at 6, 8, 10, 12, and 14 m depth. After the thermistor string reached equilibrium, temperatures between 6 and 14 m depth closely agreed and we used Monte Carlo resampling to estimate the 10 m firn temperature ($-24.9 \pm 0.2\ ^\circ C$).

The HL model parameterized by GTC15 data yielded $\phi = 6.4\%$, which is near the optimum $\phi = 6.2\%$. The MxHL parameters obtained in the vicinity of GTC15 achieved an agreeably close fit with $\phi = 7.0\%$. Table A.1 summarizes the three

HL model parameterizations and their accuracy. Figure A.3 displays the MxHL parameters overlaid on slices of Eq. (A.23) through the GTC15 parameters.

We completed the radar analyses using the MxHL model after making the following adjustments. We refined the density model using the LMO and NMO derived densities and depths to estimate the snow density-depth gradient. Using a linear model we replaced the upper one to two meters of the HL model with a piecewise segment that was extrapolated to the surface and merged with the HL model at the intersecting depth in the snow. We also refined the age model and improved the radar image quality using structure-oriented filtering (see section A.6).

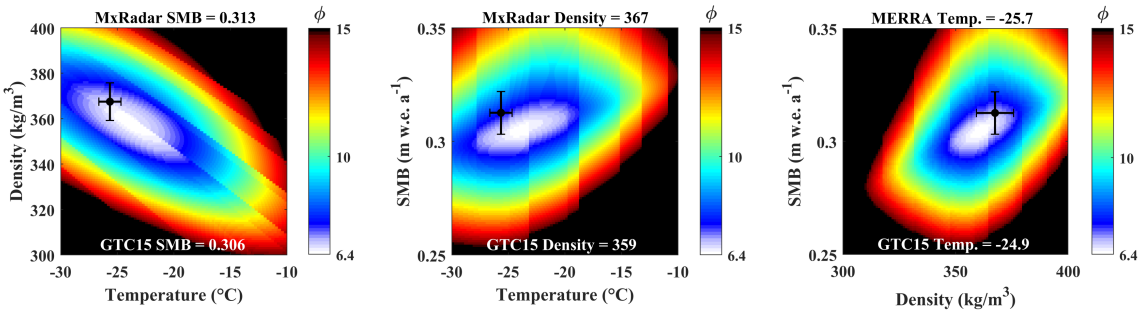

Figure A.3: Equation A.23 is represented as slices through the GTC15 parameterization. Viewing the 3D objective function this way shows the model sensitivity to the parameters. The MxHL parameters are evaluated against the GTC15 parameterization with 1σ uncertainties. These data are summarized in Table A.1.

Table A.1: HL parameters from MxRadar (MxHL), GreenTrACS Core 15 (GTC15), and Nelder & Mead (1965) optimization (NM) are compared. Uncertainties in the GTC15 and MxHL parameterizations are expressed at 1σ. Accuracy is reported for the modeled age (ϕ_τ) and density (ϕ_ρ) as the rms error and jointly as the normalized summed rms error ϕ.

Parameters	$\dot{b}$ (m w.e. a^{-1})	ρ (kg/m^3)	T (°C)	τ_{RMSE} (a)	ρ_{RMSE} (kg/m^3)	ϕ (%)
MxHL	0.313 ± 0.009	367 ± 8	-25.7 ± 1.0	0.528	20.2	7.0
GTC15	0.306 ± 0.021	359 ± 36	-24.9 ± 0.2	0.40	20.0	6.4
NM	0.306	358	-23.1	0.350	19.0	6.2

A.6 Structure-oriented Filtering in the Wheeler Domain

Accumulated snow is deposited in isochronous layers that propagate slowly as the firn stratigraphy evolves and are apparent in the radiostratigraphy (Arcone *et al.*, 2005; Ng & King, 2011). However, as demonstrated in this study, larger amplitude stratigraphic undulations with wavelengths of $\lessapprox 5\ km$ exhibit reduced coherence in the GPR imaging, an effect that is worsened by increased surface roughness. As described by Arcone *et al.* (2004), artificial fading in the GPR image along the limbs of stratigraphic folds also interrupts the horizon continuity. The fading effect can be seen in Fig. 2.8 as a discontinuity in the inflection point of a fold at 48 km distance and $\sim 11\ m$ depth. It is important to accurately capture SMB variability at $< 5\ km$ for evaluating downscaled surface mass balance models, but as we demonstrate, this effort would be limited to only a few horizon selections here because of noise contamination in the radar section.

Structure-oriented filtering techniques often determine the structure from the time or depth image by localized eigenvalue decomposition of the image gradient tensor, such as filters applying nonlinear anisotropic diffusion (Fehmers & Höcker, 2003). We imposed the isochrone structure on the image, using the age model as a proxy for the stratigraphic structure. We flattened the firn structure by converting the time domain GPR image into coordinates of stratigraphic age, known as the Wheeler (1958) domain. We then applied linear prediction filtering, because flattening the traces improves their predictability by linear modeling. Conversion to stratigraphic coordinates can be achieved using plane wave deconstruction filters to determine local

slope fields from the image (Karimi & Fomel, 2015). But it is to our advantage to work with the stratigraphic age because this information is necessary for SMB calculations. We found our approach outperformed filters that determine the structure orientation directly from the noisy image.

To implement the structure-oriented filter, we produced a noisy time domain radar section from the multi-channel imagery (Fig. 2.7) by first transferring the measured-modeled firn density to stacking velocity (V_{NMO}) and then applying normal moveout correction and offset stacking (Yilmaz, 2001). Provided that the radiostratigraphy in depth mimics the firn layering and is isochronous (e.g. Spikes *et al.*, 2004), we used the HL age-depth model to estimate the firn structure orientation and age. To do so, we first converted the age model from depth to travel-time (Fig. A.4) by a vertical stretch (Margrave & Lamoureux, 2019) using the stacking velocity model. We created a pseudo stacking velocity model (V_{pseudo}) with units of years per nanosecond by dividing the age-travel-time model by the two-way travel times. Then we converted the radar image from travel-time to the Wheeler domain by a vertical stretch using V_{pseudo} (Fig. A.5). We oversampled in the Wheeler domain to prevent signal aliasing. The age converted radargram has approximately flattened stratigraphy, such that any row of the image is isochronous. If we knew the structure orientation perfectly, and radar isochrones truly had the same age, the layers in the Wheeler domain would be theoretically flat. By picking, we calculated the residual age of five IRHs with an average epoch of 5.3 ± 2.7 years (the latest being the 1991 horizon) and used 1D shape preserving piecewise interpolation polynomials (Kahaner *et al.*, 1989) to create a grid of perturbations for the age-travel-time model (Fig. A.6). Perturbations beyond the last picked horizon were set to zero. We applied the perturbations to the

age model and re-flattened the image by stretching the traces to the updated age model (Fig. A.7). Radar amplitudes are now approximately horizontal across each row of the Wheeler domain image, indicating that the age-travel-time model fits the firn structure and IRH theory.

We applied the fx-deconvolution noise suppression algorithm (Gulunay, 1986) to the Wheeler domain radargram (Fig. A.8). Fx-deconvolution relies on autoregression modeling of the GPR signal in the frequency domain to build the optimal complex Wiener filter (Treitel, 1974). We applied the filter by averaging overlapping computations along the age axis to alleviate non-stationarity of the signal frequency. This process can benefit any GPR imagery of polar firn, provided that an initial stratigraphic age model, as a proxy for the structure, and methods to convert the image domain are available. At GTC15 Spur West, due to the large spatial gradient in SMB, it was necessary to determine the model residual and re-flatten the image before filtering. For GPR imagery expressing small or gradual SMB variability it may be sufficient to apply the structure-oriented filter without residual corrections to the Wheeler image.

A.7 Depth Imaging for Model Updates

We converted the updated age-travel-time model to depth using the stacking velocity model and then we used the age-depth model to convert the Wheeler domain image to depth. We applied a vertical stretch for each conversion operation (Margrave & Lamoureux, 2019). Figure 2.8 reveals the smooth and continuous IRHs of the depth image. The additional step of structure-oriented filtering extended the interpretable isochrone record from 1991 to 1984 (which is only limited by the time-window range of the radar acquisition). We picked 16 IRHs on the depth image with

an average epoch of 2.1 ± 1.7 years. Over an equivalent depth range, this compares to the seven IRHs at five year age resolution used by Lewis *et al.* (2019) to estimate SMB along GTC15 Spur West. In the vicinity of GTC15 the residuals between the GTC15 age-depth scale and the picked IRH ages were calculated. We created a second set of age perturbations using 1D linear interpolation with linear extrapolation to estimate perturbations beyond the deepest picked IRH (Fig. A.9), and we applied these perturbations to update the age-depth model. We then used the updated age model to calculate the instantaneous SMB.

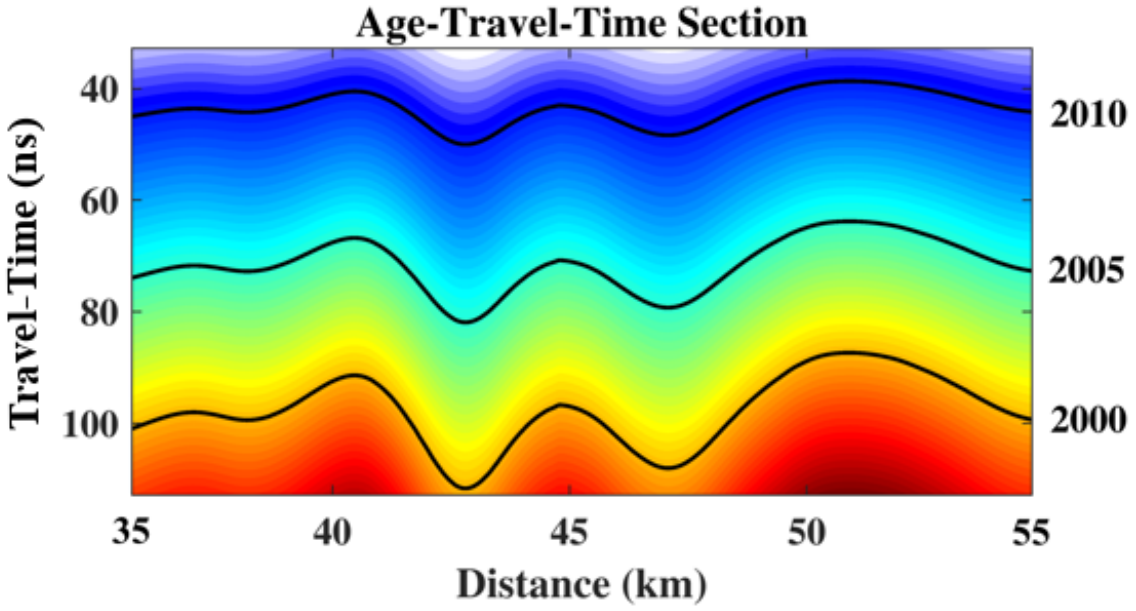

Figure A.4: The age-travel-time model was calculated from pseudo velocities. Contours of this image are isochronous travel-time horizons. January 1, 2010, 2005, and 2000 are labeled for reference. We used the age-travel-time model to flatten the radar traces, by converting the time domain image into the age domain (Fig. A.5).

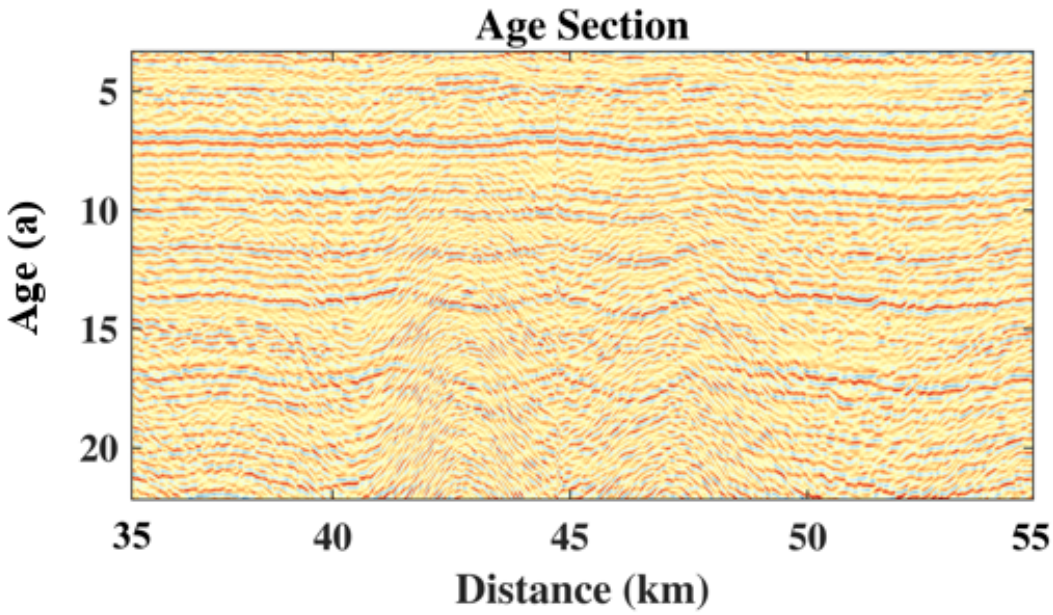

Figure A.5: Using the initial age model, the Wheeler domain radargram has minor remnant undulations. Because the rows of the Wheeler image are isochronous, the undulations that deviate from row-wise horizontal are the model residual. If the age model was correct the radar reflections would be entirely horizontal (Fig. A.7). By interpreting five horizons of this image, we interpolated the model residual (Fig. A.6) and applied these perturbations to update the age model such that it is accurate in a relative sense.

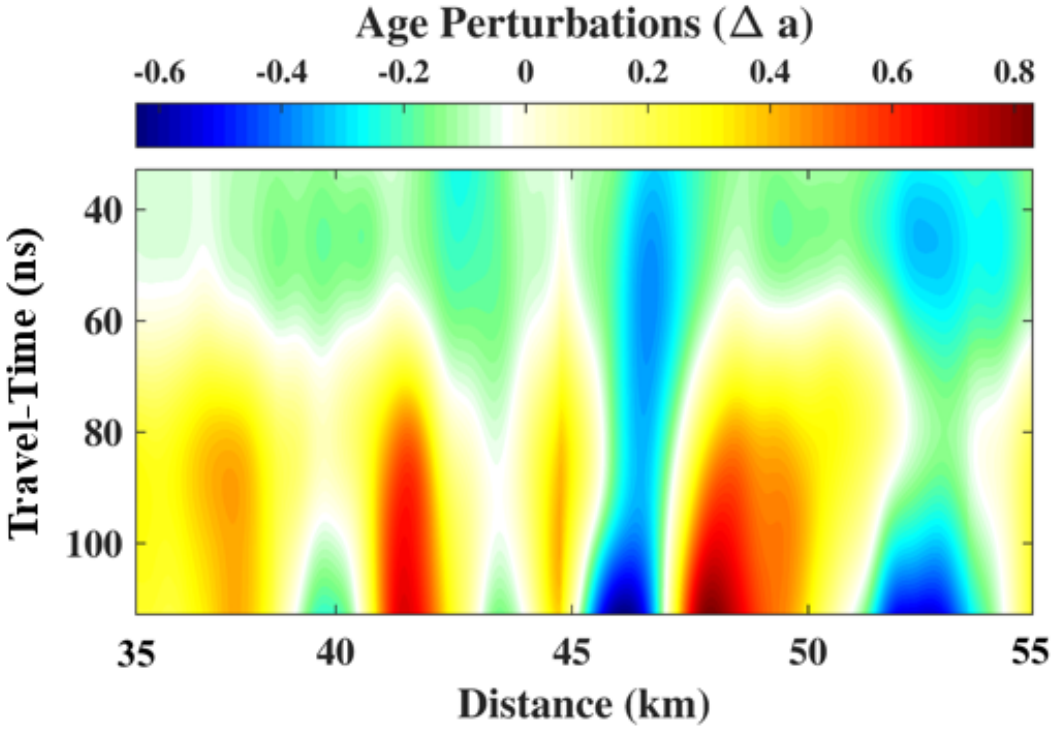

Figure A.6: Perturbations in the travel-time domain are calculated by picking IRHs in Fig. A.5. When applied, the Wheeler domain image is reflattened (Fig. A.7), which ensures that the age model is accurate in a relative sense. We rely on ages measured from the firn core for absolute accuracy in the age model.

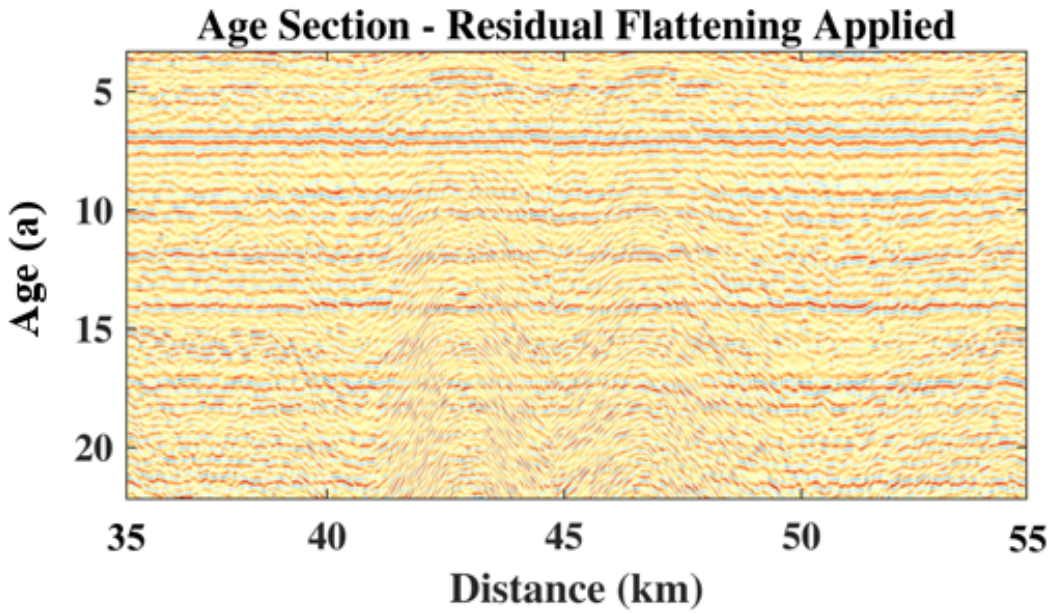

Figure A.7: After interpreting five horizons of Fig. A.5, calculating the model residual (Fig. A.6), and applying the perturbations to the age-travel-time model (Fig. A.4), we re-flattened the Wheeler image. The radar amplitudes are now approximately horizontal, indicating that the updated age model is accurate according to the IRH theory.

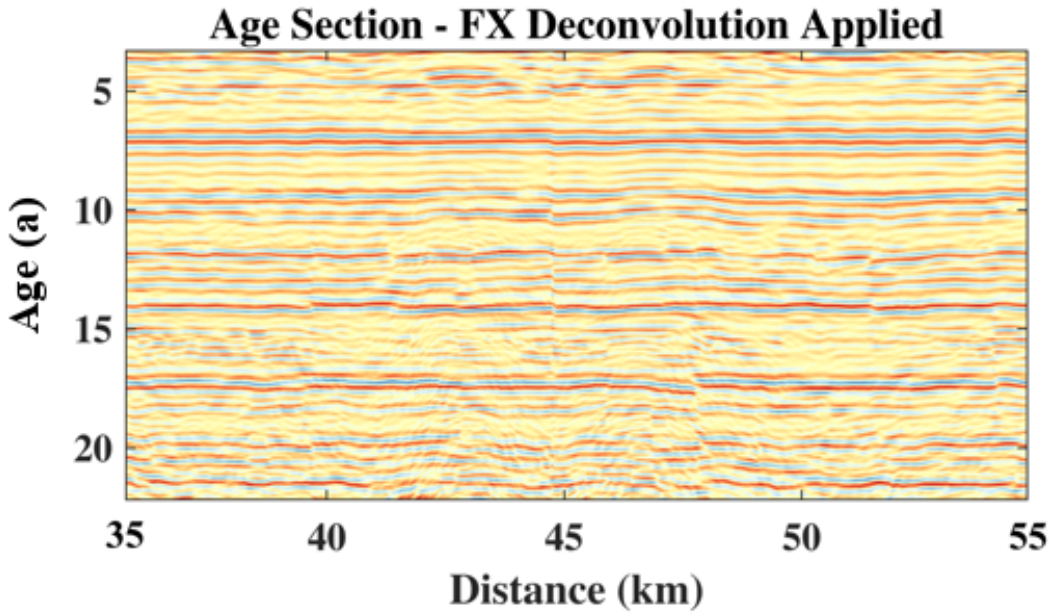

Figure A.8: Flattening the traces improves their predictability by linear modeling. We applied the fx-deconvolution algorithm (Gulunay, 1986) to suppress the random noise that contaminates the linearly predictable signal.

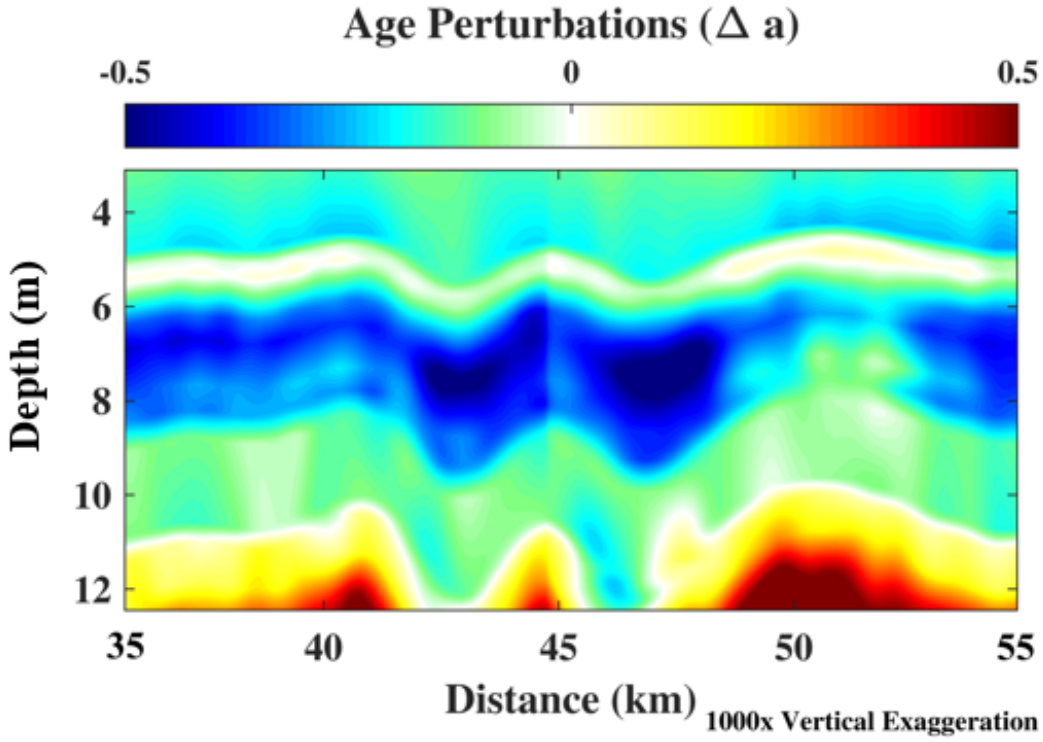

Figure A.9: We interpreted 16 IRHs of Fig. 2.8 to measure their relative age at depth. We calculated the residual between our interpreted ages and the ages measured from GTC15 and interpolated this grid of perturbations in the depth domain. We applied these perturbations to the age-depth model which was used to calculate the SMB time-series. Applying this set of perturbations makes the relative age-depth model accurate in an absolute sense.

APPENDIX B:

SPATIALLY DISTRIBUTED SNOW WATER EQUIVALENT FROM GROUND-BASED AND AIRBORNE SENSOR INTEGRATION AT GRAND MESA, COLORADO, USA

B.1 Evaluation of GPR TWTs

We evaluated the accuracy of the automatically determined travel-times at 870 intersections of the gridded GPR transects (Figure B.1). Travel-times from these cross-over locations were initially collected within a 1 m radius and then split based on the time interval separating the repeated passes. We chose an interval of 10 seconds to distinguish between the cross-over acquisitions. For each cross-over the median TWT was selected. The correlation between the median GPR TWTs at the cross-over locations is $R = 0.8$ with root-mean-square error (RMSE) of 0.9 ns and mean error of 0.0 ns.

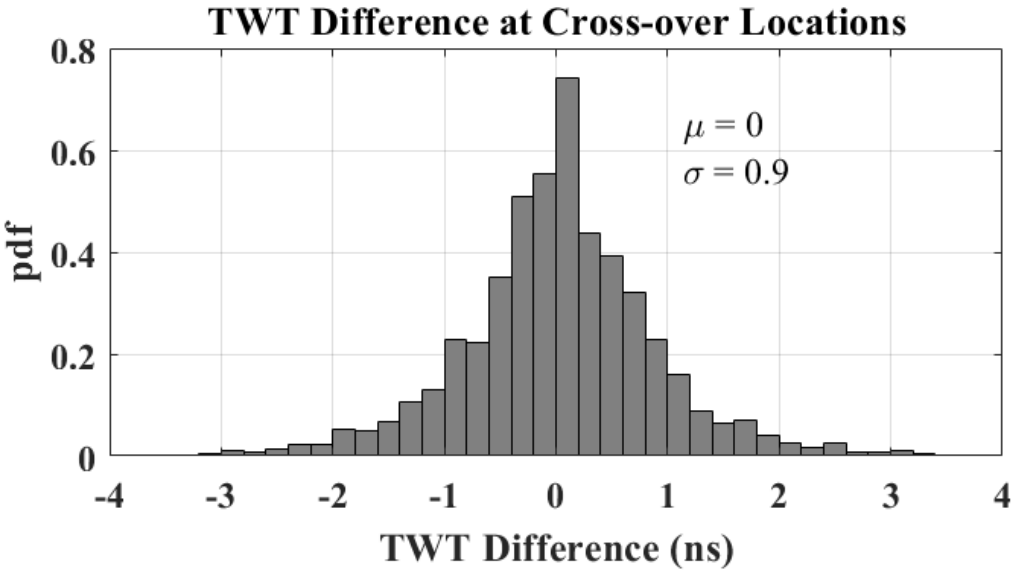

Figure B.1: The histogram of the difference in TWT at the 870 intersections of the gridded GPR transects has a mean of 0.0 ns **and** RMSE = 0.9 ns**.**

B.2 Evaluation of GPR and LiDAR Inferred Density

We conducted a sensitivity analysis to evaluate how the errors in radar travel-time and LiDAR snow depth affect the estimated snow density. This involved establishing a level curve through the average snow values of the unforested area (mean density 295 kg/m^3, mean TWT 8 ns, mean snow depth 96 cm) and applying perturbations to these values to excite the density error (Figure B.2). Perturbations of up to ± 1 ns were added to the TWT and ± 15 cm were added to the depth. After the perturbations were applied, to measure the density perturbations, the densities were evaluated and the mean (295 kg/m^3) was subtracted from this result. The error bars of Figure B.2 represent the reported LiDAR error (7 cm) and the RMSE of the GPR TWT cross-overs (0.9 ns). At the 1-sigma level, errors of approximately ± 150 kg/m^3 can be expected from this method – where the GPR TWTs contribute a maximum error in density that is roughly 30 % greater than that stemming from the errors in the LiDAR measured snow depths.

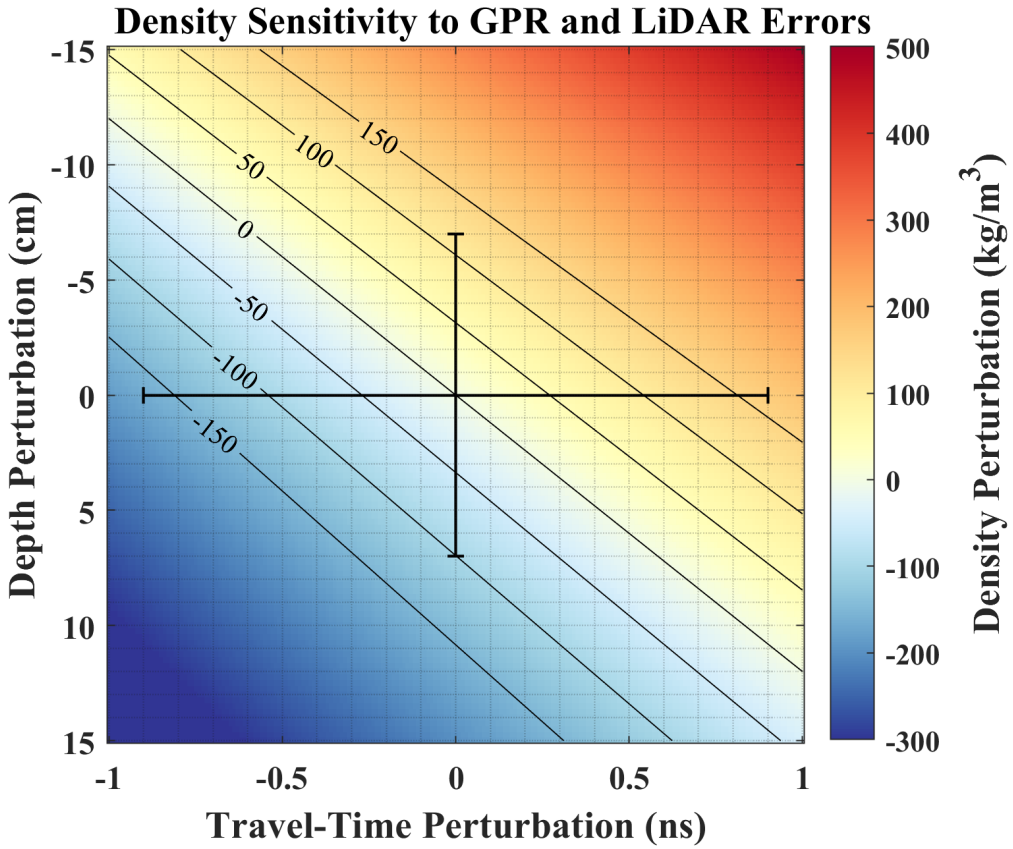

Figure B.2: Perturbations of up to ± 1 ns and ± 15 cm were added to the mean values, 8 ns TWT and 96 cm depth. The density was evaluated then subtracted from 295 kg/m^3 to measure the density perturbation. The error bars represent the reported LiDAR error and the RMSE of the GPR TWT cross-overs. Combined errors of ± 150 kg/m^3 can be expected from this method, with the GPR TWT contributing about 30 % greater error than the LiDAR snow depth.

B.2.1 Error Reduciton

The measurement errors in LiDAR elevations and GPR TWTs may translate to errors in density that are larger than the range of densities observed in the snow pits. To extract a meaningful density signal, we reduced the random error by filtering outliers. We chose the interquartile range (IQR) of the LiDAR – GPR inferred densities as the threshold for determining outliers, because the 25 % and 75 % quantiles approximately agreed with the range of snow density observed in the snow pits. The

outliers were uncorrelated spatially and temporally, as evidence that the errors are random and can be treated with filtering. We applied a 2D median window with a 12.5 m radius (chosen to approximately match the resolution of the GPR grid nodes) to smooth the densities within the IQR and interpolate those at the outlying locations. Outlier filtering reduced the RMSE from roughly 150 kg/m^3 to under 30 kg/m^3.

B.3 Multiple Linear Regression

We applied multiple linear regression to predict the average snow density estimated by the integration of snow depths and TWTs from the LiDAR and GPR data, using terrain and vegetation features developed from LiDAR rasters as predictors. The MLR model has the form

$$y = X\beta + \epsilon \quad , \tag{B.1}$$

where y is the observed density along the GPR transects, X is a matrix with columns containing the normalized LiDAR predictors at the coordinates along the GPR transects, β is the vector of the regression coefficients which we must estimate, and ϵ represents the model residual. The process of model training is described in Section B.3.1 and our method of determining the most important predictors follows in Section B.4.

B.3.1 Parameter Estimation

From the method of least squares, the regression coefficients are estimated as

$$\beta = (X^T X)^{-1} X^T y \quad . \tag{B.2}$$

Using cross-validation to assess the model accuracy and sensitivity, we estimated the MLR model parameters. We trained the model with 1000 Monte Carlo simulations

by randomly sampling 90 % of the density observations and testing on the remaining 10 %. Additionally, we repeated this process and randomly sampled only 10 % of the data and tested on the remaining 90 %. In doing so, we created two sets of parameters that robustly span the parameter space. The parameter estimates and the bootstrapped estimates of the standard deviations (Efron & Tibshirani, 1986) for the 90 % training ($\beta_{90}, \sigma_{\beta 90}$) and the 10 % training ($\beta_{10}, \sigma_{\beta 10}$) are presented in Table B.1. Using these regression coefficients, Equation 1 is computed to distribute the predicted densities. The modeled densities are insensitive to the training choice for parameter estimation, as the RMSD between the two models is less than 1 kg/m^3.

Table B.1: The MLR parameters were evaluated with cross-validation of 1000 Monte Carlo simulations to assess the model sensitivity. Cross-validation used 90 % training data (β_{90}), 10 % test data, and was repeated with 10 % training data (β_{10}), 90 % test data. The parameter values and their standard deviations ($\sigma_b eta$) estimated via Monte Carlo simulation are reported.

Predictor	$\beta_{\mathbf{90}}$	$\sigma_{\beta \mathbf{90}}$	$\beta_{\mathbf{10}}$	$\sigma_{\beta \mathbf{10}}$
ρ_0	277.27	0.03	277.30	0.25
H_s	0.48	0.03	0.48	0.27
$aspectH_s$	0.08	0.04	0.06	0.34
$slopeH_s$	3.27	0.02	3.25	0.24
∂yH_s	-0.56	0.02	-0.57	0.23
∂xH_s	-0.96	0.03	-0.95	0.28
Z_s	-43.23	2.56	-40.94	25.04
$aspectZ_s$	-0.88	0.04	-0.89	0.40
$slopeZ_s$	2.71	0.05	2.67	0.55
∂yZ_s	5.98	0.16	5.97	1.59
∂xZ_s	-0.20	0.17	-0.24	1.52
Z_g	13.01	2.56	10.73	25.02
$aspectZ_g$	1.18	0.04	1.18	0.40
$slopeZ_g$	-7.17	0.05	-7.16	0.52
∂yZ_g	11.25	0.16	11.27	1.58
∂xZ_g	-10.86	0.18	-10.81	1.61
H_{veg}	-0.87	0.01	-0.87	0.09
S_{veg}	-4.94	0.03	-4.96	0.22

B.3.2 Snow Pit Density as Training Data

We learned that bulk density measured from 96 snow pits could be modeled using LiDAR spatial predictors that were extracted from a 3 m buffer around the pits, following the techniques outlined in Section B.3.1. The resulting regression coefficients were trained using 90 % random subsampling for the Monte Carlo parameter estimation. Because of the small sample size (N = 96) and sparseness, this model was sensitive to the choice of percentage used in training and buffer size around the snow pits. The density distributed from LiDAR predictors using the coefficients in Table B.2 is presented in Figure B.3.

The density distributed by the snow-pit-trained MLR model has a mean and standard deviation of $276 \pm 7\ kg/m^3$. The modeled density is uncorrelated with snow pit observations ($R = 0.18$), and exhibits accuracy ($RMSE = 21\ kg/m^3$) comparable to densities derived from the LiDAR–GPR observations, due to the low variance. When evaluated against SWE at the snow pits (Figure B.4), this model performed about as well as the LiDAR–GPR trained model ($R = 0.75$, $RMSE = 37\ mm$).

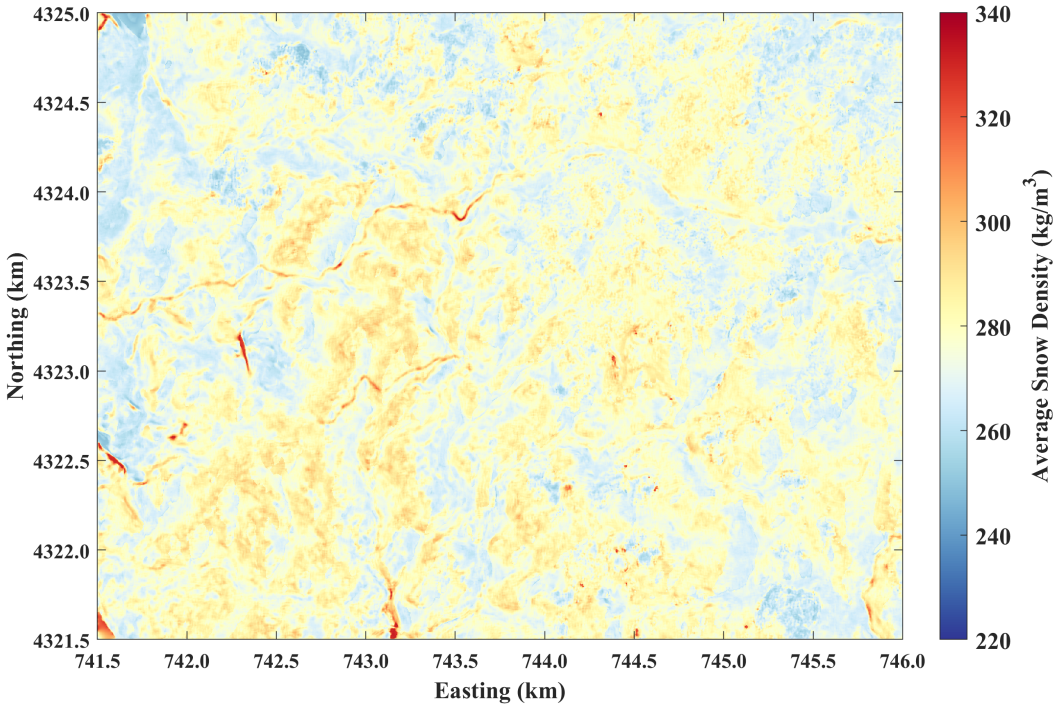

Figure B.3: The average snow density estimated by MLR, which was trained on snow pit density observations (N =96) and distributed by LiDAR spatial predictors.

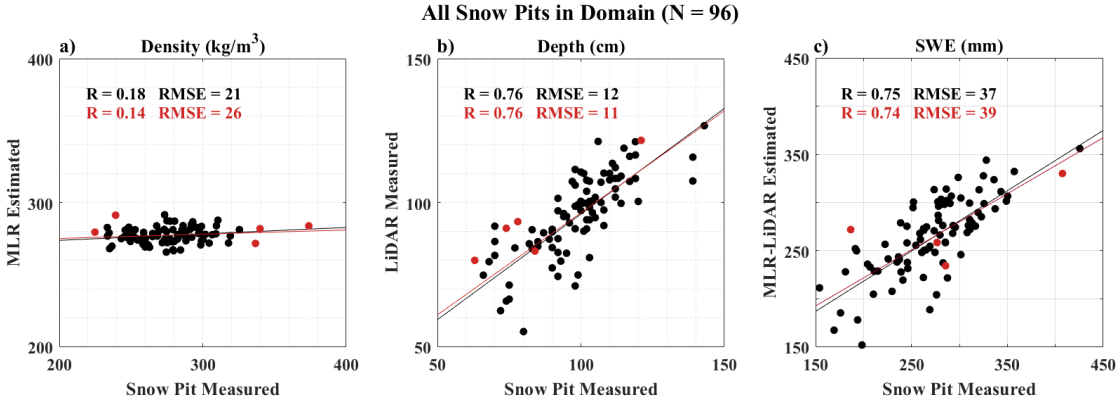

Figure B.4: *a*) **Snow density that was estimated by MLR trained on snow pit density observations,** *b*) **snow depth measured by LiDAR, and** *c*) **snow water equivalent estimated by multiplying the modeled density and measured depth are compared to the observations of the 96 snow pits that are within the** $4.5\ km \times 3.5\ km$ **domain. Red markers are outlying locations where the absolute difference between observed and modeled density exceeds** $50\ kg/m^3$**. The red trend line and statistics use all 96 data points, while the black trend line and statistics exclude the outliers.**

Table B.2: The regression coefficients for the model trained on 96 snow pit observations. Parameter uncertainties were developed from Monte Carlo Simulation with 90 % random sampling.

Predictor	$\beta_{\mathbf{snowpit}}$	$\sigma_{\mathbf{snowpit}}$
ρ_0	275.14	0.25
H_s	-0.27	0.28
$aspect H_s$	-3.55	0.38
$slope H_s$	4.87	0.28
$\partial y H_s$	-0.14	0.20
$\partial x H_s$	2.06	0.37
Z_s	92.05	10.61
$aspect Z_s$	4.21	0.27
$slope Z_s$	-9.10	0.58
$\partial y Z_s$	-2.80	1.05
$\partial x Z_s$	1.05	1.30
Z_g	-89.98	10.59
$aspect Z_g$	-2.12	0.19
$slope Z_g$	10.79	0.54
$\partial y Z_g$	1.18	1.05
$\partial x Z_g$	1.65	1.50
H_{veg}	1.95	0.18
S_{veg}	-0.74	0.06

B.4 Predictor Importance

We applied the "kitchen-sink" approach because the model that was trained using the LiDAR–GPR densities, which utilized every LiDAR predictor, exhibited the largest correlation ($R = 0.64$) to the observations. The best performing model trained on snow pit observations utilized only 12 parameters, however the 18 predictor model scored in the top 0.25 %, showing there are many possible parameter combinations that will yield equivalently high correlations. To assess the importance of the individual predictors, we assembled all combinations of 1 to 18 predictor models, solved the regression for each combination, and cross-validated against a test set of the observed

density. We considered optimal models as the top 1 % of outputs, and from these we tracked which predictors composed any model. We identified the relative importance of each predictor (Figure B.5), by summing the number of appearances for a given predictor and dividing by the number of optimal models.

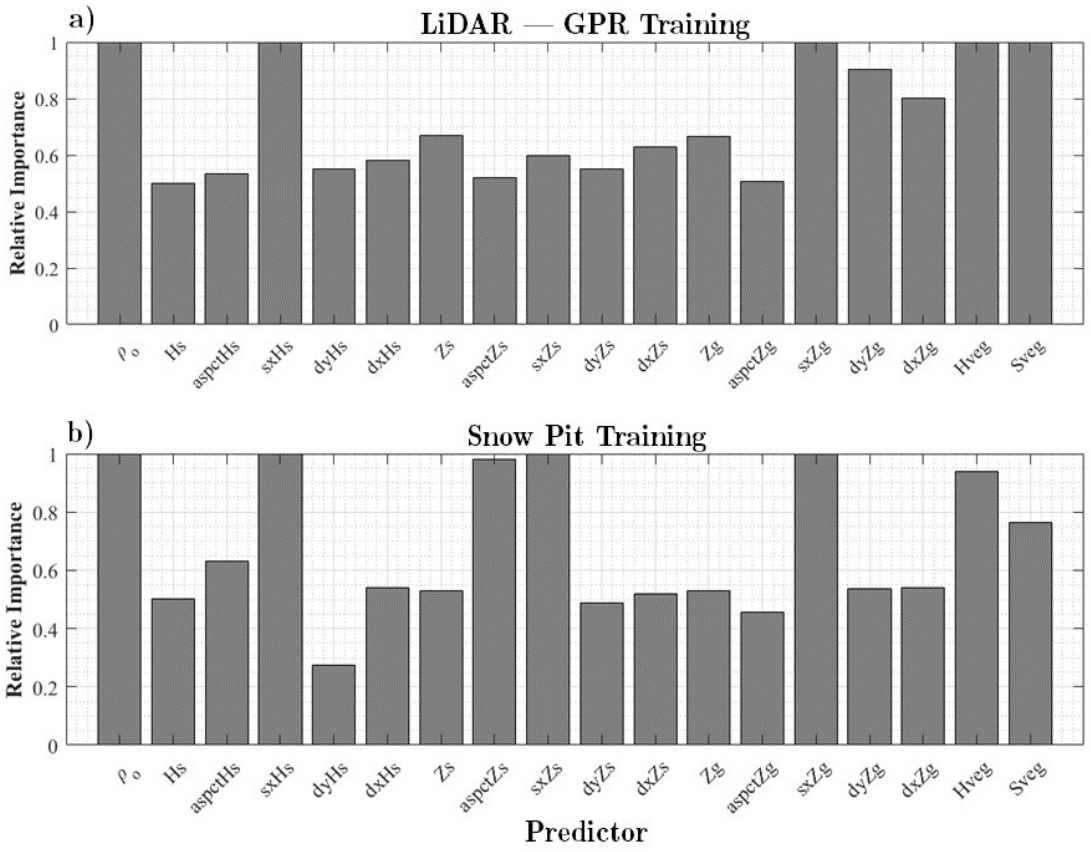

Figure B.5: The relative importance of the LiDAR derived predictors: ρ_0 intercept density, H_s snow depth, $aspctH_s$ aspect of snow depth, sxH_s slope of snow depth, ∂yH_s north component of snow depth gradient, ∂xH_s east component of snow depth gradient, Z_s the snow surface elevation and derivatives, Z_g the ground elevation and derivatives, H_{veg} vegetation height, and S_{veg} the distance to vegetation with height greater than $0.5\ m$. The predictor importance for a) the model trained on joint LiDAR and GPR data and b) the model trained on snow pit density measurements.

B.5 Evaluaiton of Depth, Density, and SWE in Forested and Unforested Areas

We evaluated the average snow density estimated from coefficients in Table B.1, LiDAR snow depth, and SWE within the unforested and forested areas to characterize the model performance. Of the 96 total snow pits in the 4.5 km x 3.5 km domain, there are 79 located in unforested areas ($H_{veg} < 0.5\ m$) and 17 located within the forest ($H_{veg} \geq 0.5\ m$). Outlying density values were identified by absolute differences exceeding 50 kg/m^3 and are marked red (Figure B.6). The correlation scores and RMSEs are presented with and without the influence of outlying data for summary. With fewer observations in the forest, the statistics are notably less robust than in the unforested domain.

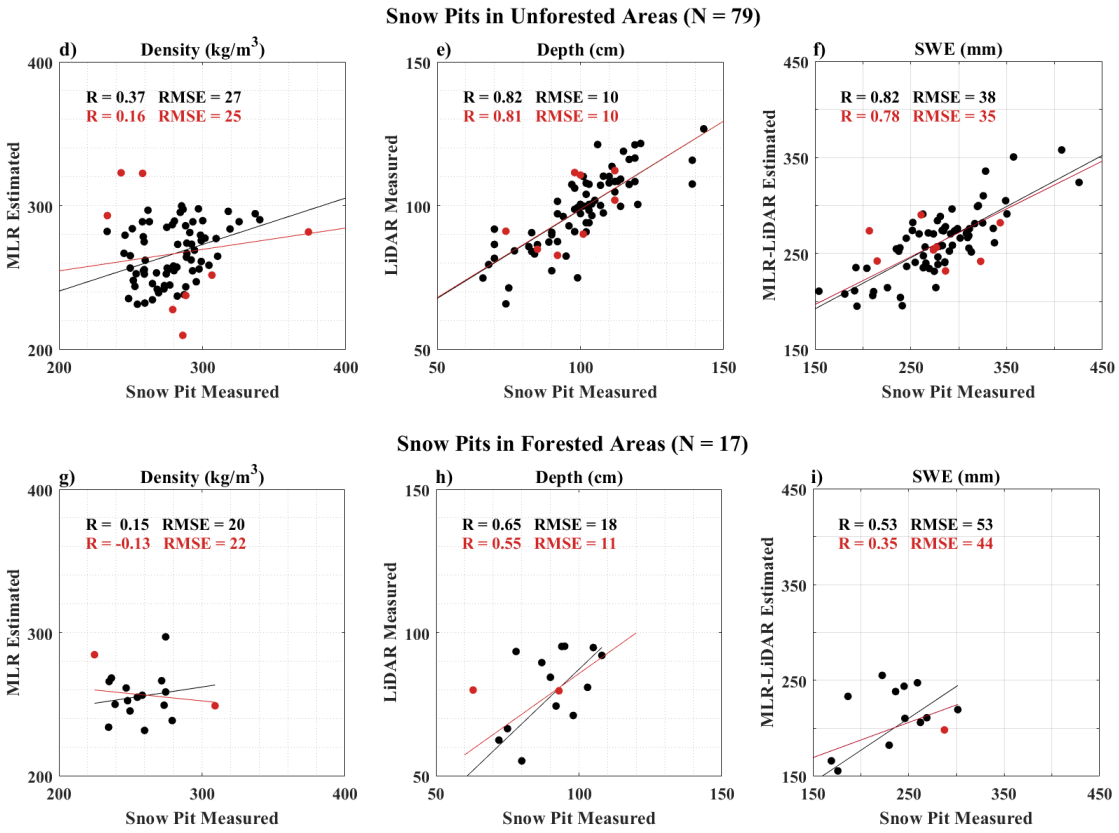

Figure B.6: Evaluation of d) density, e) depth, and f) SWE in unforested areas, and g) density, h) depth, and i) SWE in the forest. Red markers are outlying locations where the absolute difference between observed and modeled density exceeds $50\ kg/m^3$.

B.6 Wind Speed and Direction Observations

Hourly wind speed and direction data was downloaded from MesoWest for the Grand Mesa Skyway Study Plot (GMSP) Remote Automated Weather Station (University of Utah, 2022), and is presented in Figure B.7 for 20 October, 2019 through 12 February, 2020 (the dates spanning first accumulated snowfall through the ending date of the Grand Mesa IOP). Grand Mesa Skyway Study Plot (Longitude 108.06075°W, Latitude: 39.0593°N, Elevation: 3240 m) is located on the northeastern rim of Grand Mesa approximately 10 km east-northeast of our study domain. Winds out of the west-southwest are most frequent and have the maximum speeds. Weather information from the western end of Grand Mesa, would be more representative of our study site, as GMSP is sheltered by the forests of eastern Grand Mesa. However, GMSP is more representative than the next-nearby weather station, LSOS (Webb *et al.*, 2020), which is located on the northern slope of Grand Mesa and sheltered from the prevailing west-southwest wind.

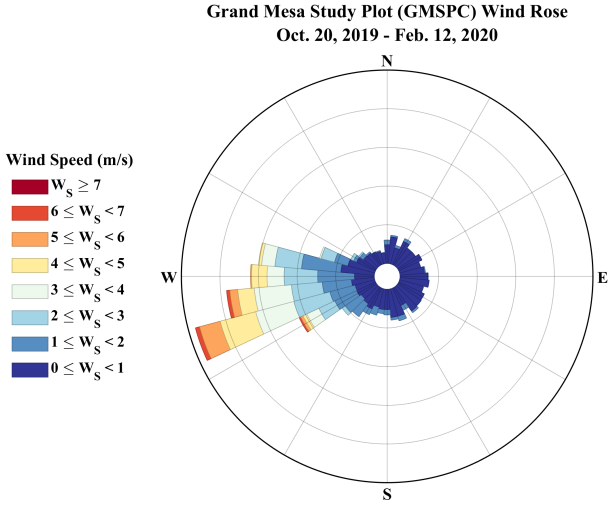

Figure B.7: Wind rose plots from hourly GMSP weather station observations for October 20, 2019 through February 12, 2020. The west-southwest wind direction prevails with the greatest number of observations and the maximum measured wind speed.